ADA278697

UNITED STATE AIR FORCE

SUMMER RESEARCH PROGRAM -- 1993

SUMMER RESEARCH PROGRAM FINAL REPORTS

VOLUME 6

ARNOLD ENGINEERING DEVELOPMENT CENTER
FRANK J. SEILER RESEARCH LABORATORY
WILFORD HALL MEDICAL CENTER

RESEARCH & DEVELOPMENT LABORATORIES

5800 Uplander Way

Culver City, CA 90230-6608

Program Director, RDL
Gary Moore

Program Manager, AFOSR
Col. Hal Rhoades

Program Manager, RDL
Scott Licoscos

Program Administrator, RDL
Gwendolyn Smith

Program Administrator, RDL
Johnetta Thompson

Submitted to: DTIC QUALITY INSPECTED 3

AIR FORCE OFFICE OF SCIENTIFIC RESEARCH

Bolling Air Force Base

Washington, D.C.

December 1993

Master Index for Faculty Members

Abbott, Ben
Research, MS
Box 1649 Station B
Vanderbilt University
Nashville, TN 37235-0000

Field: Electrical Engineering
Laboratory: AEDC/

Vol-Page No: 6- 1

Abrate, Serge
Assistant Professor, PhD
Mechanical & Aerospace En
University of Missouri - Rolla
Rolla, MO 65401-0249

Field: Aeronautical Engineering
Laboratory: WL/FI

Vol-Page No: 5-15

Almallahi, Hussein
Instructor, MS
P.O. Box 308
Prairie View A&M University
Prairie View, TX 77446-0000

Field: Electrical Engineering
Laboratory: AL/HR

Vol-Page No: 2-25

Anderson, James
Associate Professor, PhD
Chemistry
University of Georgia
Athens, GA 30602-2556

Field: Analytical Chemistry
Laboratory: AL/EQ

Vol-Page No: 2-18

Anderson, Richard
Professor, PhD
Physics
University of Missouri, Rolla
Rolla, MO 65401-0000

Field: Physics
Laboratory: PL/LI

Vol-Page No: 3- 7

Ashrafiuon, Hashem
Assistant Professor, PhD
Mechanical Engineering
Villanova University
Villanova, PA 19085-0000

Field: Mechanical Engineering
Laboratory: AL/CF

Vol-Page No: 2- 6

Backs, Richard
Assistant Professor, PhD
Dept. of Psychology
Wright State University
Dayton, OH 45435-0001

Field: Experimental Psychology
Laboratory: AL/CF

Vol-Page No: 2- 7

Baginski, Thomas
Assoc Professor, PhD
200 Broun Hall
Auburn University
Auburn, AL 36849-5201

Field: Electrical Engineering
Laboratory: WL/MN

Vol-Page No: 5-40

Baker, Suzanne
Assistant Professor, PhD
Dept. of Psychology
James Madison University
Harrisonburg, VA 22807-0000

Field:
Laboratory: AL/OE

Vol-Page No: 2-36

Baker, Albert
Assistant Professor, PhD

Field: Electrical Engineering
Laboratory: WL/MT

University of Cincinnati
,   -   0

Vol-Page No: 5-53

Balakrishnan, Sivasubramanya
Associate Professor, PhD

Field: Aerospace Engineering
Laboratory: WL/MN

University of Missouri, Rolla
,   -   0

Vol-Page No: 5-41

Bannister, William
Professor, PhD

Field: Organic Chemistry
Laboratory: WL/FI

Univ of Mass.-Lowell
Lowell, MA 1854-0000

Vol-Page No: 5-16

Barnard, Kenneth
Assistant Professor, PhD

Field: Ele   cal Engineering
Laboratory: WL/:

Memphis State University
,   -   0

Vol-Page No: 5- 1

Bayard, Jean-Pierre
Associate Professor, PhD
6000 J Street
California State Univ-Sacramen
Sacramento, CA 95819-6019

Field: Electrical/Electronic Eng
Laboratory: RL/ER

Vol-Page No: 4- 7

Beardsley, Larry
Research Professor, MS

Field: Mathematics
Laboratory: WL/MN

Athens State College
,   -   0

Vol-Page No: 5-42

Beecken, Brian
Assoicate Professor, PhD
3900 Bethel Dr.
Bethel College
St. Paul, MN 55112-0000

Field: Dept. of Physics
Laboratory: PL/VT

Vol-Page No: 3-23

Bellem, Raymond
Dept, CEM. EE cs, PhD
3200 Willow Creek Road
Embry-Riddle Aeronautical Univ
Prescott, AZ 86301-0000

Field: Dept. of Computer Science
Laboratory: PL/VT

Vol-Page No: 3-24

Bellem, Raymond
Dept, CEM. EE cs, PhD
3200 Willow Creek Road
Embry-Riddle Aeronautical Univ
Prescott, AZ 86301-0000

Field: Dept. of Computer Science
Laboratory: /

Vol-Page No: 0- 0

Bhuyan, Jay
Assistant Professor, PhD
Dept. ofComputer Science
Tuskegee University
Tuskegee, AL 36088-0000

Field: Computer Science
Laboratory: PL/WS

Vol-Page No: 3-33

Biegl, Csaba
Assistant Professor, PhD
 Box 1649 Station B
Vanderbilt University
Nashville, TN 37235-0000

Field: Electrical Engineering
Laboratory: AEDC/

Vol-Page No: 6- 2

Biggs, Albert
Professor, PhD
Electrical Engineering
Univ. of Alabama, Huntsville
Huntsville, AL 35899-0000

Field:
Laboratory: PL/WS

Vol-Page No: 3-34

Blystone, Robert
Professor, PhD
Trinity University
715 Stadium Drive
San Antonio, TX 78212-7200

Field: Dept of Biology
Laboratory: AL/OE

Vol-Page No: 2-37

Branting, Luther
Assistant Professor, PhD
PO Box 3682
University of Wyoming
Laramie, WY 82071-0000

Field: Dept of Computer Science
Laboratory: AL/HR

Vol-Page No: 2-26

Bryant, Barrett
Associate Professor, PhD
115A Campbell Hall
University of Alabama, Birming
Birmingham, AL 35294-1170

Field: Computer Science
Laboratory: RL/C3

Vol-Page No: 4- 1

SFRP Participant Data

Callens, Jr., Eugene
Assocition Professor, PhD
Industrial
Louisiana Technical University
Ruston, LA 71270-0000

Field: Aerospace Engineering
Laboratory: WL/MN

Vol-Page No: 5-43

Cannon, Scott
Associate Professor, PhD
Computer Science
Utah State University
Logan, UT 84322-0000

Field: Computer Science/Biophys.
Laboratory: PL/VT

Vol-Page No: 3-25

Carlisle, Gene
Professor, PhD
Dept. of Physics
West Texas State University
Canyon, TX 79016-0000

Field: Killgore Research Center
Laboratory: PL/LI

Vol-Page No: 3- 8

Catalano, George
Associate Professor, PhD
Mechanical Engineering
United States Military Academy
West Point, NY 10996-1792

Field: Department of Civil &
Laboratory: AEDC/

Vol-Page No: 6- 3

Chang, Ching
Associate Professor, PhD
Euclid Ave at E. 24th St
Cleveland State University
Cleveland, OH 44115-0000

Field: Dept. of Mathematics
Laboratory: WL/FI

Vol-Page No: 5-17

Chattopadhyay, Somnath
Assistant Professor, PhD

University of Vermont
Burlington, VT 5405-0156

Field: Mechanical Engineering
Laboratory: PL/RK

Vol-Page No: 3-14

Chen, C. L. Philip
Assistant Professor, PhD
Computer Science Engineer
Wright State University
Dayton, OH 45435-0000

Field: Electrical Engineering
Laboratory: WL/ML

Vol-Page No: 5-26

Choate, David
Assoc Professor, PhD
Dept. of Mathematics
Transylvania University
Lexington, KY 40505-0000

Field: Mathematics
Laboratory: PL/LI

Vol-Page No: 3- 9

Chubb, Gerald
Assistant Professor, PhD
164 W. 19th Ave.
Ohio State University
Columbus, OH   43210-0000

Field: Dept. of Aviation
Laboratory: AL/HR

Vol-Page No: 2-27

Chuong, Cheng-Jen
Associtae Professor, PhD
501 W. 1st Street
University of Texas, Arlington
Arlington, TX   76019-0000

Field: Biomedical Engineering
Laboratory: AL/CF

Vol-Page No: 2- 8

Citera, Maryalice
Assistant Professor, PhD
Department of Psychology
Wright State University
Dayton, OH   4-5435

Field: Industrial Psychology
Laboratory: AL/CF

Vol-Page No: 2- 9

Collard, Jr., Sneed
Professor, PhD
Ecology & Evolutionary Bi
University of West Florida
Pensacola, FL   32514-0000

Field: Biology
Laboratory: AL/EQ

Vol-Page No: 2-19

Collier, Geoffrey
Assistant Professor, PhD
300 College St., NE
South Carolina State College
Orangeburg,, SC   29117-0000

Field: Dept of Psychology
Laboratory: AL/CF

Vol-Page No: 2-10

Cone, Milton
Assistat Professor, PhD
3200 Willow Creek Road
Embry-Riddel Aeronautical Univ
Prescott, AZ   86301-3720

Field: Electrical Engineering
Laboratory: WL/AA

Vol-Page No: 5- 2

Cundari, Thomas
Assistant Professor, PhD
Jim Smith Building
Memphis State University
Memphis, TN   38152-0000

Field: Department of Chemistry
Laboratory: PL/RK

Vol-Page No: 3-15

D'Agostino, Alfred
Assistant Professor, PhD
4202 E Fowler Ave/SCA-240
University of South Florida
Tampa, FL   33620-5250

Field: Dept of Chemistry
Laboratory: WL/ML

Vol-Page No: 5-27

SFRP Participant Data

Das, Asesh
Assistant Professor, PhD
Research Center
West Virginia University
Morgantown, WV 26505-0000

Field: Concurrent Engineering
Laboratory: AL/HR

Vol-Page No: 2-28

DeLyser, Ronald
Assistant Professor, PhD
2390 S. York Street
University of Denver
Denver, CO 80208-0177

Field: Electrical Engineering
Laboratory: PL/WS

Vol-Page No: 3-35

DelVecchio, Vito
Professor, PhD
Biology
University of Scranton
Scranton, PA 18510-4625

Field: Biochemical Genetics
Laboratory: AL/AO

Vol-Page No: 2- 1

Dey, Pradip
Associate Professor, PhD

Hampton University
, - 0

Field: Computer Science
Laboratory: RL/IR

Vol-Page No: 4-16

Ding, Zhi
Assistant Professor, PhD
200 Broun Hall
Auburn University
Auburn, AL 36849-5201

Field: Electrical Engineering
Laboratory: WL/MN

Vol-Page No: 5-44

Doherty, John
Assistant Professor, PhD
201 Coover Hall
Iowa State University
Ames, IA 50011-1045

Field: Electrical Engineering
Laboratory: RL/OC

Vol-Page No: 4-21

Dolson, David
Assistant Professor, PhD

Wright State University
, - 0

Field: Chemistry
Laboratory: WL/PO

Vol-Page No: 5-56

Dominic, Vincent
Assustant professor, MS
300 College Park
University of Dayton
Dayton, OH 45469-0227

Field: Electro Optics Program
Laboratory: WL/ML

Vol-Page No: 5-28

SFRP Participant Data

Donkor, Eric
Assistant Professor, PhD
Engineering
University of Connecticut
Stroes, CT   6269-1133

Field: Electrical Engineering
Laboratory: RL/OC

Vol-Page No: 4-22

Driscoll, James
Associate Professor, PhD
3004 FXB Bldg 2118
University of Michigan
Ann Arbor, MI   48109-0000

Field: Aerospace Engineering
Laboratory: WL/PO

Vol-Page No: 5-57

Duncan, Bradley
Assistant Professor, PhD
300 College Park
University of Dayton
Dayton, OH   45469-0226

Field: Electrical Engineering
Laboratory: WL/AA

Vol-Page No: 5- 3

Ehrhart, Lee
Instructor, MS
Communications & Intellig
George Mason University
Fairfax, VA   22015-1520

Field: Electrical Engineering
Laboratory: RL/C3

Vol-Page No: 4- 2

Ewert, Daniel
Assistant Professor, PhD
Electrical Engineering
North Dakota State University
Fargo, IN   58105-0000

Field: Physiology
Laboratory: AL/AO

Vol-Page No: 2- 2

Ewing, Mark
Associate Professor, PhD
2004 Learned Hall
University of Kansas
Lawrence, KS   66045-2969

Field: Engineering Mechanics
Laboratory: PL/SX

Vol-Page No: 3-22

Foo, Simon
Assistant Professor, PhD
College of Engineering
Florida State University
Tallahessee, FL   32306-0000

Field: Electrical Engineering
Laboratory: WL/MN

Vol-Page No: 5-45

Frantziskonis, George
Assistant Professor, PhD
Dept of Civil Engrng/Mech
University of Arizona
Tuson, AZ   85721-1334

Field: College of Engrng/Mines
Laboratory: WL/ML

Vol-Page No: 5-29

SFRP Participant Data

Frenzel III, James
Assistant Professor, PhD
Dept of Electrical Engnr
University of Idaho
Moscow, ID 83844-1023

Field: Electrical Engineering
Laboratory: WL/AA

Vol-Page No: 5- 4

Fried, Joel
Professor, PhD
Chemical Engineering
University of Cincinnati
Cincinnati, OH 45221-0171

Field: Polymer Science
Laboratory: WL/PO

Vol-Page No: 5-58

Friedman, Jeffrey
Assistant Professor, PhD
Physics
University of Puerto Rico
Mayaguez, PR   681-0000

Field: Physics/Astrophysics
Laboratory: PL/GP

Vol-Page No: 3- 1

Fuller, Daniel
Dept. Chairman, PhD
Chemistry & Physics
Nicholls State University
Thibodaux, LA 70310-0000

Field: Chemistry
Laboratory: PL/RK

Vol-Page No: 3-16

Gao, Zhanjun
Assistant Professor, PhD
203 W. Old Main, Box 5725
Clarkson University
Potsdam, NY 13699-5725

Field: Mechanical/Aeronautical E
Laboratory: WL/ML

Vol-Page No: 5-30

Gavankar, Prasad
Asst Professor, PhD
Campus Box 191
Texas A&I University
Kingsville, TX 78363-0000

Field: Mech & Indust Engineering
Laboratory: WL/MT

Vol-Page No: 5-54

Gebert, Glenn
Assistant Professor, PhD
Mechanical
Utah State University
Logan, UT 84339-0000

Field: Aerospace Engineering
Laboratory: WL/MN

Vol-Page No: 5-46

Gerdom, Larry
Professor, PhD
Natural Science
Mobile College
Mobil, AL 36663-0220

Field: Chemistry
Laboratory: AL/EQ

Vol-Page No: 2-20

Ghajar, Afshin
Professor, PhD
Mech. & Aerospace Enginee
Oklahoma State University
Stillwater, OK   74078-0533

Field: Mechanical Engineering
Laboratory: WL/PO

Vol-Page No: 5-59

Gopalan, Kaliappan
Associate Professor, PhD
Dept of Engineering
Purdue University, Calumet
Hammond, IN   46323-0000

Field:
Laboratory: AL/CF

Vol-Page No: 2-11

Gould, Richard
Assistant Professor, PhD
Mechanical & Aerospace En
N.Carolina State University
Raleigh, NC   27695-7910

Field: Mechanical Engineering
Laboratory: WL/PO

Vol-Page No: 5-60

Gowda, Raghava
Assistant Professor, PhD
Dept of Computer Science
University of Dayton
Dayton, OH   45469-2160

Field: Computer Information Sys.
Laboratory: WL/AA

Vol-Page No: 5- 5

Graetz, Kenneth
Assistant Professor, PhD
300 College Park
University of Dayton
Dayton, OH   45469-1430

Field: Department of Psychology
Laboratory: AL/HR

Vol-Page No: 2-29

Gray, Donald
Associate Professor, PhD
PO Box 6101
West Virginia Unicersity
Morgantown, WV   20506-6101

Field: Dept of Civil Engineering
Laboratory: AL/EQ

Vol-Page No: 2-21

Green, Bobby
Assistant Professor, MS
Box 43107
Texas Tech University
Lubbock, TX   79409-3107

Field: Electrical Engineering
Laboratory: WL/FI

Vol-Page No: 5-18

Grubbs, Elmer
Assistant Professor, MS
Engineering
New Mexico Highland University
Las Vegas, NM   87701-0000

Field: Electrical Engineering
Laboratory: WL/AA

Vol-Page No: 5- 6

SFRP Participant Data

Guest, Joyce
Associate, PhD
Department of Chemistry
University of Cincinnati
Cincinnati, OH 45221-0172

Field: Physical Chemistry
Laboratory: WL/ML

Vol-Page No: 5-31

Gumbs, Godfrey
Professor, PhD
Physics & Astronomy
University New York Hunters Co
New York, NY 10021-0000

Field: Condensed Matter Physics
Laboratory: WL/EL

Vol-Page No: 5-12

Hakkinen, Raimo
Professor, PhD
207 Jolley Hall
Washington University
St. Louis, MO 63130-0000

Field: Mechanical Engineering
Laboratory: WL/FI

Vol-Page No: 5-19

Hall, Jr., Charles
Assistant Professor, PhD
Mech & Aerospace Engr.
North Carolina Univ.
Raleigh, NC 27695-7910

Field:
Laboratory: WL/FI

Vol-Page No: 5-20

Hancock, Thomas
Assistant Professor, PhD

Grand Canyon University
,   -   0

Field: Educational Psychology
Laboratory: AL/HR

Vol-Page No: 2-30

Hannafin, Michael
Visiting Professor, PhD
305-D Stone Building,3030
Florida State University
Tallahassee, FL   3-2306

Field: Educational Technology
Laboratory: AL/HR

Vol-Page No: 2-31

Helbig, Herbert
Professor, PhD
Physics
Clarkson University
Potsdam, NY 13699-0000

Field: Physics
Laboratory: RL/ER

Vol-Page No: 4- 8

Henry, Robert
Professor, PhD
Electrical Engineering
University of Southwestern Lou
Lafayette, LA 70504-3890

Field: Electrical Engineering
Laboratory: RL/C3

Vol-Page No: 4- 3

Hong, Lang
Assistant Professor, PhD
Dept of Electrical Engin
Wright State University
Dayton, OH 45435-0000

Field: Electrical Engineering
Laboratory: WL/AA

Vol-Page No: 5- 7

Hsu, Lifang
Assistant Professor, PhD

Le Moyne College
,   -   0

Field: Mathematical Statistics
Laboratory: RL/ER

Vol-Page No: 4- 9

Huang, Ming
Assistant Professor, PhD
500 NW 20th Street
Florida Atlantic University
Boca Raton, FL 33431-0991

Field: Mechanical Engineering
Laboratory: AL/CF

Vol-Page No: 2-12

Humi, Mayer
Professor, PhD
Mathematics
Worchester Polytechnic Institu
Worchester, MA   1609-2280

Field: Applied Mathematics
Laboratory: PL/GP

Vol-Page No: 3- 2

Humi, Mayer
Professor, PhD
Mathematics
Worchester Polytechnic Institu
Worchester, MA   1609-2280

Field: Applied Mathematics
Laboratory: /

Vol-Page No: 0- 0

Jabbour, Kamal
Associate Professor, PhD
121 Link hall
Syracuse University
Syracuse, NY 13244-1240

Field: Electrical Engineering
Laboratory: RL/C3

Vol-Page No: 4- 4

Jaszczak, John
Assistant Professor, PhD
Dept. of Physics
Michigan Technological Univers
Houghton, MI 49931-1295

Field:
Laboratory: WL/ML

Vol-Page No: 5-32

Jeng, San-Mou
Associte, PhD
Mail Location #70
University of Cincinnati
Cincinnati, OH 45221-0070

Field: Aerospace Engineering
Laboratory: PL/RK

Vol-Page No: 3-17

Johnson, David
Associate Professor, PhD
Dept of Chemistry
University of Dayton
Dayton, OH 45469-2357

Field: Chemistry
Laboratory: WL/ML

Vol-Page No: 5-33

Karimi, Amir
Associate, PhD
Division Engineering
University of Texas, San Anton
San Antonio, TX   7824-9065

Field: Mechanical Engineering
Laboratory: PL/VT

Vol-Page No: 3-26

Kheyfets, Arkady
Assistant Professor, PhD
Dept. of Mathematics
North Carolina State Univ.
Raleigh, NC 27695-7003

Field:
Laboratory: PL/VT

Vol-Page No: 3-27

Koblasz, Arthur
Associate, PhD
Civil Engineeing
Georgia State University
Atlanta, GA 30332-0000

Field: Engineering Science
Laboratory: AL/AO

Vol-Page No: 2- 3

Kraft, Donald
Professor, PhD
Dept. of Computer Science
Louisiana State University
Baton Rouge, LA 70803-4020

Field:
Laboratory: AL/CF

Vol-Page No: 2-13

Kumar, Rajendra
Professor, PhD
1250 Bellflower Blvd
California State University
Long Beach, CA 90840-0000

Field: Electrical Engineering
Laboratory: RL/C3

Vol-Page No: 4- 5

Kumta, Prashant
Assistant Professor, PhD
Dept of Materials Science
Carnegie-Mellon University
Pittsburgh, PA 15213-3890

Field: Materials Science
Laboratory: WL/ML

Vol-Page No: 5-34

Kuo, Spencer
Professor, PhD
Route 110
Polytechnic University
Farmingdale, NY 11735-0000

Field: Electrophysics
Laboratory: PL/GP

Vol-Page No: 3- 3

Lakeou, Samuel
Professor, PhD
Electrical Engineering
University of the District of
Washnington, DC 20008-0000

Field: Electrical Engineering
Laboratory: PL/VT

Vol-Page No: 3-28

Langhoff, Peter
Professor, PhD

Indiana University
Bloomington, IN 47405-4001

Field: Dept. of Chemistry
Laboratory: PL/RK

Vol-Page No: 3-18

Lawless, Brother
Assoc Professor, PhD
Dept. Science /Mathematic
Fordham University
New York, NY 10021-0000

Field: Box 280
Laboratory: AL/OE

Vol-Page No: 2-38

Lee, Tzesan
Associate Professor, PhD
Dept. of Mathematics
Western Illinois University
Macomb, IL 61455-0000

Field:
Laboratory: AL/OE

Vol-Page No: 2-39

Lee, Min-Chang
Professor, PhD
167 Albany Street
Massachusetts Institute
Cambridge, MA   2139-0000

Field: Plasma Fusion Center
Laboratory: PL/GP

Vol-Page No: 3- 4

Lee, Byung-Lip
Associate Professor, PhD
Engineering Sci. & Mechan
Pennsylvania State University
University Park, PA 16802-0000

Field: Materials Engineering
Laboratory: WL/ML

Vol-Page No: 5-35

Leigh, Wallace
Assistant Professor, PhD
26 N. Main St.
Alfred University
Alfred, NY 14802-0000

Field: Electrical Engineering
Laboratory: RL/ER

Vol-Page No: 4-10

Levin, Rick
Research Engineer II, MS
EM Effects Laboratory
Georgia Institute of Technolog
Atlanta, GA 30332-0800

Field: Electrical Engineering
Laboratory: RL/ER

Vol-Page No: 4-11

Li, Jian	Field:	Electrical Engineering
Asst Professor, PhD	Laboratory: WL/AA	
216 Larsen Hall		
University of Florida	Vol-Page No: 5- 8	
Gainesville, FL 32611-2044		

Lilienfield, Lawrence	Field:	Physiology & Biophysics
Professor, PhD	Laboratory: WHMC/	
3900 Reservoir Rd., NW		
Georgetown University	Vol-Page No: 6-14	
Washington, DC 20007-0000		

Lim, Tae	Field:	Mechanical/Aerospace Engr
Assistant Professor, PhD	Laboratory: FJSRL/	
2004 Learned Hall		
University of Kansas	Vol-Page No: 6- 8	
Lawrence, KA 66045-0000		

Lin, Paul	Field:	Associate Professor
Associate Professor, PhD	Laboratory: WL/FI	
Mechanical Engineering		
Cleveland State University	Vol-Page No: 5-21	
Cleveland, OH 4-4115		

Liou, Juin	Field:	Electrical Engineering
Associate Professor, PhD	Laboratory: WL/EL	
Electrical & Computer Eng		
University of Central Florida	Vol-Page No: 5-13	
Orlando, FL 32816-2450		

Liu, David	Field:	Department of Physics
Assistant Professor, PhD	Laboratory: RL/ER	
100 Institute Rd.		
Worcester Polytechnic Inst.	Vol-Page No: 4-12	
Worcester, MA 1609-0000		

Losiewicz, Beth	Field:	Psycholinguistics
Assistant Professor, PhD	Laboratory: RL/IR	
Experimental Psychology		
Colorado State University	Vol-Page No: 4-17	
Fort Collins, CO 80523-0000		

Loth, Eric	Field:	Aeronaut/Astronaut Engr
Assistant Professor, PhD	Laboratory: AEDC/	
104 S. Wright St, 321C		
University of Illinois-Urbana	Vol-Page No: 6- 4	
Urbana, IL 61801-0000		

Lu, Christopher
Associate Professor, PhD
300 College Park
University of Dayton
Dayton, OH 45469-0246

Field: Dept Chemical Engineering
Laboratory: WL/PO

Vol-Page No: 5-61

Manoranjan, Valipuram
Associate Professor, PhD
Neill Hall
Washington State University
Pullman, WA 99164-3113

Field: Pure & AppliedMathematics
Laboratory: AL/EQ

Vol-Page No: 2-22

Marsh, James
Professor, PhD
Physics
University of West Florida
Pensacola, FL 32514-0000

Field: Physics
Laboratory: WL/MN

Vol-Page No: 5-47

Massopust, Peter
Assistant Professor, PhD

Sam Houston State University
Huntsville, TX 77341-0000

Field: Dept. of Mathematics
Laboratory: AEDC/

Vol-Page No: 6- 5

Miller, Arnold
Senior Instructor, PhD
Chemistry & Geochemistry
Colorado School of Mines
Golden, CO 80401-0000

Field:
Laboratory: FJSRL/

Vol-Page No: 6- 9

Misra, Pradeep
Associate Professor, PhD

University of St. Thomas
,   -   0

Field: Electrical Engineering
Laboratory: WL/AA

Vol-Page No: 5- 9

Monsay, Evelyn
Associate Professor, PhD
1419 Salt Springs Rd
Le Moyne College
Syracuse, NY 13214-1399

Field: Physics
Laboratory: RL/OC

Vol-Page No: 4-23

Morris, Augustus
Assistant Professor, PhD

Central State University
,   -   0

Field: Biomedical Science
Laboratory: AL/CF

Vol-Page No: 2-14

Mueller, Charles
Professor, PhD
W140 Seashore Hall
University of Iowa
Iowa City, IA 52242-0000

Field: Dept of Sociology
Laboratory: AL/HR

Vol-Page No: 2-32

Murty, Vedula
Associate Professor, MS

Texas Southern University
,   -   0

Field: Physics
Laboratory: PL/VT

Vol-Page No: 3-29

Musavi, Mohamad
Assoc Professor, PhD
5708 Barrows Hall
University of Maine
Orono, ME   4469-5708

Field: Elect/Comp. Engineering
Laboratory: RL/IR

Vol-Page No: 4-18

Naishadham, Krishna
Assistant Professor, PhD
Dept. of Electrical Eng.
Wright State University
Dayton, OH 45435-0000

Field: Electrical Engineering
Laboratory: WL/EL

Vol-Page No: 5-14

Noel, Charles
Associate Professor, PhD
151A Campbell Hall
Ohio State University
Columbus, OH 43210-1295

Field: Dept of Textiles & Cloth
Laboratory: PL/RK

Vol-Page No: 3-19

Norton, Grant
Asst Professor, PhD
Mechanical & Materials En
Washington State University
Pullman, WA 99164-2920

Field: Materials Science
Laboratory: WL/ML

Vol-Page No: 5-36

Noyes, James
Professor, PhD
Mathematics & Computer Sc
Wittenberg University
Springfield, OH 45501-0720

Field: Computer Science
Laboratory: WL/FI

Vol-Page No: 5-22

Nurre, Joseph
Assistant Professor, PhD
Elec. & Computer Engineer
Ohio University
Athens, OH 45701-0000

Field: Mechanical Engineering
Laboratory: AL/CF

Vol-Page No: 2-15

Nygren, Thomas
Associate Professor, PhD
1885 Neil Ave. Mail
Ohio State University
Columbus, OH 43210-1222

Field: Department of Psychology
Laboratory: AL/CF

Vol-Page No: 2-16

Osterberg, Ulf
Assistant Professor, PhD
Thayer School of Engrg.
Dartmouth College
Hanover, NH   3755-0000

Field:
Laboratory: FJSRL/

Vol-Page No: 6-10

Pan, Ching-Yan
Associate Professor, PhD
Physics
Utah State University
Logan, UT 84322-4415

Field: Condensed Matter Physics
Laboratory: PL/WS

Vol-Page No: 3-36

Pandey, Ravindra
Assistant Professor, PhD
1400 Townsend Dr
Michigan Technological Univers
Houghton, MI 49931-1295

Field: Physics
Laboratory: FJSRL/

Vol-Page No: 6-11

Patton, Richard
Assistant Professor, PhD
Mechanical&Nuclear Engine
Mississippi State University
Mississippi State, MS 39762-0000

Field: Mechanical Engineering
Laboratory: PL/VT

Vol-Page No: 3-30

Peretti, Steven
Assistant Professor, PhD
Chemical Engineering
North Carolina State Univ.
Raleigh, NC 27695-7905

Field:
Laboratory: AL/EQ

Vol-Page No: 2-23

Petschek, Rolfe
Associate Professor, PhD
Department of Physics
Case Western Reserve Universit
Cleveland, OH 44106-7970

Field: Physics
Laboratory: WL/ML

Vol-Page No: 5-37

Pezeshki, Charles
Assistant Professor, PhD

Washington State University
Pullman, WA 99164-2920

Field: Mechanical Engineering
Laboratory: FJSRL/

Vol-Page No: 6-12

Piepmeier, Edward
Assistant Professor, PhD
College of Pharmacy
University of South Carolina
Columbia, SC 29208-0000

Field:
Laboratory: AL/AO

Vol-Page No: 2- 4

Pittarelli, Michael
Associate Professor, PhD
PO Box 3050, Marcy Campus
SUNY, Institute of Technology
Utica, NY 13504-3050

Field: Information Sys & Engr.
Laboratory: RL/C3

Vol-Page No: 4- 6

Potasek, Mary
Research Professor, PhD

Columbia University
,   - 0

Field: Physics
Laboratory: WL/ML

Vol-Page No: 5-38

Prasad, Vishwanath
Professor, PhD

SUNY, Stony Brook
Stony Brook, NY 11794-2300

Field: Mechanical Engineering
Laboratory: RL/ER

Vol-Page No: 4-13

Priestley, Keith
Research Scientist, PhD

University of Nevada, Reno
,   - 0

Field: Geophysics
Laboratory: PL/GP

Vol-Page No: 3- 5

Purasinghe, Rupasiri
Professor, PhD
5151 State Univ. Dr.
California State Univ.-LA
Los Angeles, CA 90032-0000

Field: Dept of Civil Engineering
Laboratory: PL/RK

Vol-Page No: 3-20

Raghu, Surya
Assistant Professor, PhD
Mechanical Engineering
SUNY, Stony Brook
Stony Brook, NY 11794-2300

Field: Mechanical Engineering
Laboratory: WL/PO

Vol-Page No: 5-62

Ramesh, Ramaswamy
Associate Professor, PhD
School of Management
SUNY, Buffalo
Buffalo, NY 14260-0000

Field: Magement Science/Systems
Laboratory: AL/HR

Vol-Page No: 2-33

Ramm, Alexander
Professor, PhD
Mathematics
Kansas State University
Manhattan, KS 66506-2602

Field:
Laboratory: AL/CF

Vol-Page No: 2-17

Ray, Paul
Assistant Professor, PhD
Box 870288
University of Alabama
Tuscaloosa, AL 35487-0288

Field: Industrial Engineering
Laboratory: AL/OE

Vol-Page No: 2-40

Reimann, Michael
Assistant Instructor, MS
Information Systems
The University of Texas-Arling
Arlington, TX 76019-0437

Field: Computer Science
Laboratory: WL/MT

Vol-Page No: 5-55

Rodriguez, Armando
Assistant Professor, PhD

Arizona State University
Tempe, AZ 85287-7606

Field: Electrical Engineering
Laboratory: WL/MN

Vol-Page No: 5-48

Rohrbaugh, John
Research Engineer, PhD
347 Ferst St
Georgia Institute of Technolog
Atlanta, GA 30332-0800

Field: Sensors & Applied Electro
Laboratory: RL/ER

Vol-Page No: 4-14

Roppel, Thaddeus
Associate Professor, PhD
200 Broun Hall
Auburn University
Auburn, AL 36849-5201

Field: Electrical Engineering
Laboratory: WL/MN

Vol-Page No: 5-49

Rosenthal, Paul
Professor, PhD
Mathematics
Los Angeles City College
Los Angeles, CA 90027-0000

Field: Mathematics
Laboratory: PL/RK

Vol-Page No: 3-21

Rotz, Christopher
Associate Professor, PhD

Brigham Young University
Provo, UT 84602-0000

Field: Mechanical Engineering
Laboratory: PL/VT

Vol-Page No: 3-31

Rudolph, Wolfgang
Associate Professor, PhD
Dept of Physics and Astro
University of New Mexico
Albuquerque, NM 84131-0000

Field: Physics
Laboratory: PL/LI

Vol-Page No: 3- 0

Rudzinski, Walter
Professor, PhD
Dept. of Chemistry
Southwest Texas State Universi
San Marcos, TX 78610-0000

Field: Professor
Laboratory: AL/OE

Vol-Page No: 2-41

Rule, William
Asst Professor, PhD
Mechanical Engineering
University of Alabama
Tuscaloosa, AL 35487-0278

Field: Engineering Mechanics
Laboratory: WL/MN

Vol-Page No: 5-50

Ryan, Patricia
Research Associate, MS
Georgia Tech Research Ins
Georgia Institute of Tech
Atlanta, GA 30332-0000

Field: Electrical Engineering
Laboratory: WL/AA

Vol-Page No: 5-10

Saiduddin, Syed
Professor, PhD
1900 Coffey Rd
Ohio State University
Columbus, OH 43210-1092

Field: Physiology/Pharmacology
Laboratory: AL/OE

Vol-Page No: 2-42

Schonberg, William
Assoc Professor, PhD
Engineering Dept.
University of Alabama, Huntsvi
Huntsville, AL 35899-0000

Field: Civil & Environmental
Laboratory: WL/MN

Vol-Page No: 5-51

Schulz, Timothy
Assistant Professor, PhD
1400 Townsend Dr
Michigan Technological Univers
Houghton, MI 49931-1295

Field: Electrical Engineering
Laboratory: PL/LI

Vol-Page No: 3-11

Shen, Mo-How
Assistant Professor, PhD
2036 Neil Ave.
Ohio State University
Columbus,, OH 43210-1276

Field: Aerospace Engineering
Laboratory: WL/FI

Vol-Page No: 5-23

Sherman, Larry
Professor, PhD
Dept. of Chemistry
University of Scranton
Scranton, PA 18510-4626

Field: Analytical Chemistry
Laboratory: AL/OE

Vol-Page No: 2-43

Shively, Jon
Professor, PhD
Civil & Industrial Eng.
California State University, N
Northridge, CA 91330-0000

Field: Metallurgy
Laboratory: PL/VT

Vol-Page No: 3-32

Snapp, Robert
Assistant Professor, PhD
Dept of Computer Science
University of Vermont
Burlington, VT 5405-0000

Field: Physics
Laboratory: RL/IR

Vol-Page No: 4-19

Soumekh, Mehrdad
Associate Professor, PhD
201 Bell Hall
SUNY, Buffalo
Amherst, NY 14260-0000

Field: Elec/Computer Engineering
Laboratory: PL/LI

Vol-Page No: 3-12

Spetka, Scott
Assistant Professor, PhD
PO Box 3050, Marcy Campus
SUNY, Institute of Technology
Utica, NY 13504-3050

Field: Information Sys & Engrg
Laboratory: RL/XP

Vol-Page No: 4-26

Springer, John
Associate Professor, PhD

Fisk University
,   -   0

Field: Physics
Laboratory: AEDC/

Vol-Page No: 6- 6

Stevenson, Robert
Assistant Professor, PhD
Electrical Engineering
University of Notre Dame
Notre Dame, IN 46556-0000

Field: Electrical Engineering
Laboratory: RL/IR

Vol-Page No: 4-20

Stone, Alexander
Professor, PhD
Mathematics & Statistics
University of New Mexico
Alburquerque, NM 87131-1141

Field:
Laboratory: PL/WS

Vol-Page No: 3-37

SFRP Participant Data

Sveum, Myron
Assistant Professor, MS
Electronic Engineering Te
Metropolitan State College
Denver, CO 80217-3362

Field: Electrical Engineering
Laboratory: RL/OC

Vol-Page No: 4-24

Swanson, Paul
Research Associate, PhD
Electrical Engineering
Cornell University
Ithaca, NY 14853-0000

Field: Electrical Engineering
Laboratory: RL/OC

Vol-Page No: 4-25

Swope, Richard
Professor, PhD
Engineering Science
Trinity University
San Antonio, TX 78212-0000

Field: Mechanical Engineering
Laboratory: AL/AO

Vol-Page No: 2- 5

Tan, Arjun
Professor, PhD
Physics
Alabama A&M University
Normal, AL 35762-0000

Field: Physics
Laboratory: PL/WS

Vol-Page No: 3-38

Tarvin, John
Associate Professor, PhD
800 Lakeshore Drive
Samford University
Birmingham, AL 35229-0000

Field: Department of Physics
Laboratory: AEDC/

Vol-Page No: 6- 7

Taylor, Barney
Visiting Assist Professor, PhD
1601 Peck Rd.
Miami Univ. - Hamilton
Hamilton, OH   4-5011

Field: Dept. of Physics
Laboratory: WL/ML

Vol-Page No: 5-39

Thio, Y.
Associate Professor, PhD

University of Miami
Coral Gables, FL 33124-0530

Field: Physics Dept.
Laboratory: PL/WS

Vol-Page No: 3-39

Tong, Carol
Assistant Professor, PhD
Electrical Engineering
Colorado State University
Fort Collins, CO 80523-0000

Field:
Laboratory: WL/AA

Vol-Page No: 5-11

Truhon, Stephen
Associate Professor, PhD
Social Sciences
Winston-Salem State University
Winston-Salem, NC 27110-0000

Field: Psychology
Laboratory: AL/HR

Vol-Page No: 2-34

Tzou, Horn-Sen
Associate Professor, PhD
Mechanical Engineering
University of Kentucky
Lexington, KY 40506-0046

Field: Mechanical Engineering
Laboratory: WL/FI

Vol-Page No: 5-24

Vogt, Brian
Professor, PhD

Bob Jones University
,   -   0

Field: Pharmaceutical Sciences
Laboratory: AL/EQ

Vol-Page No: 2-24

Wang, Xingwu
Asst Professor, PhD
Dept. of Electrical Eng.
Alfred University
Alfred, NY 14802-0000

Field: Physics
Laboratory: WL/FI

Vol-Page No: 5-25

Whitefield, Philip
Research Assoc Professor, PhD
Cloud & Aerosol Sciences
University of Missouri-Rolla
Rolla, MO 65401-0000

Field: Chemistry
Laboratory: PL/LI

Vol-Page No: 3-13

Willson, Robert
Research Assoc Professor, PhD
Robinson Hall
Tufts University
Medford, MA 2155-0000

Field: Physics and Astronomy
Laboratory: PL/GP

Vol-Page No: 3- 6

Witanachchi, Sarath
Assistant Professor, PhD
4202 East Fowler Avenue
University of South Florida
Tampa, FL 33620-7900

Field: Department of Physics
Laboratory: FJSRL/

Vol-Page No: 6-13

Woehr, David
Assistant Professor, PhD
Psycholoogy
Texas A&M University
College Station, TX 77845-0000

Field: Psychology
Laboratory: AL/HR

Vol-Page No: 2-35

SFRP Participant Data

Xu, Longya
Assistant Professor, PhD
Electrical Engineering
The Ohio State University
Columbus, OH 43210-0000

Field: Electrical Engineering
Laboratory: WL/PO

Vol-Page No: 5-63

Yavuzkurt, Savas
Associate Professor, PhD

Pennsylvania State University
University Park, PA 16802-0000

Field: Mechanical Engineering
Laboratory: WL/PO

Vol-Page No: 5-64

Zhang, Xi-Cheng
Associate Professor, PhD
Physics Department
Rensselaer Polytechnic Institu
Troy, NY 12180-3590

Field: Physics
Laboratory: RL/ER

Vol-Page No: 4-15

Zhou, Kemin
Assistant Professor, PhD
Dept. of Elec & Comp. Eng
Louisiana State University
Baton Rouge, LA 70803-0000

Field:
Laboratory: WL/MN

Vol-Page No: 5-52

Zimmermann, Wayne
Associate Professor, PhD
P.O. Box 22865
Texas Woman's University
Denton, TX 76205-0865

Field: Dept Mathematics/Computer
Laboratory: PL/WS

Vol-Page No: 3-40

MODEL-BASED SOFTWARE SYNTHESIS
FOR LARGE SYSTEMS

Ben A. Abbott

Research Faculty

Department of Electrical Engineering

Vanderbilt University

400 24th Avenue South

Nashville. TN 37235

MODEL-BASED SOFTWARE SYNTHESIS
FOR LARGE SYSTEMS

Ben A. Abbott

Research Faculty

Department of Electrical Engineering

Abstract

This paper describes techniques for knowledge representation and compilation of large software systems in a model-based, automatic program synthesis environment. Domain specific declarative models are used to represent specifications and implementation strategies for reactive systems. Dynamic re-synthesis of an executing system is supported, allowing the system structure to adapt to the external or internal environment. The paper describes an application of these techniques to a large, high performance parallel instrumentation system used for analysis of turbine engine strain gauge signals produced during altitude testing. The unique features of this approach include: explicit domain-specific declarative models; graphical representation of models; multiple aspect models; automatic specification of the necessary hardware architecture; and on-line re-synthesis of dynamic systems.

MODEL-BASED SOFTWARE SYNTHESIS
FOR LARGE SYSTEMS

Ben A. Abbott

Introduction

One of the most challenging problems in software engineering is to build large. high-performance systems that must perform continuous interaction with their environment. The behavior of these *reactive* systems is typically complex, concurrent, and non-deterministic. This makes them difficult to build.

Automatic program synthesis is one of the prime disciplines that can contribute to the advancement of the software engineering of reactive systems. The technique has been successfully applied to a specific "real-world" application: a large-scale, parallel instrumentation system, called Computer Assisted Dynamic Data Analysis and Monitoring System (CADDMAS). The CADDMAS system was developed in cooperation with the US Air Force at Arnold Engineering Development Center (AEDC). The software synthesized is a complex, reactive, signal processing system running on a heterogeneous network of nearly 100 processors.

Terminology

Before describing the software synthesis technique utilized, the main terms and concepts used in automatic program synthesis, reactive systems, and model-based systems are briefly defined and discussed. In some cases, the definitions are constrained to the specific needs of this paper.

- *Parallel Instrumentation System*

  Parallel Instrumentation systems use multiple computers to cooperatively convert a set of acquired input signals into a more desirable format. The need for a parallel system as

1-3

opposed to a single processor system can be a result of the raw data rate requirements, or as a result of the number of simultaneous input signals that must be processed.

- *Reactive Systems*

  Most Instrumentation Systems have their behavior driven by external inputs. In such cases, they may be classified as *reactive systems* [26]: embedded real-time systems characterized by continuous interaction with their environment. Process monitoring and control systems, and real-time signal processing systems are typical examples of this category. The complexity, concurrency, and non-deterministic behavior of reactive systems make their construction very difficult. There is an extensive research effort to find disciplines and methods that simplify construction of reactive systems.

- *System Specifications*

  System specifications are the design parameters that must be met by an instrumentation system. These parameters can include: timing constraints, accuracy requirements, cost, and bandwidth limits. There are often tradeoffs between different implementation possibilities. However, a correctly operating instrumentation system must concurrently meet all of its system specifications. Systems engineers strive to obtain, verify, test, and interrelate system specifications.

- *Automatic program synthesis*

  In a broad sense, automatic program synthesis is any automatized technique used to speed the generation of a computer program. David Barstow uses the words *automatic program generation* in this same fashion. He claims that the advent of Fortran compilers (1954) was the origin of automatic programming systems [1]. He continues and constrains his definition however, to a system that "interacts with the user in natural terms, makes all the implementation decisions, and produces robust efficient software". In this paper, the terms *automatic program synthesis, software synthesis,* and *automatic program generation* are used equally in reference to systems characterized by: combining *a priori* knowledge about how to synthesize programs according to the required *system specifications* of a particular system at design time to automatically generate correctly operating system software.

1-4

- *Search Space*

  The exact implementation of a particular instrumentation system is typically chosen by engineers from a vast set of alternatives [8]. For an alternative to be viable, it need only offer an approach that will meet the system specifications. When a computer program attempts to automatically synthesize the control software for an instrumentation system, it must search through and select from this set of alternatives. The set of alternatives is called the *search space*. The core of many Artificial Intelligence (AI) algorithms attempts to navigate through a search space of possible solutions in order to select the "best" or at least an acceptable solution without expending an exhaustive search [18].

- *Declarative Programming*

  One of the valuable contributions of AI research has been a rich set of knowledge representation formalisms [13]. Declarative programming techniques allow the programmer to represent knowledge known about a problem without describing a solution or algorithm for the problem. Rather, in a second step, a separate mechanism automatically derives a solution from the declared knowledge. These two steps of declarative programming are typically called *representation* and *interpretation* [9].

  The knowledge declarations used in a declarative programming system may be expressed in a textual or graphical fashion. The knowledge itself may be of a *general purpose* form or constrained to be *domain specific*.

  One of the main advantages of declarative programming is that it allows the programmer to express knowledge about the problem to be solved separately from the technique that will be used to solve it. This abstraction technique can be quite helpful in complex domains [14].

- *Model-Based Systems*

  Modeling is a typical problem solving technique used by the engineering community [11]. It helps engineers manage the laws and hypothesis concerning real world phenomena. Spriet [21] calls these representations *models*.

  In a broad sense, a system that incorporates an explicit model of the problem to be solved as part of its implementation is a *model-based system*. Typical examples of model-based

systems are: parameter identification systems, and control systems with explicit control models [4].

In this paper, the term *model-based system* is used to refer to a programming technique that utilizes explicit declarative language models describing engineering knowledge about system specifications for parallel instrumentation systems, and their possible implementation. The realm of possible implementations described by the model comprise the search space that should be considered by an automatic program synthesis system.

The Need for Automatic Software Synthesis

This research was motivated by the desire to provide new engineering approaches to aid in overcoming the obstacles encountered when trying to build large, parallel, instrumentation systems. The method used included building *real* instrumentation systems of this type.

"We would like to make a thinking machine...[12]" With this introductory call in his celebrated dissertation, Dennis Hillis began an era of new concepts in parallel computing, the Connection Machine. Likewise, Gregory Fox focused his thoughts by stating: "We want to solve real problems with real computers" during the early days of the CalTech Cosmic Cube experience [10]. Specifically, the goal in building the first hypercube computer was not to simply build another, faster, computer. It was to build a computer to solve real physics simulation problems that were costing too much time and money on existing computers.

One of the primary difficulties encountered when trying to build parallel instrumentation systems is with system software complexity [16]. Robert McCartney, recently introduced the primary motivation for the field of automatic program synthesis in a textbook highlighting a collection of papers about the topic by writing:

"The first disappointment for most users of computers is that real computers are not like those in science fiction stories–rather than responding to simple requests, they demand textual input in some arcane language. Even an expert user ultimately faces this problem: Computers are not easy to program. [17]"

McCartney continues by declaring we are undergoing a "software crisis" with hardware technology advances far out pacing those concerning the software development cycle. He maintains that the result of this crisis is that the continually rising demand for complex computer systems

is thwarted by missed deadlines and over spent budgets.

Fred Brooks, author of the famous collection of software engineering essays, *The Mythical Man Month* [6], uses the metaphor of werewolves to describe the problems that creep into large software projects [5]. Here Brooks claims there is no single "silver bullet" that can kill these problems thereby providing the order-of-magnitude improvements necessary to build the types of software systems currently desired.

Edward Yourdon in his call for American programmers to keep up with the current, worldwide, trends in software engineering highlights the use of automated computer aided software engineering (CASE) tools to face Brooks' monsters [24]. He includes an argument saying that this is indeed what Brooks himself indicated to be necessary. Yourdon does not contend that CASE is a single "silver bullet" that will solve the problem, but rather, includes it in a list of eleven partial bullets that all need improvement. Yourdon points out that artificial intelligence technology can be used to improve CASE tools in the following areas [25]: Debugging, Maintenance, Systems Analysis, Configuring Software Packages, Transforming analysis models into design models, Assistance in partitioning and leveling of models, Application-specific "domain models", and Advice on which methodology to use. The domain specific model-based automatic program synthesis technique described in this paper offers approaches to most of the improvement areas cited by Yourdon.

The Transformational Approach to Software Synthesis

Software Synthesis researchers have utilized a variety of approaches to their problem. The approaches are typically broken into three categories: Interactive tools such as the Programmers Apprentice [20], Theorem Proving techniques [19], and Transformational Approaches.

The technique described in this paper uses a domain specific transformational approach. Assuming that the specifications for a system are complete as well as correct, an error free implementation of the required software may be generated through a series of replacements being made on the specification. The replacements should be such that they are continually refining and transforming the specifications into an executable program. The process is often represented as a series of "if then" rules. In which case, the typical implementation has the following recursive procedure: (1) First a pattern match of the transformation rules is made against the current system definition (which starts as the system specifications). (2) Next, a transformation

is chosen from the set of matching patterns. The choice is made through a cost function. **(3)** Finally, the transformation is applied to the current system definition thereby creating a new, transformed system definition. **(4)** The updated system definition is recursively transformed in this fashion until no patterns match. At this point the system definition has been transformed into an executable program.

Each transformation step may be of a *vertical*-refining nature moving the specification closer to a program, or of a *lateral*-optimizing nature choosing between the various possible implementations for each level. Transformational systems are different from application generators because they do not represent knowledge as an explicit set of procedures. Rather, they represent it as a series of possible transformations that are subsequently used during the pattern matching and application process. The main difficulty with transformational approaches is the control of the search space. Typically there are many different implementation possibilities for any level [19]. Confining the transformation knowledge to a specific domain reduces the search space problem.

Test Case Target Domain: Turbine Engine Testing

Testing turbine engines involves running an instrumented version of the engine through various operational maneuvers (e.g. Acceleration, Deceleration or Throttle Snap) while the engine is in a test cell (wind tunnel) capable of simulating altitude, atmospheric, and air speed conditions. In order to analyze dynamic vibrations of internal components, strain gauges (and other stress sensors) are attached to the turbine blades.

The CADDMAS system was developed to analyze all data on-line. The system processes all sensor readings and presents the results both graphically and in hard copy form, during the test. The immediate availability of results opens the possibility for interactive test planning.

The CADDMAS system performs spectral analysis on a large number of channels. The spectral information is accumulated and processed into several types of computationally intensive, calibrated engineering diagrams [7]. A graphical user interface allows the user to configure the data processing and visualization screens interactively. The user can select the number of visible windows on a screen, the contents of each plot window, and the parameters of each plot.

The CADDMAS hardware consists of various computational *building blocks.* The basic building blocks are modular so as to allow systems of various size and personality to be "plugged"

together.

The CADDMAS is a high performance, reactive instrumentation system, which runs on a heterogeneous parallel processor network. Beyond the obvious software engineering complexity of building the system, there have been additional operational requirements that led to the development and application of automatic software synthesis techniques:

1. Changing Software Requirements: The CADDMAS is used to test new and redesigned turbine engines. Engine capabilities are constantly improving. Consequently, testing scenarios are updated on a test-by-test basis. When a new test is scheduled, the engine manufacturer's aero-mechanical engineers specify the number, types, and accuracy of the plots desired. The CADDMAS must be open and scalable to meet these changing and unknown needs. New data analysis techniques that produce new types of plots will need to be "plugged" into the software. Wind tunnel air time used during the engine test drives the overall test cost. Therefore, the CADDMAS system integrity is crucial. Yet, the software for each test must be unique.

2. Changing Hardware Configurations: In order to meet these changing demands, the CADDMAS hardware has been designed as a set of basic building blocks. System hardware architecture may be configured as needed by "plugging" together these blocks. The hardware configuration will change frequently based on the number of available processors and the computational demand, based on channel capacity and processing requirements.

3. Dynamically changing specifications: Number of plots to be generated; type of plots; and accuracy requirements change during the test period. It requires the use of different versions of the processing modules and reconfiguration of the program structure. The number of alternatives is too high to pre-build all of the possible alternatives. It is unacceptable to shut down, rebuild, and load the new version during a running test.

Modeling Paradigm for CADDMAS

The CADDMAS system required two aspects to be modeled. The *Signal-Flow* aspect declares the structure and alternatives of the possible instrumentation scenarios. The *Hardware Structure* aspect declares the architecture and alternatives possible considering the available resources and

1-9

their capabilities. A unique declarative language has been defined for each aspect using the declarative language tools of the Multigraph (TM) Programming Environment (MPE) [13]. Likewise, interpreters for these two aspects have been generated using tools from the (MPE).

Hierarchy plays a key role in all of the modeling techniques. It serves to limit the complexity visible to the system designer at any one time, as well as reducing the search space during the interpretation process.

The basic concept of the Signal-Flow Model (SFM) is the *module*. The *module* has three kinds of interfaces: the *signal interface*, which connects the module in the signal flow: the *specification interface*, which contains the required specifications for the module, including performance on the hardware and the *dynamic control interface*, which defines the dynamic control parameters. The modules can be *primitive* or *compound*. Primitive modules represent the elementary computation units and define their interfaces. The primitive module can be a subroutine, device handler, or interface to a hardware accelerator.

The SFM declaration of a primitive is defined as:

(**defprimitive** *<name>*
    (**interface**
        (<input-signals> -> <output-signals>)
        (*<specification-list>*)
        (*<dynamic-control-parameters>*)
)
    (**body**
        (*<primitive-name>*)
        (*<discipline>*)
        (*<environment>*)
)
)

The lists after the **interface** keyword specify the elements of: the signal interface; the specification interface; and the dynamic control interface respectively. The symbols following the **body** keyword determine the features of the computation unit itself. The *<primitive-name>* identifies the subroutine to be invoked. The subroutine can be written in C, Fortran, or Lisp.

1-10

The <*discipline*> specifies whether the control principle of the actor node is "ifall" or "ifany". The <*environment*> defines the system resource (task, or processor) where the primitive operation will be executed.

Compound modules are composed of other modules that may be either primitives or other compounds. Their primary purpose is to represent knowledge about building specific pieces of signal flow graphs. The key issues regarding the representation of "building knowledge" are: (1) what is the reasonable level of flexibility in defining possible alternatives: and (2) how the alternatives and the selection rules are structured. Reactive instrumentation systems generally have strict operational constraints. The number of structural alternatives for implementing a specific function is usually quite limited. The various alternatives need to be thoroughly tested for performance and run-time behavior. As a result, introducing enough limitations in the representation to keep the selection (or planning) process manageable while not losing all the flexibility is possible.

An important limitation is that the functional architecture of a compound structure is fixed. It is described by the declaration of the functional **units** and their connections. Flexibility is achieved by introducing the possibility that each unit can be "implemented" by various modules having the same functionality, but with different specifications. After receiving the required specifications through the "specification interface", the selection rules select the appropriate implementation module for the functional units and determine the external specifications for them. Since the selected modules on the lower-level may also have an internal structure with various implementation alternatives, this process is applied recursively down the signal flow model. This recursive process can generate a tremendous number of alternatives.

The representation technique described above decomposes the "building knowledge" into rule sets that are relevant on a given level of the hierarchy. This method is a natural way of organizing the knowledge in instrumentation systems. It helps to keep the complexity of the building process manageable.

The SFM declaration for compound modules is:

(defcompound <name>
    (interface
        (<*input-signals*> -> <*output-signals*>)
        (<*specification-list*>)
        (<*dynamic-control-parameters*>)
        (<*environment*>)

```
   )
( connections
     ( <signals> )
     ( <specifications> )
   )
( linkpoints
     ( <list of link-point specifications> )
   )
( structure
     ( <list of units> )
     ( <selection rules> )
   )
( body
     ( <S-expressions> )
   )
)
```

The *<environment>* parameter in the **interface** section determines the computing environment where the module is allocated. (This declaration has significance only in multiprocessor and multicomputer implementations.) The **connections** specify those symbols that are used to declare the internal structure of the module. The *<signals>* and *<specifications>* are a list of symbols that are referred to in the signal interfaces and the specification interfaces of the internal modules.

The *<list of units>* after the **structure** keyword specifies the functional components of the compound. The *<selection rules>* define the conditions for selecting among the functionally equivalent alternatives. The rules may refer to the external specifications passed to the module through its specification interface, and to arbitrary global variables describing the state of the execution environment. As a result of rule evaluations, the units will be assigned to specific modules. The **body** of the compound is simply a list of expressions that can be used for various initializations at build time. The **link-points** are used for linking the execution environment with the builder environment.

The hardware structure is modeled using a the *Multiprocessor Description Language* (MPDL)
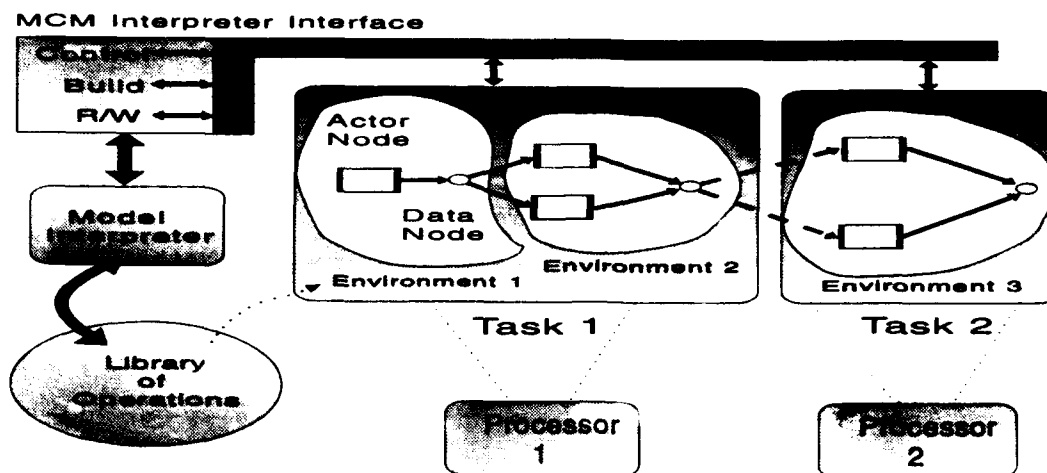
Figure 1: Multigraph Execution Environment

[15]. The purpose of hardware structure modeling in the CADDMAS application is to show the distributed processor configuration to the level of detail that allow the generation of the routing system and the modeling of the resource allocation. MPDL allows three types of components: *Processors*(**cpu**), *Linkpoints* (**link**), and *Multiprocessors* (**mpr**). Processors are the basic building blocks. They are characterized by a set of attributes, including type. memory size and unique resources. Processors can have linkpoints that are used to connect them together in a given topology. Multiprocessors are aggregates of processors comprising other multiprocessors, processors and linkpoints. The MPDL templates are the shown in [15].

Execution Environment

The interpretation process transforms the models into a set of communicating executable programs spread across a network of processors. Further, the dynamic reconfiguration capability requires that the interpreters be able to interrogate, control, and modify a set of these running programs. In order to make this dynamic program synthesis computationally feasible, the Multigraph Computational Model (MCM) is used as a unified virtual machine in the Execution

Environment. The MCM is a *macro dataflow model*, which defines the run-time structure of the executable program in terms of a control-flow graph (*CG*). *CG* is a directed bipartite graph containing *actor nodes, data nodes*, and their *connections*. An *execution structure* (*tasks* and *environments*) is used for assigning sub graphs of the *CG* to particular computational resources [2], [22] (Please see figure(1)).

Actornodes are the computational operators of the dataflow graph. Associated with an actor are: *scheduler state* (inactive, active, ready, or running); *script*, a reentrant algorithm expressed in a procedural/numeric language, usually incorporated from a *library of standard operations*; *context*, a static local memory section for state and builder-initialized variables; *input* and *output ports*, the input and output data streams.; and *control principle* determines what criteria will be used to decide when an actor should be executed: *ifall* (all data is present), *ifany*, or based on a *real-time* event. MCM kernel calls allow actor scripts to receive input tokens, access their context, and propagate output tokens.

Datanodes provide a queuing and asynchronous connection function between actornodes. Any number of actor output ports may be connected to a datanode. A datanode may be connected to any number of actor input ports. Datanodes may be enabled or disabled and have a specified length. Datanodes provide a simple interface for the *model interpreters* to control, build, and monitor an executing graph.

Environments are used to protect system resources and provide a priority mechanism for sections of the dataflow graph. All actors are assigned to an environment. Environments of the same priority are serviced in a round-robin fashion. Only one actor per environment will be executed at any one time, ensuring mutual exclusion within an environment to protect data integrity.

Tasks provide a generic interface to the basic computational resources of the underlying machine. In a multitasking environment they are simply the different processing threads available to the MCM kernel. In a multiprocessor system they are the individual processors themselves. Environments are attached to tasks. The *task* and *environment* concepts allow the actual implementation of the underlying system to be hidden from the user.

The MCM *interpreter interface* provides several functions for the management of the execution environment.

In summary, the MCM kernel provides an interface to build, modify, monitor, and control an asynchronous macro-dataflow graph. The graph may be partitioned by the concept of environ-

ments and tasks. The actual dataflow graph looks slightly different from that of a classic dataflow graph due to the introduction of the passive nodes providing queuing functions, datanodes. The use of distinct actornodes and datanodes provides the capability for the model interpreters to build, control, and monitor the dataflow graph.

Model Interpreters

The model interpreters perform a $\mathcal{M} \rightarrow CG$ (Model $\rightarrow$ Control Graph) mapping between the models and the executable system specified in terms of the MCM computational model. The interpretation process is dynamic. It can be retriggered as a response to events detected during execution, such as an operator request for a new or modified plot during the CADDMAS operation. Complex systems typically include several functional components that form the executable system. The CADDMAS monitoring system includes the signal processing system and the message router. These different subsystems are synthesized from the same integrated model database by means of different interpreters. This process, called *multiple-aspect interpretation*, helps to keep the complexity of the individual interpreters low. At the same time, it ensures that the generated subsystems will be consistent with each other.

General Structure of Model Interpretation

Each model interpreter is closely related to the modeling paradigm and the category of the target system to be generated. The logic structure of the model interpretation process for dynamically reconfigurable processing networks is shown in Figure(2).

Model Database. The declarative language representations of the models are loaded and transformed into a model database. This model database becomes part of the runtime system.

Builder Object Network. The builder object network includes one builder object for each compound and primitive in the processing model hierarchy, which were selected during the model interpretation process. The role of builder objects are: (a) to store reference to the appropriate level in the model database, (b) to store references to all of the components of the processing network (actornodes and datanodes) that are relevant to the given level of the hierarchy, and (c)
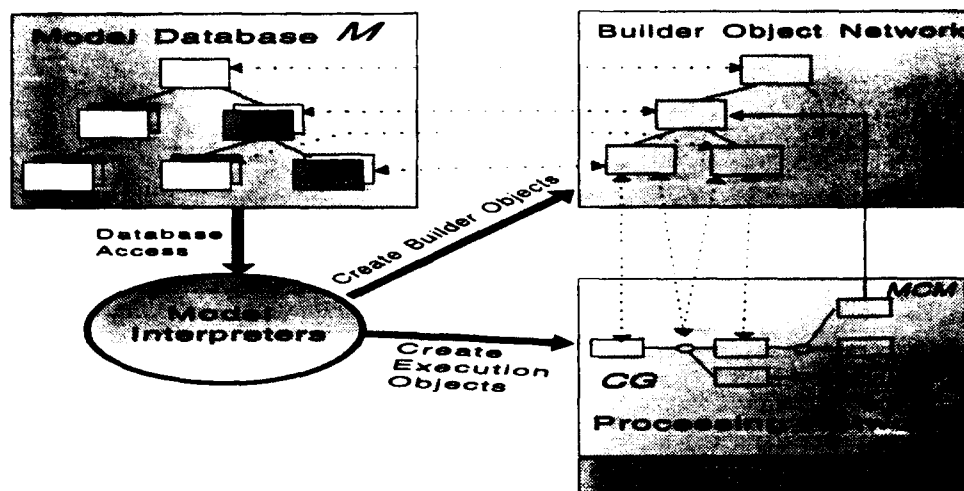
Figure 2: Multigraph Model Interpretation.

to maintain connections to the processing network (modeled as **linkpoints**) for receiving events that trigger reconfiguration.

Processing Network. The processing network constitutes the generated executable system, specified by the CG control graph and running above MCM kernel. The Builder and Control Interface of the kernel facilitates the construction, modification and control of the operation of the processing network.

Model Interpreter. The model interpreter traverses the model database in a top-down direction starting from the root of the model hierarchy, and incrementally builds the actual version of the runtime structure, including the *Builder Object Network* and the *Processing Network*. The interpretation process, which performs the mapping between the models and the runtime structure comprises the following steps at each level in the model hierarchy: **Step 1** *create* builder object. **Step 2** *evaluate* selection rules . **Step 3** *create and connect* actornodes/datanodes. **Step 4** *repeat Step 1* for each selected lower level module.

The mapping between the models and the processing network is determined in *Step 2* and *Step 3*. The selection rules determine which of the lower level modules must be selected in the given situation, which in turn defines the overall structure of the processing network. The processing

network (actornodes, datanodes, their connection and attributes) is built up by transforming modeling concepts into processing network objects according to the modeling paradigm. For instance, for each *signal* in the model a datanode is created, etc. The model interpreter, which executes these transformations is independent from the actual content of the model database, but specific to the modeling paradigm and the category of the target system to be built.

The dynamic reconfiguration of the processing network requires a solution for the synchronization between the interpreter and the processing network. The reconfiguration process is triggered by an event received by a builder object through a **linkpoint**. The event restarts the model interpreter from the referenced model, which may result in changes in the selection of component modules. The replacement of an already running processing module (which may include a complex structure of actornodes and datanodes) occurs according to the following protocol: **Step 1** Complete interpretation of the new module and build up the new processing network. **Step 2** Block the input datanodes of the old processing network using the available references and MCM calls. **Step 3** Complete the already scheduled computations in the old processing network using MCM calls. **Step 4** Disconnect the old processing network and connect already built new processing network. **Step 5** Enable the interface datanodes of the new processing network. **Step 6** Destroy the old processing network.

The problems and details of different reconfiguration methods and the related synchronization methods are described in [3].

Model Interpretation in CADDMAS

The interpretation of Signal Flow Model(SFM) structures starts by defining a set of required specifications (i.e. the engineering plots desired) for the top-level modules. The interpretation process proceeds recursively. The specifications propagate downward and the interpreter uses the selection rules to choose the appropriate modules for the functional units on the consecutive levels of the hierarchy. The result of the interpretation is: a hierarchy of the needed signal flow graph; and a set of specifications used as input for the MPDL interpreter (specifying the required hardware architecture and communication system). It is only valid to allow new physical hardware architecture generation during the very first synthesis pass. On all subsequent passes, the system specification constraints are set to lock the physical architecture. The communication

map paths (i.e. the logical architecture) may, however, be changed. The MPDL interpretation is then started.

Interpretation of the MPDL model produces the following components (as necessary) for the MCM:

- A hardware wiring list and test programs.

- A system load map for program initialization

- Communication maps telling processors how to talk to each other. These include processor hops.

After the hardware architecture has been configured, the SFM interpretation may continue where it left off. That is, the new CG is built on the execution environment under the MCM. This is accomplished by traversing the SFM and instantiating the basic compute elements as actornodes and interconnections as datanodes. At this point, the generated real-time system is ready for execution. Computations produce results as specified in the SFM without the intervention of the any interpreter. These include on-line plots, data monitoring, hard copy output, etc.

Summary

This paper has described the Model-Based Software Synthesis technique used to develop the CADDMAS system, a large parallel instrumentation system. The hierarchy and domain specific models have been used to to cut down the search space. The program generated is a Multigraph Computational Graph, a kind of macro-dataflow graph. Its basic compute elements are high performance subroutines written in traditional languages. By using the Multigraph, synchronization, performance, granularity, and synthesis issues can all be attacked.

References

[1] Barstow, D.: "Automatic Programming for Device Control Software," in Lowry, M.R. and McCartney, R.D. (Ed.) *Automating Software Design*, AAAI Press, MIT Press, pp. 123-140, 1991.

[2] Biegl, Cs.: "*Design and Implementation of an Execution Environment for Knowledge-Based Systems*," Ph.D. Thesis, Electrical Engineering, Vanderbilt University, 1988.

[3] Blokland, W.: "*Structurally Adaptive Systems*," Ph.D. Thesis, Electrical Engineering, Vanderbilt University, 1991.

[4] Brogan, W.: *Modern Control Theory, 2nd ed.*, Prentice-Hall, New Jersey, 1985.

[5] Brooks, F.: "No Silver Bullet", *IEEE Computer*, April 1987, pp. 10-19.

[6] Brooks, F.: *The Mythical Man-Month*, Reading, MA: Addison-Wesley, 1975.

[7] Cromer T.W.,Nichol, K.,.: "New Capabilities for Aeromechanical Testing and Evaluation of Aircraft Turbine Engines" *27th Joint Propulsion Conference*, Sacramento California, June 1991.

[8] Devanbu, P. et. al.: "LaSSIE: A Knowledge-Based Software Information System." in Lowry, M.R. and McCartney, R.D. (Ed.) *Automating Software Design*, AAAI Press, MIT Press, pp. 25-38, 1991.

[9] Feigenbaum, E., Barr, A., Cohen, P., *The Handbook of Artificial Intelligence*, Volumes I-III, William Kaufmann, Inc., 1981 (Volume I) , 1982 (Volumes II,III).

[10] Fox, G.: "Questions and Unexpected Answers in Concurrent Computation," in Dongarra, J. (Ed.): *Experimental Parallel Computing Architectures*, Elsevier Science Publishers B. V. (North-Holland), 1987, pp. 97-119.

[11] Franke, H.: "*Programming Environment for Model-Based Systems*," Ph.D. Thesis, Electrical Engineering, Vanderbilt University, 1992.

[12] Hillis, D.: *The Connection Machine*, MIT Press, Cambridge, MA: 1985.

[13] Karsai, G.: "*Declarative Programming Techniques for Engineering Problems*," Ph D. Thesis, Electrical Engineering, Vanderbilt University, 1988.

[14] Karsai, G.: "Declarative Programming Using Visual Tools," *Techn. Report #89-003*, Measurement and Computing Systems Laboratory, Vanderbilt University, April, 1989.

[15] Ledeczi, A., et al.: "Modeling Parallel Hardware Architectures," in *Proc. of the Int. Conf. on Signal Processing Applications and Technology*, Boston, MA., November 1992.

[16] Leveson, G.: "The Challenge of Building Process-Control Software," *IEEE Software*, pp. 55-62, November, 1990.

[17] McCartney, R.: "Knowledge-Based Software Engineering: Where We Are and Where We Are Going," in Lowry, M.R. and McCartney, R.D. (Ed.) *Automating Software Design*, AAAI Press, MIT Press, pp. XVII-XXXI, 1991.

[18] Pearl, J.: *Heuristics: Intelligent Search Strategies for Computer Problem Solving*. Reading, MA: Addison-Wesley, 1988.

[19] Rich, C. and Waters, R. (Ed.s): Introduction by Eds., pp. xi-xxi, in *Artificial Intelligence and Software Engineering*, Morgan Kaufmann, 1986.

[20] Rich, C., Waters, R.: *The Programmer's Apprentice*. ACM Press, 1990.

[21] Spriet, J., Vansteenkiste, G., *Computer-aided Modelling and Simulation*, Academic Press, 1982.

[22] Sztipanovits, J, Karsai, K., Biegl, C.: "Graph Model-Based Approach to the Representation, Interpretation and Execution of Signal Processing Systems",*International Journal of Intelligent Systems V3*, pp. 269-280, 1988.

[23] Yourdon, E.: *Decline and Fall of the American Programmer*, Prentice-Hall, Inc. Englewood Cliffs, NJ: 1992.

[24] Chapter 2 of [23].

[25] Page 173 of [23].

[26] Zohar, M., Pnueli, A. *The Temporal Logic of Reactive and Concurrent Systems*, Springer-Verlag 1992.

AUTOMATIC TEST INSTRUMENTATION
PROGRAM GENERATION

Csaba Biegl

Research Assistant Professor

Department of Electrical Engineering

Vanderbilt University

Box 1824, Station B

400 24th Avenue South

Nashville, TN 37235

AUTOMATIC TEST INSTRUMENTATION
PROGRAM GENERATION

Csaba Biegl
Research Assistant Professor
Department of Electrical Engineering
Vanderbilt University

Abstract

Aerospace system testing is a highly complex and dynamic process. Requirements are constantly changing, even as a test progresses. Handling data from aerospace tests must adapt to these changes. The algorithms to process data are typically complex, due to the variety of applicable algorithm classes and the large number of channels which must be managed. Furthermore, the processing throughput and response times require a parallel processing approach. A software system was developed to address these issues. The Transient Data Analysis System automatically generates test data processing systems for parallel processors from high level specifications. The process is dynamic in that the processing algorithms executed by the system can be changed at any time during execution.

AUTOMATIC TEST INSTRUMENTATION
PROGRAM GENERATION

Csaba Biegl

Introduction

Aerospace testing is a complex process. Typically, the test article is installed in a facility where many conditions are controlled and monitored to simulate flight conditions. The data from the measurements is extensively processed to extract the parameters necessary to determine system performance and expected reliability.

As the test progresses new information is revealed about the test object. This new information can cause the reevaluation of the information processing strategy. Subsequent reconfiguration of the data analysis software is highly desirable at this point.

Typically, on the order of thousands of sensors are monitored and analyzed. This has several impacts on the information processing system. The large aggregate bandwidth of the incoming data imposes a significant computational load. Large computers or parallel processors are required to meet these needs. The large number of channels, with varying processing algorithms combine to produce a large, complex software system. Large, complex software systems are notoriously difficult to manage [HAREL].

The conventional technique for developing these software systems is to give a high level specification, the Test Requirements Specification Document, to the software analyst, who then manually convert these to computer programs (aka mainframe Fortran). The programs are then compiled and tested by the users. The programs can not be changed until the next set of requirements documents is processed. This precludes the flexibility of on-line adaptation of changing requirements. If the target hardware is a parallel system, this manual translation process increases in difficulty.

This paper describes work done to automatically translate a high-level Test Requirements Specification into a parallel program. The specifications for the software system can be changed on-line, and a new parallel program is generated as needed without interrupting the testing process. This technique eases many of the problems faced by the conventional approach.

A prototype system was implemented for automatic program generation from a Test Requirement Specification (TRS) input. This system is capable of generating executable code for a network of Inmos Transputers [INMOS] controlled by an IBM PC (R) compatible host. It has the following main components: (see Figure 1)

- user interface
- compiler
- run-time environment

The user interface provides an interactive menu-based programming environment. It presents a spreadsheet-like interface, where the structure of the spreadsheet corresponds to the organization of the TRS data sheets used by AEDC. Application-specific editing services aid the user in data entry and/or modification. The user interface also controls the operation of the other components in the system: the compiler and the run-time environment. An example user interface screen can be seen in Figure 2.
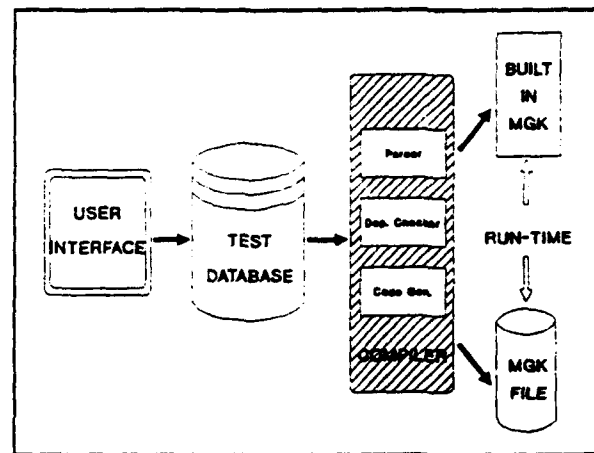
Figure 1. Prototype System Architecture

The compiler translates the TRS information entered via the user interface into executable code. It performs syntax and dependency checking on the input data before the actual translation takes place. If any error is detected, the compilation process is aborted and the user is given an explanation about the cause of the error. Additionally, the edit cursor of the user interface is set to the offending item. The user interface is capable of graphically representing various views of the executable program's structure

Figure 2. A Typical User Interface Screen

using the information produced by the compiler. Using the compiler's dependency information it is possible to display the dependency graph of the program generated from the TRS. Additionally there is an analysis module

in the system which determines the critical path and the theoretical possible best speedup (in a multiprocessor system) for the given configuration. An example dependency graph can be seen in Figure 3, while Figure 4 shows the results of the speedup analysis.

The output of the compiler is a machine independent assembly-like code. This code was designed such that its execution is very fast. Only a few machine instructions are needed for interpretation of an instruction in the compiler's output code. This will cause a small performance degradation. However, we used this solution for the following reasons:
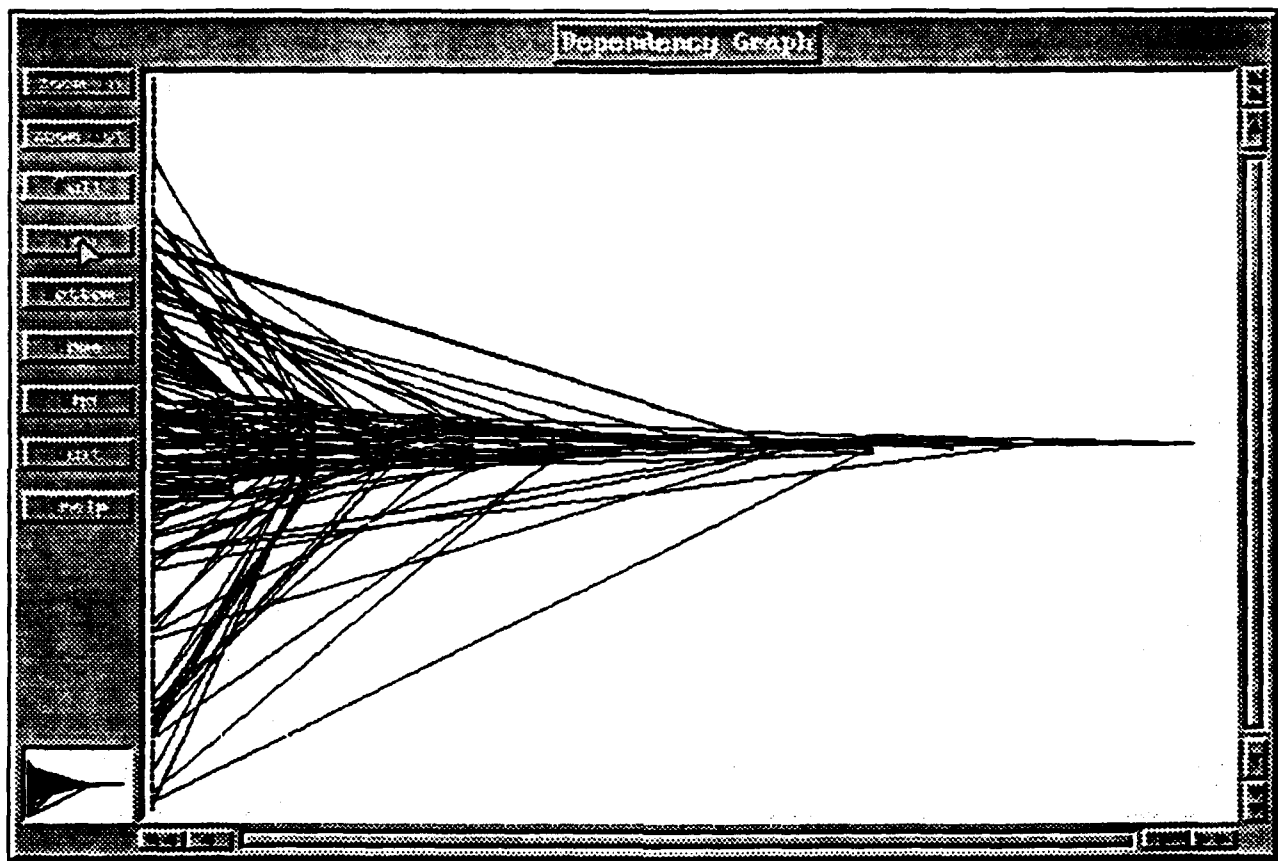
Figure 3. An Example Dependency Graph

- according to estimates, a typical program generated from the TRS sheets spends about 70-80 percent of its time in the subroutines of the Validated library used by AEDC. This means that reducing the execution speed of the remaining 20 percent is tolerable.

- the use of the machine independent code makes compiling and linking of transputer assembly code unnecessary. This is a VERY slow process on the PC based transputer development system.

2-5

- the output of the compiler is machine-independent. In fact we can run the generated code on a parallel network of Unix workstations with a few minor changes (to the network configuration information contained in the code).

The compiler generates a subroutine for each computed item in the TRS sheet. This subroutine is written according to the conventions of the Multigraph Kernel (MGK) [MGK1] which is used as the run-time environment of the system. The MGK implements a dynamically configured parallel macro-dataflow computational model on various computer architectures. It hides the machine-dependent details of
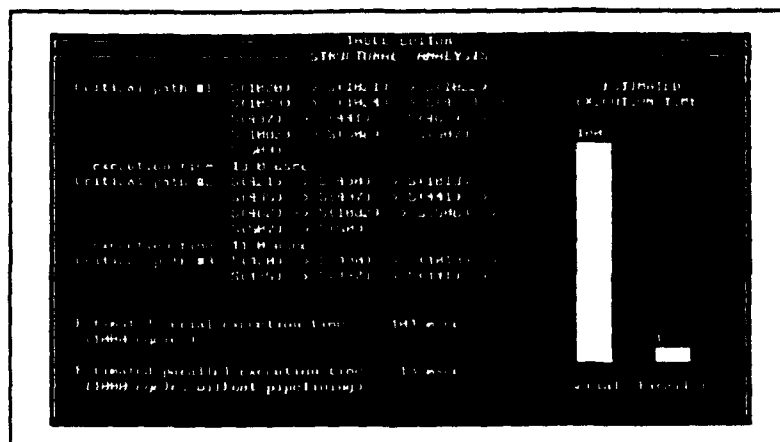
Figure 4. An Example Speedup Analysis Display

process scheduling and interprocess communication from the user, thus making code written for it highly portable. We implemented a version of the Kernel on the PC/transputer configuration expanded with the code necessary to run the machine-independent assembly output of the compiler.

The compiler has two output options. One option can generate code for a version of the MGK which is built into the user interface. This version of the Kernel runs on the PC only. It can be used for debugging purposes while developing test programs. The other output option is the generation of code for a network of multiple transputers. In this case the output is written into a file which can later be loaded into the Multigraph Kernel. The compiler optimizes the processor assignments if it generates code for a multiprocessor configuration.

Simulation Test Results

The system was tested using an example test program. This example was generated from an actual Test Requirement Sheet (TRS) representing a "typical" test. This program contains a total of 300 items (= nodes in the dependency graph) of which about 100 were computed nodes (the remaining ones were inputs and constants). We used this test program in the performance evaluation of the system. Our main interest was in obtaining the speedup curves with respect to increasing processor numbers. We think that absolute measurements at this point are less significant since we have no hard data concerning the performance of the validated library once ported

to the transputer. Our tests were geared towards analyzing the parallelization methods and the communication overhead introduced by the run-time support.
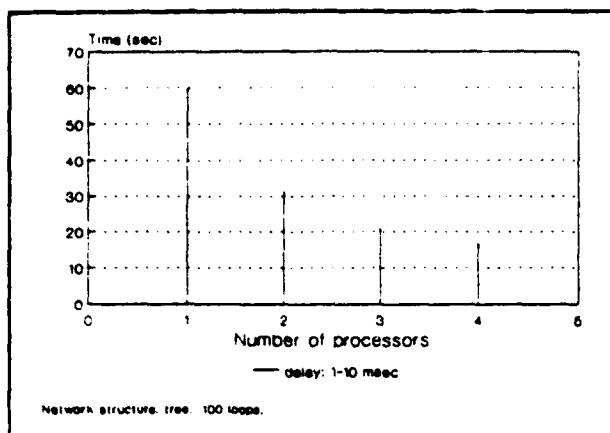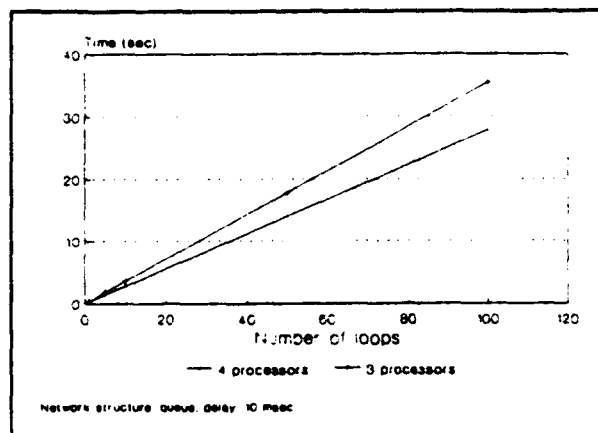

Figure 5. Test Program Execution Times

Figure 6. The Effect of Pipelining

The result of these measurements is a set of speedup curves with the independent variable being the number of transputers. We performed the tests under different conditions, with varying transputer network architectures, changing (and sometimes randomly simulated) execution times for the validated library functions, and with different processor assignment strategies. The results of these tests can be seen in Figures 5 through 8.
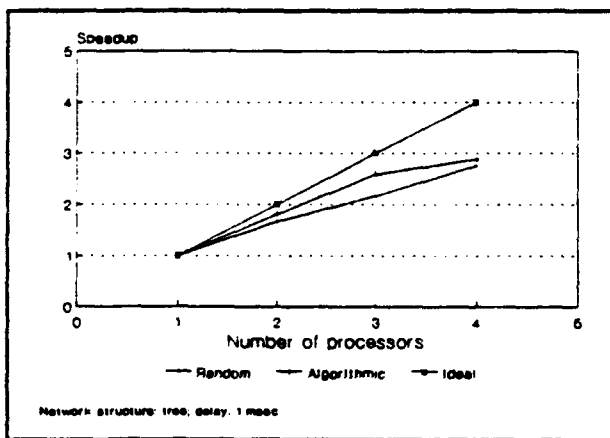
Figure 7. The Effect of CPU Assignment
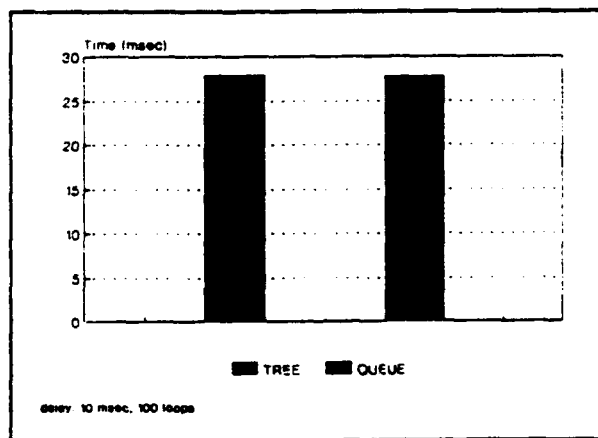
Figure 8. The Effect of Network Structure

Figure 5 shows the execution times of the test program using a different number of processors. For this test we simulated the data dependency of the library routine execution times with random delays in the 1 to 10 millisecond range.

Figure 6 shows the effects of Pipelining, that is the dependence of the execution time on the number of iterations.

Figure 7 shows the effect of the optimizing processor assignment strategy versus random assignment. Finally, the data in Figure 8 indicates that the achieved speedup is nearly independent of the transputer network architecture.

In summary we can determine that the obtainable speedup is fairly linear under varying conditions for the range of processor numbers.

Discussion

Performance:
Our evaluation of the performance measurement results is the following:

- The available data indicates that communication issues are not important in the system. The small differences between the execution times for unoptimized and optimized processor assignments on different transputer configurations justifies this conclusion.

- The scheduling overhead of the Multigraph Kernel seems to have a somewhat higher impact. However, for realistic library subroutine execution times its effect seems to be less significant, causing about a 20 percent performance loss. We think that this could be reduced measurably by:

  (1) creating a version of MGK especially optimized for the transputers. (The currently used MGK version is just a port of the 'general' Unix version.)
  (2) employing static scheduling, that is joining together nodes which run only a very short piece of code.

  On the other hand, the advantages provided by using of the Multigraph approach (dynamic system configuration, portability, etc..) must also be considered when making this evaluation. For example, it is very easy to recompile a TRS sheet for a different transputer configuration -- this is something what would be very hard to achieve without the kind of support MGK provides.
- The communication between the transputers and the host PC seems to be a bottleneck also. Therefore such communication should be minimized and vectorized.

2-8

Function Interface:

The validated library needs dynamic linking of functions to executing programs. This will allow the per-processor memory requirements to be minimized. Alternatively, static linking can also be used. In this case all possible routines must be included into the execution for each processor. It may be possible, however, to assemble a minimal collection of routines which will be used in a test in advance. In this case dynamic linking will not be necessary during the application building phase. This static linking would speed up the compile-debug cycle considerably.

Compiler Output:

Currently the compiler produces machine independent code as its output. To increase the performance of the system it might be necessary to add a direct machine code generation option. We think that the current output option should be preserved even in this case for reasons of portability and fast prototyping. The machine code output option could be used for the final version of the test program. It may be possible to generate position independent transputer code by the compiler which links to the AEDC Validated library routines using some dispatch table mechanism. In this case the generated code could be downloaded incrementally into the transputers without the costly link phase. Of course this assumes that it is possible to preload the necessary subroutines.

References:

[MGK1]   Abbott, B., Biegl, C., Sztipanovits, J.: "Multigraph for the Transputer", *Proceedings of the Third Conference of the North American Transputer Users Group*, Santa Clara, CA, April 1990.

[INMOS]   INMOS Limited: *Transputer Reference Manual*, 1989

[HAREL]   Harel, B.: "Biting the Silver Bullet", *Computer*, January 1992, pp. 8-20.

[ABBOTT]   Abbott, B., Bapty, T., Biegl, C., Karsai, G., Sztipanovits, J.: "Model Based Software Synthesis", *IEEE Software*, May 1993, pp. 42-52.

SOME SUGGESTIONS FOR THE ENGINEERING MODEL OF UNSTEADY FLOW IN A CAVITY

George D. Catalano
Associate Professor
Department of Civil and Mechanical Engineering

United States Military Academy
West Point, New York 10996-1792

PREFACE

The work reported here was done at the Arnold Engineering Development Center (AEDC), Air Force Materiel Command (AFMC), as part of the Air Force Office of Scientific Research Summer Research Extension Program. Suggestions for improving the accuracy of a mathematical model previously developed for flow past a cavity opening (the CAP Code) were made by modifying the code to include a Reynolds decomposition of the turbulent velocity, temperature and density fields. Through this approach, additional terms were developed in modeling the frequency and amplitude of the unsteady pressures acting at the rear wall. The predicted spectra were compared to both experimental data and previous predictions. The predictions using the modified CAP Code more closely produced the measured overall sound pressure level and root mean square of the turbulent pressure fluctuations. In addition, an attempt was made to develop a new damping coefficient for the pressure fluctuations, making use of ongoing efforts at the University of Tennessee Space Institute (UTSI).

CONTENTS

ILLUSTRATIONS

Some Suggestions for the Engineering Model of Unsteady Flow in a Cavity

George D. Catalano

1.0 INTRODUCTION

Flows past cavities continue to be of considerable interest to the aerodynamic research and development communities. From a basic research point of view, the flow past a cavity presents challenges to the turbulence investigator because of the complex interaction of fluid dynamic and acoustic phenomena. From a development perspective, the aerospace engineer is confronted with a challenging flow field to predict with any degree of confidence.

Research and development efforts in this area can be divided into three broad categories: experimental investigations, acoustic solutions, and Navier-Stokes equations. Dix[1] has performed an extensive experimental investigation at Arnold Engineering Development Center (AEDC). The data obtained was used to validate Navier-Stokes solutions such as those published by Om, Baysal, Rizzetta, Suhs, and Dougherty[2-7]. Unfortunately computer time on the order of 100 cpu-hr of a multiple-cpu, parallel processing, Class VI computer was required. Suhs[5] subsequently reduced the computational time to 20 cpu-hr by applying a thin-layer viscosity approximation and assuming that the cavity centerline is a plane of symmetry. However, the results did not include a computed spectrum, and as a result cannot be used to estimate the forces acting on the structure of the cavity. Acoustic theories have been used in an attempt to predict the spectrum. Unfortunately, such theories can be used only to predict the natural frequencies based on the dimensions of the cavity without predicting the magnitude of the pressures that occur at these frequencies. Caruthers and Raviprakash[8] have undertaken a parametric study of the acoustics of 2-D rectangular cavities exposed to a subsonic external flow using a panel method. Bauer and Dix[9] have taken a different approach developing a simple mathematical model (called the Cavity Acoustic Prediction Code, or CAP Code) with the intent of developing a means of predicting at least a first order estimate of both the frequency and amplitude of the tones occurring in a cavity. The CAP Code model has served as the starting point for the present investigation.

2.0 THE CAVITY ACOUSTIC MODEL

The CAP Code mathematical model developed by Bauer and Dix[9] considers the amplitudes of pressure fluctuations in a cavity to be attributable to the interaction of fluid dynamic and fundamental acoustic phenomena. A continuous spectrum of acoustic waves is assumed to be generated by a turbulent mixing zone that separates the outer flow from the internal cavity flow field. The acoustic waves then in turn trigger vortices of enhanced strength which set up in effect a closed feed-back loop circuit. Bauer and Dix[9] use a variable damping term, which is an empirical function of the relative magnitude of the frequencies of the fundamental acoustic modes of the cavity and the edge tones generated at the leading edge. From experimental results, the maximum rms pressure in a cavity is known to occur at the downstream wall where the turbulent mixing zone impinges. This serves as the justification for the assertion that the maximum rms pressure is related to the maximum rms pressure in the turbulent mixing zone.

In developing the CAP Code, Bauer and Dix[9] derived an expression for the rms pressure in a turbulent mixing zone beginning with a form of the Bernoulli equation. An important assumption was made in the assertion of a linear relationship between the Reynolds shear stress and the turbulent kinetic energy. Along with this assumption, two methods developed by Bauer[10] were used: 1) a technique to determine the shear force along the dividing streamline in a turbulent mixing region; and 2) a correction factor accounting for the existence of a boundary layer at the upstream edge of the cavity. The absolute level of the pressure spectrum (i.e. the overall or integrated strength of the vortices produced by the acoustic waves generated in the turbulent mixing region) was calculated from the rms pressure.

Using the CAP Code, it was possible to predict both the frequency and amplitude of the acoustic tones in unsteady flow past a cavity. Good agreement between predictions and an extensive database was noted for both the frequency and amplitude of moderately deep cavities (L/D = 4.5). However, comparisons of the predicted overall rms pressure and data were not within the same quality of agreement. One focus of the present work was, therefore, to improve the quality of CAP Code predictions vis-à-vis the existing data base by modifying the existing code to include concepts of turbulent fluid physics.

3.0 DEVELOPMENT OF THE MODIFIED CODE

A compressible turbulent flow can be modeled using the Reynolds' velocity decomposition as follows:

$$P = \overline{P} + p' \qquad (1)$$

$$T = \overline{T} + T' \qquad (2)$$

$$u_i = \overline{u_i} + u' \qquad (3)$$

and
$$\rho = \overline{\rho} + \rho' \qquad (4)$$

where the overbar indicates a spatial ensemble average, and the prime indicates a fluctuating quantity. Note the ensemble-averaged quantities are still functions of time in that each represents the relatively large-scale (or low-frequency) oscillations, and the primed quantities model the higher-frequency turbulent fluctuations. Substituting the decomposition into the Bernoulli equation results in

$$d\left(\overline{P} + p'\right) + \left(\overline{\rho} + \rho'\right)(u + u')d(u + u') = 0 \qquad (5)$$

where the index of the ith direction has been dropped because the flow is following along a stream tube. Expanding Eq. (5) produces

$$d\left(\overline{P} + p'\right) + \overline{\rho}\,\overline{u}\,d\overline{u} + \rho'\,\overline{u}\,d\overline{u} + \overline{\rho}\,u'd\overline{u} + \rho'u'd\overline{u} + \overline{\rho}\,\overline{u}\,du' + \rho'\overline{u}\,du' + \overline{\rho}\,u'du' + \rho'u'du' = 0 \qquad (6)$$

The ensemble average of each term taken individually yields:

$$\overline{d\overline{P}} = \overline{d\overline{p}} \qquad (7)$$

$$\overline{d\rho'} = 0 \qquad (8)$$

3-5

$$\overline{\overline{\rho}\,\overline{u}\,d\overline{u}} = \overline{\rho}\,\overline{u}\,d\overline{u} \tag{9}$$

$$\overline{\rho'\,\overline{u}\,d\overline{u}} = 0 \tag{10}$$

$$\overline{\overline{\rho}\,u'\,d\overline{u}} = 0 \tag{11}$$

$$\overline{\rho'\,u'\,d\overline{u}} = \overline{\rho'\,u'}\,d\overline{u} \tag{12}$$

$$\overline{\overline{\rho}\,\overline{u}\,du'} = 0 \tag{13}$$

$$\overline{\overline{\rho}\,u'\,du'} = \frac{\overline{\rho}}{2}\,d\overline{u'^2} \tag{14}$$

$$\overline{\rho'\,\overline{u}\,du'} = \overline{u}\,\overline{\rho'\,du'} \tag{15}$$

$$\overline{\rho'\,u'\,du'} = \overline{\frac{\rho'}{2}\,du'^2} \tag{16}$$

An order of magnitude analysis leads to the following conclusions:

$$\left|\overline{\rho}\,\overline{u}\,d\overline{u}\right|, \quad \left|\frac{\overline{\rho}}{2}\,d\overline{u'^2}\right|, \quad \text{and} \quad \left|\overline{\rho'\,u'}\,d\overline{u}\right| \quad >> \quad \left|\overline{u}\,\overline{\rho'\,du'}\right| \quad \text{and} \quad \left|\overline{\rho'\,u'\,du'}\right| \tag{17}$$

so that the resulting Bernoulli equation [from Eq. (5)] becomes:

$$d\overline{P} = -\overline{\rho}\,\overline{u}\,d\overline{u} - \frac{\overline{\rho}}{2}\,d\overline{u'^2} - \overline{\rho'\,u'}\,d\overline{u} \tag{18}$$

Assuming the existence of a Universal Equilibrium Range and an Inertial Subrange (and thus the applicability of Kolmogorov's First and Second Theorems[11]), there is a net transfer of kinetic energy from the lower to the higher frequencies. Consequently, there is a balance between the turbulent kinetic energy in the flow attributable to the oscillating shear layer, and the turbulent kinetic energy in the range of the turbulent scales. Thus:

$$\left(\overline{u}_{rms}\right)^2 = O\left(\overline{u_{rms}'^2}\right) \tag{19}$$

and Bernoulli's equation [Eq. (18)] becomes:

$$P_{rms} = \overline{\rho}\,\overline{u}\,u_{rms} + \frac{\overline{\rho}}{2}\left(u_{rms}\right)^2 + \overline{\rho'\,u'}\,u_{rms} \tag{20}$$

Addressing the correlation between the fluctuating density and velocity fields, Schlichting[12] argues that

$$\frac{\overline{u'T'}}{u_{rms}\, T_{rms}} = 0.6 \to 0.8 \tag{21}$$

Assuming the density field responds in a manner similar to that of the temperature field, then

$$\frac{\overline{\rho'u'}}{\overline{\rho}_{rms}\, \overline{u}_{rms}} \cong 0.6 \to 0.8 = a_2 \tag{22}$$

From the conservation of mass, $\qquad d(\overline{\rho}\,\overline{u}) = 0 \tag{23}$

or $\qquad\qquad\qquad\qquad \overline{u}\, d\overline{\rho} + \overline{\rho}\, d\overline{u} = 0 \tag{24}$

or $\qquad\qquad\qquad\qquad \frac{d\overline{\rho}}{\overline{\rho}} + \frac{d\overline{u}}{\overline{u}} = 0 \tag{25}$

so that $\qquad\qquad\qquad\quad \overline{\rho}_{rms} = \frac{\overline{\rho}\,\overline{u}_{rms}}{\overline{u}} \tag{26}$

from which $\qquad\qquad\qquad \overline{\rho}_{rms}\, \overline{u}_{rms}^2 = \frac{\overline{\rho}}{\overline{u}}\, \overline{u}_{rms}^3 \tag{27}$

Bauer and Dix[9] argue that it is common to assume a linear relationship between the Reynolds shear stress and the turbulent kinetic energy, or:

$$F_s = a_1 \overline{\rho}\, \tau_{KE} \tag{28}$$

where it is usually accepted that $\qquad a_1 = 0.3 \tag{29}$

A friction coefficient is defined as $\qquad C_f = \frac{F_s}{q_\infty} = a_1 \frac{\overline{\rho}\, \tau_{KE}}{q_\infty} \tag{30}$

so that one may write $\qquad\qquad \overline{u}_{rms}^2 = \frac{2 q_\infty C_f}{a_1 \overline{\rho}} \tag{31}$

Thus $\qquad\qquad\qquad \overline{\rho}_{rms}\, \overline{u}_{rms}^2 = \frac{\overline{\rho}}{\overline{u}} \left(\frac{2 q_\infty C_f}{a_1 \overline{\rho}} \right)^{3/2} \tag{32}$

and
$$(\bar{\rho})^{1/2}\,\bar{u} = (\bar{q})^{1/2}\sqrt{2} = \sqrt{2\bar{q}}$$
(33)

Dividing by q_∞:
$$\frac{\bar{\rho}_{rms}\,\bar{u}_{rms}^2}{q_\infty} = \frac{1}{\sqrt{2}}\left(\frac{q_\infty}{\bar{q}}\right)^{1/2}\left(\frac{2C_f}{a_1}\right)^{1/2}$$
(34)

Recalling that the square of the Crocco number is defined as

$$C_\infty^2 = \frac{u_\infty}{2c_p T_t}$$
(35)

and defining the velocity ratio as
$$\phi_d = \frac{\bar{u}}{u_\infty}$$
(36)

then
$$\left(\frac{q_\infty}{\bar{q}}\right)^{1/2} = \sqrt{\frac{1-C_\infty^2\,\phi_d^{\ 2}}{\left(1-C_\infty^2\right)\phi_d^{\ 2}}}$$
(37)

so that
$$\frac{\bar{\rho}_{rms}\,\bar{u}_{rms}^2}{q_\infty} = \frac{1}{\sqrt{2}}\sqrt{\frac{1-C_\infty^2\,\phi_d^{\ 2}}{\left(1-C_\infty^2\right)\phi_d^{\ 2}}}\left(\frac{2C_f}{a_1}\right)^{3/2}$$
(38)

Then the final expression for the ratio of the rms pressure to the free-stream dynamic pressure is:

$$\frac{P_{rms}}{q_\infty} = \frac{\bar{u}}{q_\infty}\sqrt{\frac{2\bar{\rho}q_\infty}{a_1}} + \frac{C_f}{a_1} + \frac{1}{\sqrt{2}}\sqrt{\frac{1-C_\infty^2\,\phi_d^{\ 2}}{\left(1-C_\infty^2\right)\phi_d^{\ 2}}}\left(\frac{2C_f}{a_1}\right)^{3/2}$$
(39)

It is useful to compare Eq. (39) with the expression derived previously by Bauer and Dix[9]:

$$\frac{P_{rms}}{q_\infty} = 2\phi_d\sqrt{\frac{\left(1-C_\infty^2\right)C_f}{a_1\left(1-C_\infty^2\,\phi_d^{\ 2}\right)}}$$
(40)

The two additional terms in Eq. (39) result from the inclusion of the turbulent velocity field along with its interaction with the fluctuating density field. Both terms serve to add in magnitude to the estimate of the maximum pressure at the rear wall of the cavity.

3.1 Relationship between the Reynolds Shear Stress and the Turbulent Kinetic Energy

In developing equations for a compressible turbulent boundary layer, Schlichting[12] notes that

$$F_s = \rho_1\bar{\varepsilon}\frac{d\bar{u}}{dy}\left(\frac{\rho}{\rho_1}\right)^2$$
(41)

Relating the compressible eddy viscosity to the incompressible eddy viscosity

$$\tilde{\varepsilon} = \frac{1}{b}\left(\frac{\gamma R T_0}{\gamma R T}\right)\varepsilon \tag{42}$$

which can be rewritten as
$$\tilde{\varepsilon} = \frac{1}{b}\left(\frac{T_-/T_{\iota_-}}{T/T_{\iota}}\right)\frac{T_{\iota_-}}{T_{\iota_-}} \tag{43}$$

Assuming an adiabatic wall
$$\tilde{\varepsilon} = \frac{1}{b}\left(\frac{1-C_-^2}{1-\overline{C}^2}\right) \tag{44}$$

where C is the Crocco number, Eq. (35).

Rewriting,
$$\tilde{\varepsilon} = \frac{1}{b}\left[\frac{1-C_-^2\,\phi_d^{\;2}}{(1-C_-^2)\phi_d^{\;2}}\right] \tag{45}$$

and finally:
$$a_{1\text{\tiny compressible}} = a_1\frac{1}{b}\left[\frac{1-C_-^2\,\phi_d^{\;2}}{(1-C_-^2)\phi_d^{\;2}}\right] \tag{46}$$

The value of the constant "b" varies from $O[1]$ to $O[1000]$ according to the work of Reichardt[13] and Rotta[14]. Unfortunately, the level of confidence in the proper value is low because of the difficulties of measuring local temperatures, temperature gradients, and velocity gradients. Therefore, for the present work, the value of "b" was set equal to 1.0 as a first effort.

3.2 Modeling of Damping Phenomena

Bauer and Dix[9] consider two different types of damping when calculating the spectra of pressures acting on the downstream wall of the cavity: 1) viscous damping when L/D << 1.0; and 2) wave damping which is attributable to the interaction of the acoustic waves with energy then lost out through the cavity opening. The following relation was proposed for the wave damping:

$$d_w = \left(1-\frac{f_c}{f_L}\right)^2 + \left(1-\frac{f_c}{f_W}\right)^2 + \left(1-\frac{f_c}{f_D}\right)^2 \tag{4}$$

In a recent report by Caruthers and Raviprakash[8], the results of a parametric study of the acoustics of 2-D rectangular cavities exposed to subsonic external flow was presented. Of primary interest for the present work was the predicted acoustic radiation damping for L/D = 4.5. Caruthers and Raviprakash[8] found that the acoustic radiation damping multiplied by the square of the reduced

frequency more closely resembled a cosine or sine wave with the minimum wave damping occurring at the edge tone frequencies as in the original cavity model. Consequently, in the present work, a different wave damping model is proposed:

$$d_w = \cos^2\left(\frac{\pi}{2}\frac{f_e}{f_L}\right) + \cos^2\left(\frac{\pi}{2}\frac{f_e}{f_W}\right) + \cos^2\left(\frac{\pi}{2}\frac{f_e}{f_D}\right) \tag{48}$$

where the magnitude of the wave damping approaches a minimum at each edge tone frequency.

4.0 DISCUSSION OF RESULTS

Comparisons of overall SPL and P_{rms}/q_∞ are illustrated in Figure 1. Experimental data are compared to the predictions of the existing Bauer-Dix code (CAP1)[9] and the modified code (CAP2) of the present effort. In these comparisons, the actual free stream total temperatures, total pressures, Mach numbers were chosen as the inputs for both the original and modified codes. The measured boundary layer thicknesses for each test case were used as well.

Examining the behavior of SPL in Figure 1, it is clear that the predictions from the CAP2 code are in significantly closer agreement with the experimental data throughout the Mach number range of primary interest (transonic, i.e., $0.95 < M_\infty < 1.20$). The agreement is within approximately 2 dB compared to 4-6 dB difference for the original code.

Two specific observations can be made from a comparison of the predictions of the codes with experimental data for the normalized rms pressure parameter, P_{rms}/q_∞. First, for the Mach number range of $0.95 < M_\infty < 1.20$, the CAP2 predictions are in closer agreement with the experimental data than are the predictions of the original CAP1 code. Second, neither the CAP1 nor the CAP2 code predictions reflect the behavior of P_{rms}/q_∞ in the subsonic régime, $M_\infty < 0.95$. The experimental evidence indicates a decrease in P_{rms}/q_∞ as M_∞ increases, yet both original and modified codes predict the opposite trend.

In Figure 2, the effects of the introduction of the new damping coefficient are examined. The modal peak amplitude predictions of the original CAP1 code are compared at several Mach numbers to the predictions of the CAP2 code using the Bauer and Dix damping coefficient[9], as well as the CAP3 code, which is the CAP2 code using a revised damping coefficient that reflects the findings of Caruthers, et.al.[8]. In all cases, both the CAP2 and the CAP3 codes slightly over-predict the SPL throughout the range of reduced frequencies. The increase in SPL is attributable to the inclusion of the two additional terms in the formulation of the P_{rms}. At the lower frequencies, i.e., for the first few modes, the revised damping coefficient serves to reduce the SPL, but as frequency increases, the SPL actually increases. This behavior violates the physical understanding of the flow field and indicates that the new damping coefficient requires more development.

5.0 CONCLUSIONS

Several suggestions for improving the CAP Code, an engineering model for flow past a cavity, have been proposed and evaluated using an extensive database. The improvements offered focused on the turbulent velocity, temperature, and density fields, and including their complex interactions and effects on the estimate of the maximum rms pressure at the rear wall of the cavity. In the Mach number range of interest, the predictions of the modified code, called CAP2, were in closer agreement with data than the original code for both SPL and P_{rms}/q_∞ parameters. A CAP3 code (which was the CAP2 code modified with a revised damping coefficient that reflected results of a separate investigation based strictly on acoustic theory) did not accurately predict the behavior of either the SPL or P_{rms}/q_∞ parameters at higher values of frequency. The damping term must undergo further study to allow the CAP code to more accurately match the existing database from experiments.

REFERENCES

1. Dix, R. E. "On Simulation Techniques for the Separation of Stores from Internal Installations." Paper presented at the SAE Aerospace Technology Conference and Exposition, Long Beach, California, October 1987.

2. Om, D. "Navier Stokes Simulation for Flow Past an Open Cavity." AIAA-86-2628, October 1986.

3. Baysal, O. and Stallings, R. L. "Computational and Experimental Investigation of Cavity Flow Fields." AIAA-87-1288, January 1987.

4. Rizzetta, D. P. "Numerical Simulation of Supersonic Flow Over a Three Dimensional Cavity." AIAA-87-1288, June 1987.

5. Suhs, N. E. "Computations of Three-Dimensional Cavity Flow at Subsonic and Supersonic Mach Numbers." AIAA-87-1208, June 1987.

6. Baysal,O., Srinivasan, S., and Stallings, R. L. "Unsteady Viscous Calculations of Supersonic Flows Past Deep and Shallow Three-Dimensional Cavities." AIAA-88-0101, January 1988.

7. Dougherty, N., et.al. "Time-Accurate Navier Stokes Computations of Self-Excited TwoDimensional Unsteady Cavity Flows." AIAA-90-0691, January 1990.

8. Caruthers, J. E. and Raviprakash, G. K. "Acoustic Resonance Calculation for Radiation Damped Two-Dimensional Cavities Exposed to Subsonic Flow." University of Tennessee Space Institute Research Report UTSI 93/07, The University of Tennessee Space Institute, Tullahoma, Tennessee, May 1993.

9. Bauer, R. C. and Dix, R. E. "Engineering Model of Unsteady Flow in a Cavity." AEDC-TR-91-17, December 1991.

10. Bauer, R. C. "Characterization of Axisymmetric and Two Dimensional Isoenergetic Jet Mixing Zones." AEDC-TDR-63-253, December 1963.

11. Monin, A. and Yaglom, A. *Statistical Fluid Mechanics, Vol. 1,* MIT Press, Cambridge, Massachusetts, 1975.

12. Schlichting, H. *Boundary Layer Theory.* McGraw-Hill, New York, 6th edition, 1968, pp. 669-676.

13. Prandtl, L. "Ueber die Flüssigkeitsbewegung bei sehr kleiner Reibung." *Proceedings of III International Mathematics-Congress,* Heidelberg, Germany, 1904, pp. 484 - 491.

14. Rotta, J. C. "Turbulent Boundary Layers in Incompressible Flow." *Progress in Aeronautical Sciences, Vol. 2, Boundary Layer Problems,* Pergamon Press, New York, New York, 1962, pp.1-219.
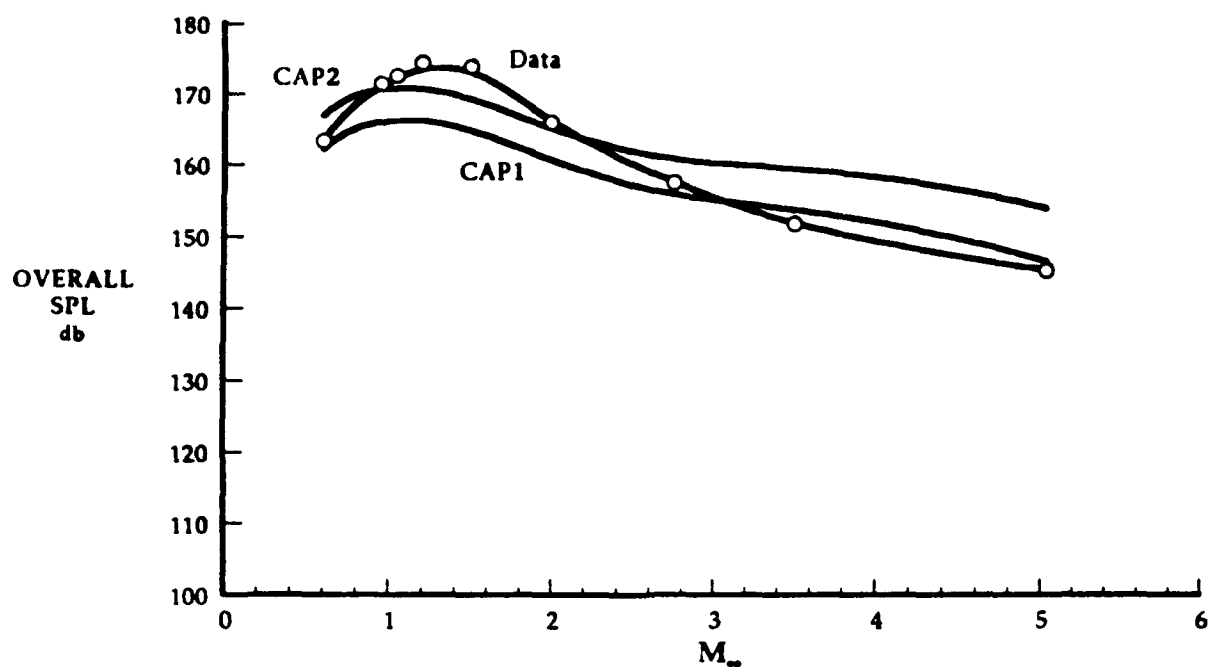
a. Overall Sound Pressure Level (OASPL)
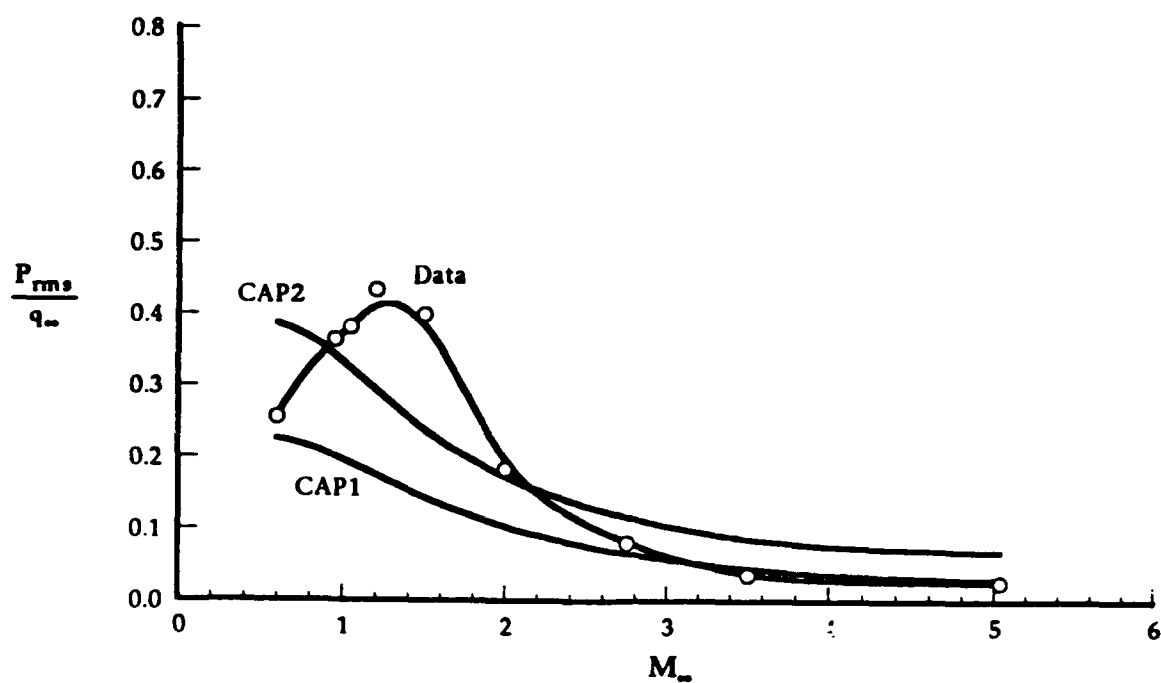
b. Normalized rms Pressure

Figure 1. Comparison of Experimental and Predicted Overall Levels at Various Mach Numbers.

3-13
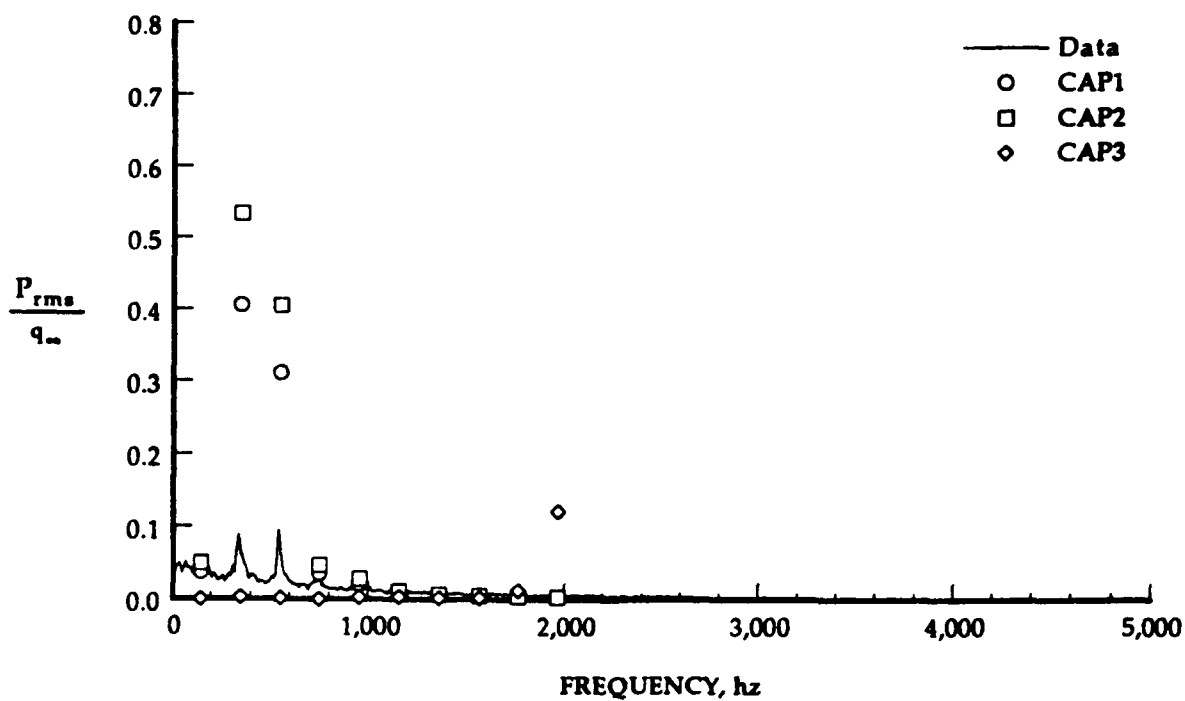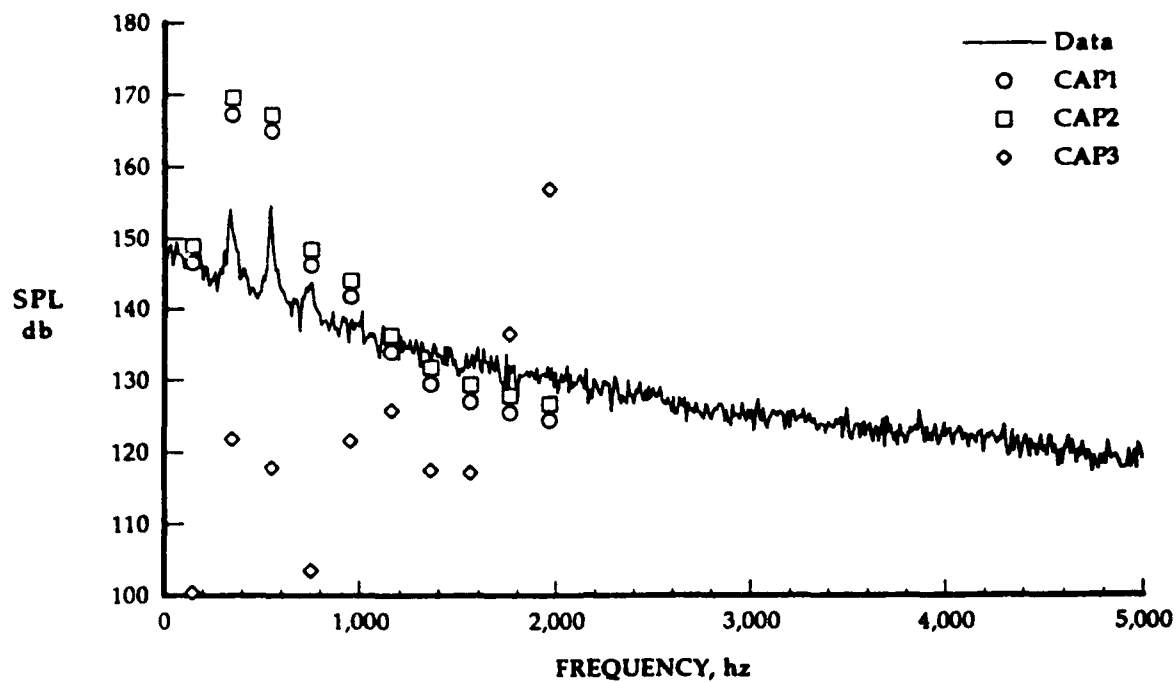
a. M∞ = 0.60

Figure 2. Comparison of Experimental and Predicted Spectra at Various Mach Numbers.
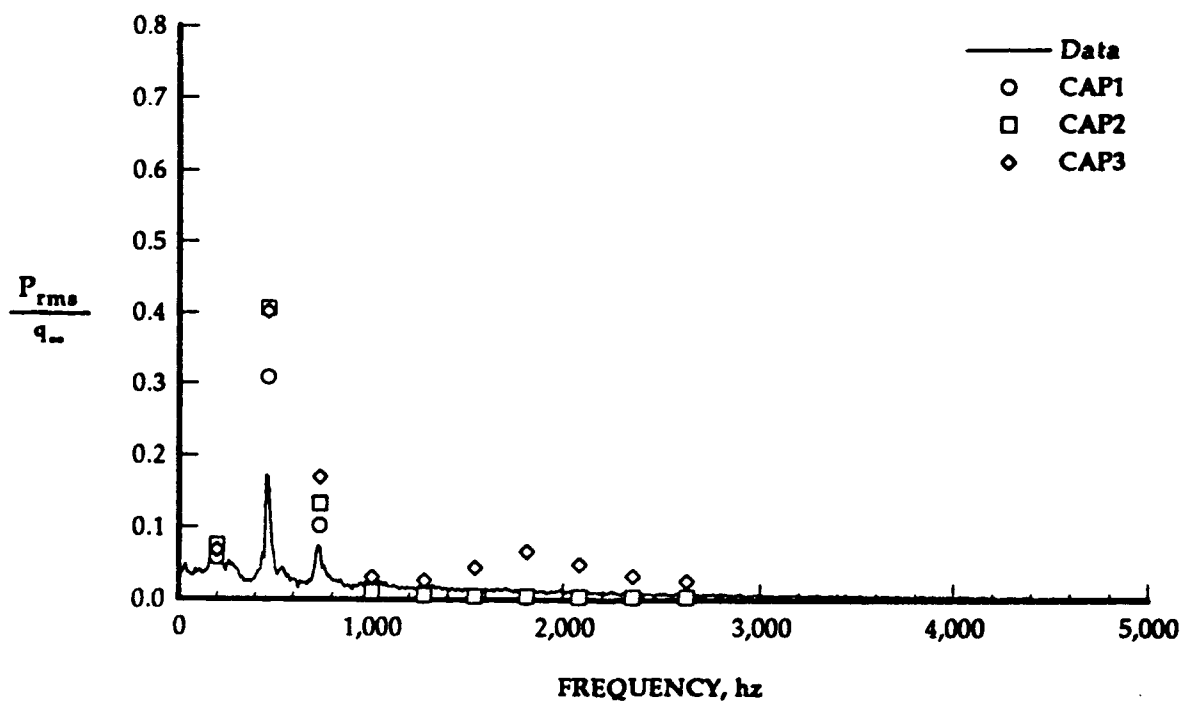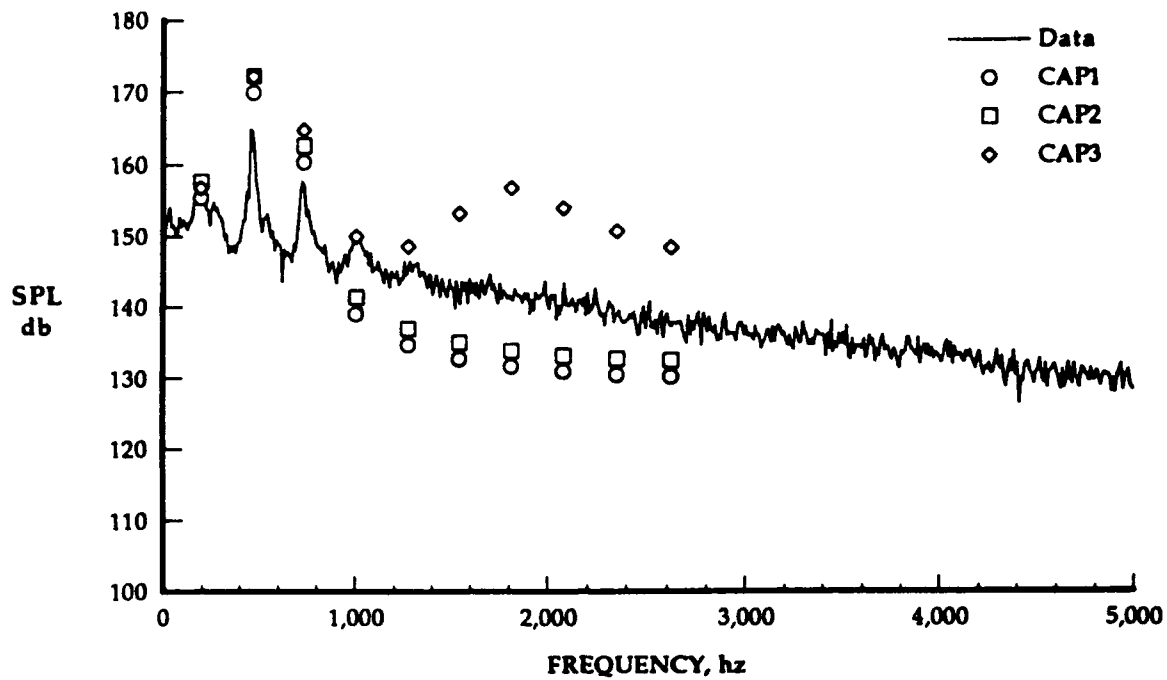
b. M∞ = 0.95

Figure 2. Continued.
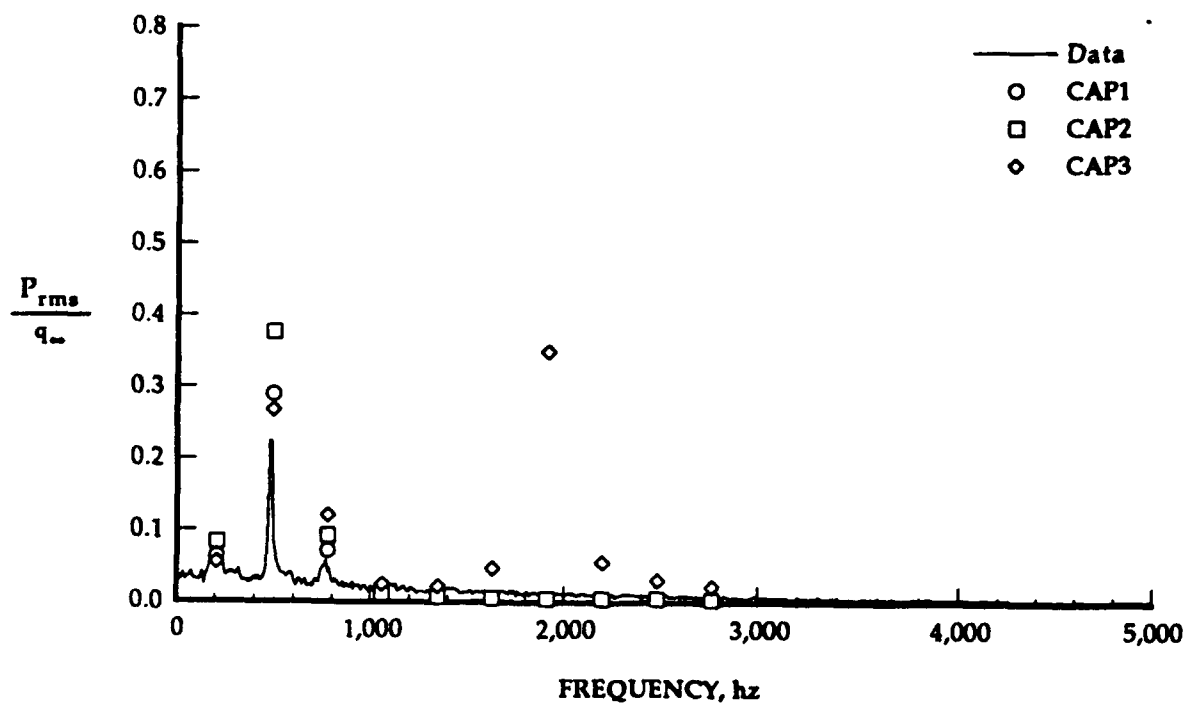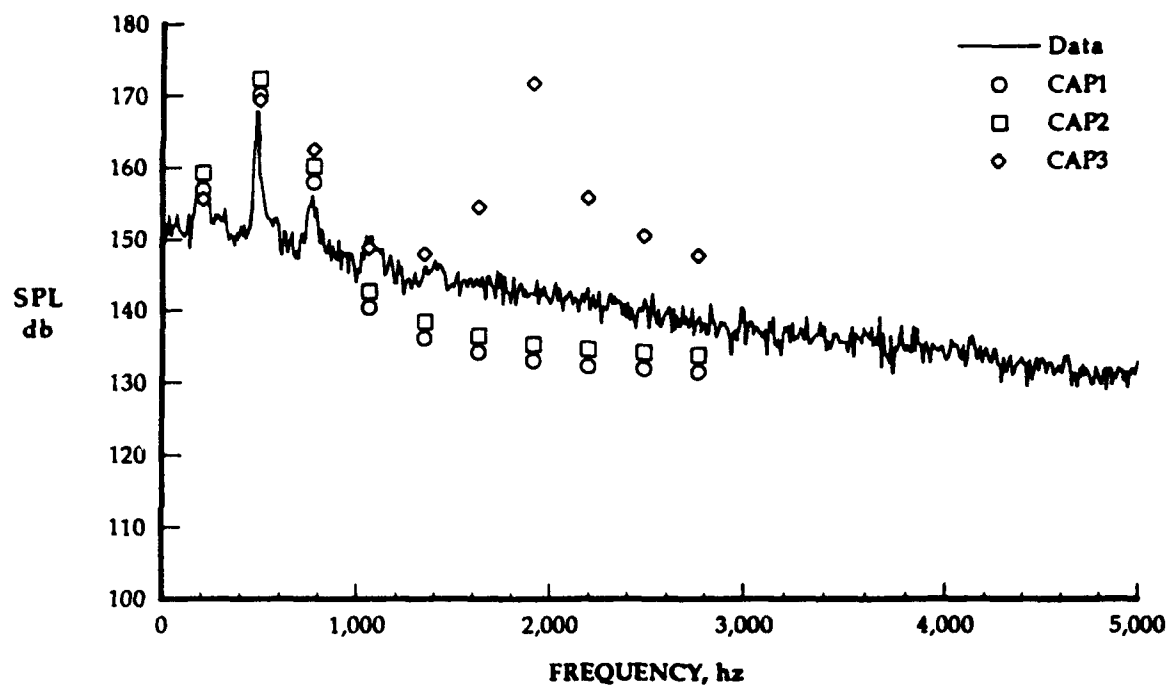
c. $M_\infty = 1.05$

Figure 2. Continued.

3-16
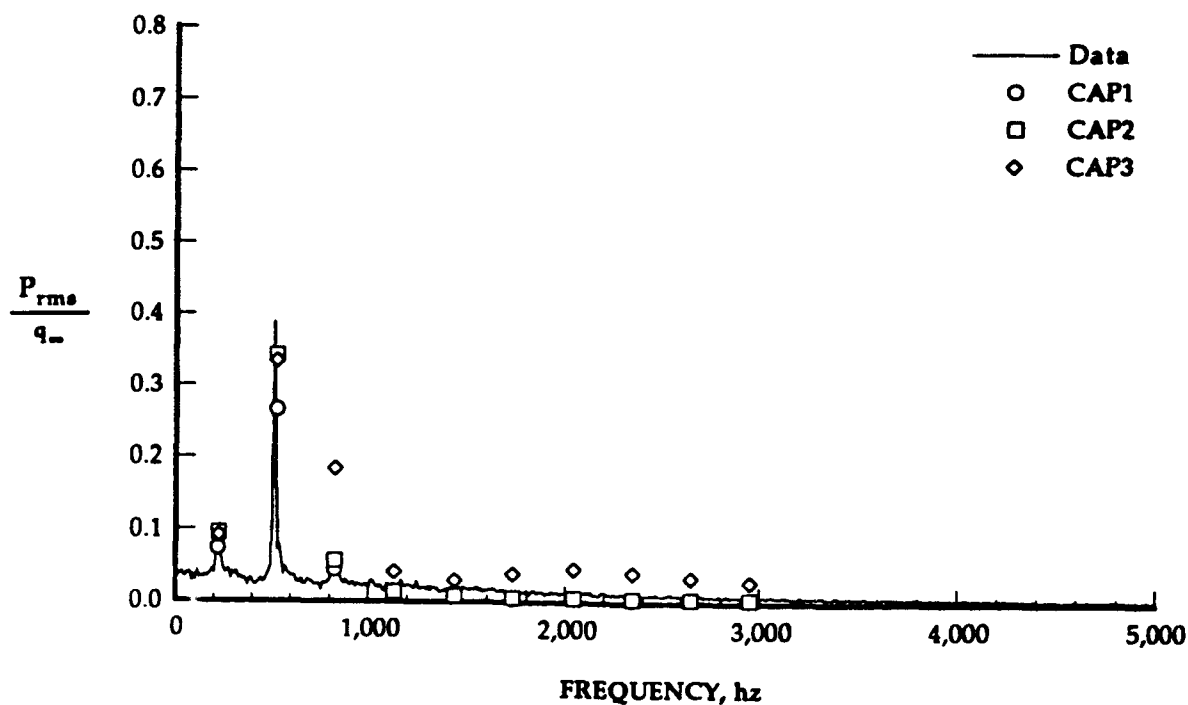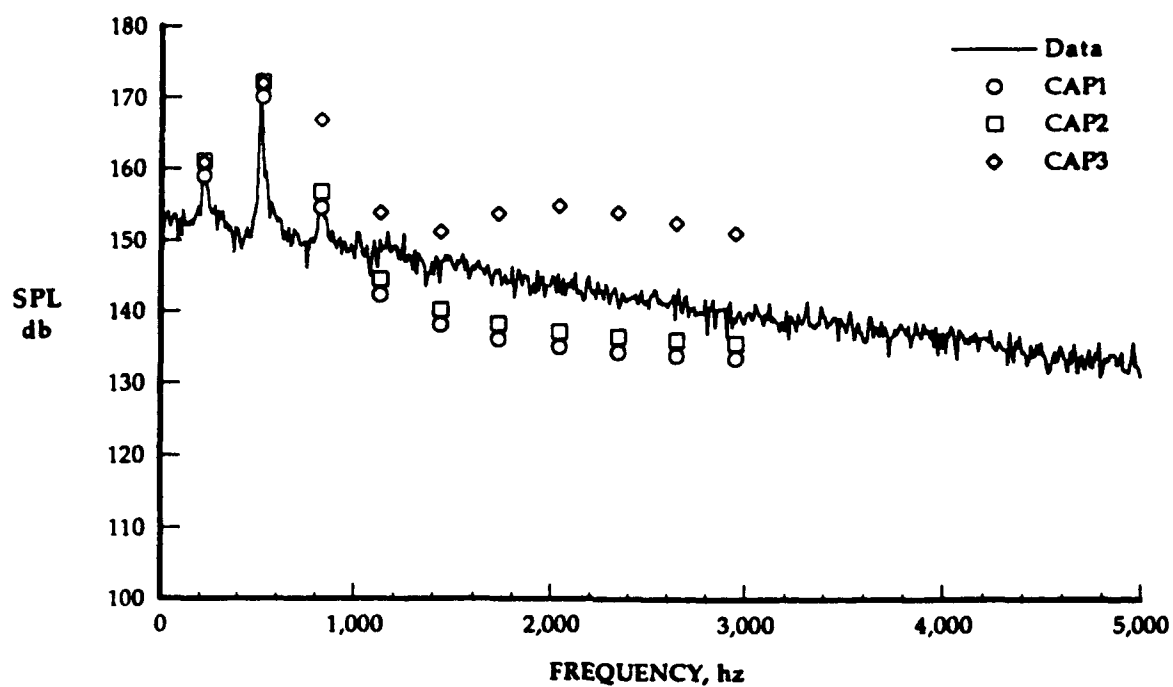
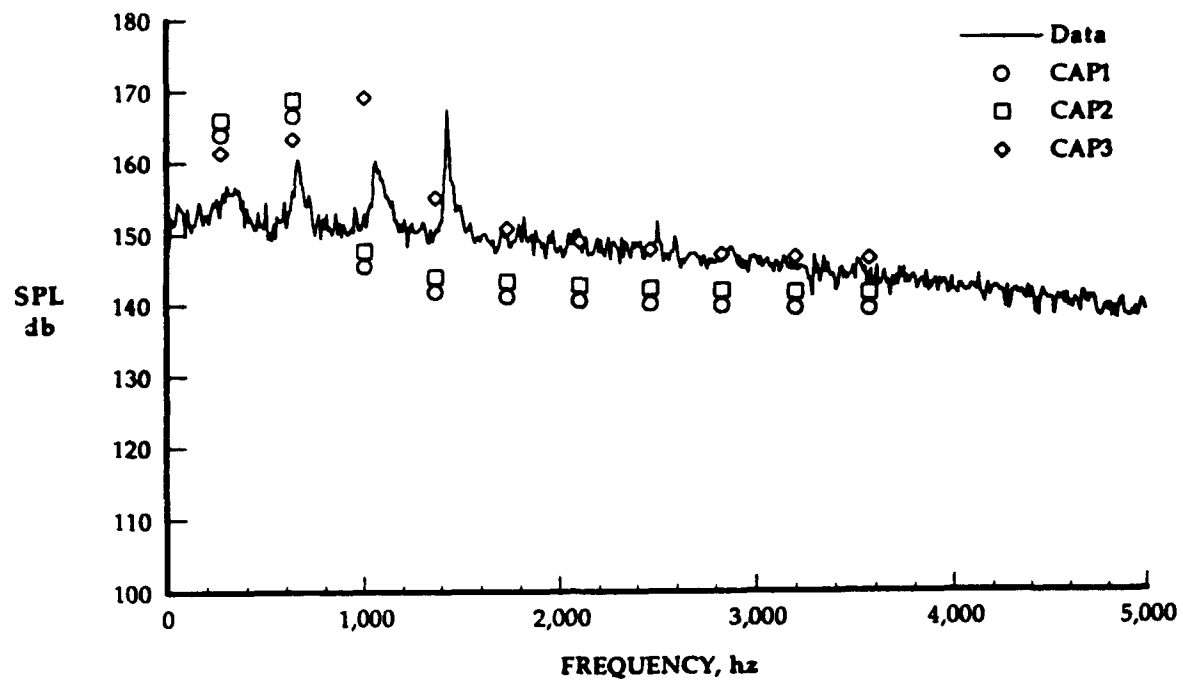d. $M_\infty = 1.20$

Figure 2. Continued.
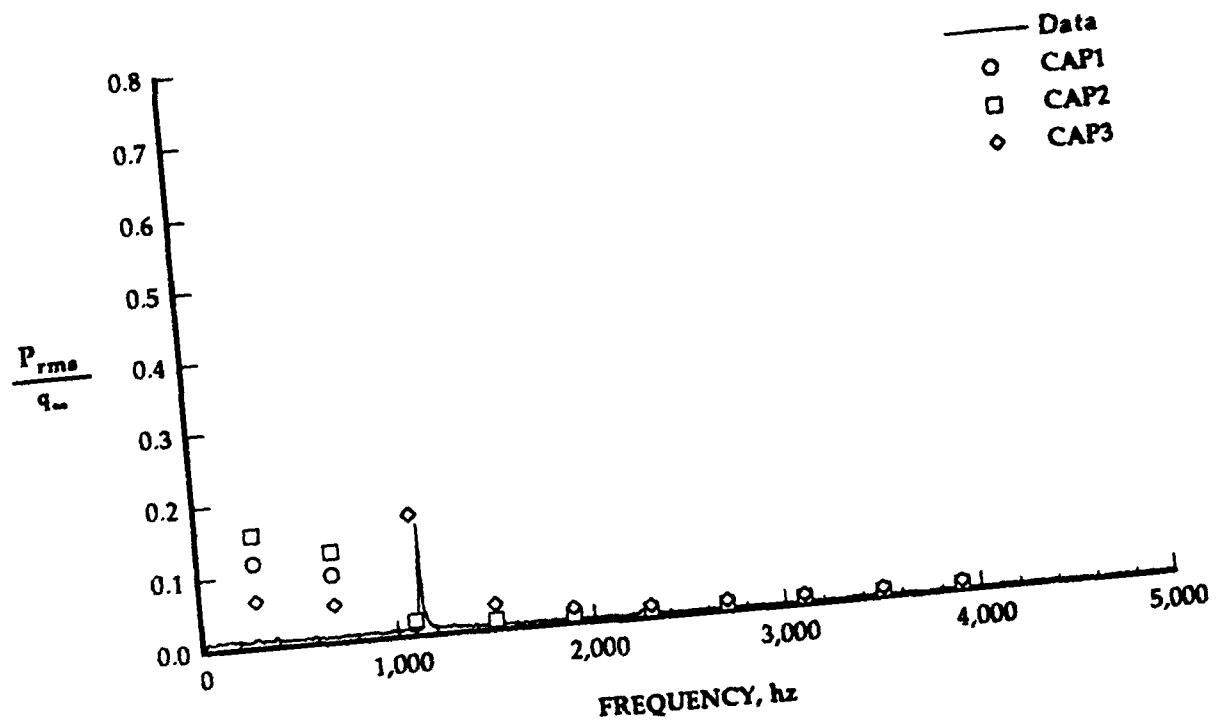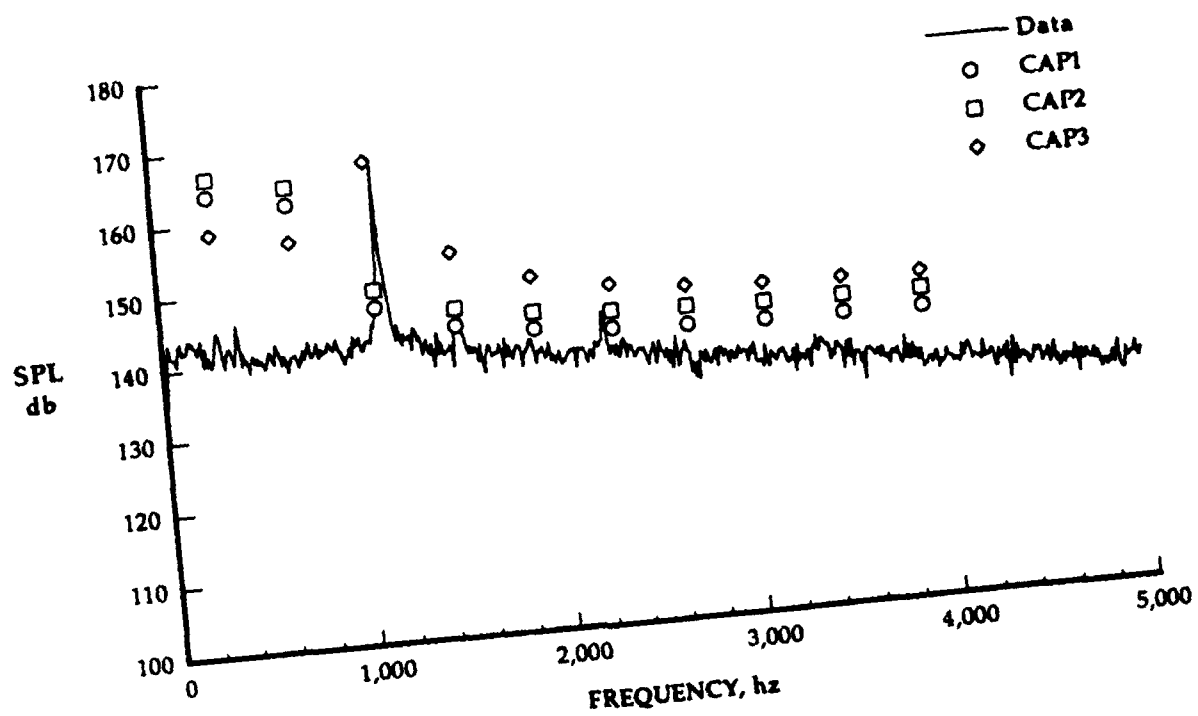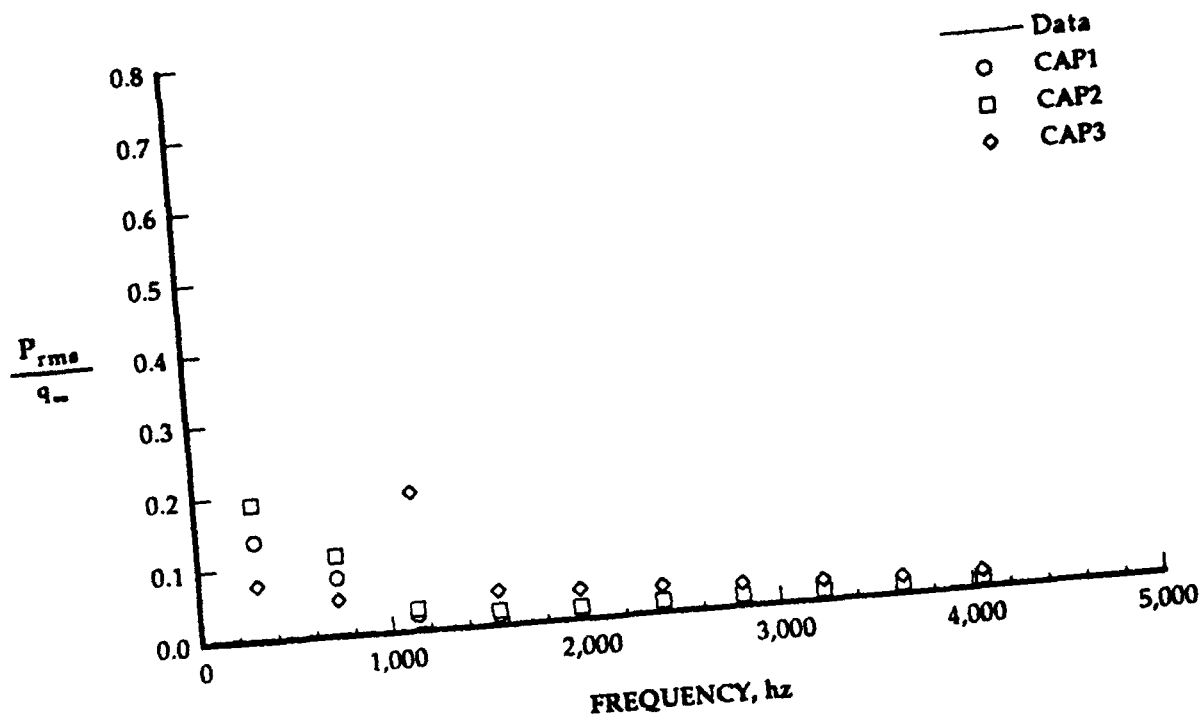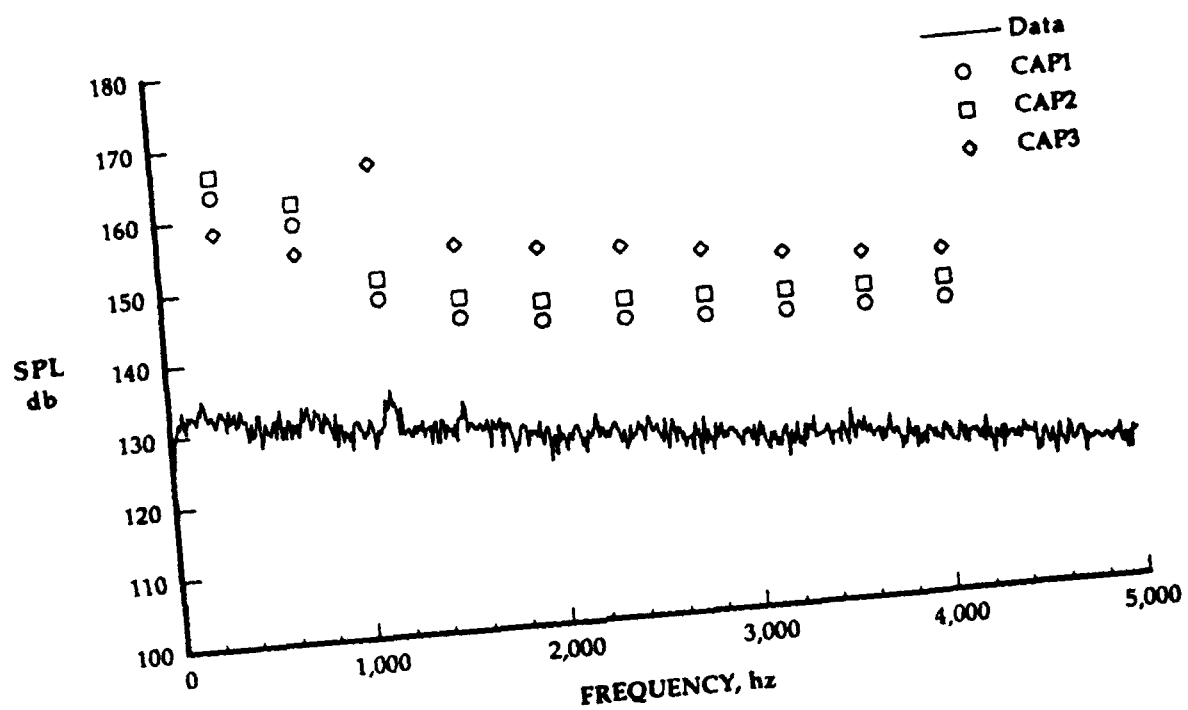
3-17
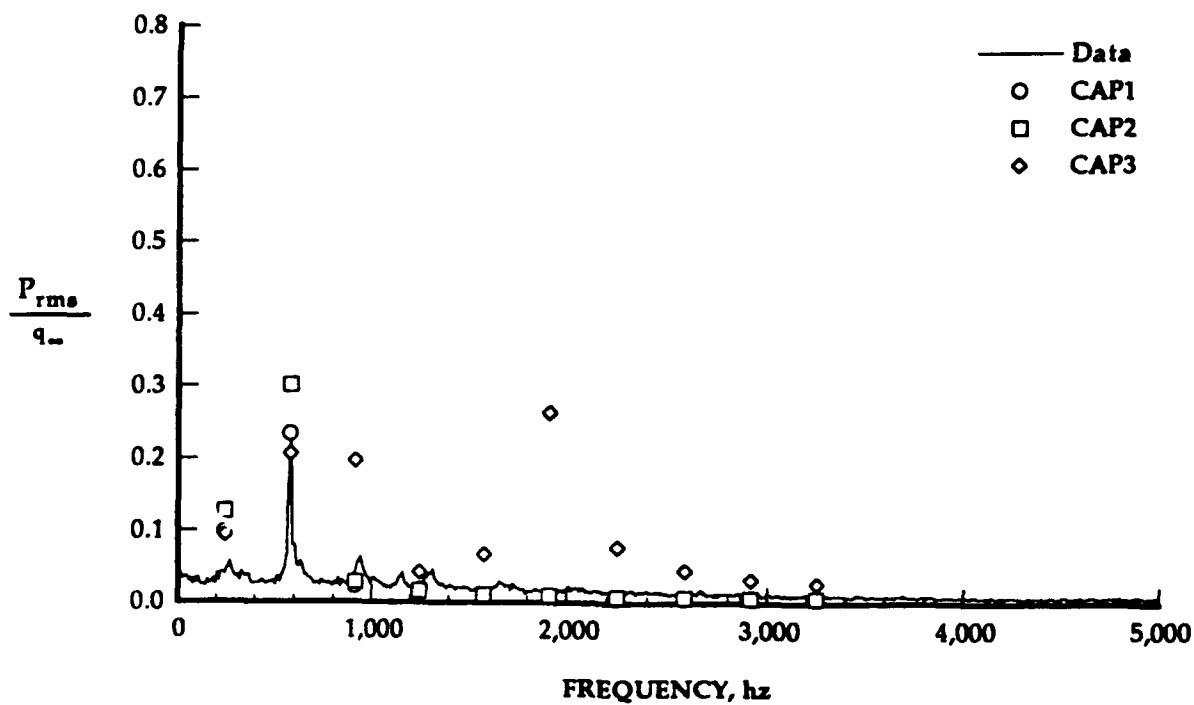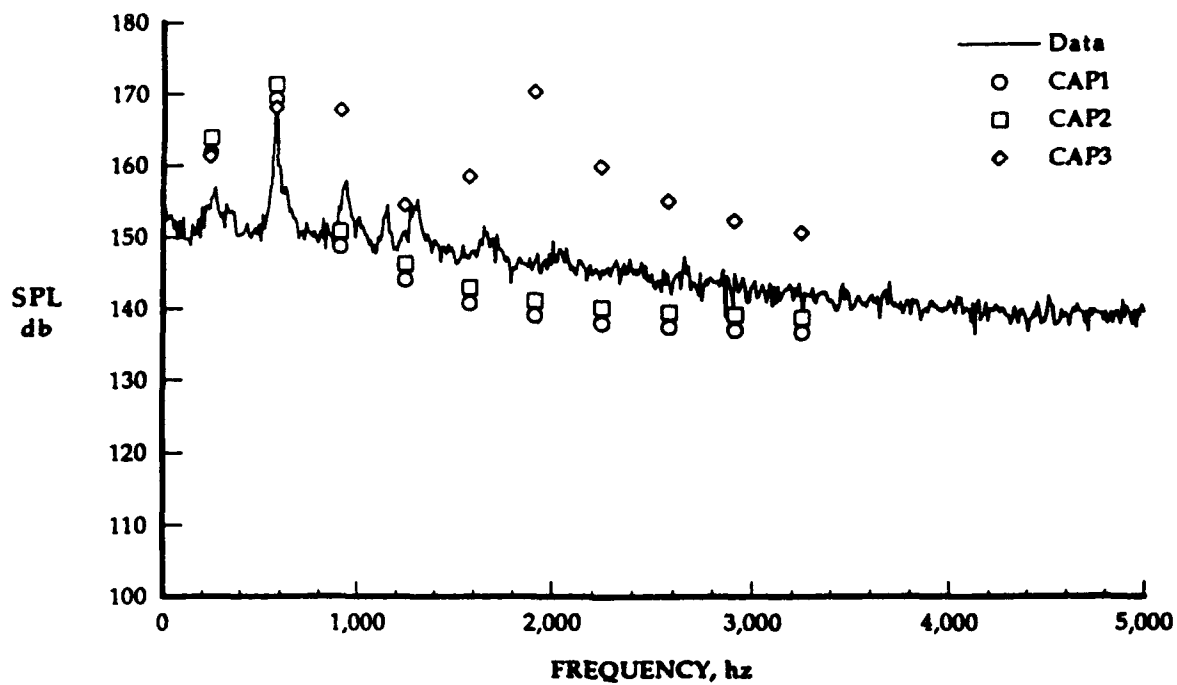
e. M∞ = 1.50

Figure 2. Continued.
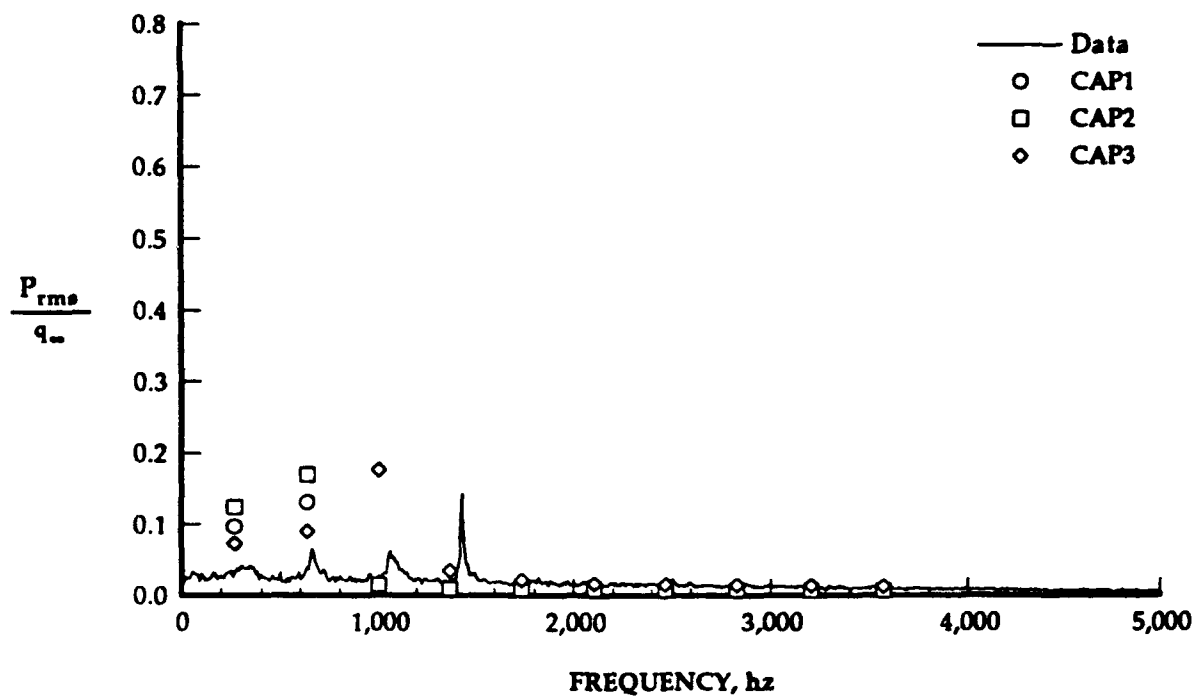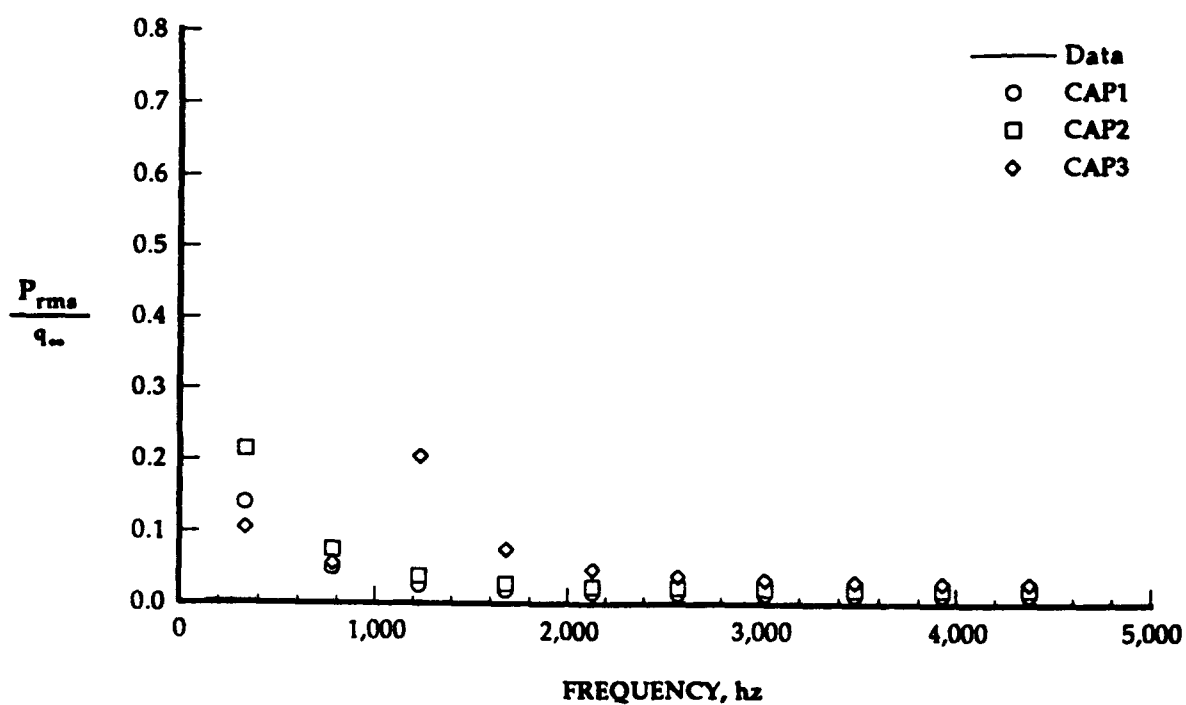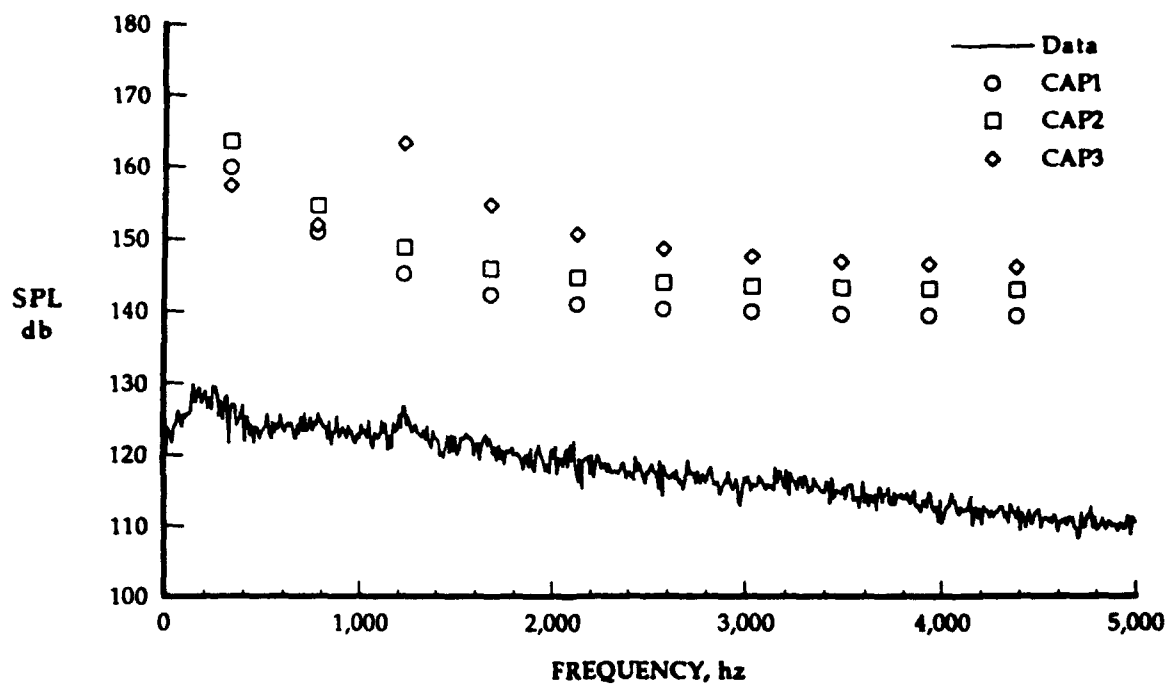
f. M∞ = 2.00

Figure 2. Continued.

g. $M\infty = 2.75$

Figure 2. Continued.

h. $M_\infty = 3.51$

Figure 2. Continued.

3-21

i. $M_\infty = 5.04$

Figure 2. Concluded.

3- 22

COMPUTATIONAL METHODOLOGY FOR WIND TUNNEL

SPRAY BAR DROPLET DIPSERSION

Eric Loth

Assistant Professor

Department of Aeronautical and Astronautical Engineering

The University of Illinois at Urbana-Champaign

104 South Wright St.

Urbana, IL 61801-2997

(217) 244-5581

Final Report for Summer Faculty Research Program

COMPUTATIONAL METHODOLOGY FOR WIND TUNNEL
SPRAY BAR DROPLET DIPSERSION

Eric Loth
Assistant Professor
Department of Aeronautical and Astronautical Engineering
The University of Illinois at Urbana-Champaign
Urbana, IL 61801-2997

ABSRACT

The objective of this research was to determine a computational methodology for robust and accurate prediction of spray bar droplet dispersion for engine icing tests. This is of significance to AEDC in that a) current ice accretion testing has resulted in non-uniform spatial distributions and b) large scale icing condition testing on the ASTF Test Cell C facilities is planned within a year and requires the implementation of a large spray bar apparatus. Therefore, it is important that a suitable predictive engineering tool be developed. Specifically, the physical mechanisms of spray bar wake turbulence and droplet evaporation must be included in order to properly model the controlling mechanisms of the flowfield. This report will identify basic flow physics, review previous computational and experimental technology, review proposed code methodology, describe initial results and make appropriate recommendations. The proposed characteristics of the computational model are as follows: three-dimensional Lagrangian droplet treatment coupled with either a two-dimensional or three-dimensional air flow field with a two-equation turbulence model, neglection of droplet collision and breakup, and neglection of turbulence modulation.

COMPUTATIONAL METHODOLOGY FOR WIND TUNNEL
SPRAY BAR DROPLET DIPSERSION

Eric Loth

1. Relevant Physics

One of the primary goals of the summer project was to establish the "first-order" physics that are chiefly responsible for controlling the spatial distribution of the liquid water content (LWC). This was completed based on review of past and recent scientific literature (including the 1993 U.S. Liquid Atomization and Spray Systems Conference and several AEDC TR's), on computer spreadsheet programs, and conservative linear estimates, as well as discussions with Dennis Lankford and Scott Bartlett. The basic description of the icing system is described in Figures 1 and 2, which show the juxtaposition of the icing spray bars in the wind tunnel and their cross-sectional view, respectively. Spray non-uniformities at the test section may be due to a combination of the following: residual wake deficits, gravitational acceleration, insufficient nozzle resolution, non-uniform nozzle output, non-uniform wind tunnel turbulence levels. It is the intention of this study to develop a computer methodology to help examine such factors, which may then allow spray uniformity to be enhanced.

Extensive research has been directed toward the understanding of dilute dispersed sprays in turbulent shear flows; the subject was reviewed in a seminal article by Faeth (1987). Measurements and analysis of dilute sprays have seen considerable progress in this area over the last two decades. For *dense sprays* near the injector, turbulence modulation (modification of the gas turbulence by the droplet presence; Tishkoff, 1989), droplet breakup and collisions of irregularly shaped drops present complex mechanics of multi-phase turbulent transport. While *dilute spray conditions*, which typically occur downstream of the dense spray regions, are generally characterized by low mass loadings and volume fractions which make turbulence modulation, droplet breakup and collisions insignificant factors in downstream droplet dispersion. Therefore, if one may initialize the spray
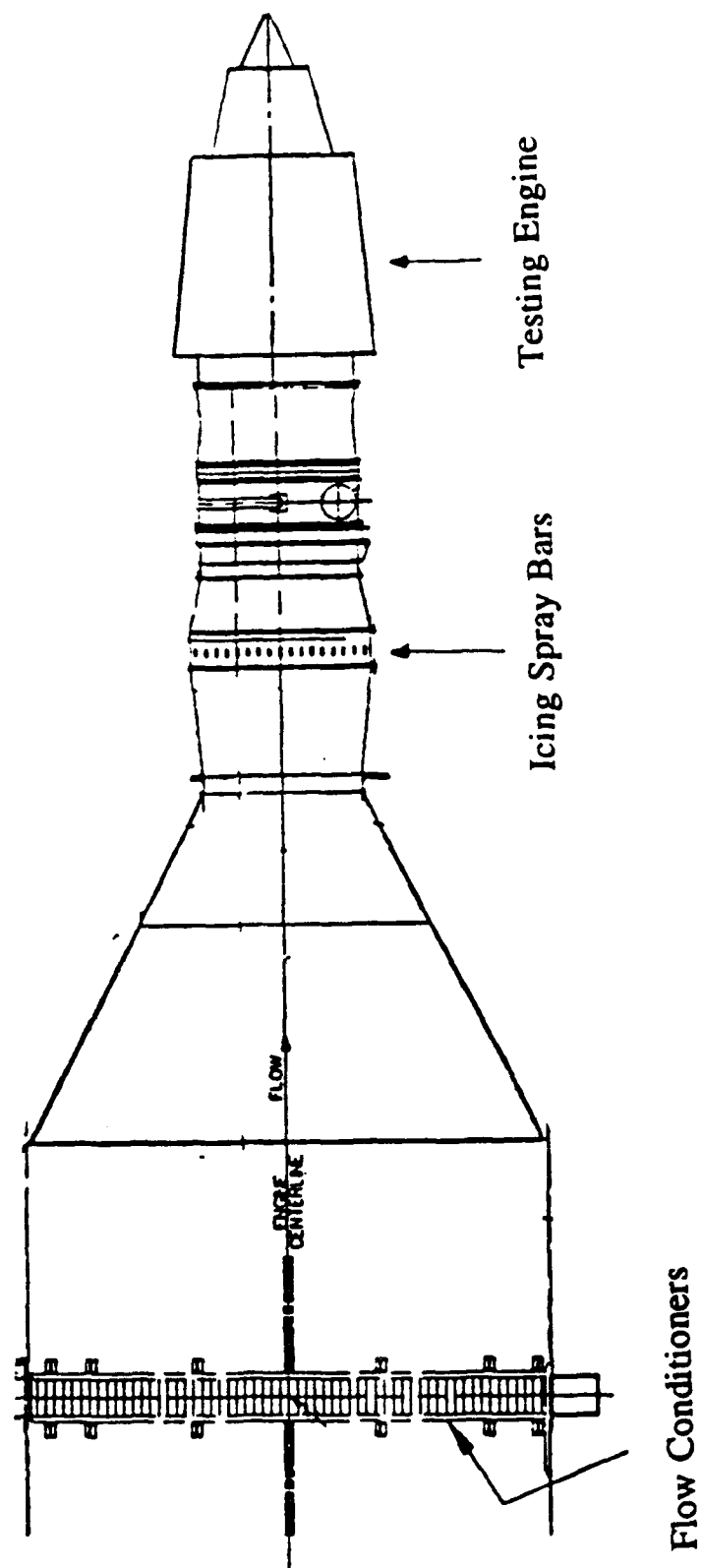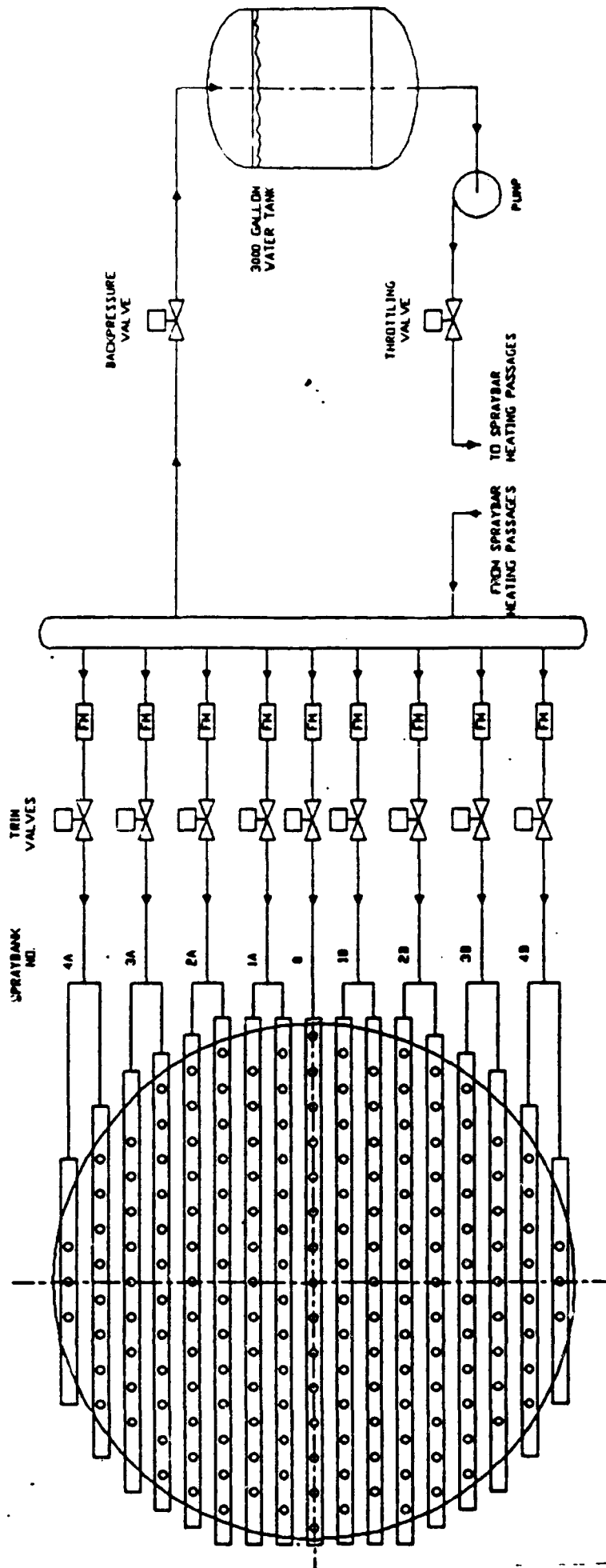
Figure 1 Schematic of Possible Icing Test Configuration for ASTF

Testing Engine

Icing Spray Bars

Flow Conditioners

FLOW

ENGINE CENTERLINE

C2 ICING SYSTEM SPRAYBAR FLOW DIAGRAM

Figure 2

4-5

conditions at a point where the dilution is sufficient, we may make two important simplifications: 1) the gas conservation equations may be computed independently of the droplet phase since the majority of the momentum is in the gas phase, 2) droplets may be treated as spherical particles which only exhibit changes due to evaporation.

Based on initial calculations (Loth, 1993), a 26B type spray nozzle (the nozzle to be used) will typically exhibit a mass loading of 3%, a volume loading of 0.005%, and a maximum Weber number of 4 just 2 cm (20 nozzle orifice diameters) downstream of the nozzle - all of which meet the requirements for neglection of collision, breakup, and modulation (Kuo, 1986). In fact, Faeth, (1987) suggests ten diameters downstream is sufficient for dilute spray considerations. Effects of the Basset history term, apparent mass and the stress gradient term (Maxey and Riley, 1982) should be be negligible due to the high density of the dispersed phase as compared to that of the carrier fluid: air.

Fortuitously, the droplet trajectories at this point will not be significantly different than quiescent condition due to the high exit velocity and the droplet (~25 μm) aerodynamic response time (Loth, 1993). Therefore, an important assumption is that the near injector region of the spray nozzles (~2 cm downstream) can be characterized in terms of drop velocity, temperature, and diameter distributions for input into the program. While this assumption can be circumvented by empirical predictions of spray breakup, it would be accompanied by a significant loss of accuracy, ~ 30% uncertainty in droplet diameter, for modern breakup models.

For typical spray bar configurations, droplet dispersion will be controlled by two main mechanisms: the initial trajectories of the droplets and their interaction with flow turbulence (stemming both from the spray bar wake and existing levels entering the spray bar chamber). The spray bar boundary layer may or may not transition from a laminar flow to a turbulent flow under high spray bar chamber velocities (> 20 m/s), but will certainly yield a turbulent wake based on the blunt trailing edge. Similarity calculations based on Schlichting (1979) yield spray bar wake deficits of 15%, but only 14 cm (~5") wide with turbulence fluctuations of 2.5% at the test section, 3 meters downstream (Loth, 1993). However, such values may overestimate the tenacity of the wake through the contraction section. The

importance of spray bar turbulence on droplet dispersion (as detailed in the initial report) was confirmed by experimental observations of Scott Bartlett.

The incoming spray bar chamber turbulence levels are expected to be significant based on free jet turbulence studies (Cooper, et al. 1992) which found the following rms values (based on the spatial average of the best case - no pitch, no yaw):

	M~0.3	M~0.5	M~0.8	M~0.9
Po_{rms}/Po	0.7%	1.0%	1.0%	0.6%
U'_{rms}/U	32%	24%	15%	10%

where a static pressure was assumed constant to compute the U'_{rms}/U values and an experimental uncertainty of 10% was cited. These levels are not small, but are not necessarily inconsistent with the levels downstream of an inlet for direct inject tests. In addition, the measurements were made in the absence of an inlet fairing, which is now in place (although not shown in Figure 1). Some incoming turbulence levels are still expected due to the upstream venturi nozzles and AEDC has recently conducted measurements to test the resulting turbulence levels, but the results are not yet available. Thus, any accurate description of their test section droplet spatial distribution should include a description of the wake flow field.

Fortunately, such a flow description is mostly two-dimensional if one may ignore the spray's effect on the gas flow, e.g. turbulence modulation, and any nozzle extensions on the bar. This first effect is quite reasonable since typical LWC values of 0.7 grams/cubic meter represents less than 0.1% of the total mass flow, and thus momentum associated with such a liquid volume is small compared to the overall gas momentum. This allows us to employ a steady 2-D description of the gas flow equation which will allow for efficient but approximate computations. However, the important wind tunnel radial distribution variations can only be computed with three-dimensional flowfields. Note, gravity effects will be negligible for 3 meters of travel: for 30 µm droplets a net downward migration of only 0.7 mm is expected, and the migration increases to only 7.0 mm for 100 µm droplets.

Therefore, three-dimensional descriptions need only study a single spray bar emanating from the origin to the tunnel wall to determine the likely distribution for all the spray bars.

To determine whether the coupling between the droplets and the water vapor is important, a linearized program similar to that used by Willbanks and Schulz (1973) was written and employed to determine the effect that local vapor pressure might have on the droplet dispersion. If one assumes a vapor mass fraction as given by the conditioned flow, then the evaporation rate may predict droplet sizes that are significantly smaller as compared to a vapor mass fraction based on the net amount of water evaporated by the droplets themselves. Since evaporation rates control droplet size, and since droplet dispersion is proportional to the square of the droplet diameter, neglection of water vapor distribution can contribute to dispersion error of up to 60%, under the testing conditions which have the maximum expected initial droplet and air temperatures, ~ 40 and 0 degrees Celsius, and maximum relative velocity, ~ 4 m/s (Loth, 1993). This finding dictates the need for a two-way coupling between the droplet dispersion and evaporation in order to avoid such errors.

Therefore, the following physical mechanisms **are not** expected to significantly influence the LWC distribution: turbulence modulation, droplet collisions, droplet non-sphericity, droplet breakup, Basset history terms. Effects that **are** expected to be significant include: wind tunnel turbulence levels and integral length scales, separated flow region of spray bar - in terms of turbulence levels and integral length scales, initial droplet size and velocity vector distribution, droplet evaporation, and distribution of water vapor. In addition, while 2-D results are important to understand the basic physics, 3-D computations are necessary to determine potential radial distributions.

2. Previous Computational Technology

Previous analytical studies of such two-phase flows has included the locally homogeneous flow approximations, where the flowfield is treated as a single-phase turbulent flow with a variable density which may be written as a function of the mixture fraction. These approximations, combined with Favre-averaged higher order turbulence

models such as k-ε-g, have shown reasonable success in predicting mean flow properties for fully developed flows (Faeth, 1987). However, *separated flow models* with properly defined initial conditions offer the best hope for accurate turbulence dispersion.

FASERVT includes the fundamental building block of Lagrangian particle transport but assumed a homogeneous turbulence level throughout the flow which was *adjusted* along with the droplet exhaust velocity to obtain reasonable agreement with experimental conditions (Lankford, 1986). This is not expected to effectively model the gas flow and the resulting droplet dispersion for a variety of flow conditions. *It must be emphasized, that computational resources at this time which this code was developed (~ a decade ago) were drastically different than they are now.* This allows for a second generation solver which can take into account the complexities of the actual spray bar flowfield. *No empirical adjustments* to correct for improved data correlation will be included in such a code in order to maintain its robustness.

3. Proposed Computer Methodology

The gas phase should be modeled such that a very reasonable distribution of the mean velocities and the turbulence values may be predicted, since they will control the droplet dispersion. Recent work by Dennis Lankford (personal communication) has found that prediction of mean and turbulent quantities of separated base flows with higher order turbulence models based on the KIVA-2 (1989) are predicted with quite reasonable accuracy. This is extremely encouraging since the wake flows will be of a very similar nature.

While the gas phase is most conveniently treated in an Eulerian approach, the droplet phase may be treated in either Eulerian or Lagrangian approach. For the specific types of droplet flows to be considered in this research, the Lagrangian appears to be better suited for the three following reasons: 1) it avoids the numerical cell diffusion associated with Eulerian treatments, 2) it conveniently allows *multiple droplet size and velocity distributions*, and 3) it allows for use of a stochastic eddy dispersion treatment (Solomon, et al., 1985). A drag

coefficient formulation can be implemented to handle the entire slip Reynolds number regime and possibly take into account the slip boundary condition (Faeth, 1987; Chiang, et al. 1989). Droplet evaporation, gravitational acceleration, Magnus effects, and Saffman lift can be readily included in such a formulation.

Extensive study was directed towards determining the best such methodology (Eulerian treatment for gas and Lagrangian for the droplets) which would include all the primary physics and be a practical engineering tool. **The codes selected for modification included PARC (1989) to determine the air velocity, temperature, and pressure distributions; and KIVA-2 (1989), a code written at Los Alamos for IC engine study, to determine the coupled droplet dispersion and vapor distribution using the converged solution from the PARC code.**

Other codes investigated for possible use included the Nicholson (PARC derived) particle code [which included only particle dispersion as a post-processor], the SAIC (PARC derived) particle code: PARCH [which employs Eulerian tracer particles without turbulent dispersion or multigrid capability], Lankford's FASERVT code [which does not account for spatial distributions of the turbulence or the humidity], and Faeth's GENMIX-SSF code [which assumes parabolic thin-layer jet flows]. Although a strong emphasis was placed on using a single PARC derived code for AEDC compatibility, the degree of modification necessary for linking the two selected codes is expected to be significantly less than that for complete modification of either.

3. Preliminary Implementation of Computer Methodology

Work completed thus far with KIVA-2 includes a basic review of the code itself and the modifications necessary, which include: steady state convergence acceleration, 2-D and 3-D periodic droplet boundary conditions, water characteristics added to look up tables, spray bar inclusion with transition point criteria, compatibility with GRIDGEN (which has already been competed by DL), and multigrid capability. Overall, it would be desirable to make the code very user-freindly such that non-CFD personnel will feel comfortable with running the

resulting program. In addition, a basic concept of the 2-D and 3-D grid structures has been determined.

The computational domains may be restricted to one nozzle (six orifices) installed in a periodic domain as described in the first report, where the gas flow is two-dimensional and the particle flow is three dimensional. This formulation will allow the minimum computation necessary in order to determine the uniformity of dispersion per nozzle. Boundary conditions of periodicity for the gas flow will be used as well as for the droplet flow (accomplished by 100% restitution reflecting wall collisions). Multi-nozzle asymmetry may also result from variations of the flow radially due to differential curvature. This can be investigated by increasing the computational domain to include all nozzles of half a spray bar, i.e. three-dimensional flow for both gas and droplets.

Convergence acceleration for KIVA-2 is expected to be maximized using a conversion to fully explicit differencing of the diffusion terms with local timestepping as constrained by stability limits, and a similar independent timestepping treatment for the convective and droplet dispersion terms. For example the droplets would be advected by the local eddy timestep. While the water vapor species description has been formulated, it has not yet been included in the modified code.

Analysis of the code, which was successfully ported over to the University of Illinois Cray YMP after some modification, yielded high levels of vectorization throughout the cpu-intensive subroutines resulting in typically 180 MFLOP's. The subroutine analysis indicate that the convection subroutines tended to require the majority of cpu time. Other changes which have been made to KIVA-2 during the summer work period include: implementation of a hybrid local timestepping scheme for the convective updates and inclusion of convergence parameters as indicated by the L_2 norm of the velocity and turbulent kinetic energy fields. A Mach 0.5 spray bar was tested without droplets using the modified KIVA-2 code in order to assess the wake turbulence characteristics and the convergence characteristics of the flowfield. It was found that turbulence levels of 10% were found approximately 0.5 meters downstream of the spray bar and that the hybrid timestepping resulted in only a factor of two speed up over the original global timestepping.

Since completion of the computational methodology and application to the pertinent spray bar problem are tasks of an involved nature, completion requires future work by personnel such as DL and/or EL, as described in the following section.

3. Recommendations for Future Work

The proposed (modified) research is recommended to allow completion of code modifications and study of the parametric variation of spray bar droplet injection conditions on LWC distribution:

(1) Upgrade KIVA-2 and PARC codes for proposed computational methodology;

(2) Determine proper initial and boundary conditions (spray conditions, tunnel conditions);

(3) Validate code for typical flow situations, including mesh/parcel resolution studies, prepare User's Manual;

(4) Complete parametric variation of test conditions to help design new spray bar facility;

Future computations may be completed on the AEDC's CRAY XMP computer or the CRAY YMP at UIUC.

If experimental data is not available to sufficiently establish the spray conditions at ~ 2 cm downstream of the nozzle orifice, it is proposed that simple experimental measurements be conducted to fill any such void. For example flash photography as discussed by McCreath, et al. (1972) could be used for particle size distributions. Probably a Technical Pan film with an intense light source would suffice. Addition of a high frequency chopper signal and a properly controlled shutter speed on a 35 mm camera with a Macro lens would allow for droplet velocities as well through displacement detection (Adrian, 1991). Small profile thermocouples and pitot probes may be useful as well.

References

Adrian, R.J. (1991) "Particle Imaging Techniques for Experimental Fluid Mechanics" *Annual Rev. of Fluid Mechanics* **23**.

Amsden, A.A., O'Rourke, P.J. and Butler, T.D. (1989) "KIVA-II: A Computer Program for Chemically Reactive Flows with Sprays" DE89-012805, Los Alamos National Laboratory, Los Alamos, NM.

Chiang, C. H., M. S. Raju, and W. A. Sirignano (1989) "Numerical Analysis of Convecting Vaporizing Fuel Droplet with Variable Properties" *AIAA Paper 89-0834*.

Cooper, G.K. and Sirbaugh, J.R. (1989) "PARC Code: Theory and Usage" AEDC TR 89-15, Arnold Air Force Base, TN.

Faeth, G. M. (1987) "Mixing, Transport and Combustion in Sprays" *Prog. Energy Combust. Sci.* **13**, p. 293.

Kuo, K.K. (1986) <u>Fundamentals of Combustion</u>, John Wiley and Sons, New York.

Lankford, D. W. (1986) "Icing Distribution Code, FASERVT" *AEDC User's Manual*

Loth, E. (1993) *Notebook for AEDC Summer Faculty Research Program*

McCreath, C. G., M. F. Roett and N. A. Chigier (1972) "A Technique for Measurement of Velocities and Size of Particles in Flames," *J. of Physics E: Scientific Instruments* **5**, p. 601.

Schlichting, H. (1979) Boundary Layer Theory, McGraw-Hill, New York.

Solomon, A. S. P., J.-S. Shuen, Q.-F. Zhang and G. M. Faeth (1985) "Measurements and Predictions of the Structure for Evaporating Sprays," *J. Heat Transfer* **107**, p. 679.

Tishkoff, J. (1989) "Interaction Between Droplets and Gas-Phase Turbulent Flows" *Proceedings of the ASCE/ASME Fluids Engineering Division*, La Jolla, CA.

Willbanks and Schulz (1973) "Analytical study of Icing Simulation for Turbine Engines in Altitude Test Cells" AEDC TR-73-144, Arnold Air Force Base, TN.

A STUDY OF WAVELET-GALERKIN METHODS FOR NUMERICAL SOLUTIONS OF DIFFERENTIAL EQUATIONS USING MULTIGRID RELAXATION TECHNIQUES

Peter R. Massopust
Assistant Professor
Department of Mathematics[1]

Vanderbilt University
Nashville, Tennessee 37240

---

[1] Present address: Department of Mathematical and Informational Sciences
Sam Houston State University
Huntsville, Texas 77341

A STUDY OF WAVELET-GALERKIN METHODS FOR NUMERICAL SOLUTIONS OF DIFFERENTIAL EQUATIONS USING MULTIGRID RELAXATION TECHNIQUES

Peter R. Massopust
Assistant Professor
Department of Mathematics
Vanderbilt University

Abstract

A Wavelet-Galerkin method for numerical solutions of second order differential equations using multigrid relaxation techniques was studied. This method combines the approximation properties of scaling functions and wavelets with the finite element Galerkin methods for solutions of differential equations and with multigrid relaxation techniques. The Daubechies scaling function $_3\phi$ and the associated wavelet $_3\psi$ provided enough regularity to qualify as trial functions for the Galerkin method. The weak formulation of the linear homogeneous boundary value problem $-u'' + \sigma u = f$, $u(a) = u(b) = 0$, where $u \in C^{1,\epsilon}([a,b])$, $f \in L^2([a,b])$, and $\sigma \in \mathbf{R}$, was used as an example to test the developed method for numerical stability and convergence. It was established that a Jacobi or Gauß-Seidel relaxation method converges numerically very slowly to the approximate solution, especially in the case of small σ. This slow convergence is due to the fact that the eigenvalues in the spectrum of the stiffness matrix range from approximately $\lambda_{\min} \approx 0.6$ to $\lambda_{\max} \approx 272.$, and that the spectral radius of the Gauß-Seidel operator is too close to one.

Several methods to overcome the problem of slow convergence are given.

A STUDY OF WAVELET-GALERKIN METHODS FOR NUMERICAL SOLUTIONS OF DIFFERENTIAL EQUATIONS USING MULTIGRID RELAXATION TECHNIQUES

Peter R. Massopust

1 Introduction

Recently, scaling functions and wavelets have been used as trial functions for Galerkin-type finite element methods (see, for instance, [6, 5]. A *wavelet* is a real-valued function $\psi \in L^2(\mathbf{R})$ with the property that every real-valued function $f \in L^2(\mathbf{R})$ can be written as a series in the function ψ, its *dilates* and *integer translates:*

$$f = \sum_{\ell \in \mathbf{Z}} \sum_{k \in \mathbf{Z}} c_{k\ell} \psi(2^k \cdot -\ell), \tag{1}$$

where the *wavelet coefficients* $c_{k\ell}$ are elements of $\ell^2(\mathbf{R})$, that is square-summable. One furthermoe requires that the L^2-norm of f and the ℓ^2-norm of the wavelet coefficient vector $(c_{k\ell})$ are equivalent; in other words, the size of the wavelet coefficients should reflect the size of the function f.

There is a natural way of constructing wavelets. This is usually done via a *multiresolution analysis*. The concept of multiresolution analysis was introduced by S. Mallat and Y. Meyer (cf. [7, 8]). The starting point is a *ladder* of subspaces $V_k \subset V_{k+1}$ of $L^2(\mathbf{R})$; each such subspace is generated by the *dyadic dilates* and *integer translates* of a *single* real-valued function ϕ, called the *scaling function:*

$$V_k = clos_{L^2}\{\phi(2^k \cdot -\ell) \mid k \in \mathbf{Z}, \ell \in \mathbf{Z}\}.$$

The intersection and the closure of the union of these subspaces over $k \in \mathbf{Z}$ is the null space and $L^2(\mathbf{R})$, respectively. The scaling function has the property that it is orthogonal to its dyadic translates and non-zero integer translates. Since the spaces V_k are nested, the direct orthogonal complement of V_{k+1} in V_k is well-defined. It can be shown that this orthogonal complement, usually denoted by W_{k+1}, is generated by the dyadic dilates and integer translates of

another *single* function ψ. This function ψ is called a wavelet, and the space W_{k+1} a *wavelet space*. Since $V_1 = V_0 \oplus W_0$, there exist square summable coefficients h_ℓ and g_ℓ so that

$$\phi(x) = \sum_{\ell \in \mathbf{Z}} h_\ell \, \phi(2x - \ell)$$

and

$$\phi(x) = \sum_{\ell \in \mathbf{Z}} g_\ell \, \psi(2x - \ell).$$

These equations are called *two-scale relations* or *dilation equations* for ϕ and ψ, respectively.

By construction one has $L^2(\mathbf{R}) = \bigoplus_{k \in \mathbf{Z}} W_k$ (this is Equation (1)); also, $L^2(\mathbf{R}) = V_k \oplus \bigoplus_{n \geq k} W_n$. The latter decomposition has the following consequence: Given a function $f \in V_{k+1}$, it can be written as

$$\begin{aligned}
f(x) &= \sum_{\ell \in \mathbf{Z}} c_{k+1,\ell} \phi(2^{k+1}x - \ell) \\
&= \sum_{\ell \in \mathbf{Z}} a_{k\ell} \phi(2^k x - \ell) + \sum_{\ell \in \mathbf{Z}} b_{k\ell} \psi(2^k x - \ell) \\
&= f_k + g_k,
\end{aligned}$$

for some square summable coefficients $a_{k\ell}$, $b_{k\ell}$, and $c_{k+1,\ell}$. The coefficients $a_{k\ell}$ and $b_{k\ell}$ can easily be calculated from the $c_{k+1,\ell}$:

$$a_{k\ell} = \sum_{j \in \mathbf{Z}} h_{j-2\ell} c_{k+1,j}, \qquad b_{k\ell} = \sum_{j \in \mathbf{Z}} g_{j-2\ell} c_{k+1,j}.$$

This procedure describes what is called the *decomposition algorithm*; one may proceed by decomposing $f_k = \sum_{\ell \in \mathbf{Z}} c_{k+1,\ell} \phi(2^{k+1}x - \ell)$ further into $f_{k-1} + g_{k-1}$, etc. This then yields after m steps the function decomposition $f_k = f_{k-m} + g_{k-1} + \ldots + g_{k-m}$.

On the other hand, given $f_k = \sum_{\ell \in \mathbf{Z}} a_{k\ell} \phi(2^k x - \ell)$ and $g_k = \sum_{\ell \in \mathbf{Z}} b_{k\ell} \psi(2^k x - \ell)$, one may reconstruct f_{k+1} by setting

$$f_{k+1} = f_k + g_k = \sum_{\ell \in \mathbf{Z}} c_{k+1,\ell} \phi(2^{k+1}x - \ell).$$

The coefficients $c_{k+1,\ell}$ are then given by

$$c_{k+1,\ell} = \sum_{j \in \mathbf{Z}} h_{\ell-2j} a_{kj} + g_{\ell-2j} b_{kj}.$$

This *reconstruction algorithm* can be used to obtain an accurate approximation of $f \in V_{k+1}$: First, f is decomposed into f_k and g_k, then f_k into f_{k-1} and g_{k-1}, etc. But, instead of reconstructing f using *all* the coefficients $b_{k\ell}$, $b_{k-1,\ell}$, ..., only those which are above a pre-determined threshold are used. This approach has been successfully applied to image compression, signal processing and data reduction.

Recently, scaling functions and wavelets have found their way into the area of numerical differential equations. The reason for choosing scaling functions and wavelets is based on their superior approximation properties over other trial functions such as sine or cosine and splines. The wavelets constructed, for instance, by Ingrid Daubechies (cf. [1]) have three properties which make them attractive for Galerkin-type methods (For another class of scaling functions and wavelets enjoying the same properties but that are constructed using fractal-geometric methods see, for eaxample, [3].):

- Compact support: The scaling functions and the associated wavelets vanish outside a compact, i.e., closed and bounded, interval. This property causes the stiffness matrix to be banded; the band width depends on the regularity of the *scaling function*: The higher the regularity the wider the band width.

- Continuity: Clearly needed for a weak solution; for a second order differential equation the weak solution has to be an element of $C^{1,\alpha}([a,b])$.

- Orthogonality: The scaling function is orthogonal to its non-zero integer translates as well as the integer translates of the wavelet. This allows the easy calculation of L^2 inner products between the scaling function/wavelet and its translates, and the derivative of the scaling function/wavelet and its translates.

Ingrid Daubechies constructed a family of scaling functions and associated wavelets of increasing regularity. This family is usually denoted by $_N\phi$ and $_N\psi$, where $N \in \mathbf{N}$ denotes the regularity. For instance, there exists an $\alpha > 0$ such that $_N\phi \in C^{[\lambda N],\lambda N-[\lambda N]}$. (Here $[\![\cdot]\!]$ denotes the greatest integer function.) As approximating spaces for a Galerkin-type method one can use the spaces V_k or W_k, or any finite combination of both. (It should be understood that the elements in these spaces must be restricted — in a proper way — to the interval over which the differential equation is defined.) The

weak solution u of the given differential equation is then approximated by a finite combination of scaling functions and/or wavelets at a certain scale. The size of the coefficients in this finite expansion is proportional of the size of the solution u; in other words, in regions where u is smooth, fewer coefficients are needed to accurately describe u. In regions where the solution is highly irregular or has steep gradients, the coefficients are "large" and more must be used to accurately approximate u.

In order to achieve a highly accurate approximation to the weak solution of a differential equation and to use as little CPU time as possible, one first needs to find ways of computing the scaling function and its derivatives, and the wavelet and its derivates. Both functions have a beautiful theoretical description: the Fourier transform of both ϕ and ψ are infinite products, and their derivates are derivatives of convolutions. However, for numerical purposes this description is almost useless. Nevertheless, using the theoretical construction of the scaling function and the associated wavelet, there exists an algebraic way of constructing the needed functions. In the first subsection of the next section we will explain how this is done. The second subsection then combines the elements of multigrid methods with those of Wavelet-Galerkin methods: in the former a natural scale is already given, and it is therefore natural to find an approximate solution $\tilde{u}_k$ to a weak solution u at a finer scale by decomposing $\tilde{u}_k$ into a blurred part $\tilde{u}_{k-1}$ and a difference part $\delta \tilde{u}_{k-1}$. One then relaxes $\tilde{u}_{k-1}$ at scale $k-1$ to obtain $\bar{\tilde{u}}_{k-1}$. Reconstruction to scale k gives $\bar{\tilde{u}}_k$. Using the simple linear second order homogeneous boundary value problem

$$ -u'' + \sigma u = f, \qquad u(a) = u(b) = 0, \tag{2} $$

where $u \in C^{1,\epsilon}([a,b])$, $f \in L^2([a,b])$, and $\sigma \in \mathbf{R}$, we explain our approach in more detail in the remainder of this subsection. We will see that unless the stiffness matrix is pre-conditioned, one has very slow numerical covergence, and some extreme cases even numerical divergence. (This is partly due to the finite register length of machines.) The last subsection then looks at remedies of these short-comings and introduces some slightly modified approaches that — at the time this report is written — are still being investigated.

2 Main Results

In this section we show how the analytical construction of the scaling function, its the derivate, the associated wavelet and its derivate gives rise to an algebraic construction that has superior numerical properties. This description is then used to obtain new formulae for the L^2-inner product of the scaling function with its derivate. Next a Wavelet-Galerkin method using multigrid relaxation techniques is introduced and investigated for Problem 2. The last subsection is an outlook of how to overcome the problems encountered in the previous section.

Since our investigation used the simple Problem 2 with $a := 0$ and $b := 5$ (This choice will become clear shortly, and is in no way restrictive. A straight-forward change of variables reduces a and b to these values.), we will concentrate only on this case. The more general setting is easily derived from this special one and will be published elsewhere.

2.1 Numerical construction of ϕ and ϕ'.

In what follows we use the notation $\phi_{k\ell}$ to denote $2^{k/2}\phi(2^k \cdot -\ell)$. The L^2-inner product is denoted by $(\cdot,\cdot)$.

Given Problem 2,

$$-u'' + \sigma u = f, \qquad u(a) = u(b) = 0,$$

one finds its weak formulation to be

$$(u',v') + \sigma(u,v) = (f,v), \qquad u(a) = u(b) = 0, \qquad (3)$$

for all $v \in H_0^1([a,b])$. (Recall that $H_0^1([a,b])$ is the closure of the space of all compactly supported infinitely differentiable functions on $[a,b]$ with respect to the norm $\|u\|_0 := (\|u\|_{L^2}^2 + \|u'\|_{L^2}^2)^{1/2}$.) In order to use the Daubechies' scaling functions and wavelets, one has to choose $N = 3$. Then $_3\phi \in C^{1,\epsilon}$, where $\epsilon \approx 0.087833$, and thus an element of $H_0^1(\mathbf{R})$. It is known that $_3\psi$, the associated wavelet, is then also an element of $H_0^1(\mathbf{R})$. The support of $_3\phi$ is $[0,5]$; this now explains the above choice for a and b. The support of the wavelet $_3\psi$ is $[-2,3]$, however, translates of $_3\psi$ are supported on $[0,5]$. To

simplify notation we write ϕ for $_3\phi$. As the approximating as well as test space we use

$$\mathcal{V}_k := \{\phi_{k\ell} \in V_k \mid \operatorname{supp} \phi_{k\ell} \subseteq [0,5]\}. \tag{4}$$

Here supp denotes the support of a function. For a given $k \in \mathbf{Z}$, the dimension of $\mathcal{V}_k$ is $5(2^k - 1) + 1$; in other words, only if $\ell \in \{0, 1, \ldots, 5(2^k - 1)\}$ the $\operatorname{supp} \phi_{k\ell} \in [0.5]$. Also note that $\phi_{k,0}(0) = 0 = \phi_{k,5(2^k-1)}(5)$, for all $k \in \mathbf{Z}$. Approximating u at scale k by the elements in $\mathcal{V}_k$, $\tilde{u} = \sum_{k=0}^{5(2^k-1)} \tilde{u}_{k\ell}\phi_{k\ell}$, changes Equation (3) to

$$\sum_{\ell=0}^{5(2^k-1)} \tilde{u}_{k\ell}((\phi_{k\ell})', (\phi_{km})') + \sigma \sum_{\ell=0}^{5(2^k-1)} \tilde{u}_{k\ell}(\phi_{k\ell}, \phi_{km}) = (f, \phi_{km}). \tag{5}$$

Using the full orthogonality of the scaling functions — $(\phi_{k\ell}, \phi_{k'\ell'}) = \delta_{kk',\ell\ell'}$ — the above equation reduces to an algebraic system

$$A^{(k)}\,\tilde{\mathbf{u}}^{(k)} = \mathbf{b}^{(k)}, \tag{6}$$

where the $(5(2^k - 1) + 1) \times (5(2^k - 1) + 1)$ matrix $A^{(k)}$ has entries given by

$$A^{(k)}_{\ell m} := ((\phi_{k\ell})', (\phi_{km})') + \sigma\delta_{\ell m}, \tag{7}$$

the $(5(2^k - 1) + 1)$ vector $\tilde{\mathbf{u}}^{(k)}$ has components $\tilde{u}_\ell$, and the right-hand side vector $\mathbf{b}^{(k)}$ consists of the (f, ϕ_{km}). The definition of $\phi_{k\ell}$ implies that the inner product $((\phi_{k\ell})', (\phi_{km})')$ can be expressed as

$$((\phi_{k\ell})', (\phi_{km})') = 2^{2k}(\phi', \phi'_{0,j}), \tag{8}$$

where $j = |\ell - m|$. Hence the stiffness matrix is found by evaluating the inner product on the right-hand side of the above equation and adding σ along the diagonal. Also note that $j = -4, -3, \ldots, 3, 4$; thus the stiffness matrix is banded with width 9. It therefore remains to find a numerically efficient procedure to compute the derivative of ϕ and then the inner product. This procedure is found as follows: It is well-known (cf. [1]) that ϕ is the fixed point of the operator $T : L^2(\mathbf{R}) \to L^2(\mathbf{R})$, $f \mapsto \sum_{\ell=0}^5 h_\ell f(2 \cdot -\ell)$. (This is the dilation equation for ϕ!) It also can be shown that the iterates of $\chi_{[-1/2,1/2)}$, the characteristic function on $[-1/2, 1/2)$, under T converge point-wise to ϕ, i.e.,

$$\forall x \in \mathbf{R}: \ \phi(x) = \lim_{n\to\infty} T^n\chi_{[-1/2,1/2)}(x). \tag{9}$$

We remark that T maps V_0 into V_1, and its restriction to functions in V_0 likewise maps into V_1. Furthermore, the nth approximation, $T^n \chi_{[-1/2,1/2)}$, of ϕ is a step function supported on intervals of length 2^{-k}.

There exist isomorphisms j_k between the following characteristic functions $\chi_{[-2^{-k-1},2^{-k-1})}(\cdot - 2^{-k}\ell)$, $k \in \mathbf{N}$, $\ell \in \{0, 1, \ldots, 5(2^k - 1) + 1\}$, and $\mathbf{Z}/2^k$:

$$j_k \chi_{[-2^{-k-1},2^{-k-1})}(\cdot - 2^{-k}\ell) := 2^{-k}\ell.$$

Let $e_i^{(0)} \in \{0,1\}^{\mathbf{Z}}$ be that 6-vector satisfying $e_i^{(0)}(j) = \delta_{ij}$ and, in general, let $e_i^{(k)}$ be that $5(2^k - 1) + 1$-vector in $\{0,1\}^{\mathbf{Z}/2^k}$ satisfying $e_i^{(k)}(j/2^k) = \delta_{ij}$. Then the action of T onto, for example, $\chi_{[-1/2,1/2)}$ corresponds to the action of a 6×11 matrix $A^{(1)}$ onto the 6-vector $e_i^{(0)} \in \{0,1\}^{\mathbf{Z}}$ yielding the 11-vector $e_j^{(1)}$ in $\{0,1\}^{\mathbf{Z}/2}$:

$$A^{(1)} e_i^{(0)} = \sum_{j=0}^{5} e_j^{(1)}.$$

It is not hard finding the matrix representation of T: it is the 6×11 matrix

$$A^{(1)} = \begin{pmatrix} h_0 & 0 & 0 & 0 & 0 & 0 \\ h_1 & h_0 & 0 & 0 & 0 & 0 \\ h_2 & h_1 & h_0 & 0 & 0 & 0 \\ h_3 & h_2 & h_1 & h_0 & 0 & 0 \\ h_4 & h_3 & h_2 & h_1 & h_0 & 0 \\ h_5 & h_4 & h_3 & h_2 & h_1 & h_0 \\ 0 & h_5 & h_4 & h_3 & h_2 & h_1 \\ 0 & 0 & h_5 & h_4 & h_3 & h_2 \\ 0 & 0 & 0 & h_5 & h_4 & h_3 \\ 0 & 0 & 0 & 0 & h_5 & h_4 \\ 0 & 0 & 0 & 0 & 0 & h_5 \end{pmatrix}.$$

The above-introduced isomorphisms j_k allow the following interpretation: Choose $x \in [0, 5)$. Then x belongs to exactly one interval of the form $[-2^{-k-1} + 2^{-k}\ell, 2^{-k-1} + 2^{-k}\ell)$, for some $k \in \mathbf{N}$ and some $\ell \in \{0, 1, \ldots, 5(2^k - 1) + 1\}$. The function value of the kth approximation of $\phi(x)$ is then equal to the ℓth component of the $5(2^k - 1) + 1$-vector $e_i^{(k)}$. Using this interpretation, one only has to iterate the banded matrix $A^{(1)}$ to quickly compute ϕ on $[0, 5]$. The input vector is $e_i^{(0)}$ and the jth component of the output vector is then

given by

$$(A^{(1)}e_i^{(0)})_j = \sum_{\max\{0,[(j-1)/2]\}}^{[(j-1)/2]} h_{j-2i}e_{i+1}^{(0)}.$$

For the code we have written, eight to nine iterations gave highly accurate approximations to ϕ.

The same procedure does also apply to the computation of the derivate of ϕ. The derivative ϕ' is the fixed point of the linear operator T' defined by

$$T'f = 2\sum_{\ell=0}^{5} h_\ell f(2 \cdot -\ell)$$

and therefore the point-wise limit of the iterates of the step function $s_0 := \chi_{[-1,0)} - \chi_{[0,1)}$ under T'. As above, there exist isomorphisms between characteristic functions supported on intervals of length 2^{-k} and now *shifted* sets $-2^{-k-1} + \mathbf{Z}/2^k$, since the "starting function" s_0 is not a characteristic but rather a step function. The vectors $e_i^{(k)}$ as introduced above now break up into two parts; one which corresponds to $\chi_{[-1,0)}$, $e_i^{(k)+}$, and the other one, $e_i^{(k)-}$, which corresponds to $\chi_{[0,1)}$. The shift in the sets $-2^{-k-1} + \mathbf{Z}/2^k$ introduces an additional component into these vectors. However, as before, the approximation to the derivative ϕ' at a given $x \in [0,5)$ is given by the corresponding component of $A^{(1)}e_i^{(k)+} - A^{(1)}e_i^{(k)-}$.

Both methods of generating the scaling functions and its derivative in a computationally satisfactory way are new to the fast-growing literature on wavelets. It should be clear that quite similar procedures are to be used when the wavelet and its derivative need to be computed. Exact definitions and precise results will be published elsewhere.

Now we are in a position to compute the L^2-inner product appearing in the stiffness matrix. First let us note that we may approximate or numerically represent the scaling function ϕ and its derivate ϕ' as a finite series of the form

$$\phi \approx \sum_{\ell=0}^{2^n 5} v_{n,\ell}\epsilon_{n,\ell},$$

and

$$\phi' \approx \sum_{\ell=0}^{2^n 5+1} w_{n,\ell}\epsilon_{n,\ell}^*,$$

where n denotes the number of iteratations used to approximate ϕ and ϕ', $v_{n,\ell} := ((A^{(1)})^k v)_\ell$, with $v \in \{0,1\}^{\mathbf{Z}}$, $v(i) = \delta_{0,i}$, $w_{n,\ell} := ((A^{(1)})^k v^+)_\ell - ((A^{(1)})^k v^-)_\ell$, with $v^\pm \in \{0,1\}^{-1/2+\mathbf{Z}}$, $v^\pm(i) = \pm 1/2 \delta_{0,i}$, and $\epsilon_{n,\ell} := \chi_{[-1/2,1/2)}(2^n \cdot -\ell)$ and $\epsilon^*_{n,\ell} := \chi_{[-1,0)}(2^n \cdot -\ell)$. After some straight-forward algebra and making use of Equation (8), we arrive at the following, easy and fast to compute, formula:

$$((\phi_{k\,\ell})', (\phi_{k\,m})') \approx 2^{2k-n} \sum_{i=1}^{2^n 5+1} w_{n,i} w_{n,i-2^n|\ell-m|}. \tag{10}$$

To compute the right-hand side of Equation (6) we proceed analogously. First expand ϕ into a finite series of the above form, and then calculate the inner product with the given L^2 function f. This can, for instance, be done using the mid-point rule from numerical integration theory. The final result is given by

$$
\begin{aligned}
(f, \phi_{k\,m}) \approx\ & 2^{-k/2-n-1} \Big[\, \tfrac{v_{n,0}}{2} \left(f(2^{-k-m-1} + 2^{-k}m) + f(2^{-k}m) \right) \\
& + \textstyle\sum_{i=1}^{2^n 5} v_{n,i} \big(\, f(2^{-k-n}(i+1/2) + 2^{-k}m) \\
& + f(2^{-k-n}(i-1/2) + 2^{-k}m)) \,\Big],
\end{aligned}
$$

where $m = 0, 1, \ldots, 5(2^k - 1)$.

Let us remark that there are other methods available to compute the above inner products. One such method, for instance, is based on so-called *stationary subdivision schemes* (cf. [2]). Ours, however, does not use additional mathematical tools besides those already implicitly given in the Daubechies wavelet theory.

Making use of the bandedness of the stiffness matrix, we have written an efficient structured code that computes the stiffness matrix and the right-hand side of Equation (6). The approximation $\tilde{u}$ of u could, at this point, be found using Gaussian elimination or LU decomposition. However, we decided to make use of existing multigrid methods to calculate $\tilde{u}$. As mentioned in the Introduction, there is a natural relation between multigrid methods and wavelets, especially the reconstruction and decomposition algorithm.

2.2 Multigrid Relaxation Techniques

The basic idea behind myltigrid methods is to relax the residual of an algebraic equation on coarser grids or lattices to achieve a better approximation on the desired finer lattice. Our aproach does not make use of the residual but uses the reconstruction and decomposition algorithms for scaling functions and wavelets. This method which is based on the so-called *full V-cycle* works as follows: Let G_{n_c} and G_{n_f} denote the coarsest and finest grid used, respectively. These grids correspond to the subspace V_{n_c} and V_{n_f}, respectively. Starting at level n_c, we relax Equation (6) with initial guess $u = 0$. The obtained approximation $\tilde{u}_c$ is reconstructed with $\delta\tilde{u} = 0$ to obtain an approximation at level $n_c + 1$. Relaxation yields $\tilde{u}_{c+1}$. Now we decompose $\tilde{u}_{c+1}$ into $\tilde{\tilde{u}}_c + \delta\tilde{u}_c$ and relax on $\tilde{\tilde{u}}_c$. The thus obtained approximation is reconstructed with the unchanged difference $\delta\tilde{u}_c$ giving the approximation $\tilde{\tilde{u}}_{c+1}$. The procedure now repeats itself with $c + 1$ playing the role of c above until the finest level n_f is reached. There, we then have an approximation $\tilde{u}_{n_f}$ to the weak solution u of Problem (2). We used a symmetric Gauß-Seidel sweep for a relaxation technique. It was shown that the corresponding Gauß-Seidel operator has spectral radius stricly less than one. (This followed immediately from a theorem due to Ostrowski (cf. for instance, R. S. Varga, *Matrix Iterative Analysis*, Prentice Hall, Englewood Cliffs, New Jersey, 1966.) Therefore, *in theory* we should expect convergence of our approximations to the weak solution u. However, our numerical experiments showed that unless $\sigma >> 1$, the convergence to u is rather slow. Our analysis of the problem then showed that this slow numerical convergence is due to the fact that the stiffness matrix is ill-conditioned; its wide range of eigenvalues, $\lambda_{min} \approx 0.6$ and $\lambda_{max} \approx 272.$, causes the spectral radius of the Gauß-Seidel operator to be very close to one. For some extreme cases, the numerical value of the spectral radius equaled or even exceeded one, resulting in divergence. The reason for this computational instability lies in the finite register length of machines.

2.3 Outlook

There are several ways to circumvent or remedy the above occuring difficulties. They are currently being investigated in order to determine which one is the computatinally most efficient method.

- Rewrite the iterative form of Equation (6), $\tilde{\mathbf{u}}^{(k)} \mapsto (I - A^{(k)})\tilde{\mathbf{u}}^{(k)} + \mathbf{b}^{(k)}$, as

$$\tilde{\mathbf{u}}^{(k)} \mapsto (I - P^{-1}A^{(k)})\tilde{\mathbf{u}}^{(k)} + P^{-1}\mathbf{b}^{(k)},$$

  where the *pre-conditioner* P is chosen in such a way that the stiffness matrix is well-conditioned. Apparent choices for such a pre-conditioner are currently investigated.

- Instead of using the spaces V_k as approximating spaces for the underlying Galerkin method, one may want to choose the wavelet spaces W_k. The behaviour of the corresponding stiffness matrix is currently under investigation.

- The choice of the Daubechies scaling functions and wavelets was motivated by the three properties they enjoy. However, there are other wavelet constructions, based on so-called *fractal interpolation functions*, which rival the Daubechies wavelets in many aspects (cf. [3]). There exists also a C^r, $r \geq 0$, family of such *fractal pre-wavelets* (cf. [4]) that can be used for a Galerkin method. The stiffness matrix for the C^1 fractal scaling functions and pre-wavelets is *tridiagonal*, but has twice the size of the stiffness matrix in Equation (6). One of the main advantages of fractal scaling functions and pre-wavelets over other wavelet construction lies in the fact that there exist *exact recursive* formulas for the inner product of the scaling functions with themselves and also their derivatives. We are currently studying the properties of this approach.

We conclude from our investigations and the analysis of the problem that the difficulties we encountered are by *no* means insurmountable. We expect that our method which is based on hybrid of Wavelet-Galerkin and multigrid methods will result in a more accurate description of the weak solution of a differential equation and a significant reduction in CPU time.

References

[1] Ingrid Daubechies, "Orthonormal bases of compactly supported wavelets", *Commun. in Pure and Appl. Math.* **51** (1988), 909–996.

[2] W. Dahmen, Personal Communication.

[3] G. Donovan, J. S. Geronimo, D. P. Hardin, and P. R. Massopust, "Construction of orthogonal wavelets using fractal interpolation functions", *preprint* (1993).

[4] J. S. Geronimo, D. P. Hardin, and P. R. Massopust, "Fractal functions and wavelet expansions based on several scaling functions", to appear in J. Approx. Th.

[5] R. Glowinski, W. Lawton, M. Ravachol, and E. Tenenbaum, " Wavelet solutions of linear and nonliner elliptic, parabolic and hyperbolic problems in one space dimension", Proceedings in Computatioanl Mathematics, 1991, 55–120.

[6] J. Liandrat, V. Perrier, and Ph. Tchamitchian, "Numerical resolution of the regularized Burgers' equation using the wavelet transform", *Technical Report CPT-89/P.2320*, Center of Theoretical Physics, Marseille, France, (1989).

[7] S. Mallat, "Multiresolution approximations and wavelet orthonormal bases on $L^2(\mathbf{R})$", *Trans. Amer. Math. Soc.* **315**(1) (1989), 69–87.

[8] Y. Meyer, *Ondelettes et Opérateurs*, Two volumes, Herman, Paris, 1990.

AN EVALUATION OF HYDRAZINE DATA

FOR THE

NEQPAK DATABASE

John M. Springer

Professor

Department of Physics

Box 15

Fisk University

Nashville, TN 37208

AN EVALUATION OF HYDRAZINE DATA
FOR THE
NEQPAK DATABASE

John M. Springer
Professor
Department of Physics
Fisk University

Abstract

NEQPAK is a FORTRAN subroutine package which calculates chemical species information for use in flow programs needed in computational fluid dynamics work. The input to the subroutines includes thermodynamic, transport and reaction rate data for the species involved in the particular environment studied. The objective of this research was to collect published data on hydrazine and construct a properties database which is appropriate for the model assumptions used in NEQPAK.

AN EVALUATION OF HYDRAZINE DATA
FOR THE
NEQPAK DATABASE

John M. Springer

INTRODUCTION

A necessary component of flow programs in computational fluid dynamics is a chemistry "package" that handles the chemical reactions and the effect of internal energy states of the gas particles on the flow itself. Curtis has constructed a large subroutine package called NEQPAK which provides such calculations and can be integrated into new flow programs. NEQPAK is intended to be usable in the hypersonic flow regime, in which the high temperatures generated greatly complicate the modeling of reactions and relaxation phenomena. An important part of the NEQPAK package is the compilation of a database of chemical information which is in a consistent format that can be read by the subroutines. Since this data is the basis on which the calculations of the reacting flows proceeds, it is necessary to review existing sources and incorporate this information into the database. This is not a simple matter for two reasons. First, good experimental data in the temperature extremes in which NEQPAK is intended to operate is not always available. Second, physical models used to calculate transport properties require molecular parameters that must be tailored to the specific models used. These parameters are often not available or must be inferred from limited data.

The task of this research project was to review the property data available in the literature for hydrazine (N_2H_4) and construct a datafile in the format necessary to provide this information to the NEQPAK subroutines. This report provides a brief description of the process followed to generate this datafile and a discussion of some of the problems encountered in constructing it.

METHODOLOGY

NEQPAK's subroutine NPCHEMIN reads the input chemical data for use by the other subroutines in the package. The data required and relevant values or comments are shown in Table 1. A more detailed discussion is given in the next section.

TABLE 1: NEQPAK Database Variables

DATA ELEMENT	VALUE
Chemical formula	N2H4
Molecular weight	32.048
Rotational degrees of freedom	3
Number of electronic energy levels	1
Characteristic vibrational energy	Originally defined for a diatomic molecule with one internal vibration; use lowest frequency vibration for polyatomic.
Heat of formation at 0° K and 1 atmosphere	109.54
Dissociation energy	2.26 eV
Ionization potential energy	8.1 (eV)
Electron-neutral energy exchange coefficients	Not available
Lennard-Jones collision diameter	4.94×10^{-30} meters
Rotational collision number	1.5
Coefficients for electronic-vibrational energy relaxation time	Not available
Number of thermo-fit segments for thermodynamic data	See below
Junction temperatures for thermo-fit segments	See below
Thermo-fit coefficients	See below
Electron level degeneracies	Not applicable
Binary diffusion coefficients	Basic data for calculation is given below
Viscosity coefficients	Basic data for calculation is given below
Relaxation time parameters for vibration-vibration energy exchange	Not available
Thermochemical equilibrium composition data	See below

In addition to NEQPAK itself, several additional programs may be used to generate transport property values and thermodynamic values from basic molecular data. This data includes:

- Molecular geometry
- Molecular moments of inertia
- Vibrational frequencies
- Interaction potentials and collision radii for relevant interaction models
- Symmetry number for molecular geometry

Each of the above parameters are discussed in greater detail where relevant to the presentation of the data for hydrazine.

DATA

Hydrazine is of obvious interest as a common propellant. A sketch of its molecular structure and geometric parameters is shown in Figure 1. Hydrazine has been the subject of many studies, but there are still questions about its structure and vibrational and electronic energy levels. This is in part due to the twisted-chair configuration it assumes in which the plane of one NH_2 group is rotated approximately 90 degree from the plane of the other. The groups are able to undergo hindered rotation about the N-N bond with two potential minima. This hindered rotation has implications for the calculation of thermodynamic properties.[2]

r = 1.02 A

r = 1.45 A

N   H   < N-N-H = 109

< N-N-H = 112
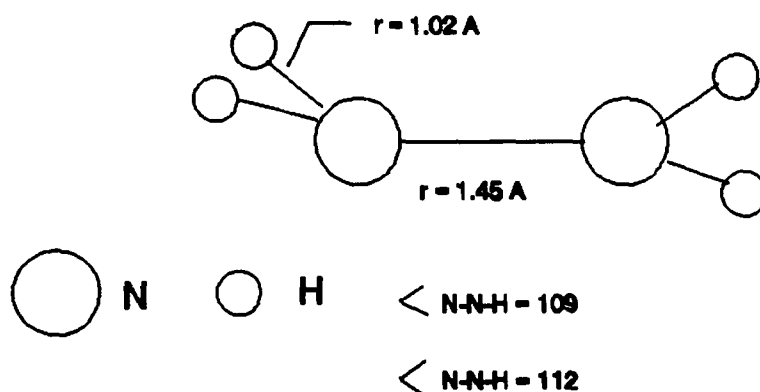
FIGURE 1: Geometry of Hydrazine

SPECTROSCOPY OF HYDRAZINE

A number of studies have been done on the microwave and infrared spectrum of hydrazine, but fewer in the visible and ultraviolet since hydrazine decomposes when exposed to UV radiation. The focus of much of the spectroscopic work on hydrazine has been the internal rotation of its amide groups. The large molecular dipole moment indicates that they do not rotate freely, but the exact form of the potential function describing the rotational barrier and its height are still not completely known. The most recent microwave rotational spectra[3] have been analyzed to yield a number of ground vibrational state molecular parameters previously unavailable.[4]

Investigations of the vibrational spectrum of hydrazine have led to a variety of assignments. This is partly due to the presence of three large amplitude vibrations in the molecule, which lead to relatively low potential barriers to inversion and internal rotation of the two amino groups. This departure from the rigid-

rotator harmonic oscillator model greatly complicates the spectrum, particularly in the vapor phase. The latest low resolution infrared and Raman studies of the complete vibrational spectrum hydrazine are by Durig, et. al.,[5,6] Their assignments differ considerably from earlier ones by Giguere and Liu[7] and by Catalano, Sanborn, and Frazer.[8] A comparison of these measurements and assignments is given in Table 2. Considerable information has been obtained on ground state and first excited vibrational state molecular

Table 2: Vibrational Frequencies for Hydrazine

	Giguere, et. al.	Catalano, et. al.	Durig, et. al.	JANAF values
Vibration	(liq), cm-1	cm-1	(matrix),cm-1	(cm-1)
1		3390	3297	3350
2			3207	3261
3		1806 (liq)	1312	
4	1124	1312	1312	1096
5	873	1087	1087	875
6	800	832	832	780
7		394	377	377
8	3338	3356	3390	3330
9	3200	3297	3356	3280
10			1608 (liq)	1275
11	1280	1265	1265	933
12		982	982	966

parameters by high resolution infrared studies of the amino wagging and inversion bands in the vapor phase. This approach was first applied by Yamaguchi, et. al.[9], by Kasuya and Kojima[10], and by Hamada.[11] The use of high resolution Fourier transform spectroscopy and infrared laser resonance techniques has provided more complete data.[12,13] The Fourier transform spectrum of the 377cm^{-1} torsional band studied by Ohashi, Lafferty and Olson has yielded a barrier to internal rotation of 215050 cm^{-1}, based on a Dennison-Uhlenbeck potential.[14]

THERMODYNAMIC PROPERTIES

NEQPAK requires the heat capacity C_p, enthalpy h, and the Gibbs free energy g at functions of temperature, as well as the heat of formation for each gas in the model system being used. The materials database provides the temperature dependent functions in the form of polynomial expansions, which allows the values to be calculated in a computationally efficient manner. For an adequate fit, the temperature range that NEQPAK uses is broken into several segments and separate polynomials are generated over each segment. In this way the thermodynamic functions are given by:

$$C_p/R = a_1 + a_2T + a_3T^2 + a_4T^3 + a_5T^4$$

$$h/RT = a_1 + \frac{1}{2}a_2T + \frac{1}{3}a_3T^2 + \frac{1}{4}a_4T^3 + \frac{1}{5}a_5T^4 + \frac{a_6}{T}$$

$$G/RT = a_1T(1 - lnT) - \frac{1}{2}a_2T - \frac{1}{6}a_3T^2 - \frac{1}{12}a_4T^3 - \frac{1}{20}a_5T^4 - \frac{a_6}{T} - a_7$$

There are a number of sources of thermodynamic tables for gases, but all principally depend on the methods of kinetic theory to generate the thermodynamic functions. NEQPAK draws on the JANAF tables[15], among others, for the basic data. Since hydrazine vapor is listed in JANAF, the molecular parameters used in this reference were taken to generate the polynomial coefficients. Rather than enter the lengthy tables directly, the vibrational frequencies, moments of inertia and heat of formation were used in a program written by Curtis and Aboulmouna[16] that uses the rigid-rotator harmonic oscillator equations to directly calculate the thermal functions. The vibrational frequencies used are given in Table 2 and are from JANAF as altered to better match the calculated thermodynamic properties with the experimental values of vapor pressure. The only modification that had to be made was to add a ln(2) term to the free energy to account for the change in the partition function needed to compensate for the hindered internal rotation of the torsional motion. With this correction, the program produced values which correlated well with JANAF's. The polynomial coefficients are given in Table 3.

Table 3: Thermodynamic Function Polynomial Coefficients for Hydrazine

Temp Range (K)	A1	A2	A3	A4	A5	A6	A7
100 - 1000	0.38211E+01	-.14912E-02	0.48542E-04	-.68776E-07	0.29575E-10	0.13174E+05	0.57948E+01
1000 - 6000	0.59285OE+01	0.80025E-02	-.26342E-05	0.39735E-09	-.22536E-13	0.12005E+05	-.83227E+01
6000 - 10000	0.64155E+01	0.43254E-02	-.75100E-06	0.58356E-10	-.17014E-14	0.17108E+05	-.67420E+01
10000 - 15000	0.48352E+01	0.36079E-02	0.38211E+01	0.23935E-10	-.48608E-15	0.27122E+05	0.79115E+01
15000 - 20000	-.14068E+03	0.36144E-01	0.59280E+01	0.11921E-09	-.17039E-14	0.54079E+06	0.11285E+04

While the above method has the advantage of being consistent with the JANAF tables, a more accurate evaluation would take into account both the actual hindered rotation plus an updated list of vibrational frequencies. The former has been done in the tables calculated by Gurvich, et. al.[17]. He uses the theory of Pitzer and Gwinn[18] and their correction tables for hindered internal rotation, plus a slightly different set of vibrational frequencies. The differences from the JANAF tables are on the order of a few tenths of a percent. Given the other uncertainties with the hydrazine data and the much greater time

required to apply Pitzer and Gwinn's corrections, it is probably not worth the extra work to add these corrections to the NEQPAK database entry for hydrazine.

TRANSPORT PROPERTIES

Where binary diffusion coefficients and gas-phase viscosity coefficients are not available from experiment, it is necessary to calculate them over the required temperature range. The calculations generally depend on the calculation of collision integrals to solve the Boltzmann equation. These collision integrals themselves require the assumption of a particular pair potential which is specific to the interacting species (although *ab initio* calculations are possible in certain cases). Given that experimental data on molecular collisions is limited except for the low molecular weight gases, one must assume a particular generic interaction potential form and use transport property data such as viscosity to calculate the interaction parameter for a give species. This potential can then be used to find diffusion and viscosity coefficients over an extended range of temperatures. Two programs available to perform these calculations are by Kee, Warnatz and Miller[19] and by Dassanayake and Etemadi.[20] The Kee program does not calculate properties for charged-neutral interactions, but the Dassanayake program does. Both programs have input property databases which are not referenced. Table 4 shows the input data required for each program, along with values for hydrazine. Similar values are needed for each additional species needed to calculate interspecies transport coefficients.

Table 4: Hydrazine Properties For Use in Program by Kee, et. al.

Property	Units	Value[a]
Lennard-Jones potential well depth ϵ/k	Degrees Kelvin	205.000
Lennard-Jones collision diameter	Angstroms (10^{-10}meters)	4.230
Dipole moment μ	Debye (10^{-18}cm$^{2/3}$erg$^{1/2}$	0.0
Polarizability α	10^{-30}meters^3	0.0
Rotational relaxation collision number Z_{rot} at 298°K	-	1.5

[a]Values from program database.

Table 5: Hydrazine Properties Used in Program by Dassanayakae and Etemadi

Property	Units	Value
Mass	A.M.U	32.048
Ionization Potential	eV	8.10 [a]
Charge Number	-	0
Polarizability	$10^{-24}cm^3$	10.97 [b]
Dipole moment	Debye ($10^{-18}cm^{2/3}erg^{1/2}$)	1.85 [c]
Atomic or Molecular Radius	-	- [d]
Interaction potential well depth	Joules	5.22×10^{-21} [e]
Collision radius	meters	4.94×10^{-10} [e]

[a]Lias. S. G. et. al., "Gas-Phase Ion and Neutral Thermochemistry", J. of Phys. and Chem. Ref. Data, 17,Suppl No. 1, 1988.

[b]Calculated from permittivity vs temperature data.

[c]Schmidt, Eckart W., Hydrazine and Its Derivatives: Preparation, Properties, Applications, (John Wiley & Sons: New York)

[d]This parameter is not actually used in the program. The source of the values given for the database supplied with the program is obscure; for molecular species they seem to represent Lennard-Jones collision diameters but for atomic species the values are too small.

[e]Estimated from critical temperature, volume and compressibility factor. See text.

The collision parameters were calculated using empirical expressions described in the literature[21,22] By this method, the Lennard-Jones potential well depth ϵ and the collision diameter σ are given by:

$$\frac{\epsilon}{k} = 0.003313\frac{T_c}{Z_c^4} \quad \text{and} \quad \sigma = 36.9V_c^{1/3}Z_c^2.75$$

where k = Boltzmann's constant, V_c is the critical volume, Z_c is the critical compressibility factor, and T_c is the critical temperature. Values for the critical temperature parameters can be found in tabulations of physical properties by Yaws[23] and by Reid and Sherwood.[24] For the interaction between different species, this program assumes the approximation that for two species i and j,

$$\epsilon_{ij} = \sqrt{\epsilon_i \epsilon_j} \quad \text{and} \quad \sigma_{ij} = \frac{(\sigma_i + \sigma_j)}{2}$$

These values are not shown here, but are easily calculated using the above data plus that in the original interaction database provided in the program.

KINETIC DATA

Since hydrazine decomposes rapidly above 380°C, for high temperature calculations the properties of its decomposition products such as ammonia are probably more relevant than those of hydrazine itself. NEQPAK assumes a rate constant which has a temperature dependence in the Arrhenius form of

$$K_r^f = A_r T_q^{B_r} e^{-C_r/T_r}$$

Kinetic data for hydrazine in the gas phase is given by Baulch, et. al.[25] The format for NEQPAK input is given by

> REACTION, TYPEF, TYPER, KPL, A,B,C,D,E,F,G,H,U

where REACTION describes reaction equation, TYPEF and TYPER refer to the relevant reaction temperature type for forward and reverse reactions, A, B, and C are the forward reaction constants in the Arhennius equation, while E, F, and G refer to the reverse rate. G, H and U are for nonequilibrium vibrational effects on the reaction and are irrelevant for the available hydrazine data. In this format the data from the compilation by Baulch et., al. is given as:

> 'C.CM/MOLE'/Baulch, et. al.
> 'N2H4 + M = NH2 + NH2 + M',1,1,1,4E15,0,20600/
> /
> 'O + N2H4 = H2O + N2H2',1,1,1,7.1E13,0,600/
> 'N2H4 + NH2 = NH3 + N2H3',1,1,1,1E13,0,0/
> 'NH2 + NH2 = NH3 + NH',1,1,1,4E12,0,2800/
> 'N2H4 + H = H2 + N2H3',1,1,1,1.3E13,0,1260/

The blank entry after the first reaction is to indicate that the catalytic efficiency for the "M" species in the line above is taken as 1.0 for all species. In actuality the efficiency is unknown.

CONCLUSION

The above result provide the data needed to add hydrazine to the NEQPAK database. Certain parameters, such as the characteristic vibrational temperature, were developed for use in describing interactions between atoms and diatomic molecules and are not well defined for larger polyatomic molecules such as hydrazine. The diffusion and viscosity coefficients are not given here but should it should be relatively straightforward to calculate them use the programs referenced above.

REFERENCES

[2]Schmidt, Eckart W., Hydrazine and Its Derivatives: Preparation, Properties, Applications, (John Wiley and Sons: New York), p 233, 1988.

[3]Tsunekawa S. and Kojima, T., J. Phys Soc. Japan 49, 1957-1964, 1980.

[4]Tsunekawa, S., and Kojima, T., J. Mol. Spect. 95, 133-152, 1982.

[5]Durig, J. R., Bush, S. F., and Mercer, E. E., J. Chem. Phys 44(11), 4238-4247, 1966.

[6]Durig, J. R., Griffin, M. G., and MacAnamee, R. W., J. of Raman Spectroscopy, 3, 133-141, 1976.

[7]Giguere. P. A., and Liu, I. D., J. Chem. Phys. 20(1), 136-140, 1952.

[8]Catalano, E., Sanbor, R. H., and Frazer, J. W., J. Chem. Phys. 38(9), 2266-2272, 1963.

[9]Yamaguchi, A., Ichishima, I., Shimanouchi, T., and Mizushima, S., Spectrochim. Acta 16, 1471, 1960.

[10]Kasuya, T. and Kojima, T., J. Phys. Soc. Japan 18, 364-8, 1963.

[11]Hamada, Yoshiaki, Hirakawa, A. Y., Tamagake, K., Tsuboi, M., J. Mol. Spectr. 35, 420-435, 1970.

[12]Tsuboi, M. and Hamada, Y., J. Mol. Spect. 108, 328-42, 1984.

[13]Jones, H. and Takami, M., J. Chem. Phys. 78(3), 1039-1045, 1983.

[14]Ohashi, N., Lafferty, W. J., Olson, W. B., J. Mol. Spectr. 117, 119-133, 1986.

[15]Chase, M. W., Jr., Davies, C. A., Downey, J. R. Jr., Frurip, D. J., McDonals, R. A., and Syverud, A. N., "JANAF Thermochemical Tables, Third Ed., J. of Phys. and Chem. Ref. Data, 14, Supplement No. 1, 1985.

[16]Curtis, J. T. and M. Aboulmouna, unpublished.

[17]Gurvich, L. V., Veyts, I. V., Alcock, C. B., Iorish, V. S., eds, Thermodynamic Properties of Individual Substances, Fourth Edition, (Hemisphere Publishing Corp: New York) 1991.

[18]Pitzer, K. S. and Gwinn, W. D., J. Chem. Phys 10, 428-440, 1942.

[19]Kee, R. J., Warnatz, J., and Miller, J. A., "A FORTRAN Computer Code Package for the Evaluation of Gas-Phase Viscosities, Conductivities, and Diffusion Coefficients", Sandia National Laboratories, SAND83-8209, March, 1983.

[20]Dassanayake, M. S. and Etemadi, K., "Transport Properties of a Multicomponent two Temperature Flame Plasma", State University of New Year at Buffalo, submitted to Bell Aerospace Textron, 1989.

[21]Stiel, L. J., Thodos, G., "The Viscosity of Polar Gases at Normal Pressures", A. I. Ch. E. Journal, 8(2), 229-232, 1962.

[22]Mason, E. A., and Monchick, L., J. Chem. Phys., 36, 1622 (1968).

[23]Yaws, Carl L., Physical Properties, (McGraw-Hill: New York), 1977.

[24]Reid, R. C., Sherwood, T. K., The Properties of Gases and Liquids: Their Estimation and Correlation, 2nd ed., (McGraw-Hill : New York), 1987.

[25]Baulch, D. L., Drysdale, D. D., Horne, D. G., Evaluated Kinetic Data for High Temperature Reactions, Vol 2, (Butterworths: London), 1973.

CHARACTERIZATION OF AN INTENSIFIED CHARGE-COUPLED DEVICE (ICCD) CAMERA USED IN PLANAR LASER-INDUCED FLUORESCENCE (PLIF) STUDIES

John T. Tarvin

Associate Professor

Department of Physics and Astronomy

Samford University

800 Lakeshore Drive

Birmingham, AL 35229

7-1

CHARACTERIZATION OF AN INTENSIFIED CHARGE-COUPLED DEVICE (ICCD) CAMERA USED IN PLANAR LASER-INDUCED FLUORESCENCE (PLIF) STUDIES

John T. Tarvin
Associate Professor
Department of Physics and Astronomy
Samford University

ABSTRACT

The optical properties of intensified charge-coupled device (ICCD) cameras used to record the ultraviolet fluorescence of nitric oxide (NO) during planar laser-induced fluorescence (PLIF) measurements of shock flows were studied. An experimental protocol using an integrating sphere and a mechanical shutter was developed to facilitate the collection of the flat-field calibration images. This setup can be used with any camera for flat-field calibration. C language programs for the analysis of the calibration images, as well as subsequent flat-field correction of images, were written. These techniques were applied to two cameras in both the visible and the ultraviolet wavelengths. The uncorrected flat-field response of these cameras was found to vary by as much as 50% across the 578x384-pixel image; however, the variation was stable and correctable. Variation after correction was typically 10% or better, with the remaining variation attributable to noise present in the intensifier.

CHARACTERIZATION OF AN INTENSIFIED CHARGE-COUPLED

DEVICE (ICCD) CAMERA USED IN PLANAR

LASER-INDUCED FLUORESCENCE (PLIF) STUDIES

John T. Tarvin

INTRODUCTION

Planar laser-induced fluorescence (PLIF) is a technique that uses a laser system and cylindrical optics to produce a sheet of ultraviolet (uv) radiation. This sheet can be used to provide noninvasive visualization of flowfields, including supersonic mixing and combustion in SCRAMJET flowfields (1), ultrasonic flow regions about various probe geometries in shock tubes (2), and the wake region of hypervelocity vehicles (3). The use of a two-wavelength technique in these measurements allows one to relate the fluorescence ratio to temperature in the flowfield (4,5). This operation, performed as a pixel by pixel ratio of the two fluorescence images, requires an exact alignment of the two images. Prior to this operation, corrections must be made to the images to insure that they accurately represent molecular fluorescence signals, and not extraneous signals caused by optical system distortion, nonuniformity in the laser beam, or nonuniformity of camera response. Such extraneous signals would create systematic errors in PLIF temperature measurements.

Single wavelength PLIF images of both the wake region of free-flight hypervelocity projectiles (3) and high Mach number

flows in a laboratory shock tube (6) have been obtained at AEDC. Implementation of a two-wavelength capability is currently under way. Characterization of the optical properties of ICCD cameras is required in order to correct for nonuniformity in the ICCD array response. This characterization should be performed at or near the expected uv wavelength. However, an initial calibration in the visible region is more convenient. This visible calibration can then be compared to a uv calibration to determine if the ICCD array responds differently in the different spectral regions. Calibration consists of exposing the ICCD to uniform illumination at known light levels. This provides a response curve for each pixel. This response curve, which is hopefully linear, can then be modeled by a least-squares straight line. These response curves enable one to correct for variable sensitivity and offset for each pixel. This process is called flat-fielding: one illuminates the ICCD with a uniform source and mathematically adjusts the image until a uniform image is obtained. These same mathematical adjustments can then be applied to any image acquired with the same camera under similar conditions to obtain an image that corresponds to a "perfect" ICCD with a uniform response in each pixel.

APPARATUS

A block diagram of the apparatus used to obtain a flat-field calibration is shown in Fig. 1. A 6-in-diameter

7-4

integrating sphere was illuminated from the side with a tungsten source. The interior of the sphere is coated with barium sulfate. This sphere served as a uniform source in the visible region of the optical spectrum. There was also sufficient uv output to calibrate in the uv region of the spectrum. In this case, a UG-5 filter (220-500 nm) was used between the source and the camera to limit illumination of the ICCD to the uv region. The ICCD was illuminated directly (no focusing lens). A blackened cardboard tube was used as a coupler between the input to the camera and the exit port of the sphere. Mounted at the camera end of this tube was a calibrated photodiode; this allowed the light level at the camera to be measured in microwatts per centimeter squared. A mechanical shutter with attached iris and electrical controller was installed between the light source and the integrating sphere. This system, which served to limit illumination of the ICCD to times when data was actually being taken, was installed as a safety precaution for the ICCD. Care was taken that no light leakage into either the sphere or the camera occurred; the shutter control was tightly mounted directly over the input port of the sphere, and the tube was similarly mounted over the exit port. A black cloth was tightly wrapped several times about the interface between the camera and the tube. Images obtained under conditions of no light (shutter closed) were not statistically different from dark current measurements.

7-5

The cameras used were microchannel plate (MCP) image intensified CCD detector heads using a Thompson 578x384 pixel CCD array (Princeton Instruments) and either 14 or 16 bits of A/D converter range. The camera was interfaced to a system which included a computer (Gateway 486/33C), a ST-130 controller card within the computer (Princeton Instruments), and a PG-10 high-voltage (HV) pulser unit (Princeton Instruments) to gate the intensifier ON. The intensifier was normally in an OFF state, and could only "see" when gated ON.

A computer program, CSMA, was provided by Princeton Instruments. This program, which also has a robust menu of image processing options, integrates the image acquisition step with the various components and their interconnection. Interconnection details among these various components is discussed in the following section.

METHODOLOGY

The above apparatus is connected in such a way that an image can be easily obtained from CSMA. Signals available with the ST-130 controller include the NOTSCAN signal. This signal is TTL LOW when the camera is not collecting data, and is TTL HIGH when it is collecting data. This signal is used to trigger the TTL input of the shutter controller. When the shutter is fully open, the x-sync on the shutter shorts a switch. This short is detected and processed to a TTL pulse using a customized circuit (7). This signal connects to the

7-6

Trigger Input of the PG-10 HV pulser. The Trigger Output of the PG-10 connects to the External Sync input of the ST-130 controller. These components then interact as follows: the operator directs the software program CSMA to acquire one data image in the External Sync Normal mode for 0.005 seconds. CSMA then causes the ST-130 to set NOTSCAN HIGH. This opens the shutter and closes the x-sync switch, which triggers the PG-10 HV pulser. The PG-10 then triggers the ST-130 External Sync and, after a programmable (via a front panel setting) delay, gates the CCD intensifier ON. As soon as the ST-130 sees the External Trigger, it starts a 0.005 second image accumulation; some time during this period, the PG-10 ga' ˜s the intensifier ON for a few tens of microseconds, and the CCD acquires an image of a uniformly-illuminated source. At the end of the 0.005 seconds, the ST-130 drives the NOTSCAN LOW, the shutter closes, and the CCD is no longer illuminated. Since the illumination is continuous, the CCD can acquire an image any time after the shutter is opened. Therefore, the delay setting on the PG-10 is unimportant since the HV pulse, which gates the CCD intensifier ON, always occurs a few tens of microseconds after the start of the CCD acquisition (the maximum is less than 100 microseconds, while the minimum CCD acquisition time is 5000 microseconds). While the intensifier if OFF, the CCD sees no light, so the effective length of the data acquisition period is the length of the HV pulse; the PG-

10 can vary this length, via front panel settings, from about 0.100 microseconds to about 100 microseconds.

In order to determine individual pixel light sensitivities, images are collected at variable levels of illumination. This variation is accomplished via an iris attached to the mechanical shutter unit. The shutter is opened briefly (the intensifier is gated OFF, so no light reaches the CCD) and a photodiode voltage measurement is made. This voltage measurement is converted to an intensity value using the calibration curve supplied with the photodiode. Initially, values with the iris fully open and fully closed (there is always a small open area in the center of the iris) are obtained, and then the voltage range is divided into N equal steps to provide N+1 illumination levels. Since the photodiode calibration curve is approximately linear, this provides a set uniformly distributed calibrations images.

Parameters are adjusted to provide maximum signal level, without saturation, of the CCD image when the iris is fully open. Variables that can be adjusted include the intensifier gain, the HV pulse width, and the light level of the tungsten lamp. The optimal procedure for adjusting these parameters was found to be as follows: gain was set to the desired value (based on usage experience from PLIF measurements), then the lamp was adjusted to as high a light level as possible (lamp specifications indicate that lamp current must not exceed 30 amps). Finally, the HV pulse width was adjusted to as short a

value as possible, This width was determined by two factors: 1)if too long, then the CCD intensifier may overload when gated ON - this condition is signaled by an audible alarm and is to be avoided; 2)the ST-130 digitizes the CCD image to (for example) 14 bits or a maximum pixel value of 16383 - too long a pulse width and the digitizer will saturate. The CSMA program displays each CCD image with 256 color levels, so regions of saturation are easily noted; one can then reduce the gain/light level/iris opening/pulse width to obtain an unsaturated image.

Following collection of several (usually 6 or 7) images at various light levels, each pixel in the CCD is examined. A least-squares line is fitted to the (intensity,digitizer value) pairs and written to a calibration file. The resulting intercepts represent the "background" values that must be subtracted from each pixel, and the slopes represent the "sensitivities" that must be divided into each pixel value. The slopes are normalized to the average slope; this results in sensitivities near 1, so that the average level of any image that is being corrected is maintained. Therefore, the flat-field operation becomes:

new image = (original image - intercepts)/(normalized slopes)
Image files suitable for CSMA use are created for the intercepts and the normalized slopes.

RESULTS

Sequentially acquired images were found to exhibit significant pixel to pixel variations due to noise. This effect can be seen in Fig. 2, in which a few adjacent pixels are plotted for three sequential acquisitions under identical conditions. The lamp source is a regulated DC supply, and the photodiode output is steady, so variations in illumination can not account for these image variations. This variation raises serious questions about the accuracy obtainable with these cameras when recording transient images. It seems likely that the major source of error in determining temperatures using PLIF techniques will be the absolute uncertainty in the individual pixels of the camera.

Additional measurements were made in an attempt to better understand the source of the above noise. Fig. 3a shows the variation of the average signal level as a function of ICCD gain for constant HV pulse width and no illumination. It can be seen that the ICCD does not "turn on" until a gain of about 700 (as measured by the 10-turn pot on the camera housing). The lower gain positions correspond to the dark current present in the system. A single row of pixels is shown in Fig. 3b; it can be seen that the major source of noise is "shot noise", in which large amplitude spikes are superimposed on a small amplitude, random noise floor. This finding verifies the findings of an earlier study using intensified CCD cameras (8). It should be noted that the two cameras investigated

7-10

showed significantly different characteristics with respect to this shot noise. The newer camera included cooling of both the CCD and the MCP intensifier, and showed a much lower noise level than the older camera, where only the CCD was cooled.

The above measurements were repeated for a constant level of illumination; the results are shown in Fig. 4. The lower gain settings again exhibit only dark current characteristics, with the ICCD turning on between 600 and 700. At higher gains, the signal level rises approximately exponentially with gain setting (Fig. 4a). The noise also increases significantly with gain setting. Now, however, the shot nature of the noise is less obvious than above; rather, the noise now includes a strong random component (Fig. 4b), as exhibited by the lack of a floor to the noise. It is anticipated that this noise will represent the major source of uncertainty for PLIF temperature measurements. Note, however, that this uncertainty represents a true random error, rather than a systematic bias of the signal level either up or down.

The effect of HV pulse width was also investigated. The camera response was found to vary in an approximately linear manner with gate width, as shown in Fig. 5. This suggests that measured characteristics, such as the flat-field calibration, should be nearly independent of gate width. Therefore, the flat-field calibration performed with gate widths of tens of microseconds should be applicable to laser images obtained with a laser pulse width of 10 ns or less.

Due to the noise discussed above, flat-field calibration images were replicated nine times; this should reduce the noise by about a factor of three. This improvement with averaging was visually obvious in the images. A representative averaged image for constant illumination is shown in Fig. 6. The regular honeycomb pattern and the gradual spatial variation in intensity are readily obvious. These features were consistent in all images at all nonzero illumination levels. They were also present in both cameras, although the orientation angle of the honeycomb was different, as was the relative distribution of "hot spots" in the 2D image array. These features were not present in the dark current images at lower gains. This suggests that these features are artifacts associated with the MCP intensifier, rather than the CCD itself.

The possibility that the above image features were due to nonuniformities in the source was also investigated. The features remained "camera fixed" for various camera positions relative to the integrating sphere, even including a 90 degree rotation of the camera. This confirmed that the observed intensity patterns were a feature of the camera and not the illumination system.

Pixel responses were generally linear functions of illumination. Noise levels increased with signal levels, but S/N ratios were approximately constant. It was noted that the first few columns of pixels were not responsive to changes in

light level; these columns should not be used in any image analysis operations. For this reason, all statistics reported here do not include an 8-row/column "skirt" around the entire image; this should eliminate any edge effects present in the image.

An image representation of the slopes obtained from the flat-field least-squares calibration is shown in Fig. 7. The intercept file shows the slow spacial variations, but not the regular honeycomb pattern. It will be noted that this image echoes the intensity patterns present in the original calibration files. Therefore, although the patterns are present in the camera response, they are reproducible and correctable. This is clearly shown in Fig. 8, where a flat-field correction has been applied to the image shown in Fig. 6. (This image was not included in the set of images used in the flat-field calibration.)

The above calibration was repeated for uv illumination, with essentially the same result. The ratio of the visible and the uv slope files was essentially flat, showing no evidence of either the honeycomb pattern or the hot spots. This suggests that these cameras respond proportionally at visible and uv wavelengths. In fact, Figs. 6 and 8 are for visible wavelengths, while the slope file in Fig. 7 was obtained at uv wavelengths.

6. Smith, M.S., private communication.

7. McClure, B.J., private communication.

8. Seitzman, J.M., Hanson, R.K., DeBarber, P.A., and Hess, C.F., "Application of Quantitative Two-Line OH PLIF for Temporally Resolved Planar Thermometry in Reacting Flows", AIAA Paper 93-0802, AIAA 31st Aerospace Sciences Meeting, Reno, NV, January 11-14, 1993.
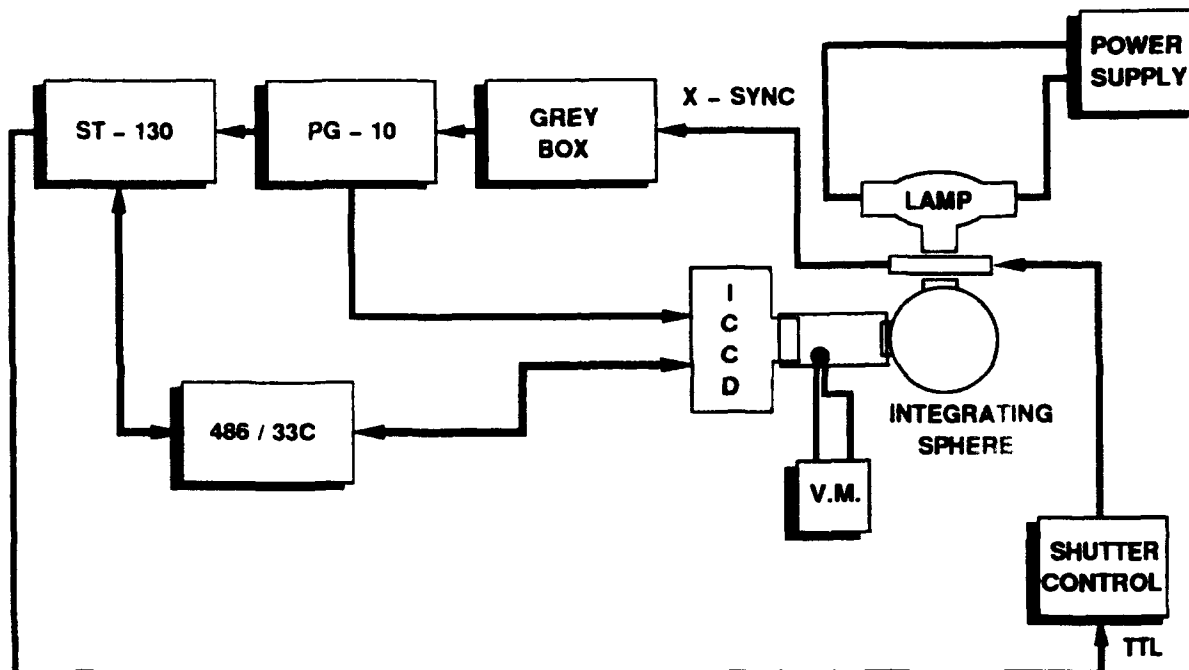
Figure 1.

Sequential Image File Noise
Gain: 825; Light: 1.22 uW/crn2

Figure 2.

ICCD Response vs. Gain (a)

ICCD Respose — 1 Row; No Illumination (b)

Figure 3.

ICCD Response vs. Gain (a)

ICCD Respose — 1 Row; 2.01 uW/cm2 - UG-5 (b)
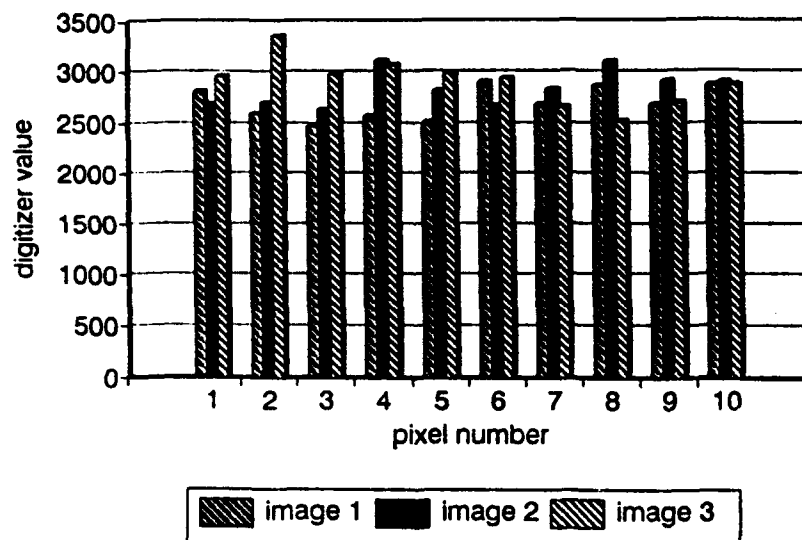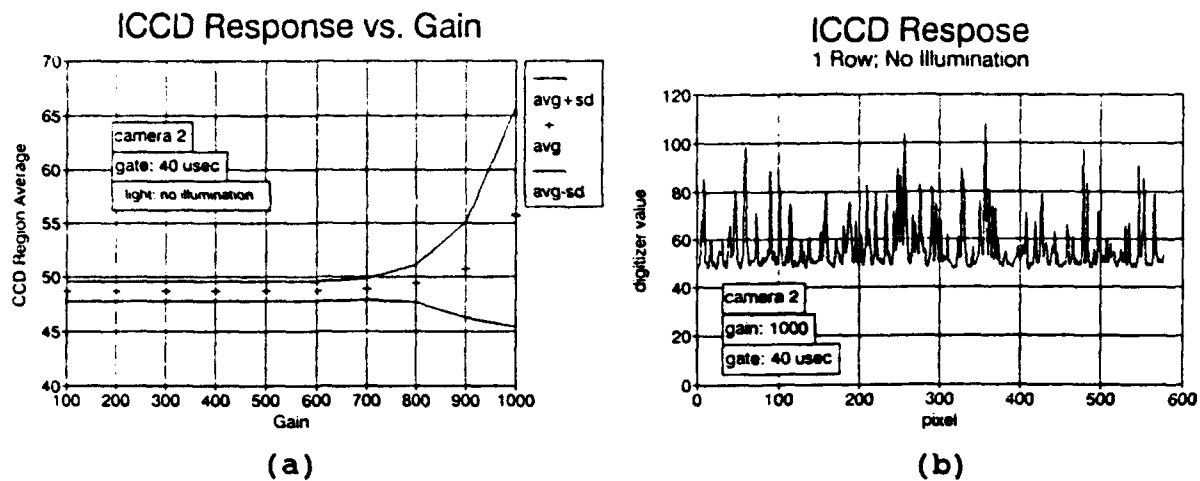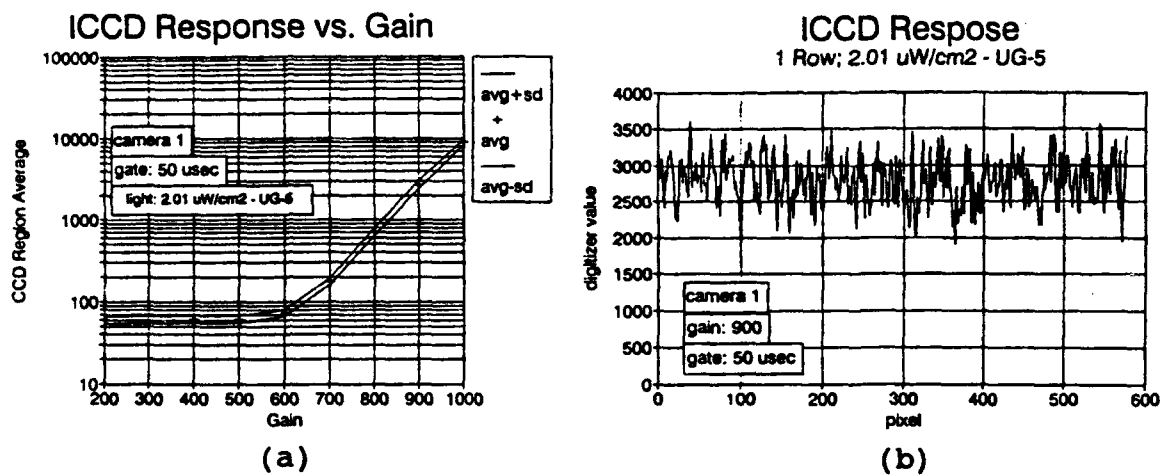
Figure 4.

ICCD Output vs. HV Gate Pulse Width
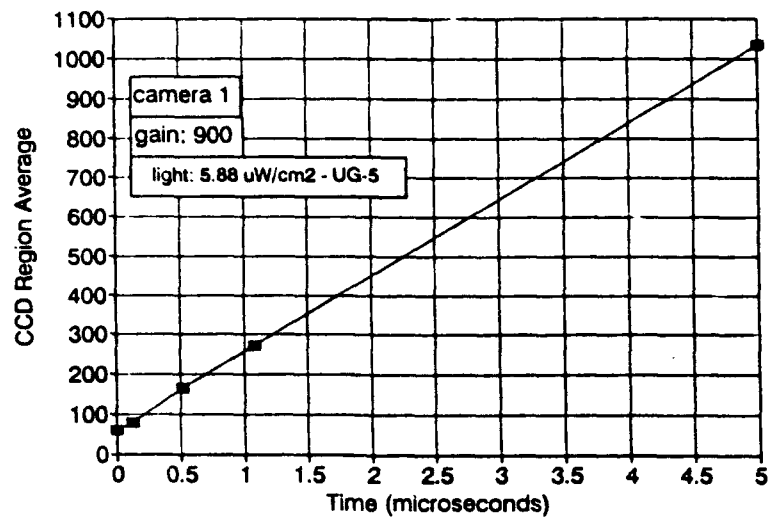
Figure 5.
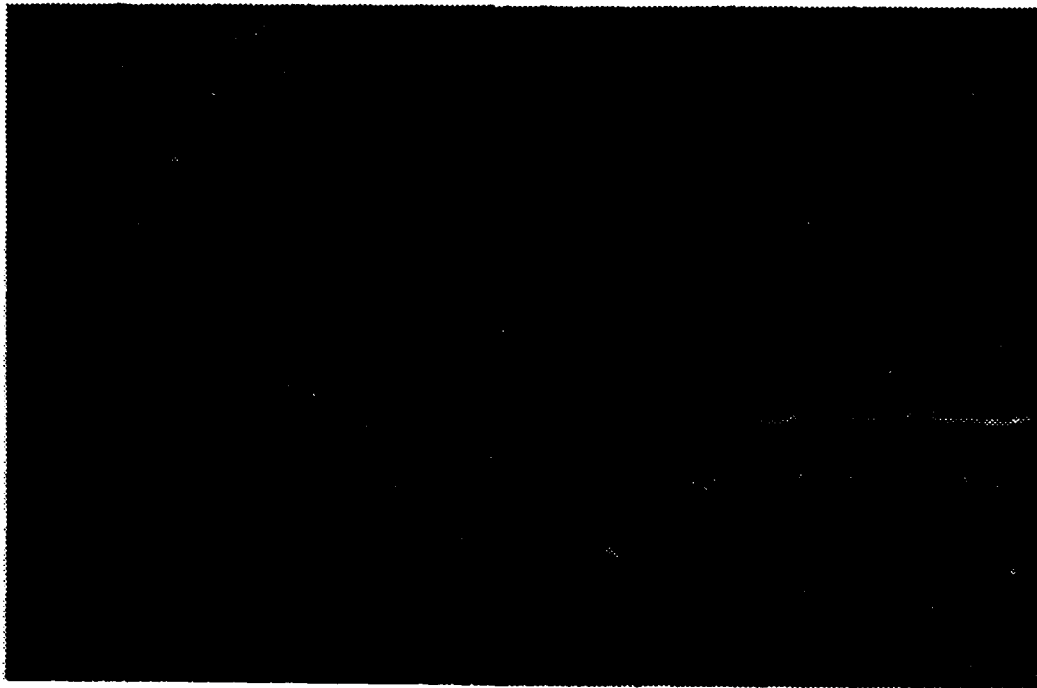
Figure 6. Uncorrected image obtained with the integrating sphere.

Figure 7. Slope image used in flat-field correction of Fig. 6.
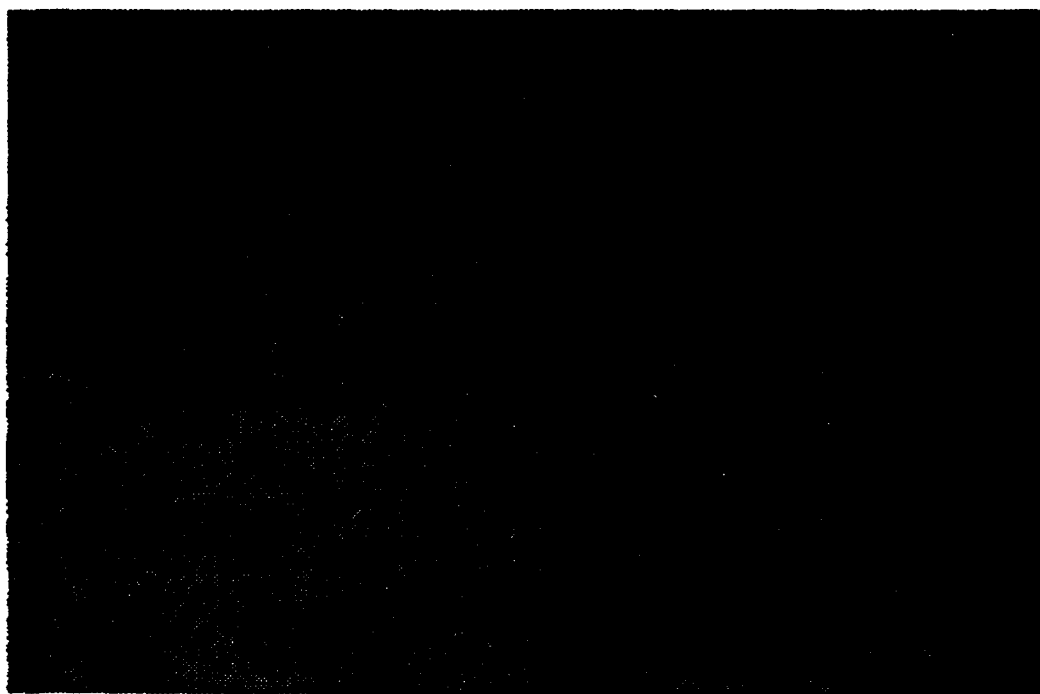
Figure 8. Flat-field corrected version of Fig. 6.

7-20

STRUCTURAL DAMAGE DETECTION OF A PLANAR TRUSS STRUCTURE USING A CONSTRAINED EIGENSTRUCTURE ASSIGNMENT

Tae W. Lim

Assistant Professor

Department of Aerospace Engineering

University of Kansas

2004 Learned Hall

Lawrence, KS 66045

STRUCTURAL DAMAGE DETECTION OF A PLANAR TRUSS STRUCTURE
USING A CONSTRAINED EIGENSTRUCTURE ASSIGNMENT

Tae W. Lim

Assistant Professor

Department of Aerospace Engineering

University of Kansas

Abstract

System health monitoring of aerospace vehicles is important not only to conducting safe operation but also to maintaining system performance. Structural health along with sensor and actuator malfunction must be monitored to perform the system health monitoring. As a step toward developing a system health monitoring scheme, this research investigates structural damage detection using a constrained eigenstructure assignment. The eigenstructure assignment is selected for the investigation since it may be used not only to perform structural damage detection but also to monitor the sensor and actuator performance in a unified manner. To employ the eigenstructure assignment in the framework of structural modeling and modal testing, a concept of constrained eigenstructure assignment is developed. The constrained eigenstructure assignment makes it possible that the computed feedback gains correspond directly to the structural parameter changes. To demonstrate the capability of the approach, a twenty-bay planar truss structure is employed. Modal tests are performed using eleven accelerometers for the undamaged structure and several missing member damage cases. Then the test data are used to locate the missing member. In spite of the incomplete mode shapes and test inaccuracies, accurate damage detection is conducted.

STRUCTURAL DAMAGE DETECTION OF A PLANAR TRUSS STRUCTURE
USING A CONSTRAINED EIGENSTRUCTURE ASSIGNMENT

Tae W. Lim

Introduction

Control system designers have traditionally used eigenstructure assignment techniques to force a structure to respond in a predetermined way. For model refinement and damage location, the desired eigenstructure, i.e., eigenvalues and eigenvectors, is the one that is measured in the test. Inman and Minas[1] and Zimmerman and Widengren[2] have derived methods that determine the pseudo (fictitious) controller which would be required to produce the test eigenstructure. The control gains can then be translated into matrix adjustments applied to the initial finite element model.

Zimmerman and Kaouk[3] applied this eigenstructure model refinement algorithm to structural damage detection. A major difficulty associated with Zimmerman's approach is that the method identifies matrix coefficients changes and thus requires an additional step of identifying structural members corresponding to the changes. This additional step will not be straightforward for complicated spacecraft structures. Also, the method requires a solution of a generalized algebraic Riccati equation and iterative solution is proposed to preserve load path of the undamaged structure, i.e., to maintain the zero-nonzero pattern of the undamaged stiffness matrix. When a structural member is completely damaged, an initial load path is broken. Thus, preserving load path for damage detection may not be valid for damage cases of entire loss of stiffness.

To perform the system health monitoring, structural health along with sensor and actuator malfunction must be monitored. As a step toward developing a system health monitoring scheme, this research investigates structural damage detection using a constrained eigenstructure assignment. The eigenstructure assignment is selected for the investigation since it may be used not only to perform structural damage detection but also to monitor the sensor and actuator performance in a unified manner. The constrained eigenstructure assignment makes it possible that the computed feedback gains correspond directly to the structural parameter changes without enforcing zero-nonzero pattern of the initial stiffness matrix. Thus, the additional step of correlating matrix coefficient changes to structural member parameter changes is avoided. Also,

the proposed approach requires neither a solution of algebraic Riccati equation nor iteration to converge to a solution.

To demonstrate the capability of the approach, a twenty-bay planar truss structure is employed. Modal tests are performed using eleven accelerometers for the undamaged structure and several missing member damage cases. Then the test data are used to locate the missing member. The results of damage detection will be presented.

Location of Structural Damage

The equation of motion governing the response of an n-DOF (degree-of-freedom) structural system is represented as

$$M\ddot{x} + D\dot{x} + Kx = Fu \tag{1}$$

where M, D, and K are the n x n system mass, proportional damping, and stiffness matrices, respectively; x is a physical displacement vector; u is an p x 1 vector of control forces and F is an n x p control influence matrix. Finite element analysis is often used to generate this discretized analytical model of the system. The undamped eigenvalue problem associated with Eq. (1) becomes

$$\left(\lambda_i^2 M + K\right)\phi_i = 0 \quad \text{for } i = 1, 2, \ldots \tag{2}$$

where λ_i and ϕ_i are the ith eigenvalue and eigenvector, respectively.

A conventional way of locating structural damage is to find the smallest changes in the system stiffness matrix that matches the measured eigenvalues and eigenvectors.[4-10] Therefore, it requires an additional step of locating damaged members using the changes in the stiffness matrix. This step is not straightforward when several structural members are connected to a finite element node. The constrained eigenstructure assignment investigated in this study makes it possible that the computed feedback gains correspond directly to the structural parameter changes. For typical modal tests, a limited number of transducers (e.g., accelerometers) are used. Thus, measured mode shapes are available only at the test DOF's, where transducers are placed. The size of the test DOF's is typically much smaller than that of the finite element DOF's. To provide compatibility in size between the test and analysis mode shapes, either the test mode shapes are expanded[6] or the system matrices are reduced[11] at the expense of losing accuracy. This loss of accuracy can create serious difficulty in performing damage location. The best

achievable eigenvector concept[12,13] is employed in this paper to perform the expansion of the test mode shapes.

For the purpose of illustrating the constrained eigenstructure assignment approach, consider the mass-spring system shown in Fig. 1 (a). The system mass and stiffness matrices are defined as

$$M = \begin{bmatrix} m_1 & 0 & 0 \\ 0 & m_2 & 0 \\ 0 & 0 & m_3 \end{bmatrix} \text{ and } K = \begin{bmatrix} k_1 + k_2 & -k_2 & 0 \\ -k_2 & k_2 + k_3 & -k_3 \\ 0 & -k_3 & k_3 \end{bmatrix} \tag{3}$$

with

$$x = \left\{ x_1 \, x_2 \, x_3 \right\}^T \tag{4}$$
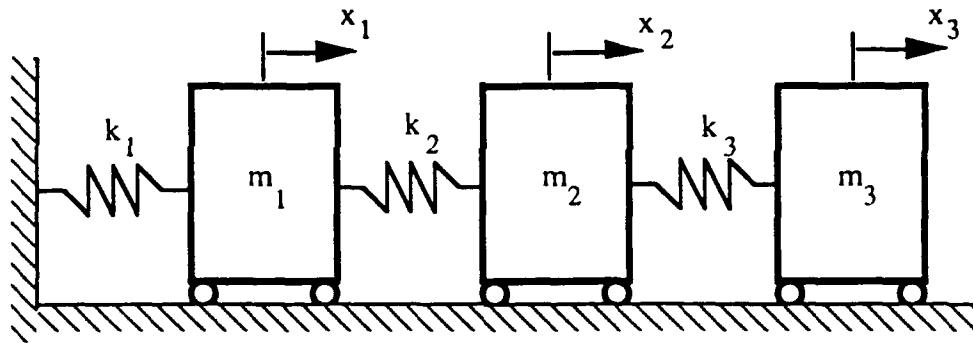
(a) without control forces
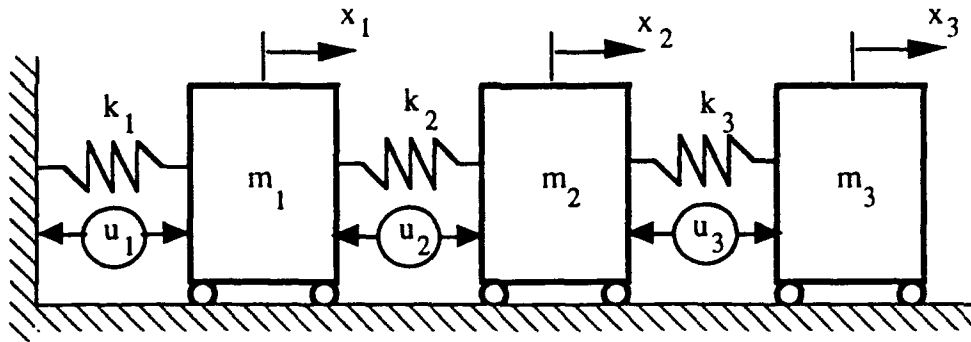
(b) with control forces

Fig. 1 A mass-spring system

Parallel to the springs, active control forces are added as shown in Fig. 1 (b). Then, the $\mathbf{F}$ matrix in Eq. (1) becomes

$$\mathbf{F} = \begin{bmatrix} 1 & -1 & 0 \\ 0 & 1 & -1 \\ 0 & 0 & 1 \end{bmatrix} \qquad (5)$$

with

$$\mathbf{u} = \left\{ u_1\, u_2\, u_3 \right\}^T \qquad (6)$$

The added control forces represent the forces generated due to the loss of stiffness which is caused by structural damage. The control influence matrix plays an important role in the eigenstructure assignment process since it provides constraints in computing feedback gains which are physically meaningful for structural damage detection.

Modal tests are performed periodically and eigenvalues and eigenvectors are measured to monitor significant changes in the measured modes. When the changes are significant, the damage detection process is initiated. The measured eigenvalues and eigenvectors are treated as "desired" eigenvalues and eigenvectors for the eigenstructure assignment algorithm to achieve using a feedback control. Since the control forces represent changes in stiffness properties, consider a displacement output feedback control with collocated sensors and actuators as

$$\mathbf{u} = -\mathbf{G}\mathbf{y} \qquad (7)$$

where $\mathbf{G}$ is a gain matrix and $\mathbf{y}$ is output feedback variables. Relative displacement measurement become

$$\mathbf{y} \equiv \mathbf{d} = \mathbf{F}^T\mathbf{x} \qquad (8)$$

where $\mathbf{d}$ is a relative displacement vector. From Eqs. (7) and (8), the control force becomes

$$\mathbf{u} = -\mathbf{G}\mathbf{F}^T\mathbf{x} \qquad (9)$$

Substitute the control force in Eq. (9) into the equation of motion, Eq. (1), and rearrange to obtain

$$M\ddot{x} + D\dot{x} + \left(K + FGF^T\right)x = 0 \tag{10}$$

The gain matrix, pre- and post-multiplied by the control influence matrix, is used to modify the system stiffness matrix. The control influence matrix, F, plays a role of redistributing the gain matrix to appropriate finite element DOF's. Assume that the gain matrix is diagonal. Then the changes in stiffness matrix due to control force j, which corresponds to structural member j, can be written as

$$\Delta K_j = F_j g_j F_j^T = g_j F_j F_j^T \tag{11}$$

where F_j is the jth column of F and g_j is the jth diagonal element of G. Each diagonal element of gain matrix represents the change in corresponding spring stiffness coefficient.

The gain matrix is now obtained to match the measured eigenvalues and eigenvectors. Consider the eigenvalue problem associated with Eq. (10) as

$$\left[\lambda_i^{d^2} M + \lambda_i^d D + \left(K + FGF^T\right)\right]\phi_i^d = 0 \tag{12}$$

where λ_i^d and ϕ_i^d are the ith desired eigenvalues and eigenvectors. They are the measured eigenvalues and eigenvectors from the test. Consider the jth structural member and rearrange Eq. (12) as

$$\phi_i^d = \left(\lambda_i^{d^2} M + \lambda_i^d D + K\right)^{-1} F_j F_j^T\left(-g_j \phi_i^d\right) \tag{13}$$

Define

$$\phi_i^d = L_{ij} \eta_{ij}^d \tag{14}$$

where

$$L_{ij} \equiv \left(\lambda_i^{d^2} M + \lambda_i^d D + K\right)^{-1} F_j F_j^T \tag{15}$$

$$\eta_{ij}^d \equiv -g_j \phi_i^d \tag{16}$$

Equation (13) indicates that the desired eigenvector, ϕ_i^d, must reside in the subspace spanned by the columns of L_{ij}. The desired eigenvector typically does not precisely reside in the subspace due to modeling and measurement errors. In this case, the eigenvector that is as close as possible, in the least square sense, to the desired eigenvector can be computed as[12,13]

$$\phi_{ij}^a = L_{ij}L_{ij}^+\phi_i^d \qquad (17)$$

where ϕ_{ij}^a is referred to as the best achievable eigenvector and the superscript + indicates a pseudo-inverse.
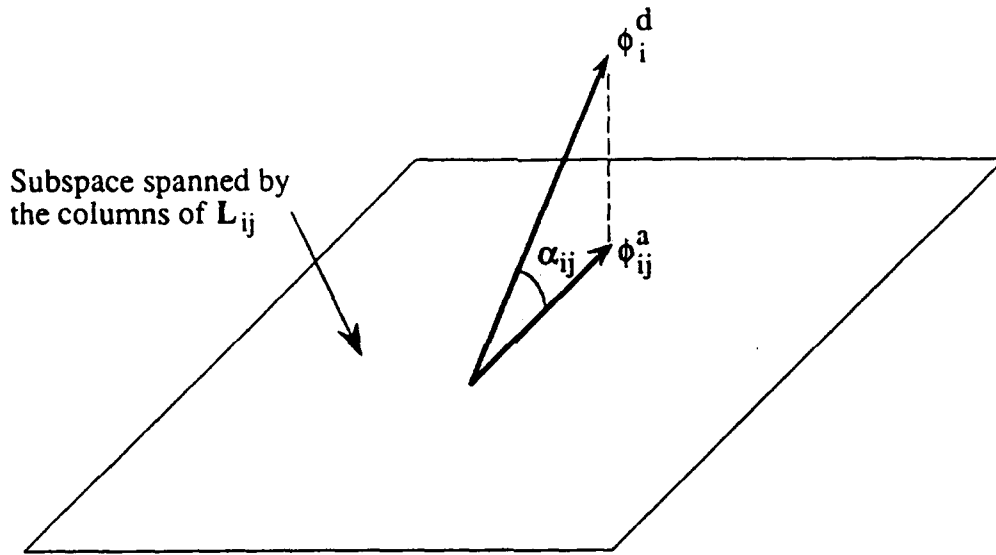
Fig. 2 Geometric interpretation of the best achievable eigenvector

Figure 2 illustrates the relationship between the vectors ϕ_{ij}^a and ϕ_i^d as well as the subspace spanned by L_{ij}. If the measured vector ϕ_i^d already lies in the subspace L_{ij}, i.e., the damage is caused by the jth structural member, then ϕ_{ij}^a and ϕ_i^d will be identical. If the damage is caused by a different element or the damage is not reflected in mode i, the two vectors will be different. If ϕ_{ij}^a is computed for all structural members that could possibly have caused the damage and the angle between ϕ_{ij}^a and ϕ_i^d is computed, the damaged element will be indicated by (in the case of perfect data) zero angle between the two vectors. All others will have non-zero values. The angle in degrees between the two vectors can be computed as

$$\alpha_{ij} = \frac{180}{\pi} \cos^{-1} \left(\frac{\phi_{ij}^{a^T} \phi_i^d}{\left\| \phi_{ij}^a \right\|_F \left\| \phi_i^d \right\|_F} \right) \qquad (18)$$

where $\|.\|_F$ represents the Frobenius norm. For a structure that has e structural members that could possibly have caused the damage and r measured modes, an e x r matrix of α's can be constructed as

$$\begin{bmatrix} \alpha_{11} & \alpha_{12} & . & . & \alpha_{1j} & . & \alpha_{1r} \\ . & . & . & . & . & . & . \\ . & . & . & . & . & . & . \\ \alpha_{i1} & \alpha_{i2} & . & . & \alpha_{ij} & . & \alpha_{ir} \\ . & . & . & . & . & . & . \\ . & . & . & . & . & . & . \\ \alpha_{e1} & \alpha_{e2} & . & . & \alpha_{ej} & . & \alpha_{er} \end{bmatrix} \qquad (19)$$

If damage is located in structural element j and this damage affects only mode i significantly so that the change in the frequency is measurable, then α_{ij} will be equal or close to zero. All other coefficients will be populated with non-zero entries. Therefore, the location of damage can be identified by searching for a value that is considerably smaller than others in the matrix.

In general, eigenvectors are not available for the entire system DOF's. In this case, partition the desired eigenvector as follows:

$$\phi_i^d = \begin{Bmatrix} v_i \\ w_i \end{Bmatrix} \qquad (20)$$

where v_i is the specified (measured) portion of the eigenvector and w_i is the unspecified portion. The best achievable eigenvector is then defined using Eq. (17) as

$$\hat{\phi}_{ij}^a = L_{ij} \hat{L}_{ij}^+ v_i \qquad (21)$$

where $\hat{L}_{ij}$ is the partition of the matrix L_{ij} containing the rows corresponding to v_i. In this case, the angle in Eq. (1) is defined as

$$\hat{\alpha}_{ij} = \frac{180}{\pi} \cos^{-1} \left(\frac{\bar{\phi}_{ij}^{a^T} v_i}{\left\| \bar{\phi}_{ij}^a \right\|_F \left\| v_i \right\|_F} \right) \qquad (22)$$

where $\overline{\phi}_{ij}^{a}$ is the partition of the vector $\hat{\phi}_{ij}^{a}$ corresponding to the measured portion of the eigenvector.

The best achievable eigenvector serves two purposes: (1) it allows partial specification of eigenvector and (2) measurement errors that are not consistent with the analytical model are filtered out. The best achievable eigenvector for mode i provides an alternative means of computing the "subspace rotation" as discussed in Ref. 14. The main difference is that the method in Ref. 14 identifies those DOF's that are affected by damage, whereas the method in this paper identifies directly the structural element that is damaged. Hence, the proposed method avoids the additional step of identifying damaged structural members from the affected DOF information due to damage, which can be cumbersome at times.

Magnitude of Structural Damage

Now the locations of damaged members are identified. The eigenstructure assignment is employed here to compute the feedback gains, i.e., the magnitude of structural damage. Rewrite the equation of motion, Eq. (1), in state-space form as

$$\dot{s} = As + B\hat{u} \tag{23}$$

where

$$s = \left\{ \begin{matrix} x \\ \dot{x} \end{matrix} \right\}, \ A = \begin{bmatrix} 0 & I \\ -M^{-1}K & -M^{-1}D \end{bmatrix}, \ B = \begin{bmatrix} 0 \\ M^{-1}\hat{F} \end{bmatrix} \tag{24}$$

The matrix $\hat{F}$ contains only those columns corresponding to the damaged members. The output equation, Eq. (8), then becomes

$$y = Cs \equiv \begin{bmatrix} F^T & 0 \end{bmatrix} s \tag{25}$$

The output feedback is thus defined as

$$u = -Gy = -GCs \tag{26}$$

Now the task is to find the diagonal gain matrix G to assign the desired (measured) eigenvalue (λ_i^d) and eigenvector (v_i). Feedback gain matrix is computed using the eigenstructure assignment technique provided by Andry et al.[12]

The best achievable eigenvectors can also be written using Eq. (23) and the desired eigenvalues and eigenvectors as

$$v_i^a = L_i \hat{L}_i^{\dagger} v_i \tag{27}$$

where

$$L_i = \left(\lambda_i^d I - A\right)^{-1} B$$

$\hat{L}_i \equiv$ the rows in the upper half of L_i corresponding to the measurement DOF's
employed in v_i

Then the system matrices (A, B and C) and the best achievable eigenvectors (v_i^a) are transformed into the format that allows partition of A matrix in a convenient manner. Unconstrained feedback gain matrix (G_u) is obtained as

$$G_u = -(Z - A_1 V)(\hat{C} V)^{-1} \tag{28}$$

where
$\hat{C}$ = a transformed C matrix

V = a matrix of transformed best achievable eigenvectors

Z = partition of a matrix which is a product of desired eigenvalues and V

A_1 = partition of a transformed A matrix

Thorough derivation of Eq. (28) is available in Ref. 12. The unconstrained gain matrix is a full matrix in general. To compute a diagonal gain matrix, let

$$\Omega \equiv \hat{C} V \quad \text{and} \quad \Psi \equiv Z - A_1 V \tag{29}$$

Then we obtain from Eq. (28)

$$G\Omega = -\Psi \tag{30}$$

or

$$\Omega^T\left[\text{diag}(g_i)\right] = -\Psi^T \tag{31}$$

The diagonal gains of G are computed independently as

$$g_i = -\Psi_i\Omega_i^+ \tag{32}$$

where Ψ_i is the ith row of Ψ and Ω_i is the ith row of Ω. The diagonal gain, g_i, corresponds to the ith stiffness change that satisfies the measured eigenvalues and eigenvectors in the least square sense.

Some of the desirable features of the approach described above include: (1) it updates the physical structural elements directly instead of updating matrix coefficients, which may or may not be physically realizable (2) measured mode shapes are not required for the entire finite element DOF's and (3) it requires neither a solution of algebraic Riccati equation nor iteration to converge to a solution compared to the other eigenstructure assignment based damage detection method.

Damage Detection of a Twenty-Bay Planar Truss Structure

The twenty-bay planar truss shown in Fig. 3 is used to implement the damage detection method described above. The diagonal and side dimensions of each square bay are 0.5 m and 0.354 m, respectively. The truss is constructed from aluminum truss members, steel joints, and transverse steel bars. The truss is oriented in a horizontal plane with its weight supported by steel balls on table tops. More information on the truss is available in Ref. 15.

For the damage detection studies, the truss is modeled using a rod element (axial stiffness only) per strut and lumped masses for the joints and steel bars. So the system has 2 DOF's per node resulting 80 system DOF's. The natural frequencies of the truss are shown in Table 1 in comparison to the test results. For modal tests, the truss was instrumented with 11 single-axis accelerometers as indicated in Fig. 3. A shaker was mounted at the free-end of the truss to provide excitation for modal tests. The first mode frequency is not consistent and varies widely (1.8 Hz to 2.2 Hz) from test to test. This lack of consistency poses difficulty in detecting the longeron damage cases as will be discussed later. The large error in the first mode frequency is contributed partly by the friction of the balls which is not modeled in the analysis, the low frequency inaccuracy of the transducers, and the modal test setup which was designed to measure all four modes simultaneously.
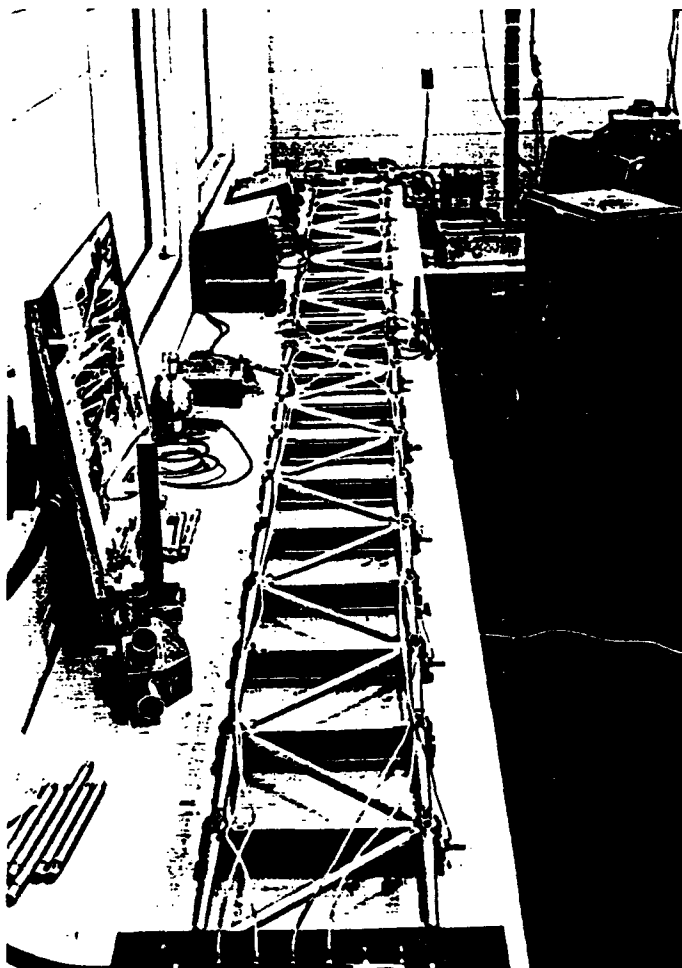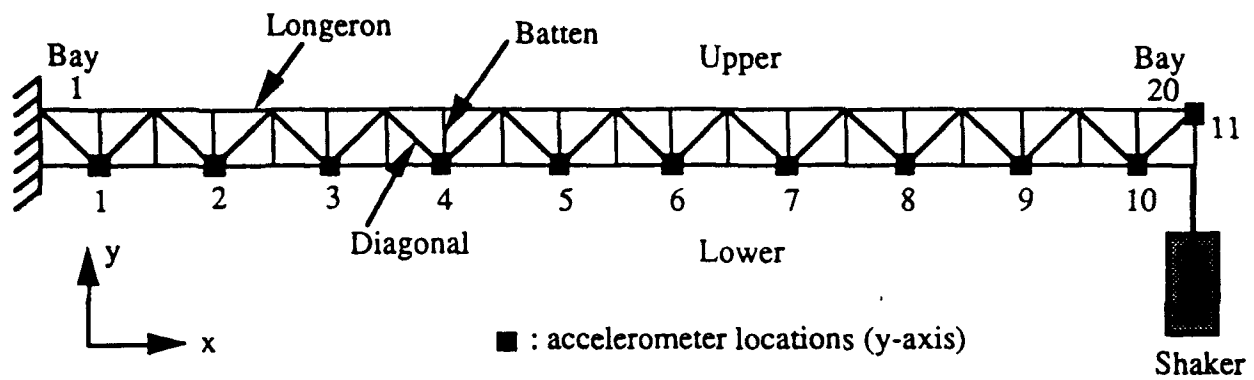
Fig. 3 A twenty-bay planar truss used for damage detection

Table 1 First four bending frequencies of the undamaged planar truss

Mode number	Analytical frequencies (Hz)	Test frequencies (Hz)	Description
1	1.60	1.80 to 2.20	first bending mode
2	9.36	9.35	second bending mode
3	24.70	24.21	third bending mode
4	43.23	42.74	fourth bending

Four damage cases shown in Table 2 are investigated including missing longerons and diagonals. The batten damage cases are not studied since the batten stiffness is dominated by the steel bars and the axial mode is not measured. All the longerons and diagonals are considered as damage candidates. Thus, the size of F matrix in Eq. (1) becomes 80 by 60. The F matrix is easily defined by replacing each strut with a control force and considering the direction of the control force. The measured frequencies for the damage cases are summarized in Table 3. Among the 11 test DOF's available, 10 test DOF's were selected to perform damage detection. The test DOF at the free end of the truss was not used.

Table 2 Damage cases investigated for the planar truss

Damage case	Damaged strut	Damage condition
A	Upper longeron in bay 2	Strut out
B	Lower longeron in bay 7	Strut out
C	Diagonal in bay 9	Strut out
D	Diagonal in bay 14	Strut out

Table 3 Measured natural frequencies due to damage (Hz)

Damage cases	Mode 1	Mode 2	Mode 3	Mode 4
A	1.27	8.00	22.00	42.56
B	0.85	8.06	17.00	42.11
C	2.07	9.41	20.80	37.39
D	2.22	9.31	23.71	29.86

Figure 4 shows the results of damage location for damage case A. The angles are computed using Eq. (22). The smaller the angle is, the more chance there is for damage. The strut numbers 1 to 20 correspond to the upper longerons from bay 1 to bay 20 and numbers 21 to
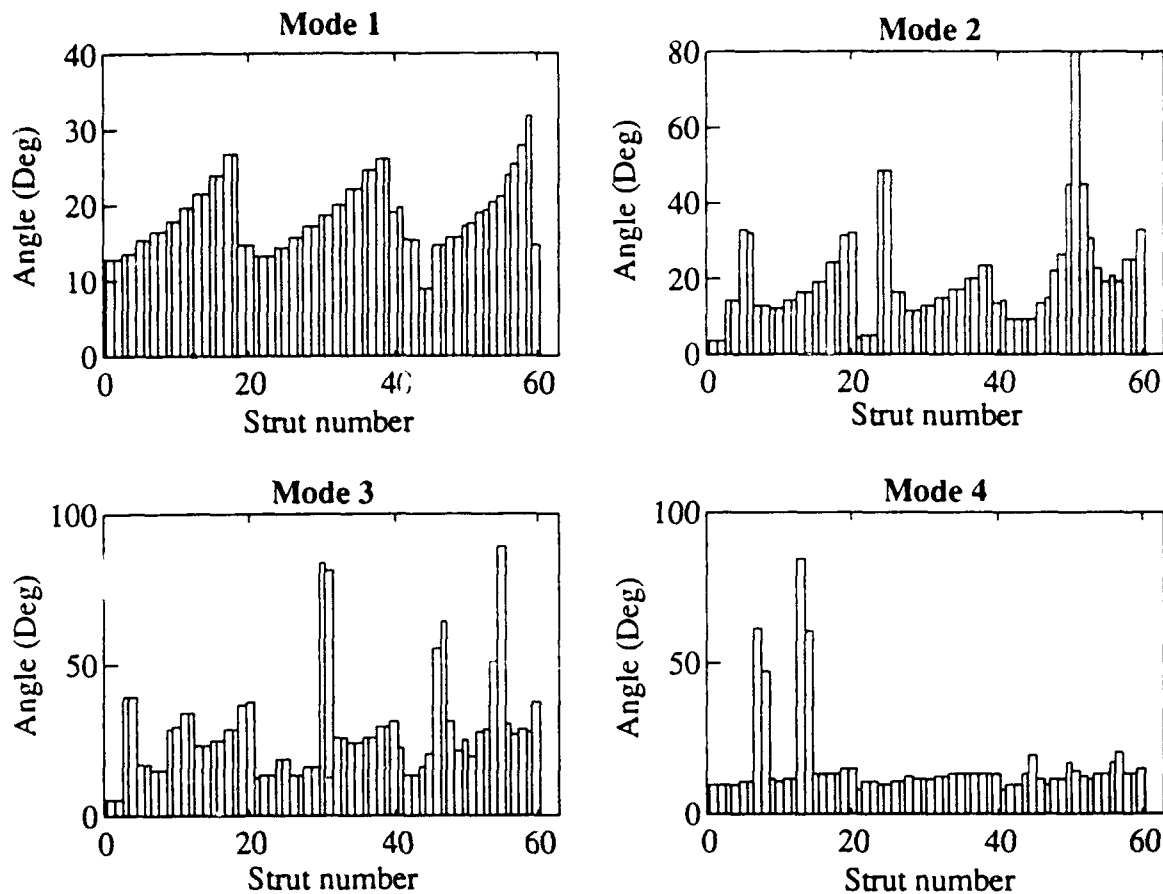
Fig. 4 Damage location results of damage case A

40 correspond to the lower longerons. The strut numbers from 41 to 60 correspond to diagonals from bay 1 to bay 20. The angles obtained using mode 1 is not accurate because of the measurement inaccuracy in mode 1. Since the damage on longerons tends to create large changes in the lower bending modes, this lack of measurement accuracy of mode 1 makes the damage location difficult. The angles obtained using mode 4 do not provide meaningful information since the frequency change in mode 4 is very small due to the upper longeron in the second bay. Modes 2 and 3 provide consistent information and it can be seen that the struts 1 and 2 consistently produce the smallest angles. Therefore, we can conclude that the damage occurred either in upper longeron 1 or 2.

Due to the lacing pattern of the diagonals in the planar truss, which is a "W" shape, the changes in modes created by the upper longerons in bays 1 and 2 are almost identical. This is true for all the pairs consisted of upper longerons in bays 3 and 4, 5 and 6, and so on. The situation is similar for the lower longerons. The lower longeron pairs 2 and 3, 4 and 5, and so
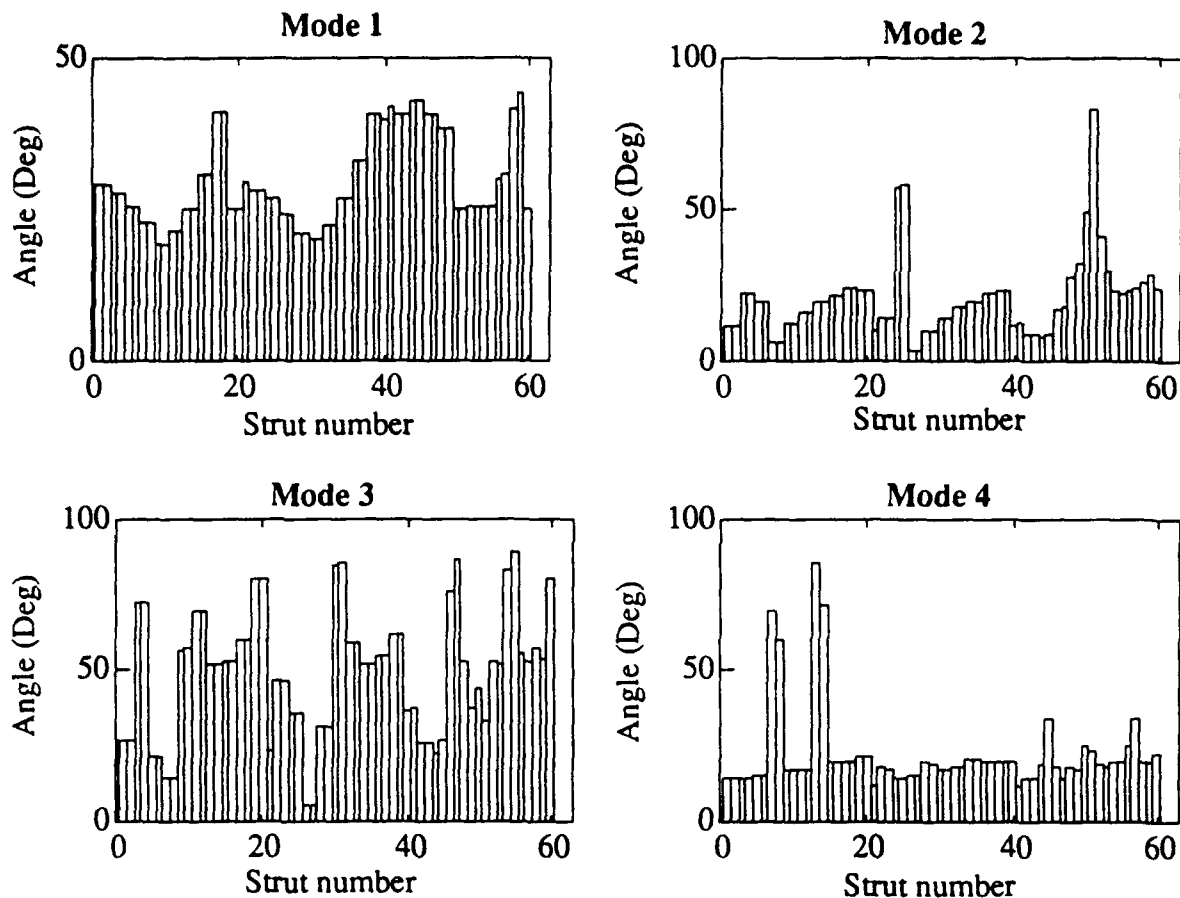
Fig. 5 Damage location results of damage case B

on, produce almost identical changes in modes. Therefore, this unique situation makes it practically impossible to single out the damaged longeron. Similar situation is there in damage case B. Results of damage case B are shown in Fig. 5. Again, due to the same reason, the angles obtained using modes 1 and 4 do not provide meaningful information. Modes 2 and 3 indicate that either lower longeron 6 or 7 is damaged.

Figures 6 and 7 show the results of damage location for damage cases C and D, respectively. The angles obtained using mode 1 is not accurate because of the measurement inaccuracy in mode 1. The second mode frequency is not affected much by the damage since the damage on diagonals tends to create large changes in the higher bending modes. Therefore, the angles obtained using mode 2 do not provide meaningful information. Modes 3 and 4 provide consistent information and it can be seen that strut 49 for damage case C and strut 54 for damage case D consistently produce the smallest angles. Therefore, we can conclude that the damage
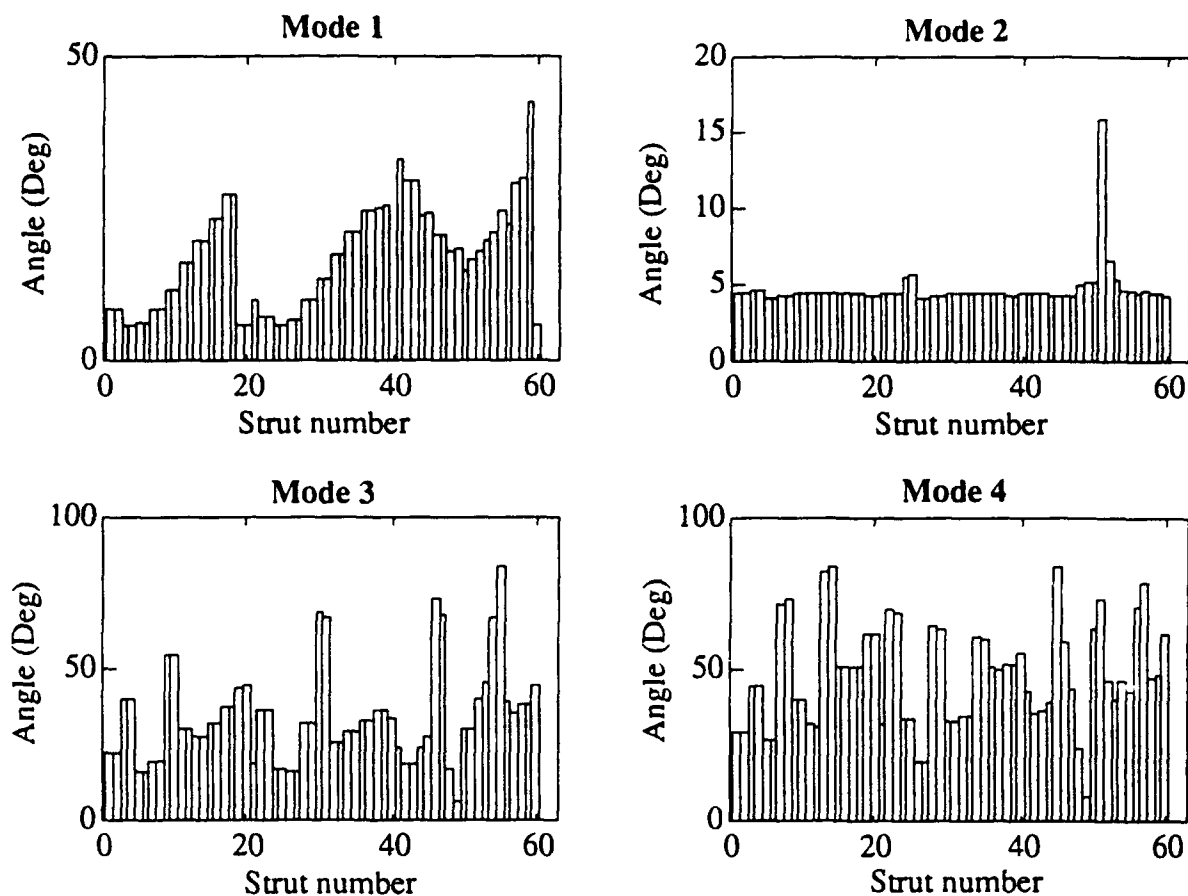
Fig. 6 Damage location results of damage case C

occurred in the diagonals in the bays 9 and 14 for damage cases C and D, respectively. Unlike the longeron damage cases, the damage diagonals can be identified uniquely. Since the location of damage is known, the magnitude of damage can be computed using Eq. (32). The constrained gains computed using modes 3 and 4 are -58,825 and -59,666 for damage cases C and D, respectively. Considering that the effective axial stiffness of the undamaged diagonal is 61,673 lb/in, the method accurately predicts, within 5% error, the amount of stiffness loss due to the missing diagonal.
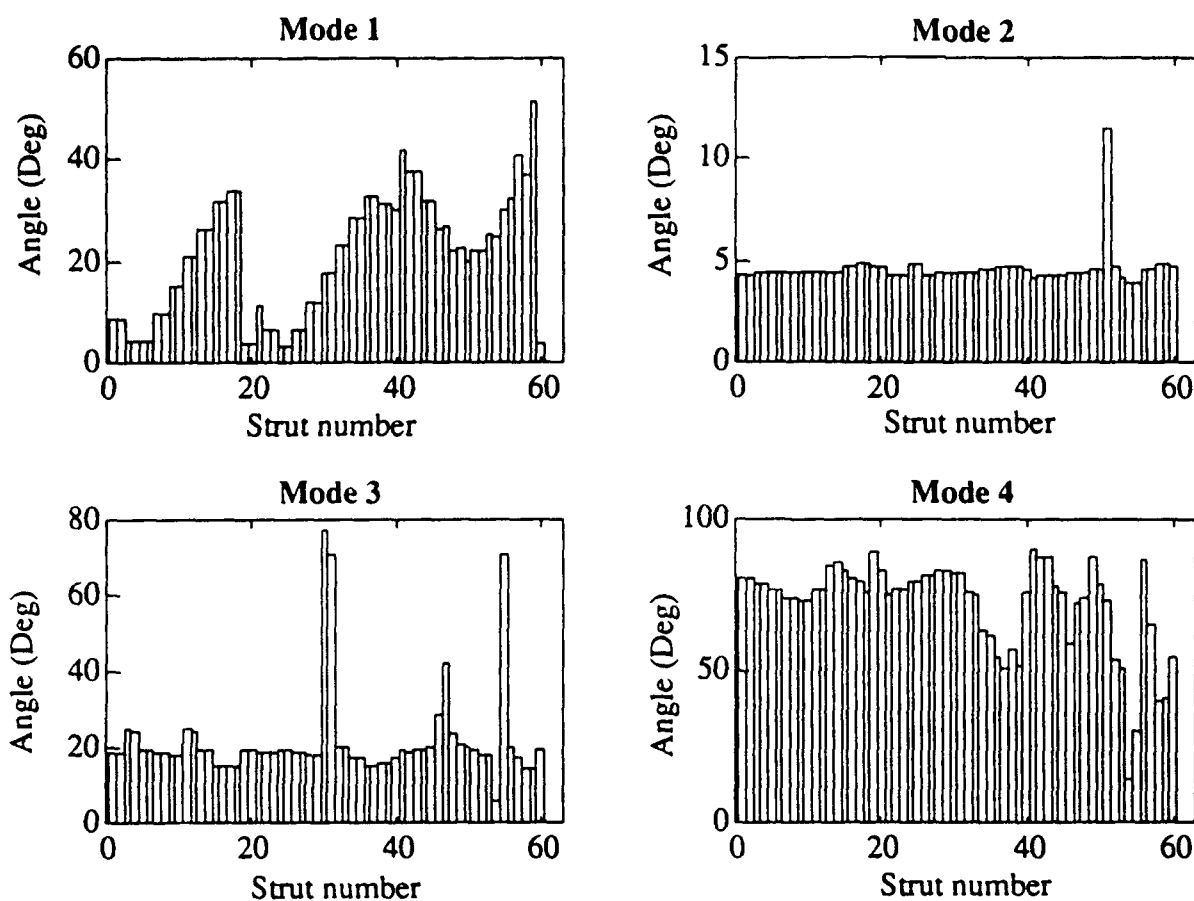
Fig. 7 Damage location results of damage case D

Concluding Remarks

A systematic approach to locating structural damage using a refined analytical model of the undamaged structure and measured modes was developed and demonstrated using the twenty-bay planar truss. This approach first locates the damage using the concept of best achievable eigenvectors and then identifies the magnitude of damage using a constrained eigenstructure assignment. Instead of identifying the changes in stiffness matrix for damage location, as most of the currently available methods do, the approach locates the damaged element directly. Thus, the additional step of locating damaged members from the stiffness matrix changes is avoided. As demonstrated in the planar truss example, the method does not require full finite element DOF mode shapes. The instrumented DOF's can be much smaller than the finite element DOF's (10 DOF's out of 80 finite element DOF's for the example). Thus the burden of using a large number of transducers for damage detection is relieved. Once the

location of damage is known, the magnitude of damage can be accurately computed using the constrained eigenstructure assignment method.

As was revealed by the planar truss example, the approach has its limitations. The limitations mainly stem from the measurement error in mode shapes and frequencies. As the test data gets inaccurate, the damage location can be blurred significantly. A judicious selection of test modes may be critical in performing a successful damage detection. Also, each individual damage cases must be able to produce unique pattern of change in frequencies and mode shapes. Otherwise, as indicated in the planar truss longeron damage cases, pinpointing the damaged member may not be feasible.

Acknowledgments

References

1. Inman, D. J and Minas, C., "Matching Analytical Models with Experimental Modal Data in Mechanical Systems," *Control and Dynamics Systems*, Vol. 37, 1990, pp. 327-363.
2. Zimmerman, D. C. and Widengren, W., "Correcting Finite Element Models Using a Symmetric Eigenstructure Assignment Technique," *AIAA Journal*, Vol. 28, No. 9, 1990, pp. 1670-1676.
3. Zimmerman, D. C. and Kaouk, M., "Eigenstructure Assignment Approach for Structural Damage Detection," *AIAA Journal*, Vol. 30, No. 7, 1992, pp. 1848-1855.
4. Brock, J. E., "Optimal Matrices Describing Linear Systems," *AIAA Journal*, Vol. 6, No. 7, 1968, pp. 1292-1296.
5. Baruch, M., "Optimal Correction of Mass and Stiffness Matrices Using Measured Modes", *AIAA Journal*, Vol. 20, No. 11, 1982, pp. 1623-1626.
6. Berman, A. and Nagy, E. J., "Improvement of a Large Analytical Model Using Test Data", *AIAA Journal*, Vol. 21, No. 8, 1983, pp. 1168-1173.
7. Kabe, A. M.," Stiffness Matrix Adjustment Using Mode Data", *AIAA Journal*, Vol. 23, No. 9, 1985, pp. 1431-1436.

8. Smith, S. W. and Hendricks, S. L., "Damage Detection and Location in Large Space Trusses," *AIAA SDM Issues of the International Space Station, A Collection of Technical Papers*, Williamsburg, VA, 1988, pp. 56-63.

9. Kammer, D. C., " Optimum Approximation for Residual Stiffness in Linear System Identification," *AIAA Journal*, Vol. 26, No. 1, 1988, pp. 104-112.

10. Smith, S. W. and Beattie, C. A., "Secant-Method Matrix Adjustment for Structural Models," *AIAA Journal*, Vol. 29, No. 1, 1991, pp. 119-126.

11. Lim, T. W., "A Submatrix Approach to Stiffness Matrix Correction Using Modal Test Data," *AIAA Journal*, Vol. 28, No. 6, 1990, pp. 1123-1130.

12. Andry, A. N., Shapiro, E. Y., and Chung, J. C., "Eigenstructure Assignment for Linear Systems," *IEEE Transactions on Aerospace and Electronic Systems*, Vol. AES-19, No. 5, 1983, pp. 711-729.

13. Lim, T. W. and Kashangaki, T. A.-L., "Structural Damage Detection of Space Truss Structures Using Best Achievable Eigenvectors," Submitted to AIAA Journal for publication, 1993.

14. Zimmerman, D. C. and Kaouk, M., "Structural Damage Detection Using a Subspace Rotation Algorithm," AIAA Paper 92-2521, April 1992.

15. Hallauer, W. L. and Lamberson, S. E., "A Laboratory Planar Truss for Structural Dynamics Testing," Experimental Techniques, Vol. 13, No. 9, 1989, pp. 24-27.

ELECTRODE DEVELOPMENT FOR AN AMMONIA FUEL CELL

Arnold R. Miller, Ph.D.

Research Associate Professor

Department of Chemistry

Colorado School of Mines[*]

Golden, Colorado   80401

[*]Formerly affiliated with the University of Colorado at Denver

ELECTRODE DEVELOPMENT FOR AN AMMONIA FUEL CELL

Arnold R. Miller, Ph.D.

Research Associate Professor

Department of Chemistry

Colorado School of Mines

Abstract

Ammonia fuel cells, which oxidize ammonia to dinitrogen and water, have a number of potential advantages as power sources for vehicles. However, no electrocatalyst is known at present that will give sufficient specific power to make this application practical. As the beginning of a research program to develop such a catalyst, development of electrodes for an ammonia cell was undertaken, starting from electrode technology reported in the literature. The main results of this work are an improved technique for applying a Teflon-bound catalyst mass to the current collectors and the use of nickel powder as an inert filler that gives strength and leak-resistance to the electrode. Ammonia fuel cells constructed with these electrodes have run a small electric fan.

ELECTRODE DEVELOPMENT FOR AN AMMONIA FUEL CELL

Arnold R. Miller, Ph.D.

Introduction

Fuel cells are energy conversion devices that convert chemical energy directly into electrical energy. Electrochemically they are similar to batteries but differ in that the electroactive materials are easily renewable and are thus stored externally in tanks rather than internally in the electrodes. The fuel and oxidant are gases or liquids. Because gases and liquids are generally covalent species, fuel cells have a high activation overpotential, and hence an electrocatalyst is required for any measurable power output. For recent general reviews, see Appleby and Foulkes (1989), Appleby (1992), and Cameron (1990).

Although the hydrogen-oxygen fuel cell was invented in 1839 by Grove, the first high-visibility and practical, but relatively low power, application of fuel cells was as the spacecraft power supply for the Gemini mission. This was a hydrogen-oxygen cell, developed by General Electric, which provided not only all electrical power for the spacecraft but also the drinking water for the astronauts, since pure water is the only chemical product of the cell reaction. If fuel cells can be made more generally practical, they would take over many applications that require large energy storage and are currently powered by heat engines or batteries. The ideal such applications are vehicle traction and propulsion. Examples of traction applications (i.e., wheeled and tracked vehicles) that I envision (for ammonia fuel cells) are locomotives, light rail (e.g., subways), intercity buses and trucks, off-road construction vehicles such as graders, earth movers, and dump trucks, and military vehicles such as tanks, trucks, and troop carriers. Propulsion applications (i.e., screw-driven vehicles) include large

passenger ships, cargo ships, submarines, prop-driven airplanes, and helicopters (although aircraft heretofore have not been considered a practical application [Adams, et al., 1960, Appleby, 1992]). These vehicles represent substantial energy use by virtue of their very large power ratings: For example, modern electric locomotives have continuous ratings in excess of 6,000 kW [Drury, 1992]; storage-battery powered submarines have ratings of about 10,000 kW [Bagotzky and Skundin, 1980].

Virtually all of these applications are currently powered, directly or indirectly, by heat engines, namely, internal combustion engines (ICEs), gas turbines, or steam turbines. To compare fuel-cell powered versions of these vehicles, which we term "electrochemical vehicles," with their current forms, we must consider both the fuel cell and the traction/propulsion motor as a cooperative unit. The potential advantages of fuel-cell powered vehicles, vis-a-vis the corresponding heat-engine powered vehicles, include the following:

(a) Low noise. The fuel cell itself will be virtually silent. Unlike familiar, low-performance motors (e.g., golf-car motors), high-performance traction or propulsion motors will generate noise; however, this noise can be suppressed by a sound absorbing barrier. A low noise level, desirable for all of the above applications, is especially important for passenger-transport and military applications.

(b) Ideal torque characteristics. The drooping torque-versus-speed characteristic of the series traction motor obviates the need for a speed-changing transmission, an additional machine with which ICE vehicles must be equipped. This advantage (less weight, lower cost, greater reliability, simplicity, smoothness) is important in all traction applications.

(c) Smoothness. Electrochemical vehicles are smoother than ICE vehicles because of lack of both vibration and speed-changing transmissions. Smoothness is

9-4

important in all applications that transport people: Trains, buses, passenger ships, and airplanes.

(d) Pollution-free. The main products of most fuel-cell reactions are innocuous materials such as water, carbon dioxide, or nitrogen. Some cells, such as the hydrogen-oxygen and ammonia-oxygen cells, do not even emit the green-house gas carbon dioxide. Being pollution free is an advantage for all vehicular applications.

(e) High efficiency. The theoretical efficiency for fuel cells, defined as $100\Delta G/\Delta H$, is typically above 85%. In contrast, heat-engined vehicles, because of the Carnot limitation, rarely exceed 35% in thermal efficiency [U.S. Dept. of Commerce, 1967]. Both fuel cells and heat engines have additional parasitic losses, but ICEs have larger losses due to requisite noise-supression and pollution-control devices. High energy-efficiency is important for long-range transportation: Trains, buses, ships, submarines, and airplanes.

(f) Lower capital and maintenance costs. Except for precious-metal catalysts, fuel cells, in contrast to heat engines, are made of inexpensive materials such as carbon and plastic and involve few critical machining operations. Electric motors are simple and robust. Low cost is important in all applications except military.

These potential advantages, while being of such great attactiveness that they justify intensive research in the field, have not so far been attained in practice. Fuel cells are not yet competitive with heat engines or batteries in most practical applications. The reasons for this are several: (a) Electrocatalysis has not advanced to the point as to give fuel cells sufficiently high specific power (see below), (b) the best of the current catalysts are noble metals and are too expensive for the catalyst loadings required, (c) the most active of the fuels, namely, hydrogen and hydrazine, are either impractical to store or are expensive and toxic, and (d) cells with relatively high specific power attained by high

operating temperature suffer from corrosion and other problems that lead to short lifetimes.

Two important parameters of vehicle power sources are specific energy and specific power. Specific energy is the storable energy per unit mass of device (kWh/kg); specific power is similarly the power per unit mass (kW/kg). Ideally, both parameters should be as large as possible so that acceptable performance is concomitant with long range. It is obvious that specific power limits vehicle performance; it is less obvious that specific energy--assuming a given range capability--does also: Without high specific energy, as for example in current battery-powered electric vehicles, achieving the desired range would make the vehicle so heavy that its performance would be low even with high specific power.

Battery-powered electric vehicles share most of the advantages of fuel cells; however, batteries exhibit a highly unfavorable inverse relationship between specific energy and specific power. What is most marked is the definite limit on battery specific energy, and the fact that the maximum that is obtainable comes at the expense of specific power, which is reduced toward zero. The essential reason for this effect is that the electroactive materials of a battery are contained wholly within the electrodes. Thus, a design that maximizes the amount of usable active material for a fixed cell mass (and hence maximizes specific energy) will be a different design from one that maximizes electrode surface area for a fixed mass (and hence maximize specific power)--in fact, the design that maximizes specific energy will minimize specific power.

Fuel cells, in contrast, have the advantages that the limit on specific energy (namely, the specific energy of the fuel itself) lies much higher, and specific power is more independent of specific energy: An increase of specific energy does not come so severely at the expense of specific power. In this regard, fuel cells behave more like heat engines. This follows from the fact that the electroactive

materials of a fuel cell, like the fuel of a heat engine, are stored externally to the electrodes. An additional advantage of external storage is that a fuel cell can be "recharged" faster than a storage battery: It has been estimated [Vincent, 1984] that the rate of chemical energy flow through a gasoline-pump delivery hose is 30 MW. Even if a storage battery could be built so as to withstand thermally such a rate of charge, its recharging efficiency would be very low due to overpotential losses.

For fuel cells to be competitive with ICEs, they need both higher specific energy and higher specific power. Comparison of typical values for energy and specific power for ICEs, nickel-cadmium batteries, and the best of current air-breathing hydrogen-oxygen fuel cells are given in Table 1. The fuel cell's energy and power densities are each 1/3 that of the ICE. (Although these parameters for the fuel cell do not include the weight of the electric traction/propulsion motor, the parameters for the ICE likewise do not include the weight of the speed-changing transmission.) The Ni-Cd battery's specific power lies between that of the ICE and fuel cell, but its specific energy lies far below either of them.

Table 1[a]

Power Source	Specific Energy	Specific Power
Automobile ICE	3.6 kWh/kg	.75 kW/kg
Nickel-cadmium battery	.034 kWh/kg[b]	.40 kW/kg[b]
Hydrogen-air fuel cell	1.2 kWh/kg	.25 kW/kg

[a]Data adapted from Appleby, 1992, except where indicated.

[b]Linden, 1984, p. 17-13.

The specific energy of a fuel cell depends largely on the molecular weight of the fuel and the mass of the storage tanks. While hydrogen has the highest specific energy of any fuel, when the mass of the storage tank is added to the fuel mass, the net specific energy of a hydrogen fuel cell is only 1/3 that of a conventional ICE (see Table 1). The value in Table 1 is for compressed hydrogen gas; the specific energy is even lower (.45 kWh/kg) for metal-hydride storage [Appleby, 1992]. (Cryogenic storage of hydrogen gives a value, 7.2 kWh/kg, twice that of the ICE, but there are practical and economic problems associated with its application [Appleby, 1992].) Thus, liquid fuels such as methanol or ammonia (under moderate pressure) are attractive as fuels because of the high specific energy resulting from lightweight tanks.

The key to specific power in a fuel cell is catalysis. That is, the rate at which the electrochemical reaction takes place, and hence the power output of the cell, is determined by the electrocatalyst. Fuel cells are different in this regard also from batteries. Since a battery has no catalyst, it seems likely that

any battery that will match the ICE in power density, while simultaneously having a practical specific energy, will be based on a highly electroactive anode such as an alkali metal, alkaline-earth metal, or aluminum. Such metals generally preclude aqueous electrolytes and require aprotic solvents, solid electrolytes, or molten salt electrolytes. Aprotic and solid electrolytes have low conductivity, which lowers substantially the potential specific power (see, for example the Na-S battery, which has a specific power of less than .1 kW/kg [DeLuca, et al., 1990]); high-temperature molten salts have excellent conductivity but suffer from corrosion problems and have a relatively long startup time. In contrast, a fuel cell can in principle have its specific power set to any desired value by using a suitably active electrocatalyst. And because the cell kinetics are based on a different principle--catalysis rather than electroactivity of the reactants--the cell can use a cheap, relatively safe, and highly conductive aqueous electrolyte.

The recent extended review by Appleby and Foulkes [1989, p. 233] ranks the common fuel-cell fuels in decreasing order of reactivity as

hydrogen > hydrazine > ammonia > methanol > hydrocarbons.   (1)

Under the same fuel-cell experimental conditions, hydrogen has an oxidation rate about 10,000 times greater than that of methanol and about 100,000,000 times that of hydrocarbons [Appleby, 1992]. Because hydrogen storage requirements result in low specific energy and because hydrazine is expensive and toxic [Appleby and Foulkes, 1989, pp. 235-236], ammonia and methanol are the most reactive of the fuels having the potential to be used in practical traction/propulsion fuel cells. The overall reactions for the two cells are given by equations (2) and (3), and some of the properties of the two fuels are collected in Table 2:

$$4NH_3 \ (g) + 3O_2 \ \longrightarrow \ 2N_2 + 6H_2O \qquad\qquad (2)$$

$$2CH_3OH + 3O_2 \ \longrightarrow \ 2CO_2 + 4H_2O \qquad\qquad (3)$$
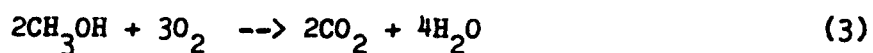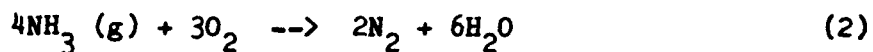
Table 2: Comparison of ammonia and methanol[a]

Property	Ammonia	Methanol
Theoretical specific energy	5.8 kWh/kg	6.1 kWh/kg[b]
Theoretical cell potential	1.17 V	1.21[c]
Theoretical efficiency	88%	97%[c]
Relative cost/MJ	4.5	4.1[d]
Vapor pressure at room temperature	10 atm[e]	< 1 atm

[a]Based on data from Appleby and Foulkes [1989] unless otherwise noted. [b]p. 200; based only on fuel density. [c]p. 18. [d]p .200; gasoline has relative cost of 1.0. [e]Interpolated value from Merck Index [1968].

The research conducted at Seiler Lab in the Summer Research Program, 1993, is the beginning of a long-term research program I am undertaking on practical ammonia fuel cells for vehicular applications. Although methanol compares similarly to ammonia is many respects (see Table 2 above), I am focusing on ammonia for the following reasons:

(1) The products of the reaction (2) are not only completely innocuous but are

also not green-house gases.

(2) Ammonia is more electroactive than methanol.

(3) Ammonia is a simpler molecule than methanol and there is evidence that the anode processes in an ammonia cell are substantially simpler than those in methanol cells. The advantage of this is that the mechanism will probably be more easily elucidated in the case of ammonia, and this can lead to rational development of active electrocatalysts.

(4) Ammonia is virtually nonflammable.

(5) The ammonia cell can use a strong alkali electrolyte, not practical for methanol because of carbonate formation, which has superior cathode kinetics and is less corrosive than an acidic system.

(6) Ammonia is only slightly soluble in concentrated alkali, and this ameliorates the crossover problem—the diffusion of the fuel to the cathode where it is chemically oxidized and therefore wasted.

In comparison to methanol, ammonia has two disadvantages:

(1) Because of its higher vapor pressure, it will require a heavier fuel tank.

(2) Ammonia is a more acute tissue irritant than is methanol. However, unlike methanol, ammonia is not a systemic or metabolic poison (but is a required nutrient and natural metabolite in humans); its pungent odor warns of its presence at concentrations that can be tolerated for hours without ill effect; and its deleterious effects in higher concentrations are generally reversible. Because of its potential irritating effects in the case of vehicle accidents, ammonia may not be suitable for consumer vehicles. Nonetheless, there are large numbers of more regulated vehicles—for example, the ones enumerated at the beginning of this Introduction—of high power rating, for which its use could be entirely practical.

In summary, ammonia fuel cells have the potential of efficiently powering a

large class of high-power rating vehicles without many of the disadvantages of the current ICE-powered vehicles. The central problem to be solved is electrocatalysis.

Results

As a starting point for our ammonia fuel-cell research program, the work of Simons, et al., (1969) and McKee, et al., (1969), all at General Electric, on a high-performance ammonia cell was replicated and improved. The General Electric cell used a porous, conducting electrode constructed by sintering a mixture of finely divided Teflon and the catalyst at 350°C and high pressure [Niedrach and Alford, 1965]. The catalysts examined by the earlier researchers were platinum black, platinum-iridium alloy, and platinum on graphite. The electrolyte was 54% aqueous potassium hydroxide.

The cell constructed at Seiler Laboratory, which used an improved Teflon/nickel/platinum anode described below and in later versions used a pump-driven recirculating electrolyte (54% KOH) subsystem, was operated on both ammonia and hydrogen. On either fuel, the cell will operate a small electric motor driving a propeller. Potential-versus-current performance curves for an early version of the cell, using approximately 250 mg platinum-black in each electrode, are shown in Fig. 1. Consistent with the inequalities (1), the performance of hydrogen is substantially greater than ammonia. Very nearly the theoretical open-circuit potential of 1.23 V for hydrogen/oxygen was observed. However, we never observed an open-circuit potential above 0.7 V for ammonia/oxygen (at approximately 20°C) even though the theoretical value is 1.17 V (at 25°C). This is consistent with the published GE wc : [Simons, 1969], which reported an open-circuit potential of about 0.75 V at 60°C. This low open-circuit potential indicates a high activation overpotential, that is, a relatively low effectiveness

Fig. 1: Performance Curves

Potential (V)

Current (mA)

9-13
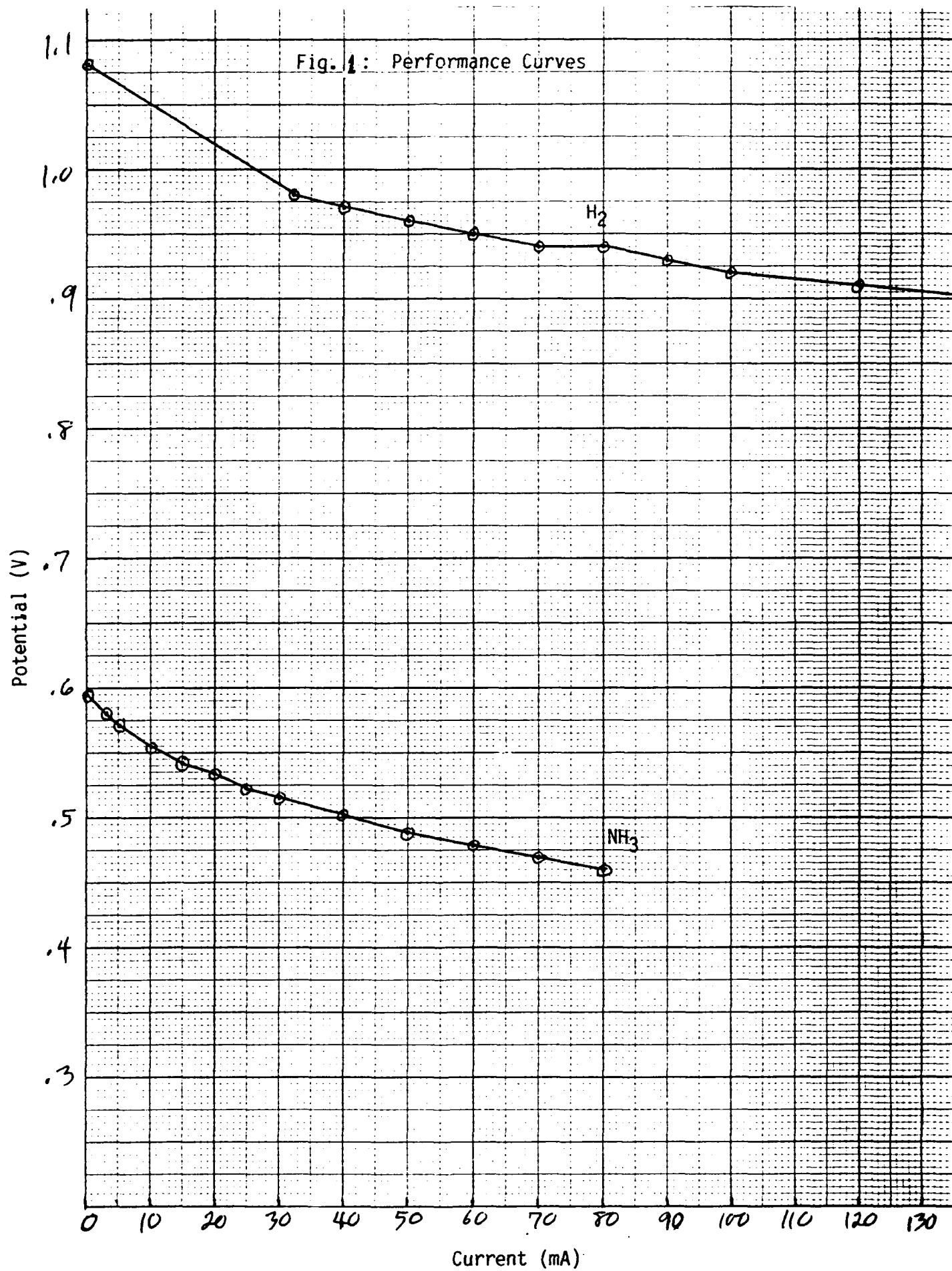
of the electrocatalyst in lowering the activation energy of reaction (2). With a high activation overpotential, we would expect the potential to increase as a function of cell temperature; hence, our cell would probably develop at least 0.75 V at 60°C (see below for planned variable-temperature experiments).

Two improvements in the electrodes were made: (1) My electrodes were prepared from a mixture of Teflon, nickel powder, and the catalyst. The rationale for this is that the nickel, which is essentially inert at the anode, provides strength and thickness to the electrode. The GE workers reported leakage of the electrolyte through their electrodes; however, with our nickel-matrix electrodes, we observed negligible leakage after the electrode had been in the cell for at least four days. (2) In large part because the nickel admixture gives greater catalyst volume, I was able to develop a technique of applying the catalyst mixture directly to the nickel-screen current collectors (rather than use the indirect technique of first applying the mixture to pieces of aluminum foil as described in the literature.) This is a simpler technique and I believe it allows better control of electrode physical dimensions.

Using these techniques, I developed electrodes of Teflon/nickel/platinum-black and Teflon/nickel/platinum-on-carbon. The latter has exceptionally good wetting properties; it will be performance-tested in the near future (see below).

A Teflon/silver cathode was also developed, and it works essentially as well as the Teflon/nickel/platinum-black cathode. This is presumably the case because the current-limiting process of the cell is at the anode. Because silver is much cheaper than platinum, silver powder serves as both catalyst and filler, and hence no nickel is necessary.

This work is continuing and I continue to collaborate with Dr. Carlin at Seiler by visiting the Lab once per week. Work that was largely completed during

my tenure as an SRP faculty associate but which we will incorporate into the research program in the near future are the following: (1) I designed, and have had constructed by the Seiler shop, an improved fuel-cell casing design in which the recirculating electrolyte enters and leaves from the face of the cell and passes through the cell via channels cut into the gaskets. The advantage of this design is that it allows reliable pipe-thread fittings to connect the cell to the electrolyte recirculation subsystem. (2) I designed, and have had constructed by the Seiler shop, a large temperature-controlled air bath in which the fuel cell and electrolyte subsystem can be operated. This is necessary for the accurate study of cell performance because, in a cell with large activation overpotential such as the current ammonia cells, the cell potential will generally be an (increasing) function of temperature. With this apparatus, we can more reliably determine the performance curve for the cell and study the cell performance as a function of temperatures up to about $50^{\circ}C$.

Experimental

Nickel-screen current collectors. Nickel screen (50 mesh with 0.005" wire size), originally manufactured by Metal Weave, Cleveland, OH, was purchased (by Prof. S. Cowley at Colorado School of Mines) from Eltech Research Corporation, Chardon, OH. Disks of 2" diameter and containing a tab of 1/2" by approximately 2" were cut from the nickel screen. These were cleaned by washing with acetone, soap/water, and lightly etching in 5% nitric acid for about 1/2 hr. They were thoroughly rinsed with de-ionized water and distilled water, blotted, and air dried.

Teflon/nickel/platinum-on-carbon electrode. A homogeneou   ure of 1.664 g of nickel powder (Johnson Matthey, 99.9%, 2.2-3.0 micron, catalog number 10255) and 0.333 g of 10% platinum on activated carbon (Aldrich, catalog number 20,595-8) was

prepared. A sample of 1.001 g of this powder was mixed with 0.566 g of 35.3% Teflon suspension, prepared by adding distilled water to a sample of Du Pont Teflon-30 dispersion (also provided by Prof. Cowley), which contained 60.2% Teflon by mass. Additional distilled water was added to the mixture until a gelatinous mass was obtained. (Note: apparently, the platinum catalyzes the polymerization of the Triton X-100 wetting agent in the Teflon suspension to give a gummy mixture.) This was uniformly spread on the nickel-screen current collector, masked with a template of aluminum foil so as to restrict the catalyst mixture to a circle of 1 1/2" diameter in the center of the 2" disk. The electrode was air-dried and dried on a hot plate at about 150°, heated on a hot plate at $350^{o}C$ for 2 min (to expel any remaining Triton), and wrapped in aluminum foil, which was lubricated with alumina (see below). The assembly was pressed as described below. The aluminum foil was dissolved in 20% potassium hydroxide, and the resulting electrode was thoroughly rinsed with de-ionized water, lightly scrubbed with a paper wipe, rinsed with distilled water, and dried.

An additional 1.001 g of the dry catalyst mixture was mixed with 1.989 g of 10.1% Teflon suspension and spread on the s   side of the electrode using the same technique used on the first side above. (Alternatively, the 35.3% suspension as above could have been used; no additional water is necessary with this more dilute suspension.) The electrode was air died and further dried on the hot plate (estimated temperature of $150^{o}C$).

A thin Teflon film was placed on this (second) side of the electrode; it will become the gas-side of the electrode in the final cell [Niedrach and Alford, 1969]. A 5 X 5" square was drawn on the shiny side of a piece of aluminum foil with a black marker. The electrode was taped inside of the square, and 0.356 g of 10.1% Teflon suspension was uniformly sprayed over the area of the square with an air brush (Badger model 100-GXF); the Teflon suspension was weighed directly into

the cup of the air brush.

The electrode was heated on a hot plate at approximately $350^{\circ}C$ for 2 min; some white fumes (Triton) were observed. The uncovered nickel screen around the periphery of the electrode (the region beyond the 1 1/2" diameter catalyst region) was covered with Teflon pipe-thread tape, which when fused in the press acts as a seal. The electrode was pressed and worked up as previously to give a complete electrode.

Silver electrode. The electrode was prepared analogously to the platinum-on-carbon electrode described above. 2.000 g of silver powder (Atlantic Equipment Engineers, 1-5 micron) and 0.666 g of 60.2% Teflon suspension were used on the first side, and 0.999 g of silver powder and 0.332 g of 60.2% Teflon suspension on the second.

Platinum-black electrode. At least six of these were constructed during the course of the work. However, because the techniques were being developed, none of the actual procedures would lend itself to a recipe. From my experience, I can recommend the following as a procedure to give a practical electrode: Use a total of 0.300 g Platinum black, 2.70 g of nickel powder, and 1.70 g of 35.3% Teflon suspension (i.e., the Teflon is 20% by mass of the total metal mass), and otherwise follow the silver-electrode procedure.

Pressing operation. The general procedure is as follows: The electrode to be pressed is covered with aluminum foil lubricated with alumina to prevent its sticking to the anvils. (A slurry of alumina in water is applied as a thin coating with a spatula and then dried on the hot plate.) The anvils are disks of 416 stainless steel having a diameter of about 2 1/8" and thickness of 1". They contain a radial hole into which a thermocouple probe can be inserted and are covered on their working faces with a thin sheet of nickel metal. (The nickel sticks less to the aluminum foil than does the bare stainless steel.) The anvils

are heated in an oven to 410°C. After being insulated with strips of glass cloth, they are placed in the platens of a Carver (Model C) press. When the temperature of the lower anvil drops to 385°C, the aluminum-foil covered electrode assembly is placed between the anvils, and a gauge pressure of 6000 lb is applied. (This would correspond to an approximate average pressure of 2000 lb/in^2 for the 2" electrode disk; however, the disk is not homogeneous.) The pressure is applied for 2 1/2 min, during which time the temperature of the lower anvil falls from about 380°C to 350°C.

Discussion

We have successfully constructed an ammonia fuel cell that compares favorably with an ammonia cell reported in the literature. It readily operates a small electric fan. The performance curve (Fig. 1) indicates that the cell suffers from a very high activation overpotential, which means that the catalyst is not very effective in lowering the activation energy for reaction (2). While the cell constructed would be practical for running low-power applications (for example, a radio), it is not practical, as is, for vehicular applications: The specific power is too low and the cost of the precious-metal catalyst required to drive a vehicle would be prohibitive.

Our limited objective in constructing this cell was to establish a baseline of performance for ammonia fuel cells. The long-term goal of our research program is to develop a highly active yet inexpensive anode catalyst for ammonia-fueled traction/propulsion fuel cells. Our near-term objective, which will be continued at Seiler Lab and then transferred to Colorado School of Mines when external funding is obtained, is as follows:

(1) We will construct several additional electrodes, including

platinum-on-carbon of varying platinum loading, palladium -on-carbon, pure

Teflon-bound nickel (as a control electrode), and possibly platinum-iridium alloy

[McKee, 1969] and platinum-ruthenium alloy [Gliner and Moser, 1972]. The

performance curves at controlled but variable temperatures will be determined.

(2) Since it is laborious to construct the performance curve for a fuel cell,

we want to correlate the performance curve with the cyclic voltammogram of the

anode. This technique would allow rapid testing of proposed catalysts.

(3) We will begin kinetic and mechanistic studies of the chemical and

electrochemical processes occurring at the anode of the ammonia cell. A small

amount of work on this subject has been reported in the literature [Despic, et al.,

1966]. The purpose of this work will be to elucidate the mechanism of the

processes occurring at the anode and thereby allow the rational design of active

catalysts.

References

D. R. Adams, P.-Y. Cathou, R. E. Gaynor, R. D. Jackson, Jr., J. H. Kirsch, L.
   L. Leonard, G. S. Lockwood, Jr., W. P. Warnock, and R. E. Wilcox, Jr.,
   Fuel Cells: Power for the Future, Fuel Cell Associates, Cambridge, MA,
   1960.

A. J. Appleby and F. R. Foulkes, Fuel Cell Handbook, Van Nostrand Reinhold,
   New York, 1989.

A. J. Appleby, "Fuel Cell Technology and Innovation," Journal of Power
   Sources, 37, 223-239 (1992).

V. S. Bagotzky and A. M. Skundin, Chemical Power Sources, Academic Press,
   New York, 1980.

Cameron, D. S. "World Developments of Fuel Cells: Major Opportunity for
   Platinum Electrocatalysts," Platinum Metals Rev, 34, 26-35 (1990).

W. H. DeLuca, A. F. Tummillo, J. E. Kulaga, C. E. Webster, K. R. Gillie, and R. L. Hogrefe, "Performance Evaluation of Advanced Battery Technologies for Electric Vehicle Applications," Proc. 25th InterSoc. Energy Conv. Engr. Conf., Vol.3, American Inst. of Chem. Engineers, New York, 1990, pp. 314-319.

A. R. Despic, D. M. Drazic, and P. M. Rakin, "Kinetics of Electrochemical Oxidation of Ammonia in Alkaline Solution," Electrochemica Acta, 11, 997-1005 (1966).

G. H. Drury, "Russian Railroading, Close Up," Trains, 52, 58-63 (1992).

J. D. Giner and J. R. Moser, "Electrochemical Cell with Platinum-Ruthenium Electrode and Method of Using with Ammonia," U.S. Patent 3,650,838, March 21, 1972.

D. Linden (Ed.), Handbook of Batteries and Fuel Cells, McGraw-Hill, New York, 1984.

D. W. McKee, A. J. Scarpellino, Jr., I. F. Danzig, and M. S. Pak, "Improved Electrocatalysts for Ammonia Fuel Cell Anodes," J. Electrochem. Soc., 116, 562-568 (1969).

L. W. Niedrach and H. R. Alford, "A New High-Performance Fuel Cell Employing Conducting-Porous-Teflon Electrodes and Liquid Electrolytes," J. Electrochem. Soc., 112, 117-124 (1965).

E. L. Simons, E. J. Cairns, and D. J. Surd, "The Performance of Direct Ammonia Fuel Cells," J. Electrochem. Soc., 116, 556-561 (1969).

U.S. Department of Commerce Report, "The Automobile and Air Pollution: A Program for Progress, Part II," U.S. Government Printing Office, Washington, D.C., 1967.

C. A. Vincent, Modern Batteries: An Introduction to Electrochemical Power Sources, Edward Arnold, London, 1984.

ELECTRIC FIELD INDUCED SECOND HARMONIC GENERATION IN GERMANIUM DOPED

SILICA PLANAR WAVEGUIDES

Ulf L.Österberg

Peter S.Weitzman

Thayer School of Engineering

Dartmouth College

Hanover, NH 03755

ELECTRIC FIELD INDUCED SECOND HARMONIC GENERATION IN GERMANIUM DOPED SILICA PLANAR WAVEGUIDES

Ulf L.Österberg
Peter S. Weitzman
Thayer School of Engineering
Dartmouth College

Abstract

Frequency doubling in germanium doped silica planar waveguides deposited on fused silica substrates is studied. It is demonstrated that an externally applied, periodic DC field can cause instantaneous frequency doubling in these waveguides. The periodicity which causes frequency doubling corresponds to the beat length between fundamental and second harmonic light propagating in the waveguide. A current has been measured from these periodic electrodes which corresponds to the generation of a periodic DC field internal to the glass when illuminated with both fundamental and second harmonic light.

ELECTRIC FIELD INDUCED SECOND HARMONIC GENERATION IN GERMANIUM DOPED SILICA PLANAR WAVEGUIDES

Ulf L.Österberg

Peter S. Weitzman

Introduction

Efficient frequency doubling of 1.064nm radiation was first observed in germanium doped silica fibers in 1986 [1]. Recently this has also been achieved in planar dielectric waveguides made from the same materials [2]. Second harmonic generation (SHG) in amorphous materials is interesting due to the fact that the second order susceptibilty, $\chi^{(2)}$, is zero. There have been several theories proposed to explain this phenomenon [3,4,5,6]. All of these theories are based on Stolen and Tom's original hypothesis that an internal DC electric field is responsible for an effective $\chi^{(2)}$ and that the periodicity of this field provides the quasi phase matching necessary for efficient SHG [7]. Assuming that phase matching has been achieved, the conversion efficiency is dependent on the overlap integral between the fundamental and second harmonic optical fields and the DC electric field, which is given by the equation

$$\eta \propto \left| \chi^{(3)} \iint E_{DC} E_{\omega} E_{\omega} dA \right|^2 \tag{1}$$

where η is the conversion efficiency and the integral is over the transverse cross section of the waveguide. This effect has been studied extensively in fibers, however the planar waveguide geometry provides easy access to the core region of the waveguide where this internal electric field can be modified and probed.

In 1975, Levine and Bethea [8] applied a periodic electric field to a liquid planar waveguide. In 1989, Kashap [9] applied an external periodic DC field to the exposed core of an optical fiber and was able to induce SHG. In this paper we present results of using a similar technique on a planar dielectric waveguide. We have applied a periodic electric field to the planar waveguide and observed SHG and have also applied both 1.064 micron (IR) and 0.532 micron (green) radiation simultaneously to a planar waveguide and observed the buildup of the internal electric field by monitoring the current in the periodic electrode structure.

In order to provide the correct periodicity for quasi phase matching, the nonlinearity must be strong only at points where the fundamental and second harmonic are in phase. This periodicity, Δz is given by the expression

$$\Delta z = \left| \frac{2\pi}{2\beta_\omega - \beta_{2\omega}} \right| \tag{2}$$

where β_ω is the propagation constant for the IR light and $\beta_{2\omega}$ is the propagation constant for the green light. The planar waveguide geometry provides a simple means for determining these propagation constants by prism coupling. Figure 1 Illustrates the geometry of the planar waveguide and coupling prisms. The propagation constants are determined from the internal prism angles by the equation

$$\beta = n_p k_0 \cos\theta_p \tag{3}$$

where n_p is the prism refractive index, θ_p is the incidence angle of the light internal to the prism and k_0 is the optical wavenumber in free space. These propagation constants can also be determined from knowledge of the film thickness and refractive index by solving the appropriate

10-4

eigenvalue equation [10]. The same eigenvalue equation can also be used to determine the film thickness and index of refraction from the observed coupling angles for a number of modes in the waveguide.

Methodology

The waveguides used to obtain the results in this paper were fabricated using argon ion beam sputtering of silica and germanium onto commercial, optical grade fused silica substrates. The sputtering rate was 0.11nm/sec in a partial pressure of 10^{-4} Torr of oxygen. The two films used in this study were approximately 2.0 and 3.5 microns thick. Auger analysis indicated that the GeO_2 content of the films was approximately 6m%. The refractive index of the substrate is 1.4607 at 0.532μm and 1.4496 at 1.064μm. The refractive index of the film was measured to be 1.546 at 0.532 μm and 1.532 at 1.064μm using the prism coupling method.

Figure 2 illustrates the geometry of the planar waveguide used along with the periodic electrode structure mounted on the surface of the waveguide. This waveguide/electrode combination is mounted in the setup illustrated in figure 3. Some of the output from a Q switched, mode locked Nd:YAG laser is frequency doubled in a KTP crystal, subsequently the Fundamental and SH beams are separated into two paths. Using this technique, the input coupling angle of the two wavelengths can be adjusted independently, as can their power levels, polarization and relative phase. The disadvantage of separating the beams is that the slight relative phase fluctuations between the paths can wash out the grating as it is forming using the seeding technique [11]. Despite these phase fluctuations, we have still been able to prepare these films for SHG. The output SH signal is detected with a photomultplier and averaged with a boxcar integrator. Typically 3000 q-switched pulses are averaged and read by the computer.

We have performed two different types of experiments. In the first experiment, the voltage source is applied to the electrode structure, only IR light is coupled through the waveguide and the angle of the electrodes with respect to the optical path is varied in order to optimize the detected SH signal. By adjusting the angle of the electrodes, the effective periodicity can be modified. Once the SH signal is optimized, the SHG is measured as a function of applied voltage.

In the second experiment, the optimized electrodes are kept in place but they are connected to an electrometer capable of measuring current as low as 100aA. The waveguide/electrode assembly and associated wires are placed in a metal box to shield them from electromagnetic interference. At this point, both IR and green light can be coupled simultaneously into the waveguide. Care was taken to insure that they travel along the same region of the waveguide. The current induced in the electrodes is measured by the electrometer as a function of the propagation of various optical frequencies within the waveguide.

Results

Using equation (2) it was determined that the quasi phase matching period for the 3.5μm waveguide is 26.7 μm and for the 2μm waveguide it is 20.2 μm. This was for the lowest order TM mode in both the green and IR. The TM modes were used due to the fact that more efficient SHG has been observed in these modes. (2) We chose to use the lowest order modes because they have the largest overlap integrals with the applied DC field. We found the greatest SHG on the 3.5 micron thick waveguide using an electrode structure with a 26μm periodicity rotated 7.9 degrees to the optical path. This provides an effective electrode periodicity of approximately 26.25μm, very close to what we calculated using equation (1). The maximum SHG with 50 volts applied across the electrodes was a visible green spot at the correct angle to indicate that it was in the TM_0 mode. The power produced by the SHG was strongly dependent on the periodicity of the waveguide. A rotation of less than 1 degree from the optimum caused a 90% decrease in the SHG produced.   With the

electrode periodicity fixed at 7.9 degrees the SHG was measured as a function of applied voltage (Fig 4). The observed quadratic dependence of the electric field induced SHG is expected due to the dependence of the conversion efficiency on the square of the electric field in equation 1 .

We were also able to generate a signal in the TM_2 mode in this film by changing the electrode periodicity to $70\mu m$, close to the calculated Δz value for this mode. The data for SHG in the TM_2 mode vs applied voltage is plotted in figure 5. It is several orders of magnitude lower than what was observed for the TM_0 mode. We also tried to generate the TM_1 mode but were unable to see any signal. This is expected due to the cancellation in the overlap integral. We also tried to produce SHG with the input light in the TE_0 mode, and the electrodes aligned to produce quasi phase matching between the TE_0 modes in IR and green. For this configuration, no SHG was observed. This is most likely due to the fact that the applied electric field was almost perpendicular to the electric field of the optical modes.

With the electrodes optimized for quasi phase matching the TM_0 mode, we disconnected the voltage source and connected the electrometer to the electrodes. We then measured the current induced into the electrodes with both the IR and green light coupled into the film, the IR only, the green only, and no light. The measured current changed with time at a rate which was dependent on the coupling of light through the waveguide. With no light present, an increasing current was detected, due to the discharging of the electrodes through the electrometer. When a combination of both IR and green light was coupled through the waveguide, the current was obsevred to decrease. When only green or IR alone was coupled in, the current increased. This data is plotted in figure 6.

One of the problems with the current measurement is that the green and the IR beams are separated in our experiment, see fig.3. The reason for the two paths is so that we can independently manipulate the two wavelengths for optimum input coupling. Unfortunately, the two different optical paths results in random phase fluctuations between the green and IR, severely reducing the

10-7

signal-to-noise ratio for the current measurement. By going to thinner waveguides (< 2µm) we would be able to couple in green and IR at the same angle making it unnecessary to split up their paths. Thinner waveguides means that the periodicity Δz, equation 2, will be smaller and subsequently we require masks with finer periodicity. Testing masks with 19 µm and 14 µm periodicity reveals that these masks have two and four orders of magnitude lower resistivity, respectively, compared to the 26 µm masks. These lower resistivities were believed to be due to inadequate etching. A result of these lower resistivities was a much less well-defined electric field under the periodic electrodes, resulting in a much smaller and noisier EFISH signal, see fig.7.

Discussion

We have presented a device consisting of a germanium doped glass waveguide and a periodic electrode structure which is capable of instantaneously frequency doubling light. We have demonstrated that a periodic DC electric field is capable of inducing this frequency doubling in glass if the periodicity is correct for quasi phase matching. We have been able to selectively excite different modes in the SH by varying the electrode periodicity. The efficiency of the electric field induced SHG is greatly reduced for higher order modes. This can be explained by examining the overlap integrals involved. The conversion efficiency is determined by the overlap integral in equation 1.

The three lowest order modes and the electric field distribution in the waveguide are illustrated in figure 8. From this figure, it is observed that the positive and negative lobes in the higher order modes will cancel out when integrated across the applied electric field. The applied field does decrease as the distance from the electrodes is increased. This will result in a slightly nonzero overlap integral for the first order mode, however the separation between the electrodes is much larger than the film thickness so the change in electric field across the film is less than 10% based on the conformal mapping calculation presented by Ramer [12].

The observation of a decreasing current when both the fundamental and SH light are propagating through the waveguide, and an increasing current when only fundamental or only SH light is sent through strongly supports the SHG models which rely on the buildup of a DC field in the glass. When no light is present, a current was observed to flow due to the charging of the electrodes by the electrometer. When a combination of green and IR is present, the buildup of an internal electric field in the glass causes a current to flow in the electrodes which opposes the existing current and the total current is observed to decrease.
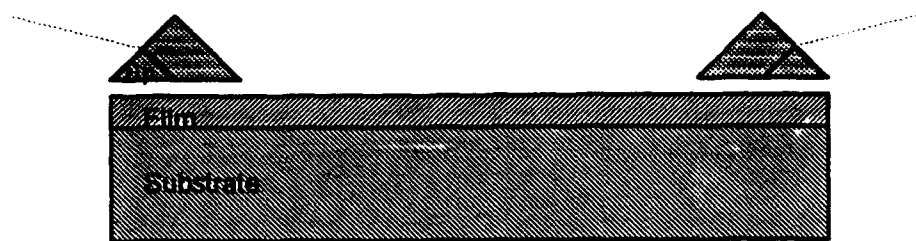
Figure 1. Planar waveguide geometry with prism coupling
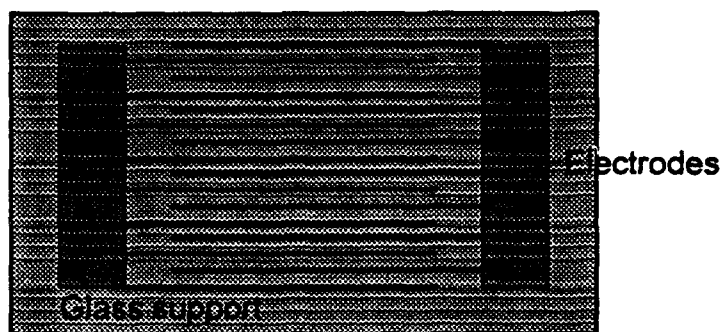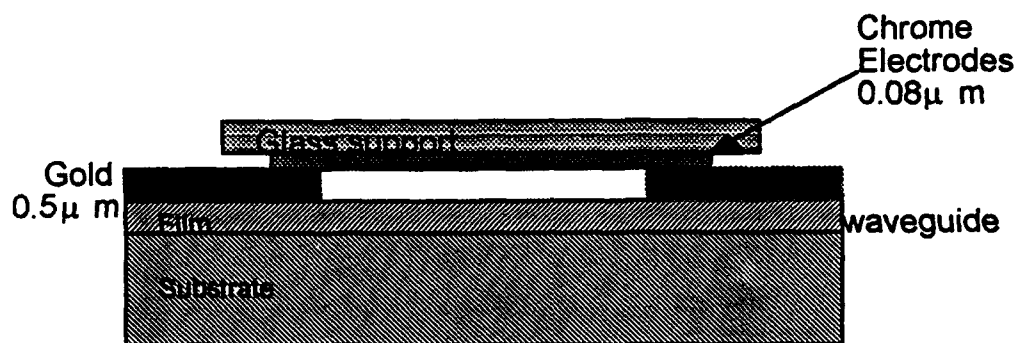
Figure 2. Planar waveguide with periodic electrode structure
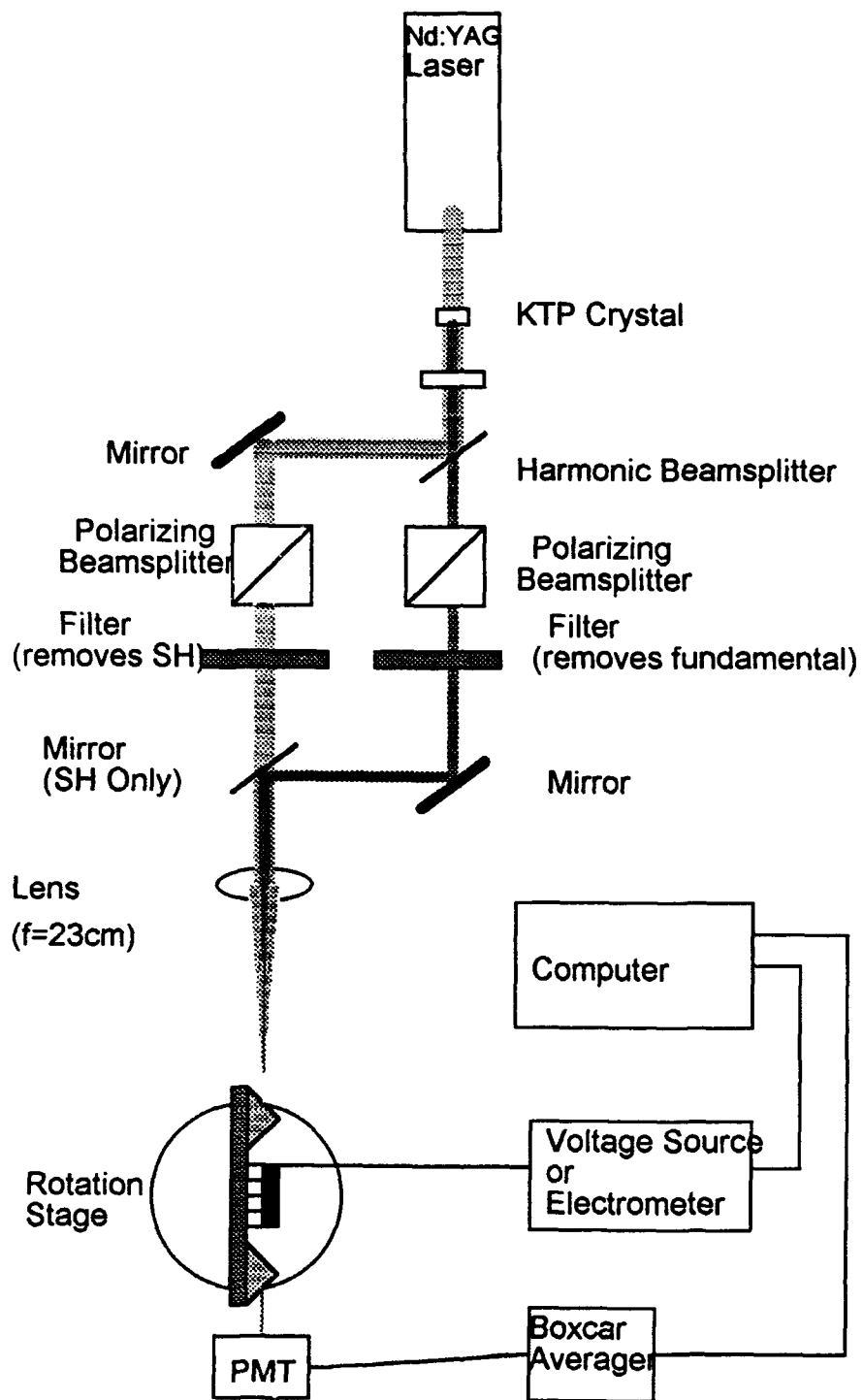
Figure 3. Experimental setup
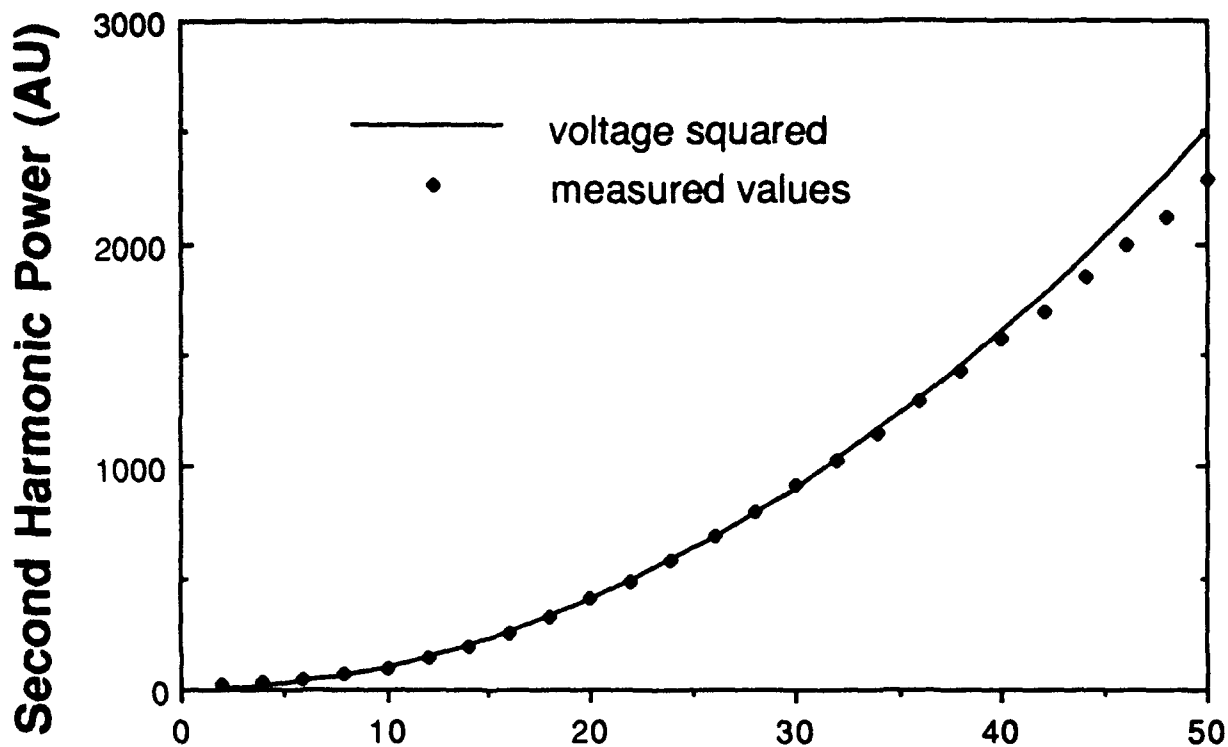
Figure 4. Generated second harmonic as a function of applied voltage. The input IR is in the TM_0 mode and the output green is detected in the TM_0 mode.
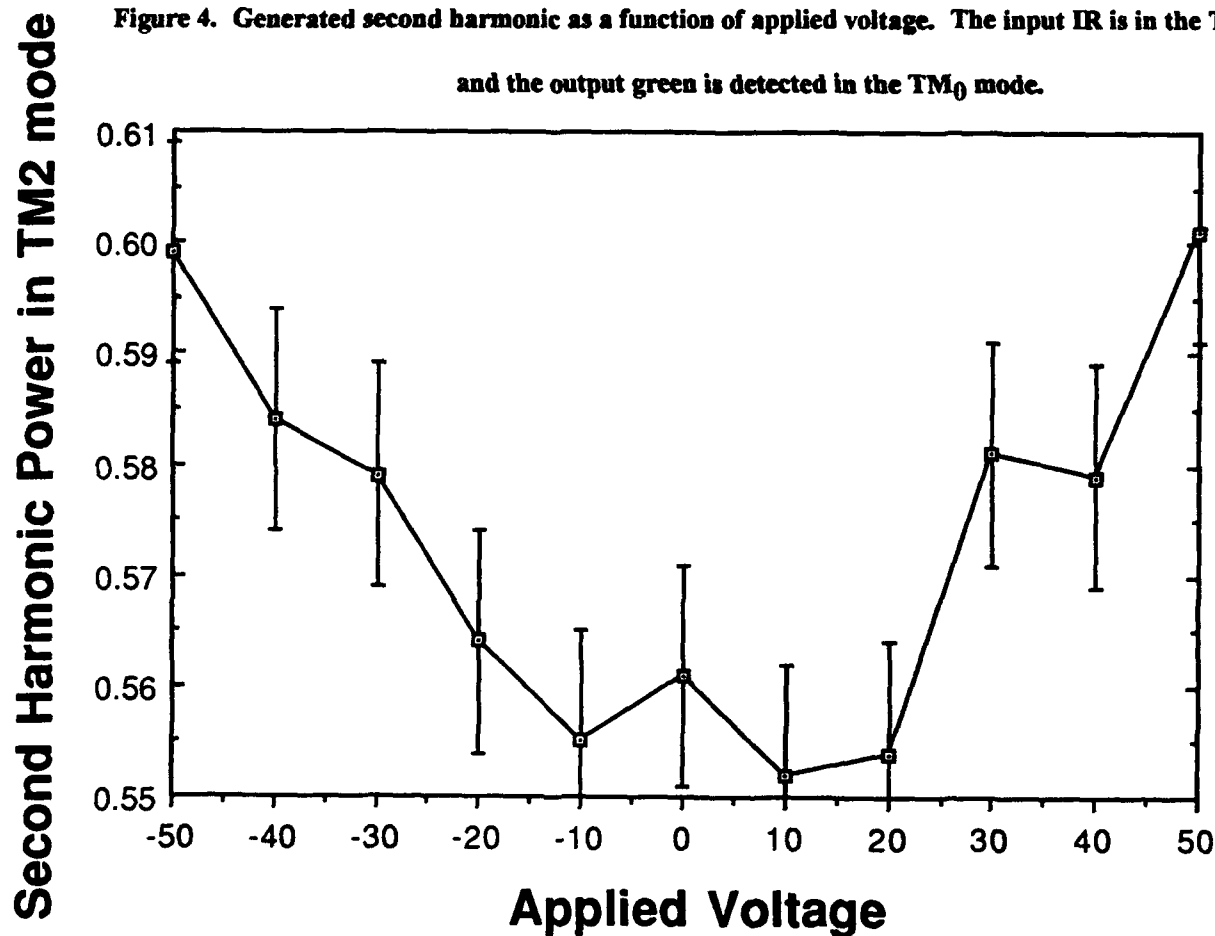
Figure 5. Generated second harmonic as a function of applied voltage. The input IR is in the TM_0 mode and the output green is detected in the TM_1 mode.
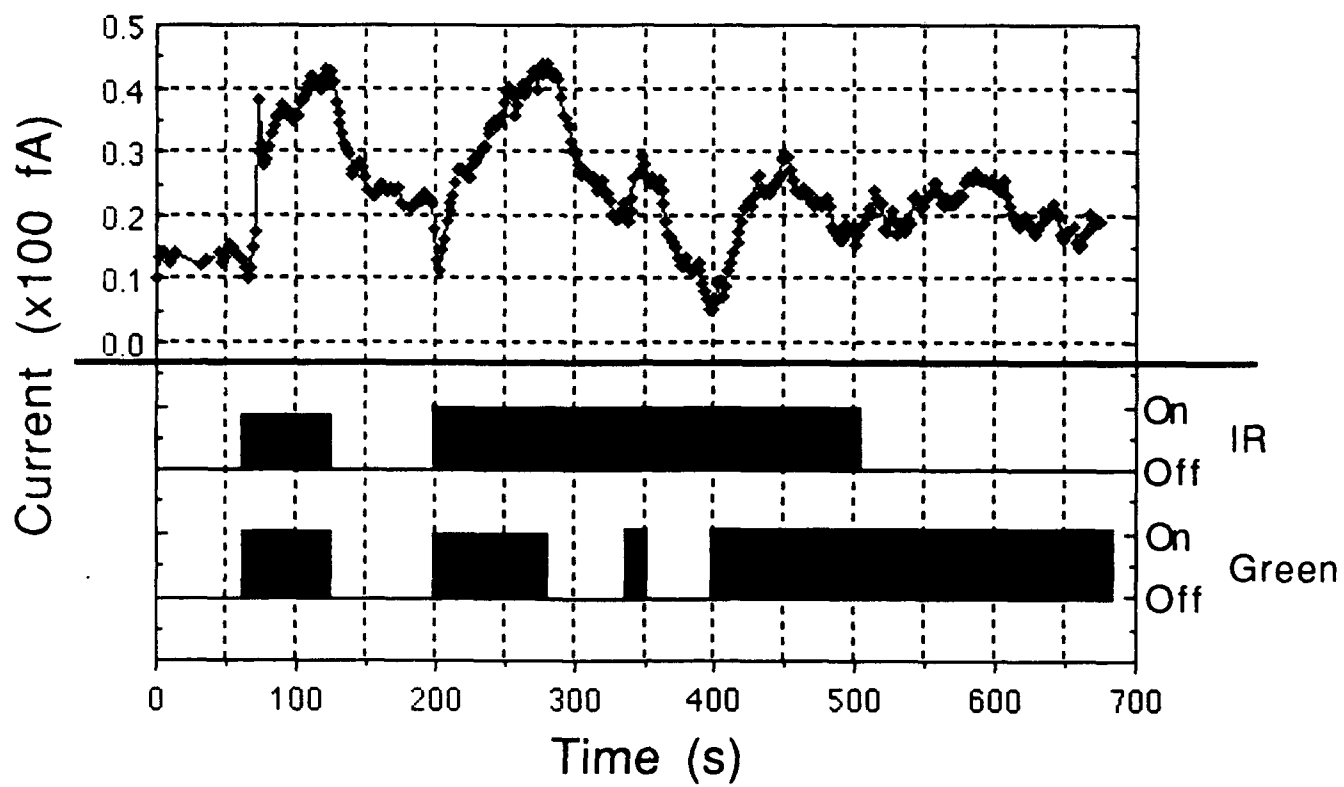
Figure 6. Effect of coupling in fundamental, SH, and both simultaneously on the current induced in the periodic electrode structure.
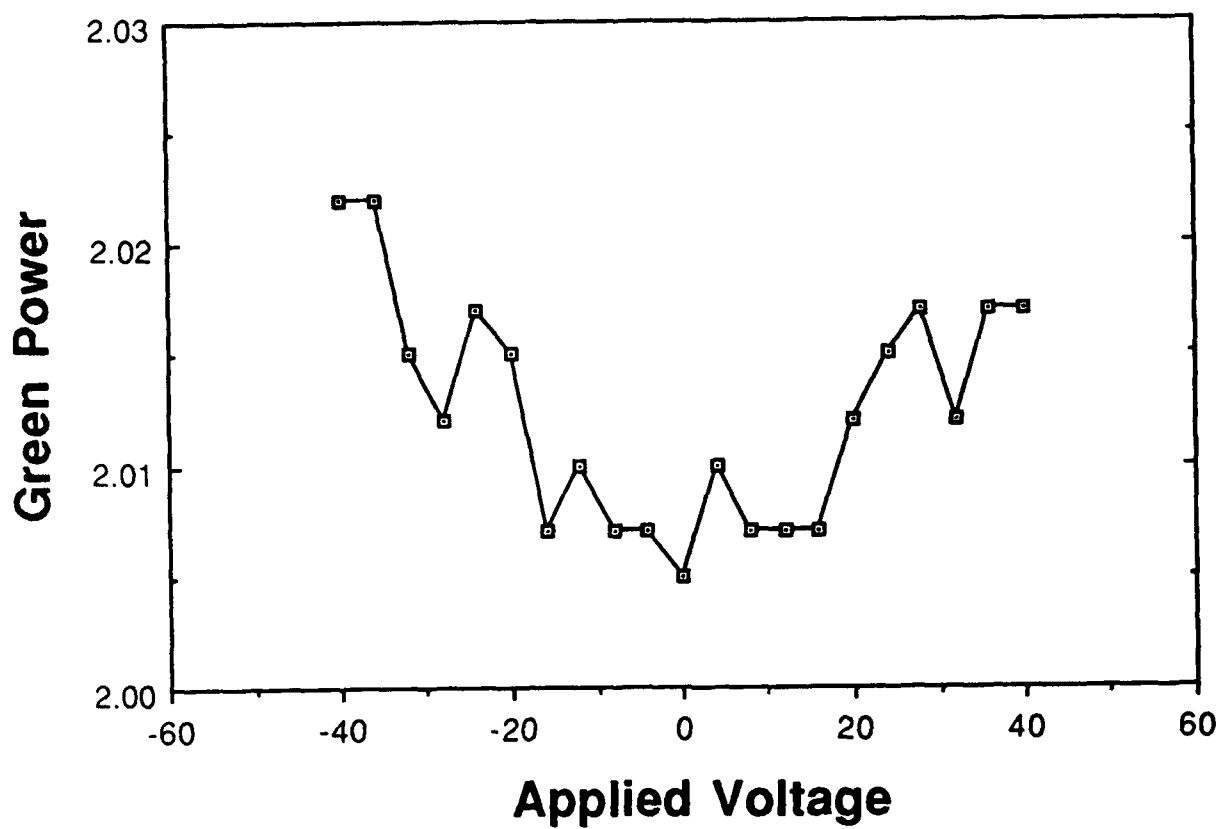
Figure 7. EFISH signal from a 1.9 μm waveguide and a 19 μm periodicity mask.
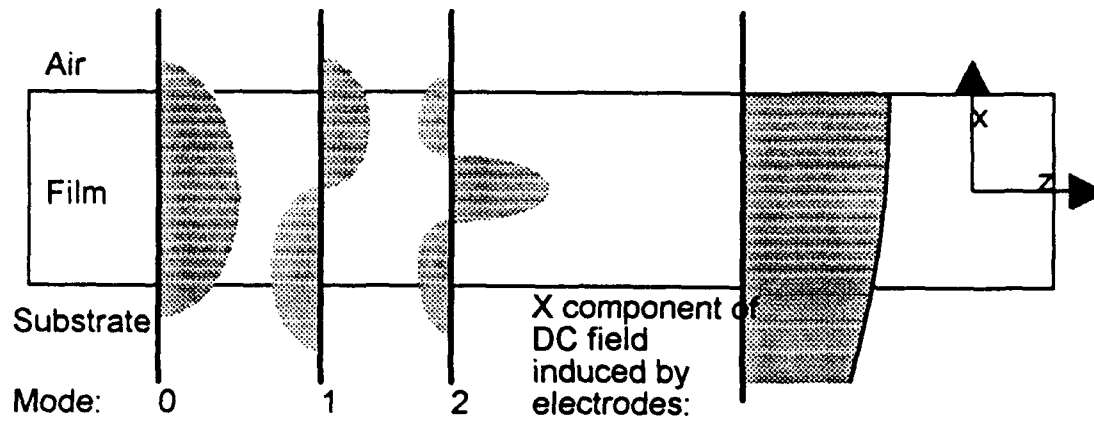
Figure 8. Electric field distributions in the waveguide for optical and applied DC fields.

1. U. Osterberg and W. Margulis, Opt. Lett. **11**, 516 (1986).

2. J. J. Kester, P. J. Wolf and W. R. White, Opt. Lett **17**, 1779 (1992).

3. D. Z. Anderson, V. Mizrahi and J. Sipe, Proc. Soc. Photo-opt. Instrum. Eng. **1516**, 154 (1991).

4. E. M. Dianov, P. G. Kazansky and D. Y. Stepanov, Soviet Lightwave Communications **1**, 381(1991).

5. N. M. Lawandy, Optics Communications, **74** 180 (1989).

6. M. C. Farries, P. St. J. Russel, M. Fermann and D. N. Payne, Electronics Letters. **23**, 322(1987).

7. R. H. Stolen and H. W. K. Tom, Optics Letters, **12**, 585(1987).

8 B. F. Levine and C. G. Bethea, J. Chem. Physics, **63**, 2666(1975).

9. R. Kashap, J. Opt. Soc. Am. B, **6**, 313(1989).

10. B. E. A. Saleh and M. C. Teich, *Fundamentals of Photonics.* (John Wiley, New York, 1991).

11. D. M. Krol, M. M. Broer, K. T. Nelson, R. H. Stolen, H. W. K. Tom and W. Pliebel, Opt. Lett. **16**, 211(1991).

12. O. G. Ramer, IEEE J. Quant. Elec. **18**, 386(1982).

NONLINEAR OPTICAL PROPERTIES OF THE [GEO₄] CENTERS IN SILICA

Ravindra Pandey

Assistant Professor
Physics Department, Michigan Technological University, Houghton, MI 49931.

August 1993

Nonlinear Optical Properties Of The [GeO$_4$] Centers In Silica

Ravindra Pandey
Assistant Professor
Physics Department, Michigan Technological University, Houghton, MI 49931.

ABSTRACT

Semi-empirical PM3 calculations are performed on the Ge centers in Silica using a cluster approximation in the Hartree-Fock framework. We simulate Ge-doped Silica as a cluster consists of a GeO4 unit together with its four nearest SiO4 units. Electron trapping does distort the local symmetry of the Ge center where the GeO4 unit is not exactly tetrahedral. The calculations of the microscopic NLO properties in terms of static hyperpolarizabilities show a large, noticeable increase in β related to second-harmonic generation or Kerr effect for the Ge(1) center upon electron trapping.

Nonlinear Optical Properties Of The [GeO$_4$] Centers In Silica

Ravindra Pandey

I. INTRODUCTION :

It has been well-known that various point-defects play an important role in the optical behavior of silica-based glasses.[1-2] These point-defects have been identified via correlation of the radiation-induced optical absorption and the ESR technique.[3-4] Specifically, the isoelectronic impurity Ge in silica is found to trap either electron or hole thereby forming anionic or cationic centers in the network. For the anionic centers, spin resonance studies have suggested that the electron trapping occurs at the four-coordinated Ge substituting Si.[4-5] This has also been the case in the crystalline α-quartz where Weil and coworkers[6-8] have reported two kinds of paramagnetic centers, referred to as Ge(I) and Ge(II). These centers are proposed to be energetically inequivalent configurations of the Ge^{3+} center which is formed by trapping of an electron by the substitutional Ge^{4+} ion in the lattice. For the cationic case, the analysis of hyperfine splitting arising from ^{73}Ge in silica glass has identified a hole trapping center, referred to as GeE' which consists of an oxygen vacancy with a nearest-neighbor Ge.[4]

These point-defects associated with the Ge center has been linked with the observation of frequency-doubling effect in optical fibers. For example, Tsai et al.[9] have reported a correspondence between the strength of the second-harmonic generation (SHG) and the formation of GeE' centers in Ge-doped silica fibers. Surprisingly, on the theoretical front, rather little work has been performed to explore the relationship between the Ge centers and their non-linear optical (NLO) properties.

We have embarked upon such a theoretical project to provide a microscopic view of the Ge centers in Silica using well-established quantum chemistry techniques. Our aim will be to understand the origin of the NLO effects in Ge-doped Silica at the molecular level by performing hyperpolarizability calculations that are related to the microscopic NLO properties. In the primilinary work reported elsewhere, we have shown that the cluster configuration induced by the presence of a defect plays a significant role in determining the non-linear response of the Si(OH)4 and Ge(OH)4 clusters.[10] In the present paper, our efforts will be focused on the Ge

centers acting as electron traps in Silica. It is to be noted here that earlier theoretical studies[11-12] were focused on providing a qualitative explanation of Ge being an electron trap in α-quartz.

In the following section we describe briefly the computational model. The calculated results including structural configuration. spin populations and non-linear optical properties are compared and discussed with the corresponding experimental results in Sec. III.

II. COMPUTATIONAL MODEL :

Our computational model simulates Silica (pure or imperfect containing defects such as Ge) by a cluster of atoms with appropriate boundary conditions assuming that cluster wave function is well localized. We consider a cluster consists of a GeO4 unit together with its four nearest SiO4 units (Fig. 1). This is based on the fact that the various forms of SiO2 (either crystalline or amorphous) are known to share a similar short-range order, consistent with the chemistry of the Si-O bond[13] : each Si atom is coordinated (nearly) tetrahedrally with four O neighbors, and each O atom has two Si neighbors with a Si-O-Si angle of about 150⁰. In this cluster, each oxygen atom at the cluster boundary is attached to a hydrogen atom to suppress the so-called surface effects arising from the dangling bonds of outermost atoms.[14] For calculations, we use a molecular orbital program package, MOPAC employing the semi-empirical Hamiltonian PM3.[15]

To judge the predictability of semi-empirical PM3 calculations, we first consider a smaller cluster consisting of a single GeO4 unit. This smaller cluster facilitates *ab initio* calculations which are more demanding for computational resources. The program package, GAMESS[16] is used for *ab initio* calculations in the Hartree-Fock (HF) approximation. Here, the molecular orbitals associated with the cluster atoms are described with the double-zeta valence (DZV) Gaussian basis sets. The DZV basis set consists of 6s and 4p Gaussian functions (i.e. 531111/4211) for Si, 6s, 4p and d (i.e. 821111/6311/5) for Ge, 3s and 2p (i.e. 721/41) for O and 2s (i.e. 3/1) for H.[16]

Table 1 shows the results of (semi-empirical) PM3 and (ab initio) HF-DZV calculations for Si(OH)4 and Ge(OH)4 clusters. It appears that both the calculations do indeed yield the similar cluster configurations indicating the reliability of the semi-empirical approach employed here.

III. RESULTS and DISCUSSION :

A. Structural Configuration :

The results of PM3 calculation on the 33-atom cluster (i.e. X(OSi(OH)3)4, X=Si or Ge) are given in Table 2. It shows the geometric parameters, namely the bond-length and the bond-angles of the optimized configurations of both pure and Ge-doped cluster. For the pure cluster, the results reproduce the C_2 symmetry of the SiO4 unit. This symmetry is observed in α-quartz with two sets of Si-O bonds, called long bond ($R_>$) of 1.614 Å and short bond ($R_<$) of 1.610 Å. The calculated values of R> and R< are 1.660 and 1.658 Å respectively in the pure cluster. Thus it appears that the PM3 calculation overestimates the bond-length by about 3% as compared to the experiment. The calculated O-Si-O and Si-O-Si bond-angles come out to be in the range 108-111⁰ and 136-139⁰ respectively. The corresponding experimental values in α-quartz are about 109⁰ and 143⁰ respectively.

When we substitute Ge for Si in the cluster retaining the twofold symmetry, the impurity Ge introduces an outward relaxation of about 7%, 4% and 2% of first-neighbor oxygens, second-neighbor silicons and third-neighbor oxygens respectively. This is what we expected due to relatively larger ionic radius of Ge^{4+} in comparison to that of Si^{4+}.

For the case of the anionic [GeO4]- center, the calculated results predict its stability (with respect to the neutral center) in the network by about 1 eV. Atomic charges associated with the cluster atoms (given in Table 3) indicate that the excess electron is trapped essentially by the Ge ion resulting in the C_1 symmetry of the ground state. In the optimized configuration, the nearest-neighbor oxygens are found to relax outwardly by about 3% (Table 2).

Since amorphous and crystalline SiO2 have similar short-range order, we now compare the results with electron paramagnetic resonance studies (EPR) of Ge-doped α-quartz. Weil and coworkers[6-8] have identified two types of Ge electron centers, referred to as Ge(I) and Ge(II) in α-quartz. Assuming that the GeO4 unit substituting for the SiO4 unit has a similar structure, they have determined the local symmetry of these centers as C_1 and C_2 respectively from the analysis of hyperfine splitting arising from [73]Ge and [17]O. Our calculated results do agree with the EPR results in assigning the ground state of the anionic [GeO4]- center predicting that about half of the spin population is located on the Ge atom (Table 4). However, a disagreement appears with the experiment for the spin populations of nearest-neighbor oxygens. Our calculations indicate that only one of the nearest-neighbor oxygens has rather large spin populations whereas the experimental analysis suggest large spin populations on two of the nearest-neighbor oxygens. It is to be noted here that the calculated spin populations on nearest-neighbor oxygens for the

11-5

Ge(II) center do show the presence of two symmetry-related pairs (Table 4) as also indicated by the experimental analysis.

B. Nonlinear Optical Properties :

We note here that the non linearity effect in a dielectric medium may be of microscopic or macroscopic origin. The polarization density $P = N \mu$ is a product of molecular dipole moment μ and the number of density of dipole moments N. The nonlinear behavior may have its origin in either μ or in N. For the dipole moment of a molecule interacting with a static electric field (F), we can write :

$$\mu_i = \mu_{i0} + \alpha_{ij} F_j + (1/2) \beta_{ijk} F_j F_k + (1/6) \gamma_{ijkl} F_j F_k F_l + ... \qquad (1)$$

where μ_{i0} is the permanent dipole moment and α_{ij}, β_{ijk} and γ_{ijkl} are tensor elements of the linear polarizability, and first and second hyperpolarizabilities, respectively of the molecule.[10] Likewise, one can write an expression for dynamic fields relating β and γ to experiments such as second harmonic generation, optical rectification, and Kerr effect.[11] In the eq. (1), the subscripts i, j, k, and l represent cartesian axes and the summation of repeated indices is assumed.

Table 5 lists dipole moment and the hyperpolarizabilities for the GeO4 unit surrounded by 4 SiO4 units. The substitution of Ge for Si (i.e. q=0) does not make any changes in both β and γ. However, the anionic centers (with q=-1 and q=-2) show a noticeable increase in β.

A sequential substitution of the near-neighbor Si atoms by Ge atoms results in the configurations shown in Fig. 2 which are referred to as the Ge(1), Ge(2), Ge(3) centers respectively. The calculated hyperpolarizabilities reveal the dependence of β on the impurity Ge concentration in Silica. Trapping of the electron by the Ge(1) center yields in a two-fold increase of β (Fig. 3). But the increase of the number of near-neighbor Ge atoms in the cluster (i.e. Ge(2) and Ge(3) centers) shows a decreasing trend of β. At the molecular level, the most active NLO center is therefore predicted to be the Ge(1) center. Work is now in progress to study the NLO properties of the GeE' center (acting as hole traps) and to include frequency-dependent hyperpolarizability calculations of these Ge centers so that the calculated results can be compared directly to experiments.

REFERENCES:

[1]. J. D. Mackenzie, C. Y. Li and Y. Xu, Chemistry Express, 6, 903 (1991).

[2]. P. St. J. Russell, L. J. Poyntz-Wright and D. P. Hand, SPIE 1373 Fiber Laser Sources and amplifiers II, 126 (1990).

[3]. D. L. Griscom, Mate. Res. Symp.Proc. 61, 205 (1986).

[4].E. J. Friebele and D. L. Griscom, Mate. Res. Symp.Proc. 61, 319 (1986).

[5]. H. Kawazoe, J. Non-Cryst. Solids 71, 231-243 (1985).

[6]. Isoya J., Weil J. A., and Claridge R. F. C., 1978, J. Chem. Phys. 69, 4876.

[7]. McEachern R. J., Weil J. A. and Sawyer B., 1992, Solid State Comm. 81, 207.

[8]. McEachern R. J. and Weil J. A., unpublished.

[9]. T. E. Tsai, M. A. Saifi, E. J. Friebele, D. L. Grsicom and U. Osterberg, Opt. Lett. 13, 512 (1988).

[10]. R. Pandey, M. Coolidge and W. Lauderdale,submitted for publication.

[11] Ekenberg U. A., Robertson J. and Dow J. D., 1984, Phys. Rev B. 29, 2216.

[12] Hagon J. P., Jaros M. and Stoneham A. M., 1985, J. Phys. C :Soild State Phys. 18, 4957.

[13]. F. L. Galeener, in The Phsics and Technology of Amorphous SiO_2, ed: R. A. B. Devine (Plenum, New York, 1988), pp. 1-13.

[14].For a detailed discussion, we refer to J. K. Rudra and W. B. Fowler, Phys. rev. B 35, 8223 (1987).

[15].J. P. Stewart, MOPAC : a general molecular orbital package, Quantum Chemistry Program Exchange, No. 455, (1983), Version 6 (1990).

[16]. M. W. Schmidt, K. K. Baldridge, J. A. Boatz, J. H. jensen, S. Koseki, M. S. Gordon, K. A. Nguyen, T. L. Windus, S. T. Elbert, QCPE Bulletin, 10, 52 (1990).

TABLE 1

Structural Configuration of [XO4] cluster where x=Si or Ge obtained by semi-empirical PM3 (MOPAC) and *ab initio* HF-DZV (GAMESS) calculations.

	R(X-O(i), i=2,5) (Å)	A(O(2)-X-O(i), i=3,5)
Si(OH)4		
PM 3	1.685, 1.685, 1.685, 1.685	107.8, 112.9, 107.8
ab initio	1.652, 1.652, 1.652, 1.652	107.3, 113.8, 107.3
Ge(OH)4		
PM3	1.798, 1.798, 1.798, 1.798	107.9, 112.7, 107.9
ab initio	1.726, 1.726, 1.726, 1.726	107.6, 113.3, 107.6

TABLE 2

Structural Configuration of $(X-(O-Si-(OH)_4)_3)$ cluster where X=Si or Ge with different charge states. (See also Fig. 1.)

| X | | Bond Length (Å) | |
		X-O(i), i=2, 5	X - Si (j), j=6, 9
Si :	q=0	1.658, 1.660, 1.660, 1.658	3.307, 3.311, 3.331, 3.307
Ge(0) :	q=0	1.771, 1.775, 1.775, 1.771	3.429, 3.436, 3.436, 3.429
	q=-1	1.807, 1.822, 1.800, 1.796	3.457, 3.467, 3.450, 3.448
	q=-2	1.832, 1.833, 1.847, 1.829	3.481, 3.482, 3.497, 3.471
Ge(1) :	q=0	1.782, 1.776, 1.778, 1.770	3.558, 3.435, 3.437, 3.431
	q=-1	1.771, 1.785, 1.792, 1.794	3.593, 3.442, 3.446, 3.451
	q=-2		
Ge(2) :	q=0	1.779, 1.772, 1.775, 1.783	3.553, 3.433, 3.435, 3.560
	q=-1	1.807, 1.788, 1.796, 1.826	3.576, 3.436, 3.439, 3.589
	q=-2	1.835, 1.822, 1.827, 1.854	3.598, 3474, 3.478, 3.619
Ge(3) :	q=0	1.778, 1.781, 1.774, 1.781	3.553, 3.555, 3.436, 3.558
	q=-1	1.807, 1.828, 1.791, 1.806	3.577, 3.588, 3.445, 3.575
	q=-2	1.840, 1.840, 1.835, 1.838	3.608, 3.605, 3.484, 3.606
Ge(4) :	q=0	1.776, 1.780, 1.780, 1.776	3.552, 3.555, 3.556, 3.554
	q=-1	1.804, 1.820, 1.803, 1.799	3.573, 3.583, 3571, 3.569
	q=-2	1.837, 1.838, 1.840, 1.837	3.605, 3.604, 3.607, 3.605

		Bond Angle (°)	
X		O(2) - X - O(i), i=3, 5	X - O(i) - Si (j), (i,j) = (2,6), (3,7), (4,8), (5,9)
Si :	q=0	111.3, 107.8, 108.0	136.5, 139.6, 139.6, 136.5
Ge(0) :	q=0	112.0, 106.8, 108.9	136.0, 133.2, 133.2, 136.0
	q=-1	93.3, 95.2, 119.6	130.7, 126.0, 133.9, 128.8
	q=-2	173.0, 88.7, 92.1	123.5, 121.4, 121.4, 127.6
Ge(1) :	q=0	108.3, 113.3, 106.9	129.2, 132.9, 133.6, 136.5
	q=-1	113.4, 117.8, 110.9	146.8, 131.2, 131.1, 130.4
	q=-2		
Ge(2) :	q=0	108.3, 115.2, 105.6	133.0, 133.4, 134.8, 130.9
	q=-1	100.2, 92.3, 153.1	133.7, 132.9, 141.1, 120.0
	q=-2	92.1, 91.1, 176.3	131.7, 118.0, 118.0, 116.5
Ge(3) :	q=0	107.5, 115.6, 106.1	133.4, 130.5, 134.7, 132.1
	q=-1	152.4, 96.8, 100.4	136.8, 124.2, 132.4, 126.8
	q=-2	179.1, 90.5, 90.1	123.5, 122.9, 126.4, 124.1
Ge(4) :	q=0	108.1, 114.9, 106.3	134.0, 131.4, 131.0, 132.8
	q=-1	97.3, 100.5, 119.8	129.1, 120.6, 140.0, 124.7
	q=-2	90.5, 90.5, 177.2	124.8, 122.8, 124.9, 125.4

TABLE 3

Total energy and atomic charges associated with the cluster atoms of $(X-(O-Si-(OH)_4)_3)$ cluster where X=Si or Ge. (See also Fig. 1.)

		Energy (eV)	Atomic Charges			
			X	O	Si	O
Si :	q=0	-5278.35 eV	+1.31	-0.62	+1.26	-0.52
Ge(0) :	q=0	-5290.28	+1.01	-0.57	+1.25	-0.51
	q=-1	-5291.25	+0.67	-0.58	+1.14	-0.52
	q=-2	-5289.94	+0.18	-0.56	+1.00	-0.52
Ge(1) :	q=0	-5302.88	+1.01, +0.97	-0.56	+1.26	-0.50
	q=-1	-5303.90	+0.89, +0.68	-0.58	+1.19	-0.52
	q=-2					
Ge(2) :	q=0	-5315.44	+1.01, +0.97	-0.55	+1.26	-0.48
	q=-1	-5316.80	+0.69, +0.88	-0.55	+1.16	-0.50
	q=-2	-5315.58	+0.19, +0.80	-0.51	+0.99	-0.51
Ge(3) :	q=0	-5327.99	+1.01, +0.97	-0.54	+1.26	-0.46
	q=-1	-5329.47	+0.68, +0.89	-0.54	+1.16	-0.48
	q=-2	-5328.64	+0.20, +0.81	-0.48	+1.00	-0.50
GE(4) :	q=0	-5340.53	+1.01, +0.97	-0.52	---	-0.45
	q=-1	-5342.18	+0.67, +0.90	-0.51	---	-0.47
	q=-2	-5341.54	+0.21, +0.81	-0.48	---	-0.48

TABLE 4

Spin Populations associated with the cluster atoms of $(Ge(OSi(OH)_4)_3)$ cluster where negative charge state. The local symmetry of the Ge(I) and Ge(II) centers are C1 and C2 respectively. (See also Fig. 1.)

	Ge(I)		q=-1 Ge(II)	
	s	p	s	p
Ge	0.11	0.55	0.31	0.04
O(2)	0.01	0.02	0.05	0.08
O(3)	0.00	0.17	0.01	0.03
O(4)	0.03	0.01	0.01	0.03
O(5)	0.00	0.03	0.05	0.11
Si(6)	0.00	0.00	0.04	0.05
Si(7)	0.00	0.00	0.01	0.02
Si(8)	0.02	0.03	0.01	0.02
Si(9)	0.01	0.01	0.04	0.05

TABLE 5

The calculated dipole moment and polarizabilities of (X(OSi(OH)4)3) cluster with different charge states.

	dipole (debye)	α (esu) x 10^{-23}	β (esu) x 10^{-30}	γ (esu) x 10^{-36}
Si : q=0	2.23	3.98	0.16	13.2
Ge(0) : q=o	1.07	4.28	0.24	13.6
q=-1	0.77	4.44	1.11	19.8
q=-2	1.30	4.28	1.55	17.6
Ge(1) : q=0	2.68	4.48	0.11	17.4
q=-1	5.25	5.13	9.79	41.3
q=-2				
Ge(2) : q=0	2.19	4.72	0.02	19.2
q=-1	1.08	5.07	3.3	26.5
q=-2	0.8	4.80	0.20	23.4
Ge(3) : q=0	2.05	4.94	0.21	21.2
q=-1	1.70	5.31	0.17	31.2
q=-2	1.40	5.00	0.75	23.7
Ge(4) : q=0	1.67	5.16	0.45	10.3
q=-1	0.48	5.56	0.50	38.2
q=-2	1.74	5.22	0.01	25.6

S.02

Ge(O) Center

Fig. 1

11-14
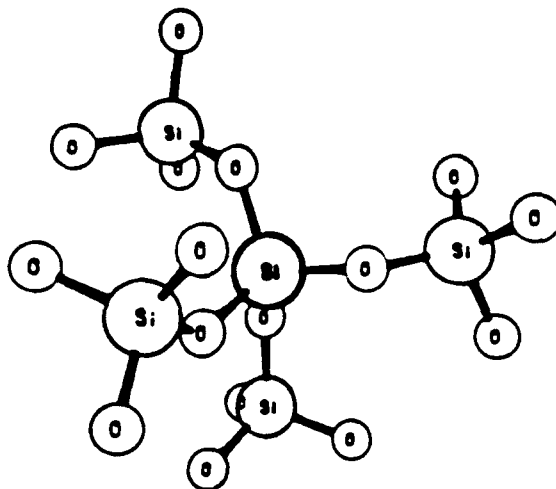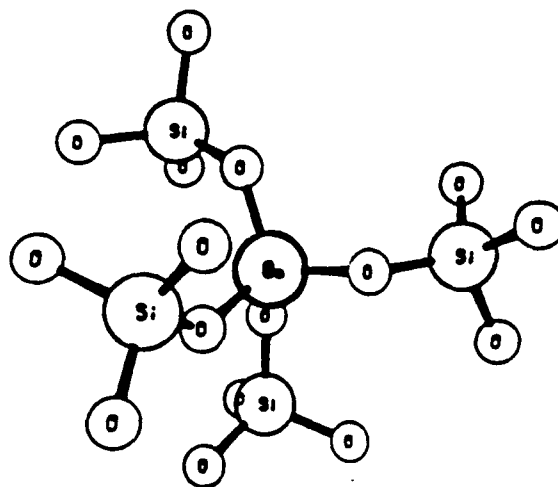
Ge(1) Center
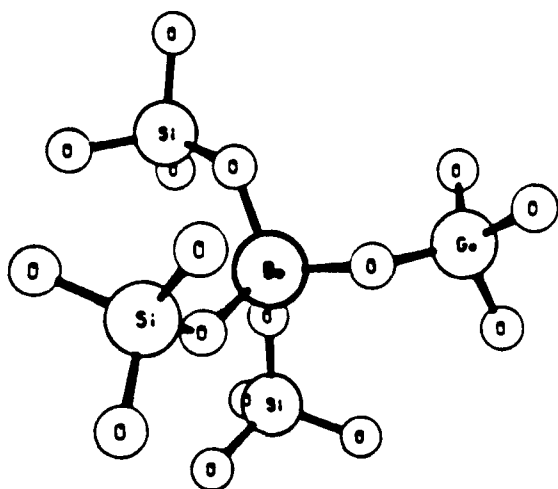
Ge(2) Center
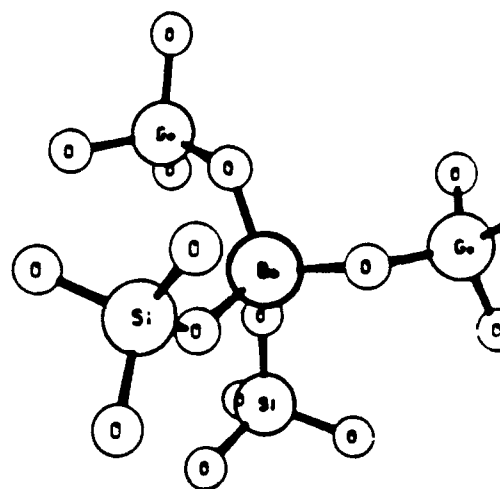
Ge(3) Center
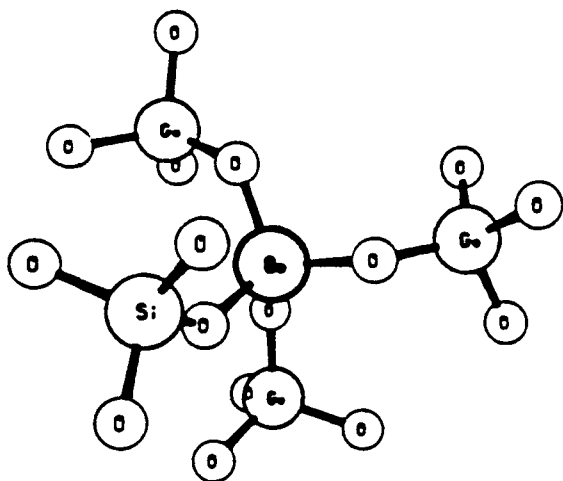
Ge(4) Center : GeO2

Fig. 2

Fig. 3

Application of the Volterra Functional Series
Approach for Understanding Control of Flow Separation
Downstream of a Pitching Airfoil

Charles Pezeshki
Assistant Professor
Department of Mechanical and Materials Engineering

and

Wyatt O. Davis
Graduate Student

Washington State University
Pullman, WA 99164-2920

Application of the Volterra Functional Series Approach for Understanding Control of Flow Separation Downstream of a Pitching Airfoil

Charles Pezeshki
Assistant Professor
Department of Mechanical and Materials Engineering
Washington State University

and

Wyatt O. Davis
Graduate Student

Abstract

A combination experimental/numerical investigation of flow separation for a static airfoil has been conducted using Higher-Order Spectral Analysis (HOS) and the Volterra functional series approach. Input and output time series were recorded downstream of the airfoil at certain points in the flow to investigate and quantize the natural energy transfer mechanisms present. Time series were recorded for two angles of attack, and hot-film anemometers were used to record input and output flow velocities downstream from the airfoil at various fractions of the chord length downstream. Linear and quadratic transfer functions were calculated for these trajectories. These functions were then examined for evidence of natural energy transfer mechanisms in the flow.

Following this analysis of the unforced flow, a study was conducted using pulsed air as a mechanism for control of flow separation. Linear and quadratic transfer functions were calculated for these test cases, and insights were obtained on the mechanism by which the angle of incipient flow separation is increased.

Introduction

A large body of previous work has been done on controlling growth of a two-dimensional mixing layer. In particular, the work of Oster and Wygnanski [OSTE] examined the use of a small flap to periodically force the flow and alter the growth of the flow instability downstream of the plate. Ho and Huerre [HO] discussed the use of acoustic as well as mechanical forcing for control of the mixing layer. More relevant to the problem of flow separation downstream of a static airfoil, Lovato [LOVA] investigated active control of the shear layer on an airfoil using external acoustic forcing and internal-tangential pulsed air control. Their results showed that the airfoil shear layer responds to the active forcing akin to a free shear layer.

An extensive amount of research has been performed concerning the analysis of fluid flows using Higher-Order Spectral analysis (HOS). Of particular interest to the research discussed below is the work of Miksad, Jones et. al [MIKS]. They studied the transition of a laminar two-dimensional wake to establish the role of amplitude and phase modulations in the spectral-broadening and energy-redistribution process. Later work by Ritz, Powers and Miksad et. al. [RITZ] concerned the spectral dynamics of transitioning flow in the wake of a flat plate. For this work, quadratic transfer functions from a Volterra functional approximation were calculated to examine the nonlinear spectral dynamics occurring between two sensor points. Finally the work by Hajj, Miksad and Powers [HAJJ] involving quantification of the possible nonlinear and parametric resonance mechanisms associated with the transition to turbulence in plane mixing layers was most influential in the following research. In this paper, HOS analysis techniques were used to investigate both nonlinear and parametric transfers of energy to lower frequencies.

The work performed by the principal investigator this summer of 1993 builds on the above work by examining the flowfield downstream from a static airfoil fixed at an angle of attack. Many comparisons have been formed with the flow downstream of an airfoil and both a mixing and shear layer [LOVA]. Hot film anemometry was used to record two time series simultaneously downstream from the airfoil at various relative positions to the airfoil. Quadratic transfer

functions were then calculated for the time series data using the approach developed by [RITZ], and these were analyzed to confirm fundamental flow frequencies and basic energy transfer mechanisms in the flow. In addition, a brief study was done on the energy transfer mechanisms involved in the dynamically pitching airfoil. A similar analysis was conducted as for the static case, with the hot film anemometers held at a fixed position relative to the pitching airfoil. This work will lead to future study of this important problem.

Experimental Set-up

The hot film anemometry experiments were conducted in the Frank J. Seiler Laboratory's open return, low speed wind tunnel at the U.S. Air Force Academy. The .91m x .91 m test section is designed for use with flow visualization and flow sensor measurements, and has free stream turbulence intensity levels below 0.5% A NACA-0015 airfoil with a 15.2 cm chord and a 61.0 cm span was used for all tests. Chord Reynolds numbers were at 24,000 for the hot-film data. The two time series were recorded using dual 60 mil hot-film probes in conjunction with a TSI Model 1054A anemometer. The overheat ratio was set at 30%. All data acquisition utilized a MassComp MC-5500 micro-computer. The flow was sampled at a frequency of 80 Hz for use in the HOS and transfer function analysis. The signals were all filtered with a low-pass filter at 300 Hz.

Flow modification was accomplished individually by internal tangential-pulsed air blowing. Pulsed air was directed through a downstream facing slot located on the upper airfoil surface. The slot was 1.6 mm wide and spanned the middle 15.0 cm of the airfoil, or 25% of the entire span, located at the leading edge of the airfoil. The system employed two solenoid valves capable of pulsing between zero and 45 Hz. The valves were controlled through a timing circuit using a square wave generator. Compressed air was supplied at 30 psig through tygon tubing into each end of the slot, resulting in a peak injection velocity of 8.5 m/sec. The blowing momentum coefficient, C_μ, was 0.07 for a chord Reynolds number of 24,000.

Transfer Function Calculations

The method for calculating nonlinear transfer functions to second order is summarized in [RITZ] and [HAJJ]. The general idea behind such work is that a nonlinear response of a dynamical system can be condensed, up to second order, into additive responses consisting of a linear frequency response, $L(f_m)$, plus a quadratic frequency response, Q, as given by

$$Y(f_m) = L(f_m)X(f_m) + \sum \sum_{f_i \pm f_j} Q_{f_i \pm f_j}^{f_m} X(f_i)X(f_j) \quad f_m = f_i \pm f_j$$

Basically, it involves solving two moment equations in the frequency domain, given by [RITZ] as

$$E[Y(f_m)X^*(f_m)] = L(f_m)E[X(f_m)X^*(f_m)] + \sum \sum_{f_i \pm f_j} Q_{f_i \pm f_j}^{f_m} E[X(f_i)X(f_j)X^*(f_m)]$$

and

$$E[Y(f_m)X^*(f_k)X^*(f_l)] = L(f_m)E[X(f_m)X^*(f_k)X^*(f_l)] + \sum \sum_{f_i \pm f_j} Q_{f_i \pm f_j}^{f_m} E[X(f_i)X(f_j)X^*(f_k)X^*(f_l)]$$

where

$$f_m = f_i \pm f_j = f_k \pm f_l$$

where f_m is the output frequency of the model, E is the expectation operator and $X(f_j)$ and $Y(f_j)$ are the Fourier transforms of the input and the output respectively. Importantly, these two equations allow one to express both transfer functions in terms of the various HOS moments that are given by the upstream and downstream sensors of the probe [HAJJ]. For example, the LHS of the first equation is the cross-spectrum, the RHS of the first equation associated with the linear transfer function is the power spectrum, and with the quadratic transfer function, the auto-bispectrum. For the second equation, the LHS is the cross-bispectrum, the term associated with the linear transfer function is the auto-bispectrum, and the term associated with the quadratic transfer function is the fourth-order spectral moment. Both these equations generate a square matrix with enough equations to solve for all the unknowns in both the linear and quadratic transfer functions.

This summer, a large program was written that would assemble these two equations into a matrix and solve for both the linear and quadratic transfer

functions. The name of this program is SKETCHY. SKETCHY initially reads in the input and output time series recorded from the hot-film anemometry probe. Following this, the time series is broken up into a number of blocks, and the various averaged spectral moments are calculated, such as the auto- and cross-spectrum, the auto- and cross bispectrum and the fourth-order spectral moment. These moments are then used to construct a large two-dimensional square matrix associated with the unknowns, along with a column vector for the various terms in the transfer functions. This is solved using a lower/upper triangular solver. The unknowns are then reassembled into appropriate matrices representing the linear and the quadratic transfer functions. The magnitudes of these complex arrays are taken and the results are written to output files, which are displayed using a plotting application developed by W. Davis using the graphics language IDL (Interactive Display Language) by Research Systems Incorporated. To further understanding of the quadratic transfer function results, a non-dimensional quadratic transfer function is also calculated, defined as   [HAJJ]

$$Q^{2}(f_i,f_j) = E\left[\left|Q^{f_m}_{f_i,f_j}\right|^2 \left(\left|X(f_i)X(f_j)\right|^2\right)^{\frac{1}{2}}\right], \quad f_m = f_i + f_j$$

This nondimensionalized quadratic transfer function shows the magnitude of the energy transferred due to a given interaction, combining affinity for a given three-wave interaction to exchange energy multiplied by the actual energy present to be transferred.

The program was verified for correctness of results by experimenting with sample cases where the linear and quadratic transfer functions were known. In particular, two input-output combinations, one to test for a pure linear response, and the other to test for a pure quadratic response were analyzed, and both cases yielded the correct answer. However, preliminary examination of the matrix used to solve for the linear and quadratic transfer functions indicate that the matrix is poorly conditioned. One of the highest priorities upon continuance of this work will be to use a sparse matrix solver designed for poorly conditioned matrices, as well as implement the entire code in double precision. Because of the size of the matrices manipulated, this will involve use of a supercomputer.

Results and Discussion

Quadratic transfer functions were calculated using 16384 points collected by the Masscomp computer, subdivided into 64 point blocks for the averaging techniques. The sampling rate was chosen to be 80Hz, well above the necessary Nyquist frequency needed to examine the higher frequency content. The lowest frequency available for examination was 1.25Hz. This was deemed adequate for a preliminary study of the phenomena; however, the final study to be conducted this winter will use more data and a 128 point block size.

For the static case, hot film pair measurements were made in a variety of positions downstream of the airfoil. Two angles of attack were chosen: 15° and 20° . Six cases were analyzed for the 15° angle of attack and seven cases for the 20° angle of attack downstream of the airfoil.

Figure 1 is a representative plot of the nondimensionalized quadratic transfer function at 15° angle of attack for the unforced case. The transfer function shows that the flow is self-organizing, with energy from all frequencies in the input being coupled to, or transferring energy to 5 Hz, the lowest subharmonic present in the flow, 20 Hz, the main harmonic, and 30 Hz, the first superharmonic. The primary frequency triads present in this plot are (15Hz, 5Hz, 20Hz), (10Hz, -5Hz, 5Hz), and (20Hz, 10Hz, 30Hz).

Figure 2 is the plot of the nondimensionalized quadratic transfer function at 20° angle of attack. The flow is also self-organizing, transferring energy primarily to approximately 4 Hz, the lowest subharmonic, and 30 Hz, the first superharmonic in the flow, with large energy coupling mechanisms at (10Hz,-6Hz,4Hz) and (20Hz,10Hz,30Hz).

Because of the large amount of coupling observed between for the frequency values of 5Hz, 10Hz and 20Hz in the natural flow case, indicating strong flow organization because of these frequencies, a pulsed air control at these frequencies was used to control flow separation at 20° angle of attack. For 5Hz pulsed air frequency, the flow quickly becomes organized and periodic, with

strong frequency content at 10Hz, 15Hz, and 25Hz. Figure 3 shows the nondimensionalized quadratic transfer function for a typical trial. Strong coupling exists between 5Hz in the input and 10Hz in the output, from frequency triad (5Hz, 5Hz, 10Hz). In addition, the pulsed air serves as a strong organizer of the flow, as all energy from all frequencies is directed into the 10Hz, 15Hz and 25 Hz frequencies in the output.

Conclusions

Preliminary work concerning flow control for separation from a static airfoil mounted at given angles of attack was completed this summer by the P.I. The Volterra functional series/ quadratic transfer function calculation method was implemented and used to obtain results for flow control. Initial results are promising; fundamental flow frequencies are successfully identified, and energy transfer mechanisms in the flow are highlighted. Future work will involve examining the dynamic pitching airfoil for energy transfer mechanisms so that a control scheme can be proposed for delaying the onset of dynamic stall, and enhancing airfoil performance in the post-stall regime.

Bibliography

[HAJJ] Hajj, M.R., Miksad, R.W., and Powers, E. J., (1992) "Subharmonic Growth by Parametric Resonance", J. Fluid Mech., vol. 236, pp. 385-413.

[HO] Ho, C.M. and Huerre, P. (1984) "Perturbed Free Shear Layers," Ann. Rev. Fluid Mech., Vol. 119, pp. 443-473.

[LOVA] Lovato, J.A., (1992) "Active Control of the Separation Region on a Two-Dimensional Airfoil", FJSRL TR-92-0001.

[MIKS] Miksad, R.W., Jones, F.L. Powers, E.J., Kim, Y.C., and Khadra, L., (1982) "Experiments on the Role of Amplitude and Phase Modulations during Transition to Turbulence", J. Fluid Mech., Vol. 123, pp. 1-29.

[OSTE] Oster, D. and Wygnanski, I. (1982) "The Forced Mixing Layer Between Parallel Streams," J. Fluid Mech., Vol. 123, pp 91-130.

[RITZ] Ritz, C. P., Powers, E.J., Miksad, R.W., and Solis, R.W., (1988) "Nonlinear Spectral Dynamics of a Transitioning Flow", Phys. Fluids. Vol. 31(12), pp. 3577-3588.

Quadratic Transfer Function — Linear Scale
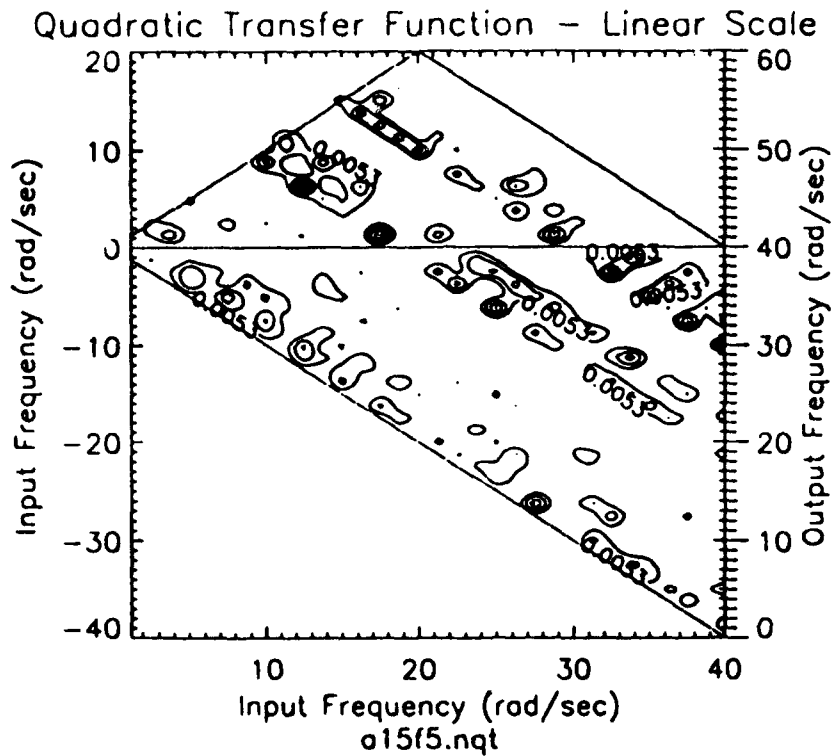
Figure 1. Nondimensionalized quadratic transfer function, angle of attact 15°, unforced case.

Quadratic Transfer Function — Linear Scale
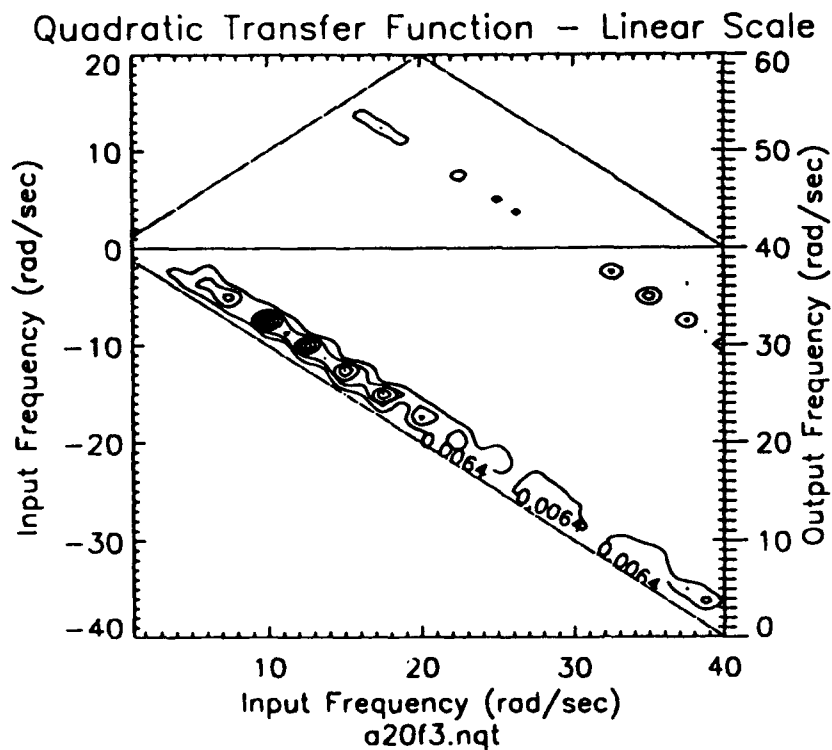
Figure 2. Nondimensionalized quadratic transfer function, angle of attack 20°
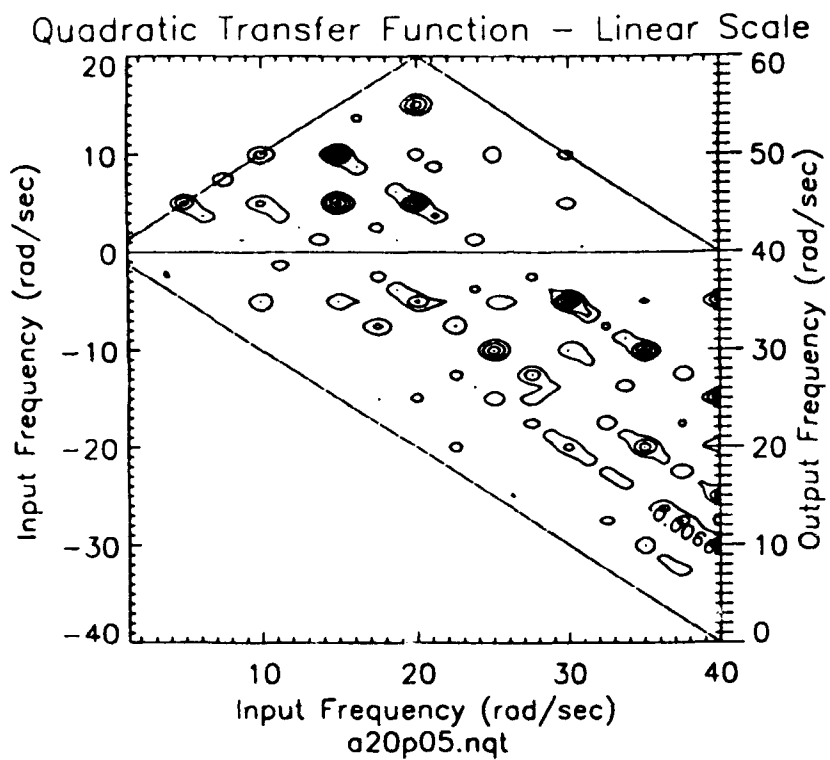
Figure 3. Nondimensionalized quadratic transfer function, angle of attact 20°, pulsed air forcing at 5Hz.

ACTIVATED REACTIVE LASER DEPOSITION OF GeO$_2$ FILMS

Sarath Witanachchi

Assistant Professor

Department of Physics

University of South Florida

Tampa, FL 33620

Final Report for:

Faculty Summer Research Program

Frank J. Seiler Research Laboratory

USAF Academy, Colorado.

Sponsored by:

Air Force Office of Scientific Research

Bolling Air Force Base, Washington, D.C.

September 1993

ACTIVATED REACTIVE LASER DEPOSITION OF GeO$_2$ FILMS

Sarath Witanachchi

Assistant Professor

Department of Physics

University of South Florida

Abstract

Laser ablation technique has been used to grow amorphous GeO$_2$ optical films in an oxygen ambient. Application of a partially ionized oxygen plasma facilitated stoichiometric film growth in a low ambient pressures. Emission spectroscopy of the plume revealed an enhancement in the ionic and the neutral excited species as well as the atomic oxygen in presence of the plasma. Though the effect of the plasma on the gas phase reaction was insignificant, the substrate surface reaction was enhanced considerably. This technique enabled stoichiometric film growth in 30 mT oxygen pressure and 300 ^{o}C substrate temperature. Deposition at this low pressure produced uniform films over a large area, that are suitable for waveguide fabrication. Dependence of the film oxygen content on the ambient gas pressure, the substrate temperature, and the plasma conditions is discussed.

ACTIVATED REACTIVE LASER DEPOSITION OF GeO_2 FILMS

Sarath Witanachchi

INTRODUCTION

Laser ablation of a target in vacuum or in a reactive gas ambient is a well established technique for the growth of superconductor[1-3], semiconductor[4,5], and dielectric[6,7] thin films. Congruent evaporation in multicomponent systems leading to stoichiometric film growth, and the ability to deposit films in high pressure ambient gases, are two of the unique advantages of this method over conventional techniques. Laser-target interaction produces a material plume whose expansion into the ambient is mainly governed by the pressure gradient across the plume. The plume expands rapidly in vacuum, while at high ambient pressures the diminished pressure gradient across the plume suppresses the plume expansion. The highly forward directed plume profile has been shown to assume a $cos^n\theta$ functional behavior at high pressures[8], where n ranges from 8 to 16. In addition, the short mean free path at high pressures limits the plume propagation distance to a few cm from the target. In the growth of materials that require the incorporation of a gaseous species to produce the proper stoichiometry, the gas phase reaction promoted by the collisions between the plume species and the ambient gas plays a major role. Film growth at high pressure leads to enhanced gas phase reactions. However, at high ambient pressures the film growth is carried out closer to the target, and thus, the films become highly none uniform.

In this study, we have applied the laser ablation technique to grow stoichiometric GeO_2 films in the amorphous state. Amorphous GeO_2 is a promising material for the fabrication of optical wave guides[9]. Sputter deposition of high quality GeO_2 films have been reported previously[10,11]. Laser ablation has also been successfully used to grow

stoichiometric films at high pressures. Recently, P. J. Wolf et. al. have reported the laser deposition of stoichiometric films in a 150 mT ambient pressure[12]. At these pressures the films were observed to be highly none uniform. In this report, we present the results of an experiment conducted to produce stoichiometric GeO_2 films at a low ambient pressure that leads to uniform film growth over a large area. The gas ambient has been activated by generating a glow discharge plasma between the target and the substrate. The plasma is intended to enhance the gas phase and the substrate surface reactions. A similar technique has been used previously in plasma assisted laser deposition of high T_c superconducting film growth[2]. The effect of the plasma on the propagating plume was investigated by emission spectroscopy. Spectroscopic information aided the optimization of the plasma conditions for film growth. The extent of the gas phase reaction at different pressures, in presence of the plasma, was gauged by the oxygen content of the deposited films at room temperature. The film stoichiometry was deduced from the infrared (IR) transmission spectroscopic measurements of the films. Furthermore, increase in the substrate temperature was seen to enhance the film oxidation at the substrate. Films deposited at different substrate temperatures and pressures were analyzed to determine the lowest possible pressure for stoichiometric film growth.

EXPERIMENTAL

High purity GeO_2 targets were prepared by melting GeO_2 powder in an alumina crucible. This procedure produced an extremely smooth high density targets suitable for laser ablation. Target placed in a turbo-pumped vacuum chamber was ablated by focusing an ArF excimer laser. The laser beam incident on the target at 45° with an energy density of about $1J/cm^2$. The flounce at the 1mmx3mm spot on the target was above the $0.3J/cm^2$ fluence threshold for GeO_2[13]. The target was constantly rotated to

avoid formation of craters. The oxygen glow discharge was created by placing a 2" diameter ring electrode between the target and the substrate. Application of a -1000 to -1500V voltage to the electrode produced a strong plasma near the ring. Oxygen was introduced through a nozzle placed near the substrate. The laser plume that passed through the ring was deposited on a substrate whose temperature was controlled between the room temperature and 300°C. The experimental set-up is shown in Fig. 1.

The plume emission was observed by using a image-intensified optical multichanal analyzer (OMA III). The emitted radiation from a point 3 cm above target was imaged approximately 1:1 by two quartz aspheric lenses onto the entrance slit of a 0.5 m spectrometer with a 0.17nm resolution. Signals were averaged over ten laser shots to improve the signal-to-noice ratio.

Film deposition was carried out on IR transmitting Si substrates. Solvent cleaned substrates were mounted on the heating block using silver paste for better thermal contact. To study the effect of the ambient oxygen pressure on the gas phase reaction, a series of films were grown in room temperature with pressures ranging from 0 to 100 mT. Since the mean free path decreases with increasing pressure, substrate-to-target distance was reduced from 7.5 cm in vacuum to 4.0 cm in 100 mT gas pressure. The oxygen content of the films were deduced from the infrared transmission spectra of the films which were obtained using a Nicolet 510P FT-IR spectrometer.

The effect of the surface reaction at the substrate was investigated by depositing films at temperatures ranging from 20°C to 300°C. The films grown at different temperatures and pressures were analysed using infrared spectroscopy to determine the film oxygen content. Furthermore, x-ray diffraction techniques were used to observe
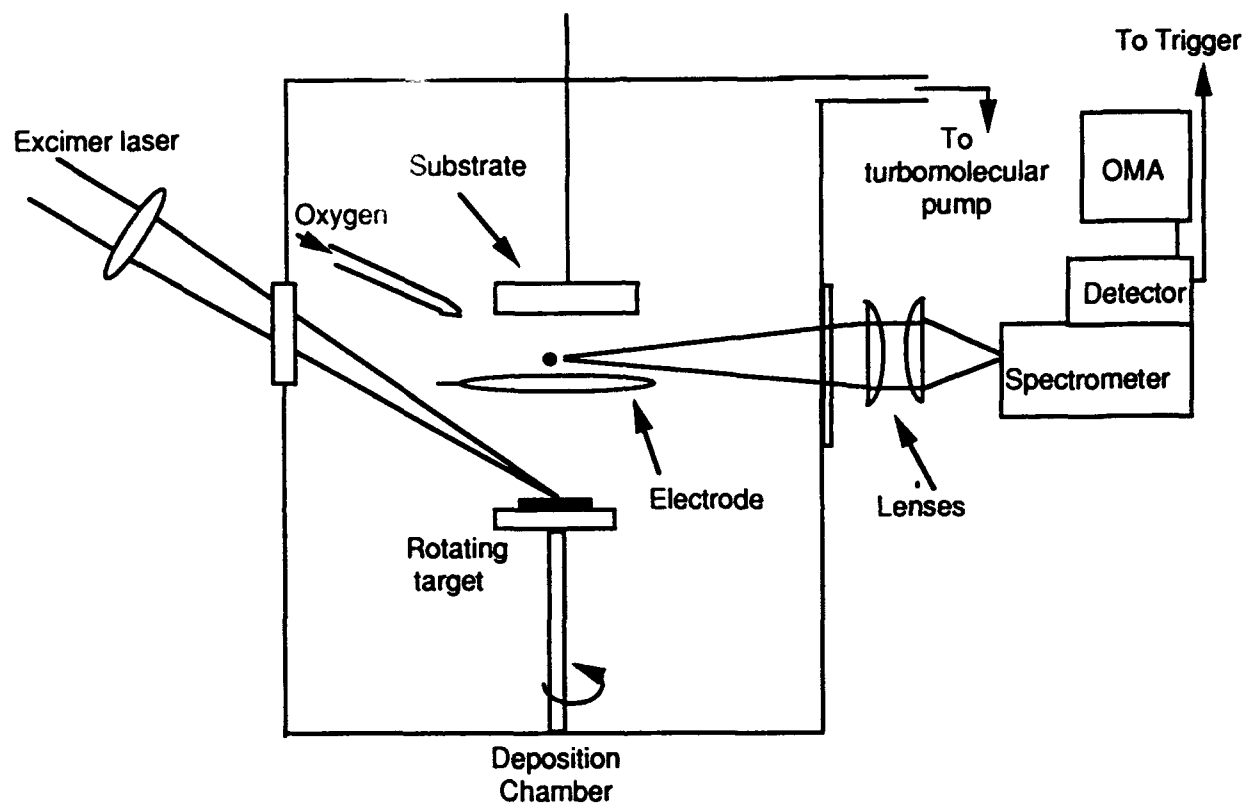
FIG. 1: A schematic diagram of the experimental set-up.

any changes in crystallinity of the films grown at elevated temperatures. The thickness variation of the films deposited under different pressures were measured using a stylus surface profiler.

RESULTS

Emission from the laser generated plume was recorded with and without the oxygen plasma in the wavelength region 250 nm to 850 nm. In absence of the plasma, the spectrum consisted mainly of excited neutral Ge atoms. Application of the plasma produced strong emission from excited Ge ions and enhanced the neutral atomic emissions. Figure 2 &3 show emission from the spectral regions centered at 480 and 520 nm, respectively. Intensity of the line at 465 nm, which corresponds to Ge II emission, is increased in presence of the plasma, whereas a more dramatic incense in the ionic emission at 474 nm, 481nm, 514nm and 518nm were observed. Furthermore, formation of atomic oxygen in the plasma was indicated by the strong emission from excited O(I). Figure 4 & 5 show emission spectra centered at 720 and 780 nm, with and without the presence of the plasma. The emission at 715nm, which corresponds to $O^*(^1D)$, was not observed without the plasma. Formation of this metastable atomic oxygen species in the plasma is indicated in Fig. 4. In addition, a significant increase in the emission at 777nm, which corresponds to $O^*(^5S)$ state, was also observed.

Films deposited under the plasma conditions at different pressures were analyzed by infrared spectroscopy to determine the oxygen content. The structure of amorphous GeO_2 can be described as $Ge-Ge_yO_{4-y}$ tetrahedra connected by bridging oxygen atoms. The asymmetric stretch vibration mode of Ge-O-Ge in Stoichometric GeO_2 has been

13-7

Ge (I) 468.916

Ge (II) 474.236

Ge (II) 482.022

a

b

Wavelength (nm)

Intensity × 10³
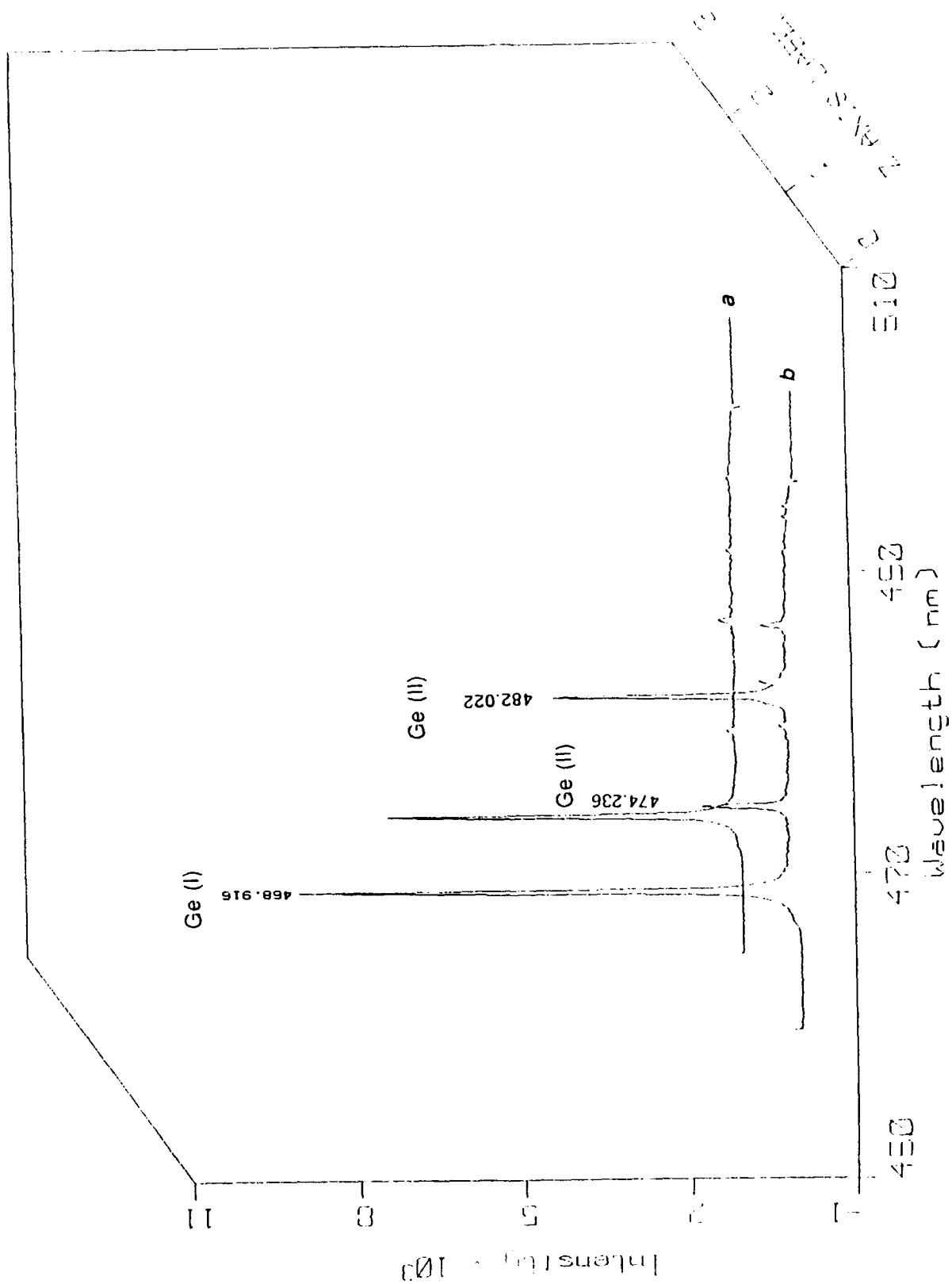
Plume emission centered at 480 nm. (a) without the plasma, (b) with the plasma.

FIG. 2

13-8
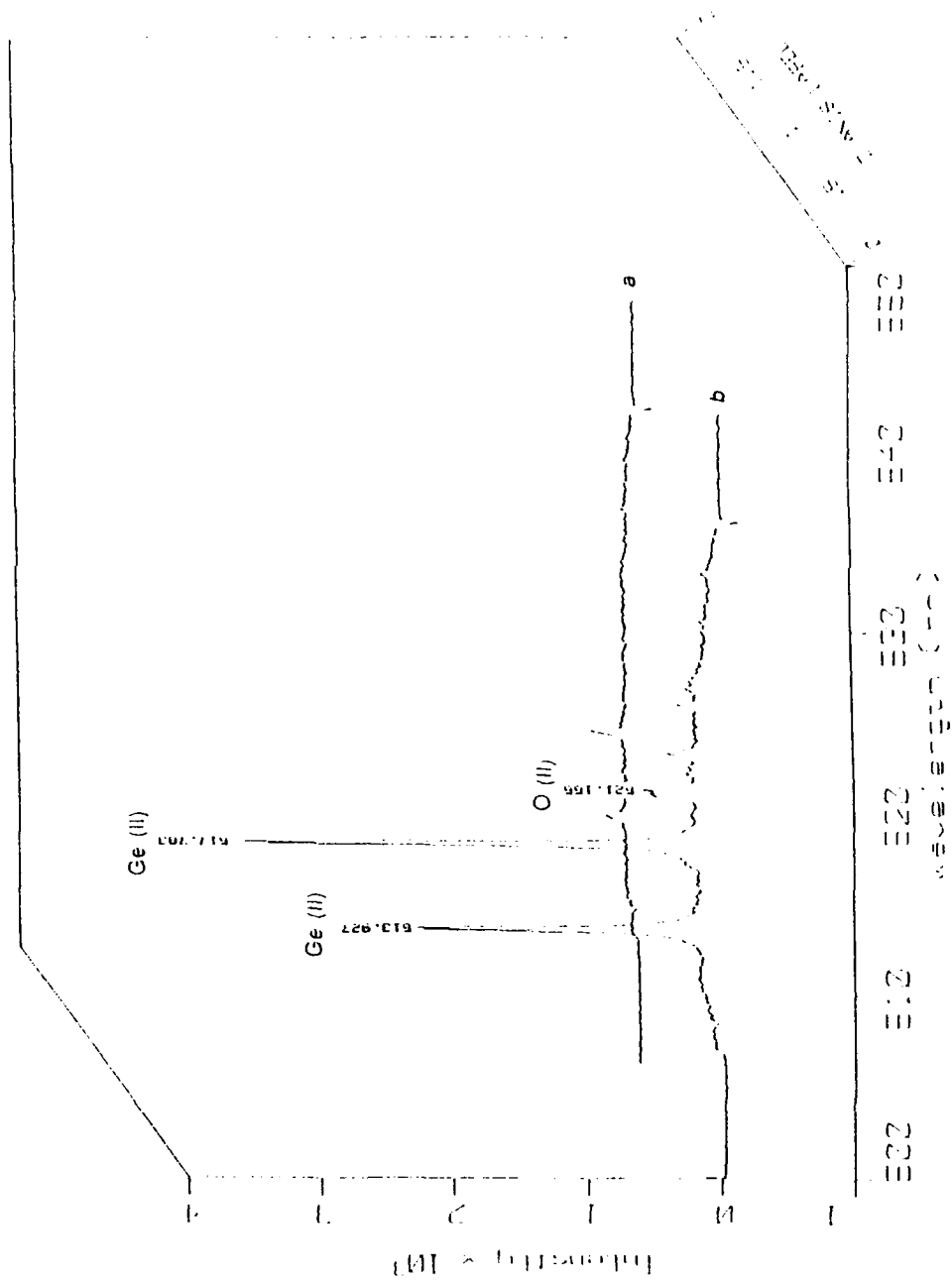
FIG. 3 Plume emission centered at 520 nm. (a) without the plasma, (b) with the plasma.

13-9
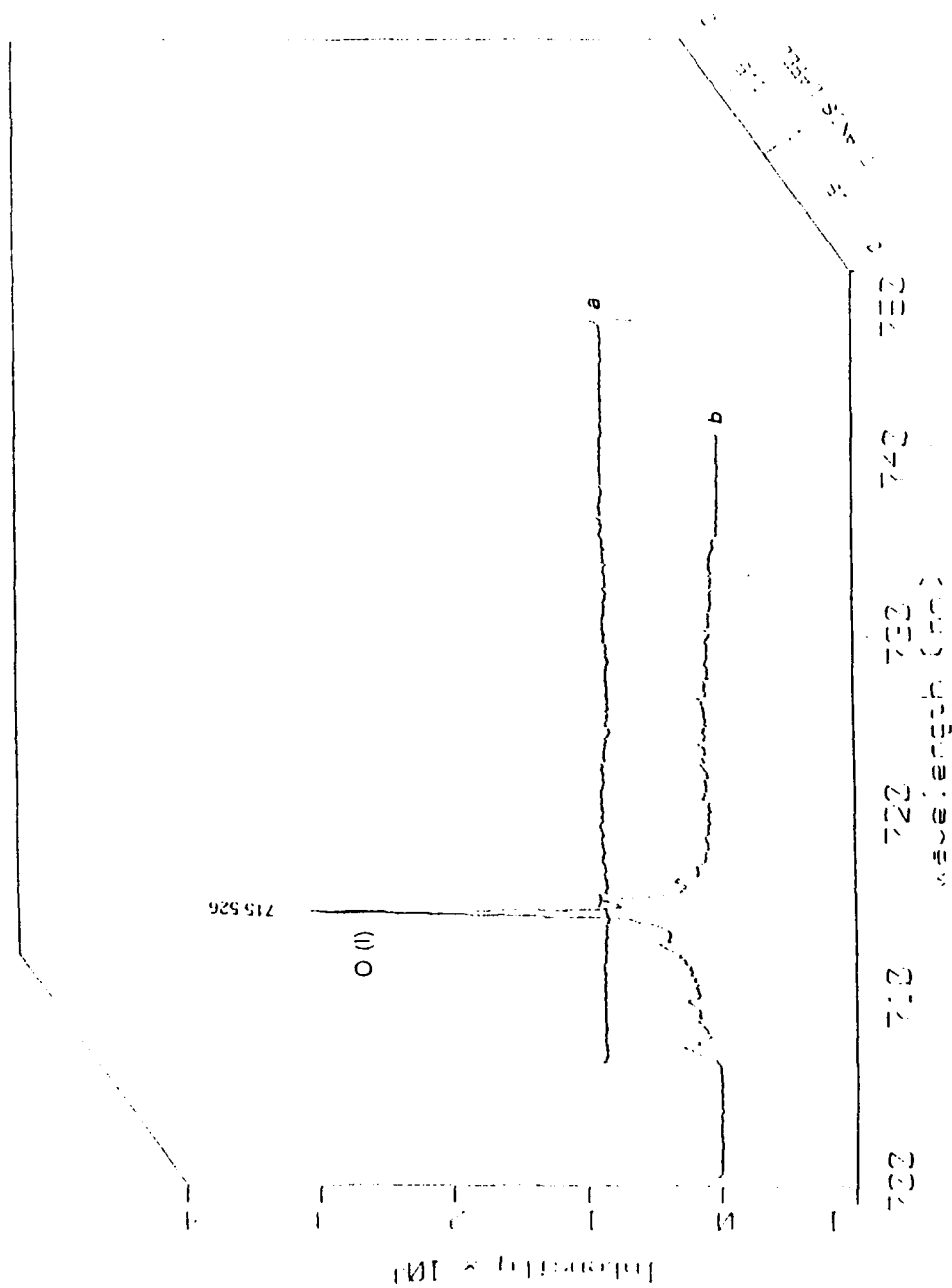
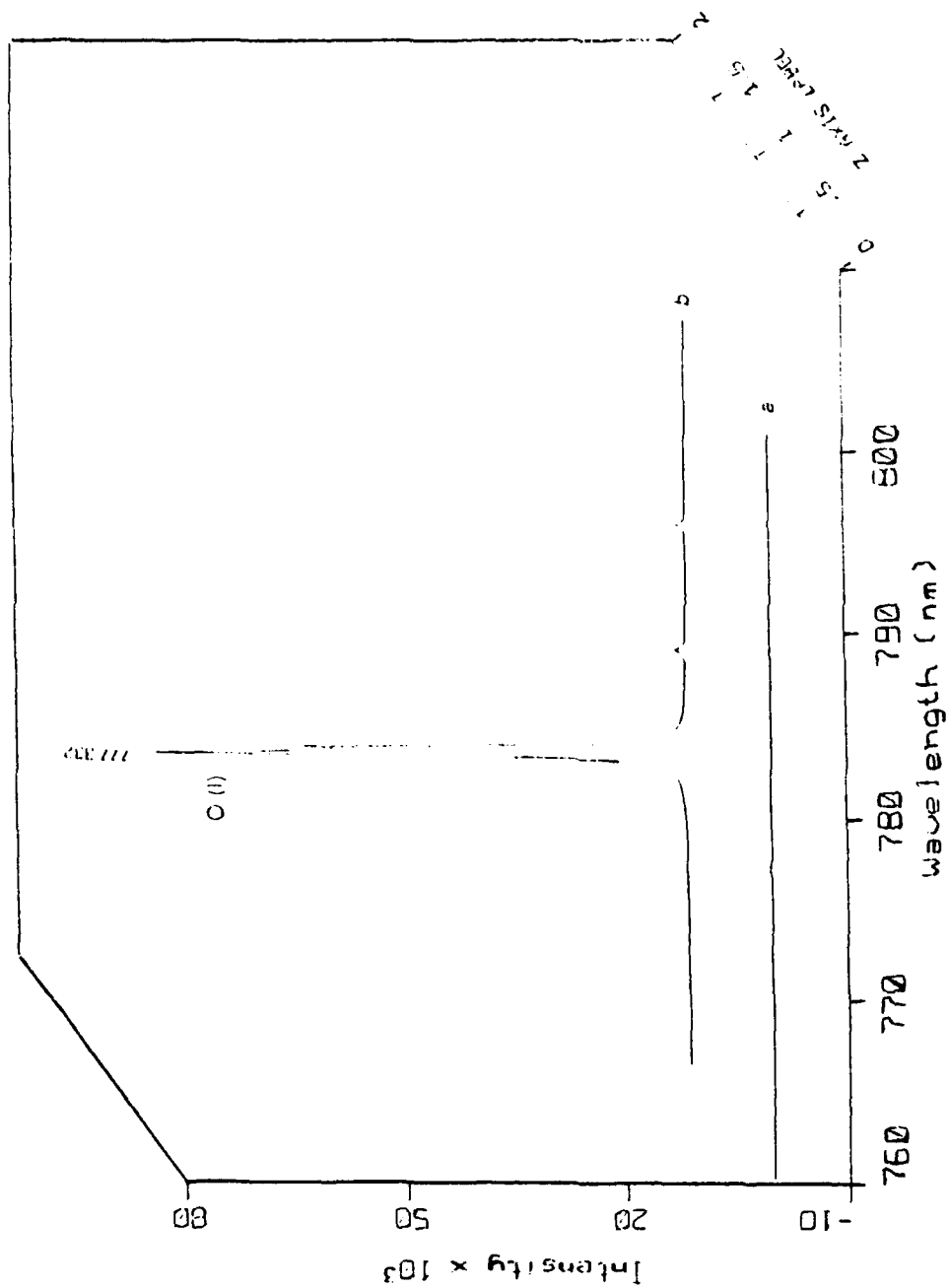FIG. 4   Plume emission centered at 720 nm. (a) without the plasma , (b) with the plasma.

13-10

FIG. 5   Plume emission centered at 780 nm.   (a) without the plasma, (b) with the plasma.

Intensity x 10³

wavelength (nm)

Z AXIS LEVEL

O (I)

777.322

shown to be at 885 cm^{-1}. The vibration frequency of oxygen deficient structures, for y= 0 to 4, changes linearly from 885 cm^{-1} to 740 cm^{-1} according to the equation[14]

$$v(x) = 72.4 \ x + 743 \ (cm^{-1})$$

where, x is the oxygen content that ranges from 2 to 0. The oxygen stoichiometry of the films has been computed using this equation. Changes in the oxygen content of the films grown at room temperature as a function of the ambient oxygen pressure is shown in Fig. 6. The oxygen stoichiometry of the film increased from 1.3 to 1.8 as the deposition pressure is changed from 5x10^{-4} T to 100 mT. This indicates a significant gas phase reaction even at very low pressures. An enhancement in the substrate surface reaction was obtained by increasing the substrate temperature. The change in the film oxygen stoichiometry with increasing substrate temperature with and without the oxygen plasma in a 30mT ambient pressure is shown in Fig. 7. This result reveals that the surface reaction at high temperature is more efficient in presence of the plasma. Under these plasma conditions, the films deposited in 30mT of oxygen became stoichiometric at 300°C substrate temperature. An IR spectroscopic scan of a film deposited in 30mT pressure and 300°C substrate temperature is shown in Fig. 8. The IR spectra and x-ray diffraction of the films deposited at this temperature gave no indications of crystalline structure.

The pressure dependence of the film oxygen content at different temperatures is shown in Fig. 9. At a 300°C substrate temperature the films deposited above 30mT oxygen pressure tend to be stoichiometric. The film growth in 100mT pressure was carried out 4cm from the target, whereas the films were grown 7.5cm from the target in 30mT pressure, and thus, produced films uniform over a larger area. The rectangular laser spot at the target gave rise to an elliptical plume. For the films grown at 30mT, the thickness along the major axis of the elliptical profile varied only 10%
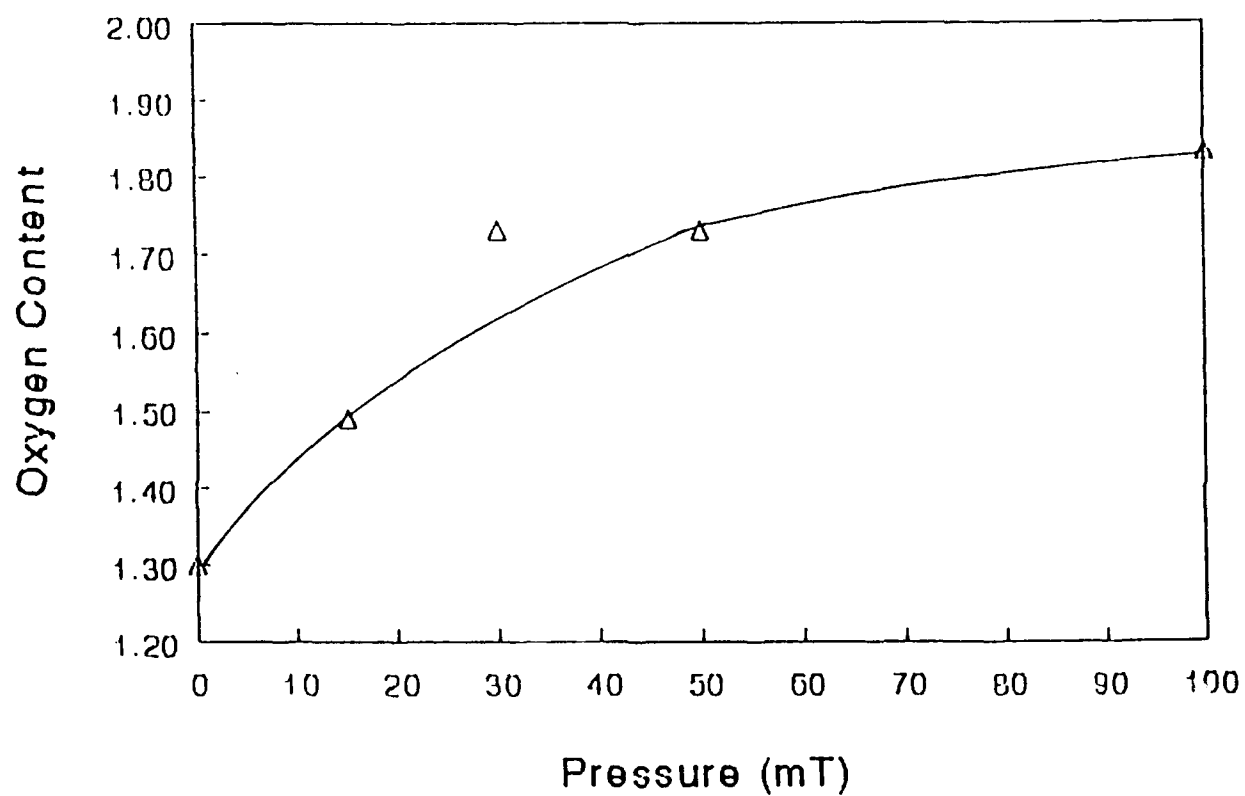
FIG. 6   Variation of film oxygen content with ambient oxygen
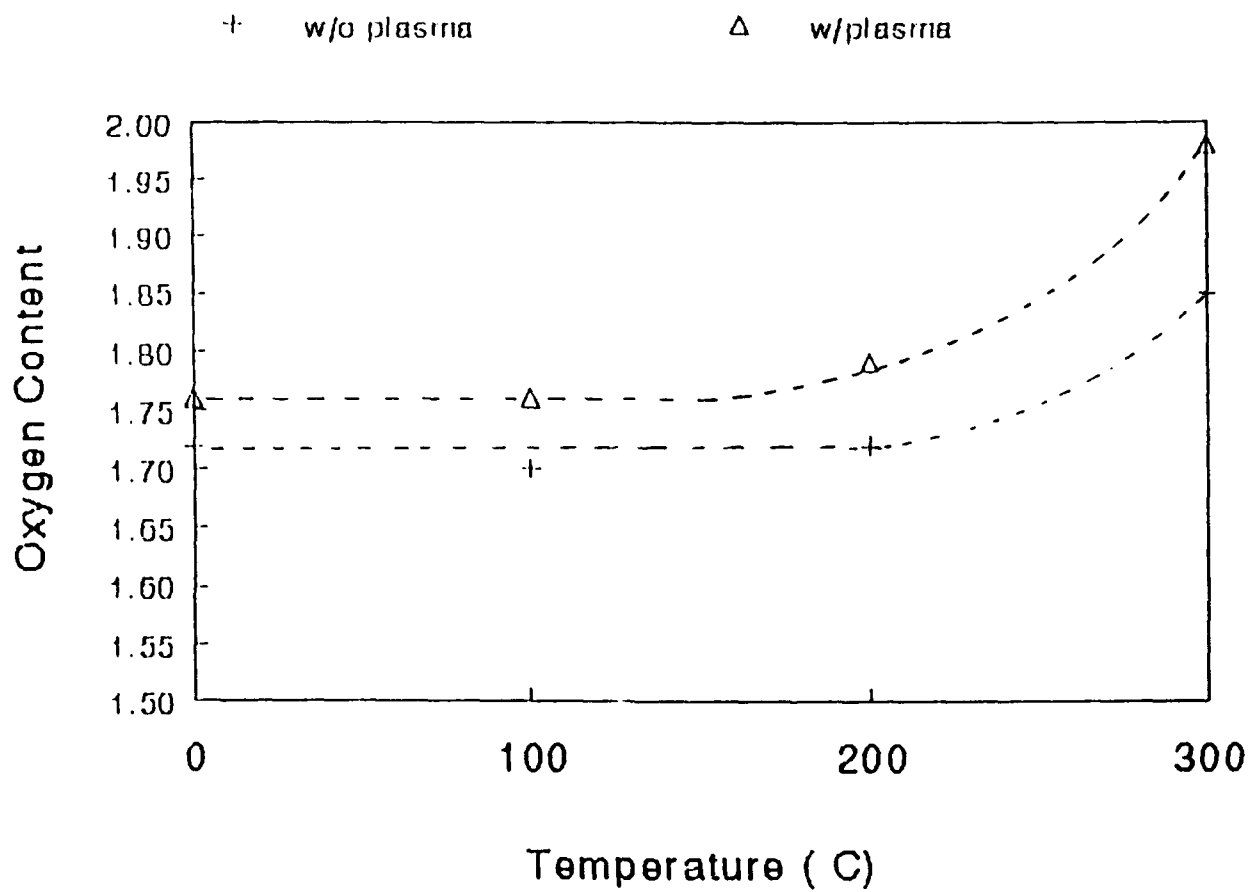   pressure in room temperature deposition.

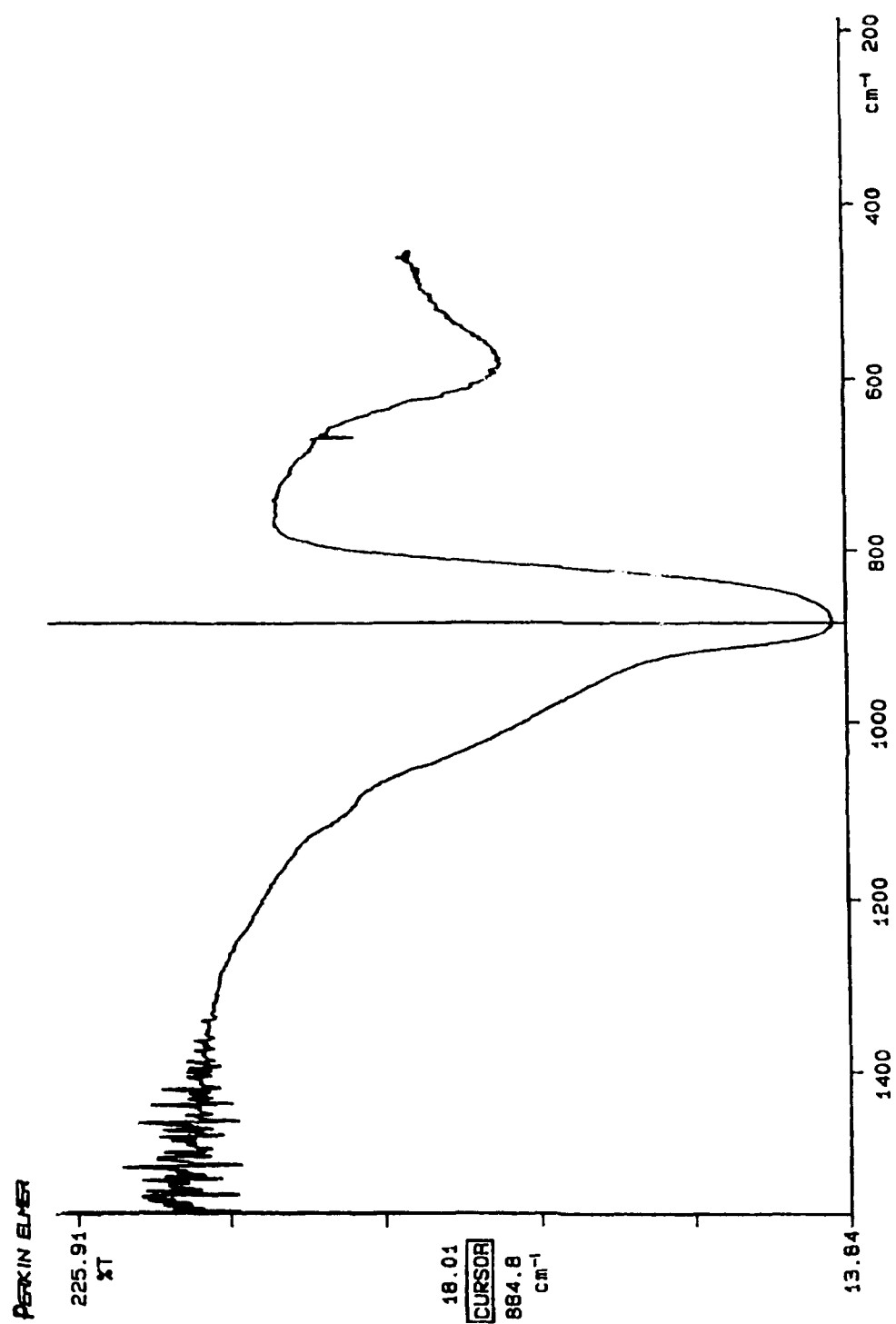FIG. 7   The effect of the plasma on film oxygen content at different substrate temperatures.

13-14

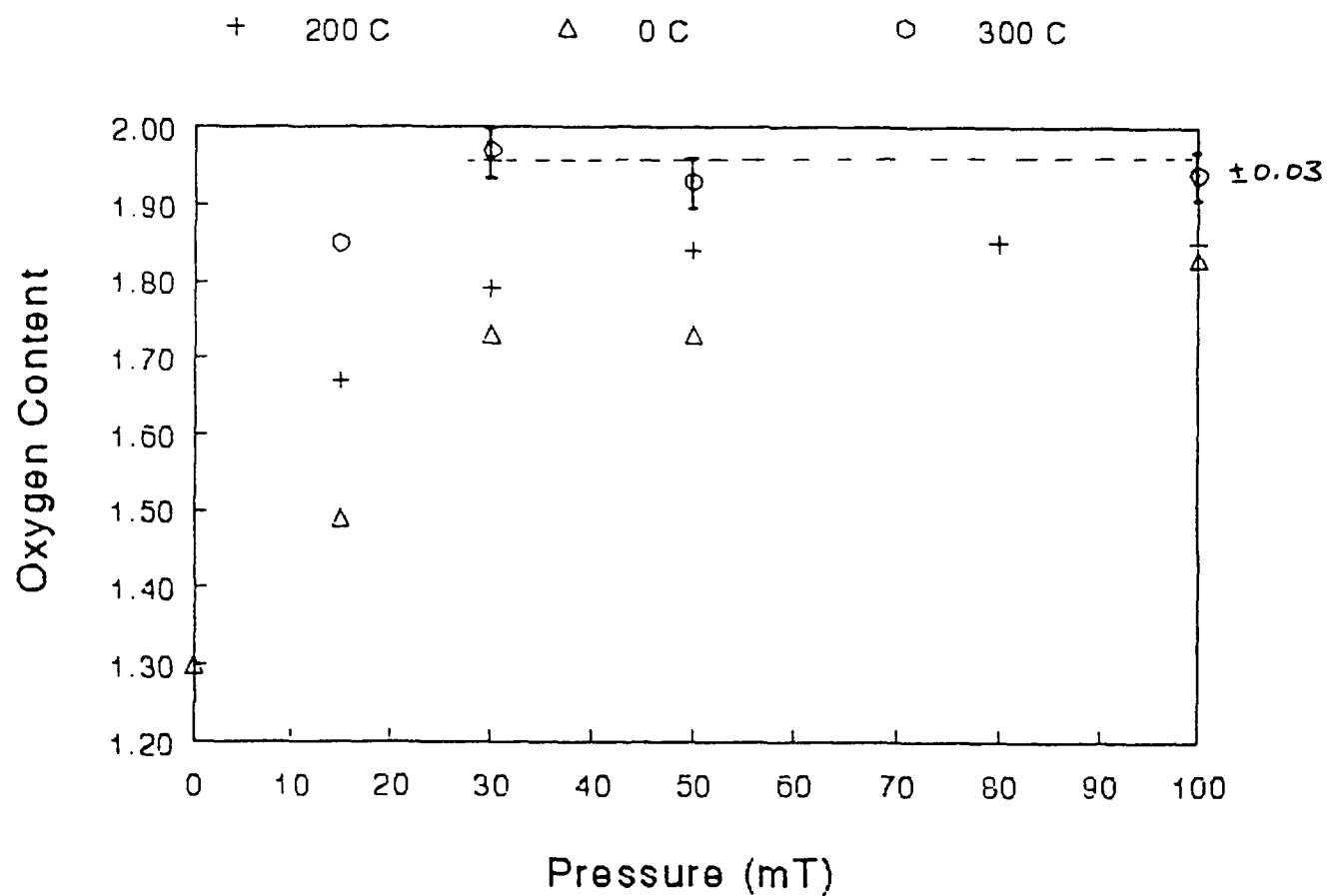Fig. 8   FTIR spectroscopic scan of a film deposited at 300°C and 30 mT oxygen pressure

FIG. 9   Variation of film oxygen content with ambient oxygen
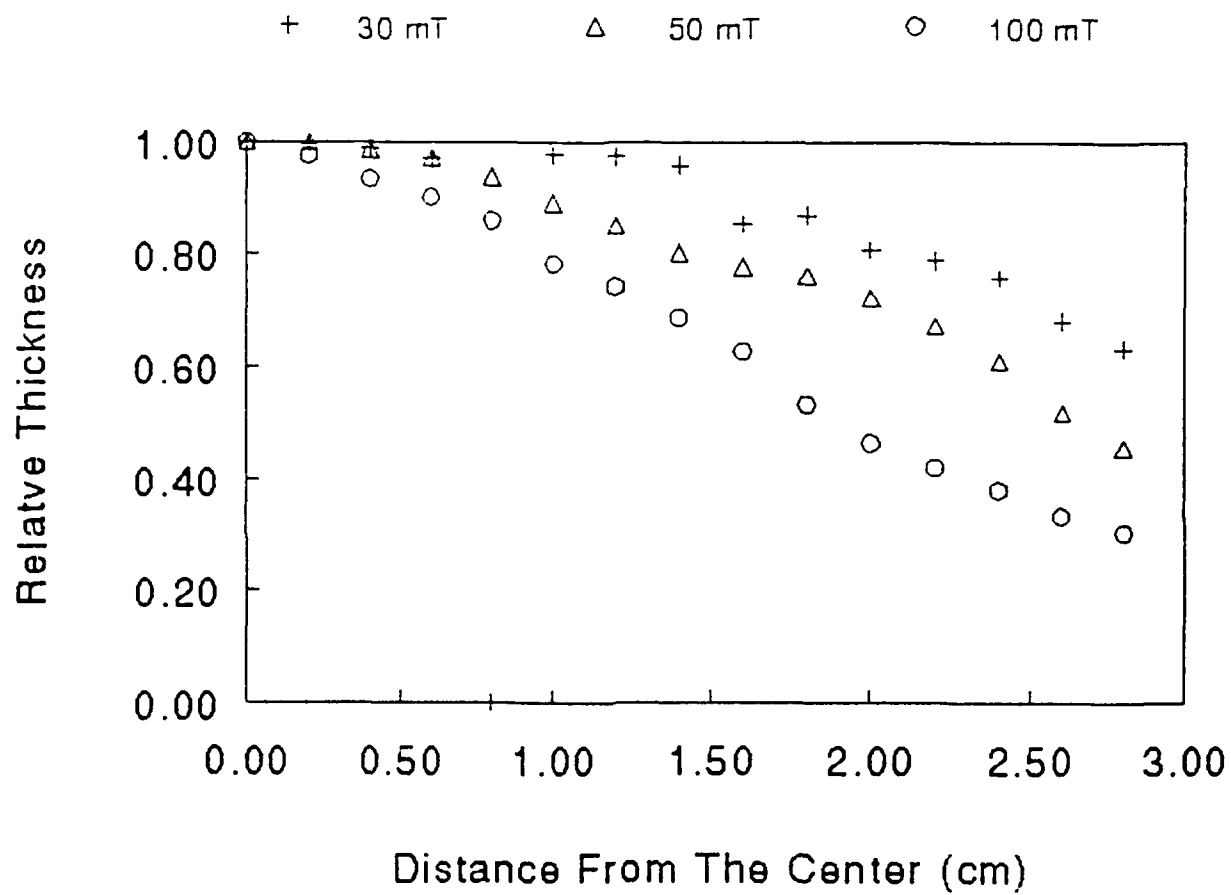   pressure at different substrate temperatures.

13-16

FIG. 10   Film thickness variation with pressure, along the major axis.
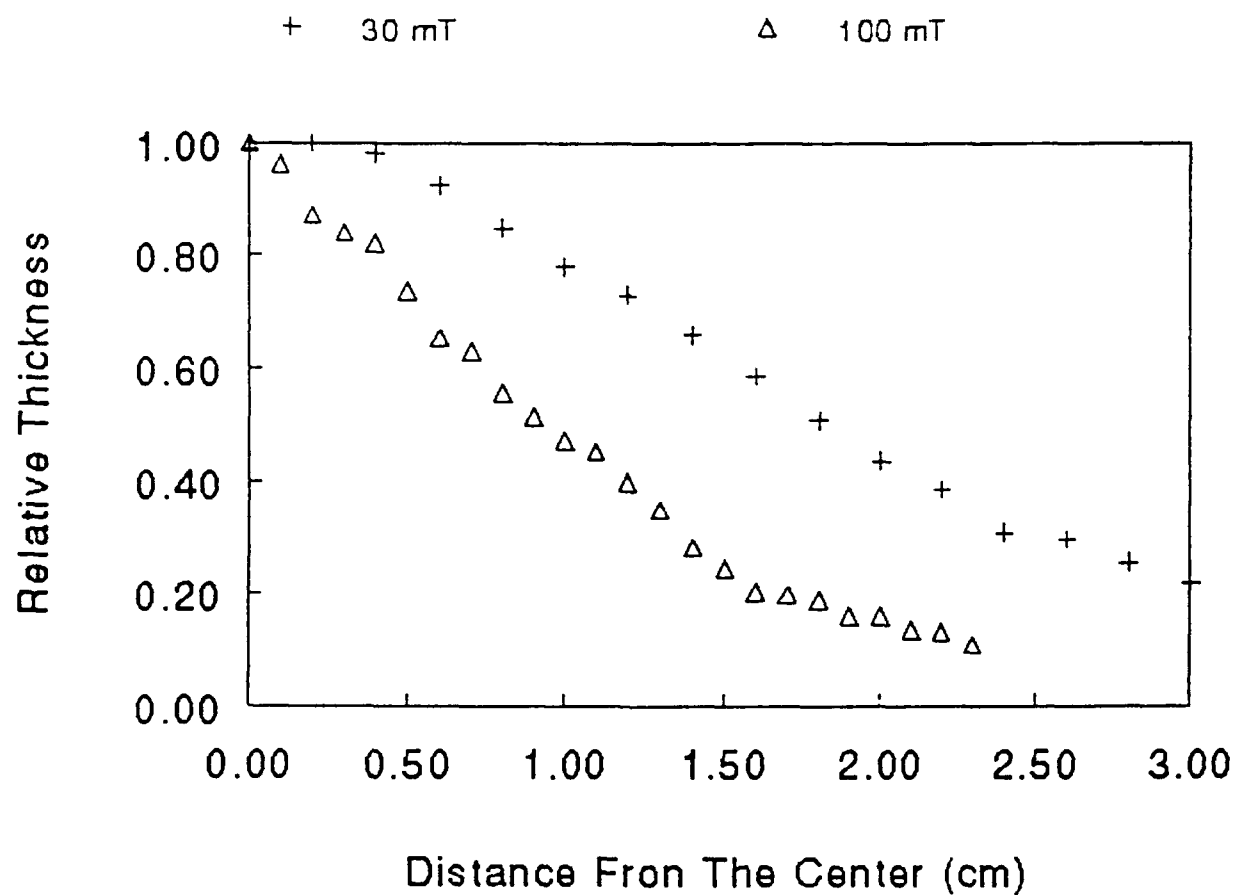
FIG. 11   Film thickness variation with pressure, along the minor axis.

over a 3.5cm length across the film, while for the film grown in 100mT pressure thickness varied 10% within a 1.2cm length of the film (Fig. 10). Thickness variation was more prominent along the minor axis (Fig. 11).

DISCUSSION

Oxygen content of the films is determined by the degree of gas phase and substrate surface reactions. It is seen from the experimental results that even at a very low pressure a significant gas phase reaction is present. Oxygen required to form $GeO_{1.3}$ during the ablation in vacuum may have been produced in the laser-target interaction. This is consistent with the observation of atomic oxygen emission in a GeO plume expanding in vacuum. The absence of GeO molecular emissions in the plume made it difficult to confirm the formation of GeO in the gas phase. Since the exothermisity of the $Ge + O^* ---> GeO$ reaction is only 1.93 eV [15], molecules are expected to be in the ground state and therefore none emitting. The GeO molecules formed in the gas phase through collisions will undergo a disprportionation reaction $2GeO ---> GeO_2 + Ge$ on the substrate. The atomic oxygen produced by the plasma and the elevated substrate temperature, lead to more efficient oxidation of the excess Ge at the substrate. However, the presence of the plasma does not bring about an appreciable change in the gas phase reaction. This is reflected in the observed small change in the oxygen content (1.72 to 1.76 at 30mT pressure) of the films grown with and without the plasma at room temperature. In contrast, the reaction at the substrate was significantly affected by the plasma at high temperatures.

ACKNOWLEDGMENTS

REFERENCES

[1] A. Inam, M. S. Hegde, X. D. Wu, T. Venkatesan, P. England, P. F. Miceli, E. W. Chase, C. C. Chang, J. M. Tarascon and J. B. Wachtman, Appl. Phys. Lett. 53, 908 (1988).

[2] S. Witanachchi, H. S. Kwok, X. W. Wang and D. T. Shaw, Appl. Phys. Lett. 53, 234 (1988).

[3] R. K. Singh, J. Narayan, A. K. Singh and J. Krishnaswamy, Appl. Phys. Lett. 54, 2271 (1989).

[4] H. S. Kwok, J. P. Zheng, S. Witanachchi, L. Shi and D. T. Shaw, Appl. Phys. Lett. 52, 1815 (1988).

[5] J. T. Cheung and H. Sankur, CRC Critical Reviews in Solid State and Materials Science. 15, 63 (1988).

[6] Masahara Tsuji, Naoki Itoh and Yukio Nishimara, Jap. J. Appl. Phys. 31, 2536 (1992).

[7] H. Sankur and J. T. Cheung, Appl. Physics A47, 271 (1988).

[8] T. Venketesan, X. D. Wu, A. Inam and J. B. Wachtman, Appl. Phys. Lett. 52, 1193 (1988).

[9] Z. Yi Lin and B. K. Garside, Appl. Opt. 21, 4324 (1982).

[10] C. Caperaa, G. Band, J. P. Besse, P. Bondot, P. Fessler and M. Jacquest, Mat. Res. Bull. 24, 1361 (1989).

[11] P. Bohac, L. Jastrabik, D. Chvostova and V. Zelezny, Vacuum, 41, 1466 (1990).

[12] P. J. Wolf, T. M. Christensen, N. G. Goit and R. W. Swinford, J. Vacuum Sci. Tech. Sep 1993.

[13] P. J. Wolf, to be published.

[14] D. A. Jishiashvili and E. R. Kutelia, Phys. Stat. Sol. 143, K147 (1987).

[15] G. A. Capelle and J. M. Brom Jr., J. Chem. Phys. 63, 5168 (1975).

THE EFFECT OF CALCIUM CHANNEL BLOCKERS AND NEUROPEPTIDE Y
ON VASCULAR SMOOTH MUSCLE CELL PROLIFERATION
IN CULTURE

Lawrence S. Lilienfield

Professor

Department of Physiology & Biophysics

Georgetown University School of Medicine

3900 Reservoir Rd., N.W.

Washington DC   20007

THE EFFECT OF CALCIUM CHANNEL BLOCKERS AND NEUROPEPTIDE Y
ON VASCULAR SMOOTH MUSCLE CELL PROLIFERATION
IN CULTURE

Lawrence S. Lilienfield
Professor
Department of Physiology & Biophysics
Georgetown University School of Medicine

Abstract

As an index of cell proliferation, incorporation of ^{3}H-thymidine, into pig coronary artery rings cultured without serum and into embryonic rat scular smooth muscle cells (A-10) cultured in medium with 2% fetal calf um, was determined during exposure for 48 hours to the calcium channel blocking agents verapamil, diltiazem and nifedipine and during exposure to porcine neuropeptide Y (NPY). Uptake after exposure to each of the channel blockers plus NPY was also studied. Results were different in the rings as compared to the studies of pure smooth muscle cells although, because of the small sample size, only a few of results of the study of the pig artery rings were statistically significant. The channel blockers alone in doses near 10^{-4} M and probably at 10^{-5} M diminished ^{3}H-thymidine uptake in the rings but clearly produced significant inhibition in the cells in pure culture. Although NPY had no measureable effect on the coronary rings it was significantly mitogenic when used in the pure cell culture studies. The combination of channel blockers with NPY did not totally eliminate the stimulating effect of NPY on cell proliferation although verapamil was most potent in this regard. We conclude that NPY is a mitogen whose cell proliferative effects are not totally mediated by the entry of calcium ion into the cells. Taken all together the results support the hypothesis that calcium for mitogenesis may be derived from both intracellular and extracellular sources. Further we speculate that the calcium channel blockers used in treating patients may not inhibit all of the coronary artery intimal smooth muscle proliferation in stressed patients who have increased NPY secretion but that verapamil, and to a lesser extent, nifedipine and diltiazem in that order of potency may diminish this undesireable effect. Additional studies are required to prove this hypothesis.

THE EFFECT OF CALCIUM CHANNEL BLOCKERS AND NEUROPEPTIDE Y
ON VASCULAR SMOOTH MUSCLE CELL PROLIFERATION
IN CULTURE

Lawrence S. Lilienfield

INTRODUCTION

In recent years it has become apparent that some patients with presumed essential hypertension show evidence of progressive coronary and renal disease despite control of their blood pressure. It has been recognized for some time that although good control of blood pressure removes most of the other risk associated with hypertension, the excess risk of coronary artery disease is reduced only in half.(1,2)

In the case of the kidney, the models which have generally been cited when considering possible explanations for the failure of blood pressure control to prevent renal disease have been the remnant kidney and the diabetic kidney. In each of these models evidence has been presented (in rats) that there is, ultimately, mesangial proliferation and glomerulosclerosis.(3,4) Recent studies have emphasized the importance of cytokines, cytoxins, and growth factors in producing the mesangial reaction. Many of these substances are also involved in the processes leading to atherosclerosis with intimal smooth muscle proliferation and/or left ventricular hypertrophy.(5,6,7)

Cellular growth is in part regulated by circulating and locally produced peptide hormones. Calcium mobilization is an integral part of transmitting the growth-regulatory signal produced by growth factors. It is possible that some of the therapeutic benefits of Ca^{++} channel blocking agents apart from their lowering blood pressure could be related to a resulting antiproliferative effect on coronary smooth muscle.(8)

This preliminary study tested this hypothesis by determining whether and which commonly used anti-hypertension agents reduce cell proliferation in segments of coronary artery and/or in pure cultures of vasular smooth muscle cells. Three Ca^{++} channel blockers and an angiotensin converting enzyme (ACE) inhibitor commmonly used to treat hypertension were studied.

14 - 3

Because of a possible role of neuropeptide Y in hypertension and because it has recently been suspected to have mitogenic properties, NPY alone and in combination with the Ca^{++} channel blocking agents or ACE inhibitor was included in the study.(9)

METHODOLOGY

Coronary artery rings:

Fresh pig hearts were obtained from 12 anesthetised immature female domestic swine weighing approximately 50 Kg used for training surgery residents and which, under approved protocols, were to be euthenized. None of the animals had had thoracotomy or laparotomy. All had had pretreatment with atropine, anesthesia induction with thiopental and, after intubation and attachment to a respirator, maintenance of anesthesia with halothane. Blood pressure and ECG were continuouusly monitored. After 2 to 3 hours, during which trainees practiced skin incision and suturing as well as some muscle debridment, the thorax was opened, the vena cavae and aorta, double-clamped and tied and the hearts removed under sterile precautions. One animal had a permanent cardiac arrest about 40 minutes before the heart was removed. Data from this animal is not included. Three of the animals were partially exsanguinated before cardiectomy. All of the hearts were rinsed quickly by submersion in normal saline, drained and then placed immediately in ice-cold Ringer-lactate solution in which they were stored for no longer than 1 hour. Ring segments (6 to 12 per heart) were cut under sterile conditions in a laminar flow hood from the left anterior descending coronary artery (LAD) 5 to 120 mm from their ostium just after exit of the circumflex. The rings were placed for 30 minutes in sterile oxygenated ice-cold DMEM containing 50 ug/ml gentamycin. Oxygenation of the DMEM was accomplished by exposure of the cold medium to 100% oxygen in a hyperbaric chamber at 2 times atmospheric pressure for 30-60 minutes. After this period the segments were placed in 24-well dishes containing 0.7, 0.8 or 0.9 ml IMEM solution supplemented with L-glutamine containing gentamycin (25 ug/ml) but no FCS. The results of the measurement of "blood gases" in a sample of the oxygenated cold DMEM used to treat the coronary

arteries are tabulated in Appendix A. It is apparent that the oxygen tension remains high in the solution for at least two hours.

Vascular smooth muscle cell culture:

Frozen viable vascular smooth muscle cells (A10) were obtained from the American Type Culture Collection, Rockville, Md. These cells were derived from embryonic rat aorta. Upon receipt the cells were thawed, placed in appropriate culture medium in a culture flask and incubated in a humidified 5% CO_2 atmosphere at 37 ^oC. The culture was examined daily and subcultured after trypsinization when approximately 75% confluent. Two days before they were to be used aliquots of trypsinized suspensions of cells were transferred to 24-well plates containing IMEM with glutamine and 2% FCS.

^3H-thymidine incorporation:

The coronary vessel segments in well plates were incubated overnight in a tissue culture incubator in a humidified 5% CO_2 atmosphere at 37 ^oC. After this period, 100 ul ^3H-thymidine (2 uCi/ml) was added together with either 100 ul of verapamil, diltiazem, nefedipine to achieve final concentrations of approximately 0.2 and 0.02 mM. ^3H-thymidine (2 uCi/ml) alone was added to at least one segment from each pig as a control. Forskalin (0.1 uM), NPY (0.001 mM) and (0.0001 mM) alone and in combination with the other agents and 10% fetal calf serum (FCS) were also tested. The segments (1 to 10 for each test solution) were further incubated for 48 hours. After removal from the medium the rings were washed with phosphate buffered saline (PBS) and incubated with cold thymidine (1 mM) for 20 minutes. After aspiration of the thymidine solution the rings were homogenized in 0.5 ml of PBS containing 2 x 10^{-3} M EDTA. An aliquot of the suspension was frozen and stored at -70 ^oC for future DNA determination. (See Appendix B.) Another 200 ul aliquot was digested in 0.4 ml of 0.5 N NaOH at 56 ^oC overnight and neutralized by addition of 100 ul of an equimolar amount of HCl. This solution was used for ^3H counting and for protein assay.

Similar treatment was given to the A-10 cell cultures growing in the well plates except that the concentrations of the calcium channel blockers

during the 48 hour treatment was 0.1 and 0.01 mM and the homogenization step before digestion was omitted.

^{3}H-thymidine determination:

A 100 ul aliquot of each sample of neutralized digested suspension was added to counting vials containing 3.0 ml of Aquascint. Duplicate samples were counted using an automatic liquid scintillation counter programmed to correct for background, and the results were tabulated in counts per minute (CPM).

Protein determination:

Protein concentration was determined in duplicate from 10 ul aliquots of the suspension employing the Pierce BCA method. Fresh working solution was prepared for each analysis in 96-well microliter plates. To the aliquots in the wells, 200 ul of working solution was added and the plates incubated for 1 hour at 37 °C. Standard solutions of albumin over the range of 0 to 1000 ugm/ml were also placed in the plates for analysis and curve plotting for conversion of optical density to concentration.

Test solutions:

Verapamil and diltiazem were dissolved in a 7.4 pH phosphate saline buffer (PBS) solution to make the stock solution (concentration 10 mM). nifedipine (10 mM), was dissolved in a 60% ethanol 40% PBS mixture. The mixture without nifedipine was also prepared as a nifedipine control. Forskalin was dissolved in DMSO to a stock concentration of 5 mM. Frozen lyophilized porcine NPY was rehydrated with minimal amounts of distilled water and diluted to a concentration of 0.01 mM with IMEM just before use. All stock solutions other than NPY were further diluted 1:10 or 1:100 with IMEM before use.

Analysis of the data:

Results were expressed as ^{3}H-thymidine uptake in cpm/mg of protein. Normalization of the data was required. The data was transformed and expressed as a decimal fraction of control uptake or incorporation. The

14 - 6

intra-experiment variation with the technique was high. The Neuman-Keuls
method for multiple comparisons analysis was used for ad-hoc comparisons.
P values of <0.05 were required as the limit for statistical significance
and were determined using a StatView computer program for a two-tailed t
test assuming a population mean of 1.0

RESULTS

Coronary Artery Rings:

The results of the incubaton of pig coronary artery segments with
calcium channel blockers are shown in Table 1. Control segments were
incubated in medium only with ^{3}H-thymidine. When verapamil, nifedipine or
diltiazem was present in concentrations in the medium of 0.18 mM, each
appeared to have inhibited thymidine uptake although in 1 of the 4 segments
where it was used, verapamil was associated with an increased uptake.
Inhibition seems to have also occurred at concentrations of 0.018 mM
although the small number of rings preclude a conclusion of statistical
significance. Ethanol at concentrations of 6.0 and 0.6 % seemed to reduce
uptake but the small number of ring segments studied also precludes
assumption of significance

The results of the incubation of pig coronary artery segments with NPY,
forskalin, and FCS are shown in Table 2. NPY had no effect at
concentrations of 0.001mM or 0.0001 mM. Forskalin (0.09 mM) significantly
decreased uptake and FCS (10%) increased uptake in 2 of 4 segments treated.

The results of the incubation of segments with a combination of NPY and
calcium channel blockers are shown in Table 3. NPY (.001 mM) did not semm
to alter the inhibiting effect of verapamil or nefedipine on thymidine
uptake. However in 3 of 7 segments, the NPY plus diltiazem combination
markedly increased thymidine incorporation.

Captopril at a concentration of 0.18 mM and at 0.018 mM decreased uptake
(Table 4). In the 1 segment treated with captopril plus NPY the uptake was
increased.

14-7

Table 1. Effect of Calcium Channel Blockers on Thymidine Uptake
in Coronary Artery Segments from Adolescent Pigs. Ratio of
CPM / mg protein in Samples to CPM / mg protein in Control Rings

Treatment	Ratio	Average	S.E.	N
Verapamil (0.18 mM)	0.94 3.66 0.24 0.41	1.31	0.80	4
Verapamil (0.018 mM)	0.26	0.26		1
Diltiazem (0.18 mM)	0.51 1.10 0.23 0.17 0.78 0.39 0.69 0.23	0.51	0.12	8
Diltiazem 0.018 mM	0.40 0.34	*0.37	0.03	2
Nifedipine (0.18 mM)	1.33 0.23 0.27 0.26 0.76 0.30 0.72 0.36	*0.53	0.14	8
Nifedipine 0.018 mM	0.42 0.31	0.37	0.05	2

* P < 0.05 vs control   Control rings were untreated.

Table 2. Effect of FCS, Forskalin and NPY on Thymidine Uptake
in Coronary Artery Segments from Adolescent Pigs. Ratio of
CPM / mg protein in Samples to CPM / mg protein in Control Rings

Treatment	Ratio	Average	S.E.	N
FCS '(10%)	1.02 0.52 2.72 1.44	1.43	0.47	4
Forskalin (0.09 mM)	0.89 0.28 0.42 0.39 0.32 1.30 0.00 0.48 0.36 0.59	*0.50	0.11	10
NPY 0.001 mM	0.45 0.29 1.06 0.82 1.29 0.53 1.39 0.93	0.85	0.14	8
NPY 0.0001 mM	0.48 0.77 1.10	0.78	0.18	3

* P < 0.05 vs. controls   Control rings were untreated.

Table 3. Effect of Calcium Channel Blockers plus NPY on Thymidine Uptake in the Coronary Artery Segments from Adolescent Pigs. Ratio of CPM / mg protein in Samples to CPM / mg protein in Control Rings

Treatment	Ratio	Average	S.E.	N
Verapamil	0.25	0.87	0.42	4
(0.18 mM)	0.80			
plus NPY	2.08			
(0.001 mM)	0.34			
Diltiazem	2.21	1.79	0.56	7
(0.18 mM)	4.50			
plus NPY	1.13			
(0.001 mM)	0.73			
	0.48			
	1.39			
	3.76			
	0.16			
Nefedipine	0.26	*0.30	0.04	2
(0.18 mM)	0.35			
plus NPY				
(0.001 mM)				

*P <0.05 vs. control   Control rings were untreated.

Table 4. Effect of An ACE Inhibitor (Captopril) on Thymidine Uptake in the Coronary Artery Segments from Adolescent Pigs. Ratio of CPM / mg protein in Samples to CPM / mg protein in Control Rings

Treatment	Ratio	Average	S.E.	N
Captopril	0.37	*0.49	0.13	4
(0.18 mM)	0.30			
	0.87			
	0.42			
Captopril	0.26	0.73	0.21	4
(0.018 mM)	0.51			
	1.21			
	0.94			
Captopril	1.83	1.83		1
(0.018 mM)				
plus NPY				
(0.001 mM)				

*P < 0.05 vs control   Control rings were untreated.

Vascular Smooth Muscle Cell Culture:

The results of the incubation of cultures of rat embryo thoracic aorta smooth muscle cells (A-10) with calcium channel blockers are shown in Fig. 1 and Table 5.
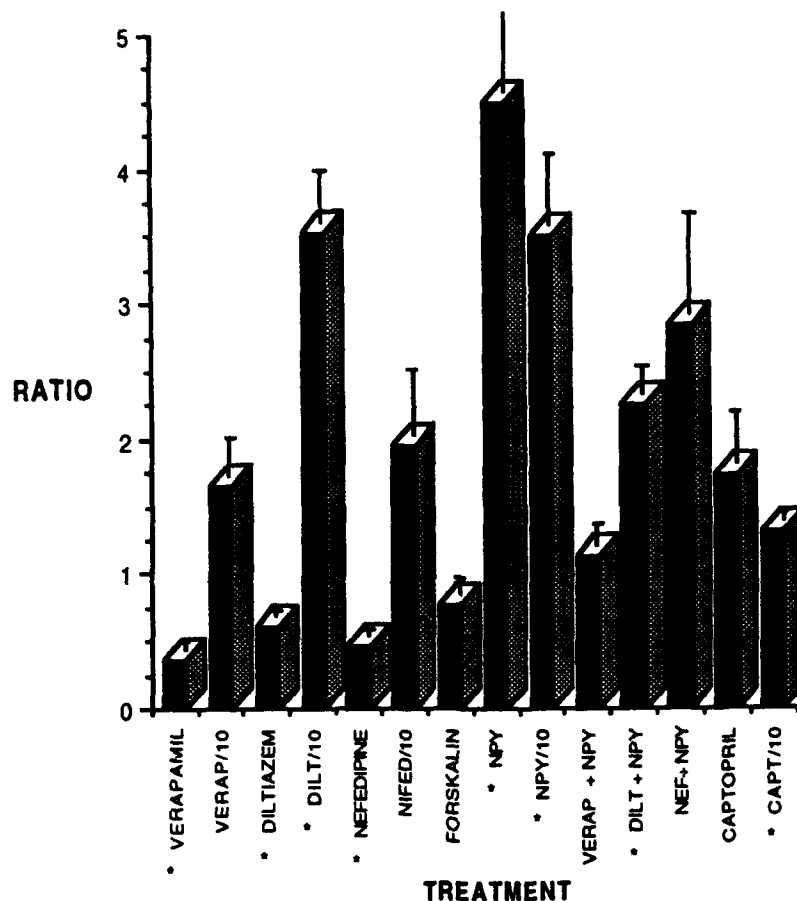
FIGURE 1. Ratio of thymidine uptake in treated vascular smooth muscle cells as compared to untreated controls. Statistical significant ratios (P < 0.05) are marked with *. Error bars show standard error of the mean of samples similarly treated.

Verapamil, diltiazem and nifedipine in concentrations of 0.1 mM decreased thymidine incorporation. At concentrations of 0.01 mM all of the blockers were associated with an increase in uptake although this was only statistically significant for diltiazem.

Table 5. Effect of Treatment with Calcium Channel Blockers on Thymidine Uptake by Vascular Smooth Muscle Cells in Culture. Ratio of CPM / mg protein in Treated Cells to CPM / mg protein in Untreated Cells.

Treatment	Ratio	Average	S.E.	N
Verapamil (0.1 mM)	0.65			
	0.27			
	0.28	*0.36	0.06	6
	0.30			
	0.31			
	0.32			
Verapamil (0.01 mM)	1.09			
	1.13			
	1.20	1.65	0.28	6
	2.85			
	2.04			
	1.61			
Diltiazem (0.1 mM)	0.63			
	0.62			
	0.63	*0.61	0.03	6
	0.65			
	0.66			
	0.47			
Diltiazem (0.01 mM)	2.91			
	4.43			
	2.77	*3.52	0.40	4
	3.96			
Nifedipine (0.1 mM)	0.52			
	0.61			
	0.36	*0.47	0.04	6
	0.38			
	0.55			
	0.40			
Nifedipine (0.01 mM)	2.94			
	0.68			
	3.75	1.96	0.47	6
	1.41			
	1.83			
	1.19			

* P < 0.05 vs control   Control rings were untreated.

NPY in concentrations of 0.001 mM and 0.0001 mM significantly increased uptake, three to fourfold (Table 6), whereas forskalin at 0.1 mM seemed to diminish uptake. The addition of the calcium channel blockers at concentrations of 0.1 mM to NPY at 0.001 mM (Table 7) produced a reduction in the stimulating effect of NPY as compared with controls but only verapamil completely abolished the NPY effect.

The results of the use of captopril and NPY plus captopril are shown in Table 8. At both 0.1 mM and at 0.01 mM captopril stimulated uptake. When combined with 0.001 mM NPY, the uptake quadrupled as compared to controls.

DISCUSSION

In both cultured coronary artery segments and in cultures of vascular smooth muscle cells all of the calcium channel blockers at concentrations of 10^{-4} or 10^{-5} M inhibited cell proliferation. The small number of segments studied thus far precludes firm conclusions regarding sensitivity but the results are suggestive that the vascular segments respond better than the pure smooth muscle cells to the lower concentrations. This could be related to the presence in the segments of endothelium and its associated factors. Further studies are needed to clarify this important point. No differences were noted among the three calcium blocking agents when used alone except that, and only at the lower concentration, diltiazem seemed to stimulate proliferation in the pure cell cultures, a phenomenon not observed with the other calcium channel blockers.

Captopril is a potent angiotensin converting enzyme inhibitor. In the vascular segments this ACE inhibitor apparently cosiderably reduced cell proliferation although the small number of segments studied was not sufficient to be conclusive. This inhibitory effect was not found in the studies of pure cells in culture where in fact captopril, if anything, seemed to stimulate proliferation. It is possible that the known mitogenic effect of angiotensin II requires endothelial factors.

NPY at concentrations of 10^{-6} and 10^{-7} M markedly stimulated cell proliferation in the pure cell cultures but not in the vascular segments. The addition of verapamil to the NPY completely prevented the proliferation whereas the addition of nifedipine had an inconsistent effect. Diltiazem

Table 6. Effect of Treatment with Forskalin and NPY on Thymidine Uptake by Vascular Smooth Muscle Cells in Culture. Ratio of CPM / mg protein in Treated Cells to CPM / mg protein in Untreated Cells.

Treatment	Ratio	Average	S.E.	N
Forskalin (0.1 mM)	0.52 0.81 0.93	0.76	0.12	3
NPY 0.001 mM	7.35 4.89 2.93 3.36 3.97	*4.50	0.79	5
NPY 0.0001 mM	4.18 3.05 4.56 2.24	*3.51	0.53	4

* P < 0.05 vs. controls   Control rings were untreated.

Table 7. Effect of Calcium Channel Blockers plus NPY on Thymidine Uptake by Vascular Smooth Muscle Cells in Culture. Ratio of CPM / mg protein in Treated Cells to CPM / mg protein in Untreated Cells.

Treatment	Ratio	Average	S.E.	N
Verapamil (0.1 mM) plus NPY (0.001 mM)	0.94 1.15 0.95 0.77 1.83 1.08	1.13	0.16	6
Diltiazem (0.1 mM) plus NPY (0.001 mM)	2.95 1.87 2.47 1.97 2.06	*2.26	0.20	5
Nefedipine (0.1 mM) plus NPY (0.001 mM)	2.80 4.70 2.80 1.07	2.84	0.74	4

P <0.05 vs. control   Control rings were untreated.

14-13

Table 8. Effect of An ACE Inhibitor (Captopril) on Thymidine Uptake by Vascular Smooth Muscle Cells in Culture. Ratio of CPM / mg protein in Treated Cells to CPM / mg protein in Untreated Cells.

Treatment	Ratio	Average	S.E.	N
Captopril (0.1 mM)	1.00 0.32 2.34 2.40 1.61 2.76	1.74	0.38	6
Captopril (0.01 mM)	1.24 1.14 1.54 1.33 1.25 1.43	*1.32	0.06	6
Captopril (0.1 mM) plus NPY 0.001 mM	6.19 1.17 2.91 2.98 8.19 5.28	*4.45	1.05	6

*P < 0.05 vs control   Control rings were untreated.

consistently only partially inhibited NPY induced proliferation. Captopril had no inhibiting effect on NPY induced proliferation.

NPY's mitogenic potential was first reported by Zukowska *et al* in studies on vascular smooth muscle cells in culture.(9) This study confirms their findings. NPY is well known to be a very potent vasoconstrictor which works synergistically with norepinephrine when released during strong sympathetic nervous system stimulation. During severe and chronic stress measureable amounts of NPY can be detected in serum. It is possible that the progression of coronary atherosclosis in chronically stressed patients may at least be partially attributed to the effect of NPY on intimal smooth muscle proliferation. The lack of complete effectiveness in preventing progression of coronary artery disease in patients treated with anti-hypertensive drugs may be related to differences in the drugs effects on cell proliferation. From the present study it could be concluded that verapamil has an advantage over the other calcium blockers in its potency as an inhibitor of NPY induced proliferation. Further confirmation would be essential to validate this important conclusion.

All of the calcium channel blockers studied would appear to be useful in inhibiting vascular smooth muscle cell proliferation induced by mitogens other that NPY. Which mitogens and the mechanism(s) for this inhibition remain another subject for future investigation.

REFERENCES

1. Shulman NB, Ford CE, Hall WD et al. Prognostic value of serum
creatinine and effects of treatment of hypertension on renal function:
results from the Hypertension Detection and Follow-up Program.
Hypertension 13(suppl):180-193 1989

2 Walker WG, Neaton JD, Cutler JA, et al. Renal function change in
hypertensive members of the Multiple Risk Factor Intervention Trial.
JAMA: 268:3085-3091 1992

3. Brenner BM. Nephron adaptation to renal injury or ablation. Am J
Physiol: 249:F324-337 1985

4. Schultz, PJ,and Raij L. The glomerular mesangium: role in initiation
and progression of renal injury. Am J Kid Dis: XVII (suppl 1):8-14 1991

5. Raij L. Mechanisms of vascular injury: the emerging role of the
endothelium. JASN 2 (suppl 1): 52:58 1991

6. Appel RG. Growth-regulatory properties of atrial natriuretic factor.
Am J Physiol. 262 (6 Pt 2):F911-918 1992

7. Laporte S, and Escher E. Neointima formation after vascular injury is
angiotensin II mediated. Biochem Biophys Res Commun. 187(3):1510-6 1992

8. Re RN, and Chen L. Growth factors and cardiovascular structure:
implications for calcium antagonist therapy. A J Hypertens. 4:460S-465S
1991

9. Zukowska-Grojec Z, Pruszczyk P, Colton Z, Yao J, Shen G, Myers A and
Wahlestedt C. Mitogenic effect of neuropeptide Y in rat smooth muscle
cells. Peptide 14:263-268 1993

Protocol:

A sterile specimen cup was used to hold approximately 200 ml of DMEM solution to which gentamycin (50 u/ml) had been added. The container was surrounded with ice and placed in a hyperbaric chamber.   After exposure for 30 minutes to 100% oxygen at 2 atmospheres of pressure the chamber was rapidly decompressed and measurements made over the subsequent 1 1/2 hours as follows:

Time from 0 (min)	pH	pCO2	[K +]	[Ca ++]	Temp	pO2
3	7.53	37.8	5.0	1.40	37	523
33	7.54	36.7	5.0	1.40	37	516
49	7.55	36.2	5.0	1.41	37	520
72	7.58	33.4	5.0	1.40	37	499
105	7.59	32.6	5.0	1.40	37	483

Conclusion:

The pO2 after oxygenation by this method remains high over the next 100 minutes.

$y = 529.91 * 10^{(-3.5045e-4x)}$ $R^2 = 0.865$
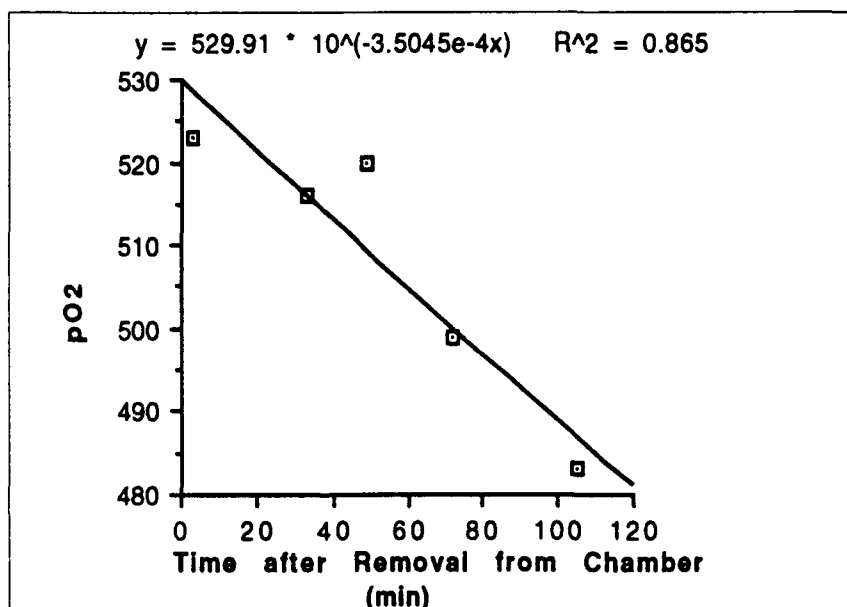
FIGURE 2.   Disappearance of oxygen from DMEM solution exposed to 100 % oxygen at 2 atmospheres of pressure.

14-17

DNA ASSAY

The purpose of this subproject was to develop a method for use in the Laboratory of Clinical Investigations for the rapid measurement of DNA in homogenized tissue samples and/or cell suspensions employing the assay procedure developed by Labarca and Paigen. The method is based on the fluorescence developed when bisbenzimidazole (Hoechst 33258) binds to DNA. Tissue homogenates were made with or cells were suspended in PBS (pH 7.4) containing 2 M NaCl and 2 mM EDTA.

It was necessary at first to determine optimum excitation and emission settings for the Perkins-Elmer U-V fluorescent spectrophotometer in the laboratory. Standards solutions of DNA were made over a range of concentrations and standard curves developed. An excitation slit of 5 nM and an emission slit of 7 nM gave optimum signal to noise ratios. Disposable plastic cuvettes were found to be suitable although quartz cuvettes gave more consistent results. Reusing the same cuvette was found to be important in comparing samples. Two dilutions of the dye were studied in order to determine whether sensitivity could be improved. Although at the lower dye concentration the "background" intensity was reduced, the slope of the standard curves was diminished (Fig 8).
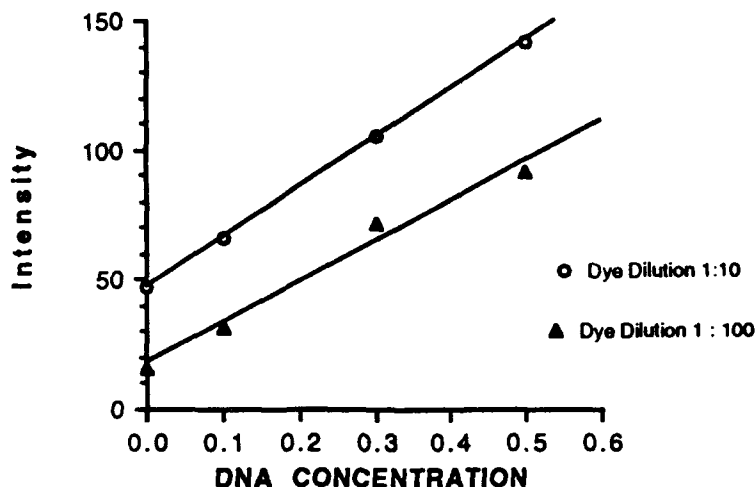

Figure 3. Comparison of Standard DNA Curves at Dye Dilutions of 1:10 and 1:100 The slope of the 1:10 curve is significantly steeper than that of the 1:100 dilution.

Tests were also run to determine the effect of time after addition of dye on the subsequent measureable emission intensity. Small but significant differences between water and protein blanks were also observed.

14-18

Studies of the time course of emission intensity of cell suspensions demonstrated a doubling of intensity over a 2 hour period following addition of dye.

Table 8. Intensity at 458 nM of
different amounts of cell suspensions
at times (minutes) after dye addition

Time	300 ul	200 ul	100 ul
5	69	49	28
30	78	59	35
45	89	66	44
60	96	79	53
90	115	93	50
120	131	106	62

Approximately 1,000,000 cells/ml.

The intensity of emission from pure DNA standards after dye addition however were quite stable over this period.

Blanks were prepared with only PBS and with PBS containing albumin at a concentration of 1%. The background fluorescence was almost twice as high from the albumin containing solution.

Additional studies need to be done to determine the optimal waiting time following the addition of the dye to cell suspension and tissue homogenate samples. Until this is done it would be prudent to read each sample intensity at approximately the same time following the dye addition. In this regard it was noted that most of the intensity develops with these DNA containing samples within the first minute and increases at a rate near 1% per minute for 2 hours.

1992 USAF-RDL FACULTY RESEARCH PROGRAM
Sponsored by the
AIR FORCE OFFICE OF SCIENTIFIC RESEARCH
Conducted by the Research and Development Laboratories

FINAL REPORT

TEMPERATURE EFFECTS ON AQ. POLYMER AND BIOPOLYMER SOLUTION VISCOSITIES, AND ERYTHROCYTE SEDIMENTATION RATES AND CELL VOLUMES IN MAMMALIAN BLOOD.

Prepared by: W. Drost-Hansen
                                          Mag. scient. (Ph.D.)
                                          Associate #: 91

Academic Rank: Professor

Department and University: Lab. for Water Research
                                          Department of Chemistry
                                          University of Miami
                                          Coral Gables, FL 33124

Research Location: Clinical Investigation Directorate
                                          Wilford Hall Medical Center
                                          Lackland AFB
                                          San Antonio, TX 78236

Student Co-Investigator: Julio L. Camacho
                                          Department of Chemistry
                                          University of Miami

USAF Researchers: Lt. Col. Wayne Patterson, Ph.D.
                                          Col. John H. Cissik, Ph.D.

Date: September 25, 1992

INTRODUCTION

After more than 70 years the Erythrocyte Sedimentation Rate continues to be used extensively in clinical and veterinary medicine (especially overseas.) However, the detailed dynamics of the ESR continues to escape a rigorous description although in principle many of the factors which influence the sedimentation process are well understood. The primary factors involved are the tendency for rouleaux formation (reflecting the RBC surface adsorption from the complex, macromolecular chemistry of the blood plasma), the plasma viscosity, shear rate, hematocrit, erythrocyte morphology, and a number of other factors of less direct influence.

We have continued our studies of the ESR over a wide temperature range; thus, while our previous measurements were restricted to approx. the range from 24° to 52° C, we have now extended the range down to about 8 °C for number of previously studied species (and a few new species.) At the same time, because of the expected Stokesian involvement of "particle size", we have continued our Mean Cell (RBC) Volume [MCV] measurements (and also Mean Platelet Volume [MPV] measurements) as functions of temperature. These volume measurements are highly useful for delineating the effects of temperature on the osmotic processes involved in volume control of the cell sizes. Finally, because of the importance of the plasma viscosity we have also measured viscosities of aqueous solutions of a variety of polymers: both model polymers (such as Polyvinyl pyrrolidone, Polyethylene oxide and Dextran) and some biochemically important macromolecules (such as Bovine Serum Albumin [BSA], Fibrinogen and Cytochrome-c.) Anomalous thermal responses continue to be observed at the Drost-Hansen thermal transition temperatures (T_k, near 15, 30, and 45 °C) in nearly all parameters measured!

PART I.   ESR MEASUREMENTS

Erythrocyte sedimentation rates have been measured in whole blood from a number of healthy humans ana various mammals, including some not investigated in our earlier studies. In some cases, the range of the ESR measurements have been extended to include lower temperatures, namely to encompass the 15 ^{O} C anomaly of the vicinal water (i.e. the cell-associated water and the water of hydration of the aqueous macromolecules of the blood plasma.) As in previous years, the measurements are made using Wintrobe tubes placed in the Temperature Gradient Incubator (TGI = "polythermostat") for varying lengths of time. The results — distance settled after Y hours -- is plotted as a function of the Well number in the TGI. The Well # is

essentially proportional to the actual temperature (i.e. usually the temperature gradient in the bar is approximately linear.) In all graphs shown for ESR, MCV and MPV data, a few temperatures are indicated in the graphs; other temperatures may be estimated by linear interpolation. A typical example of a sed. curve is shown in Fig. 1; data for a killerwhale after incubation for 4.0 hrs.
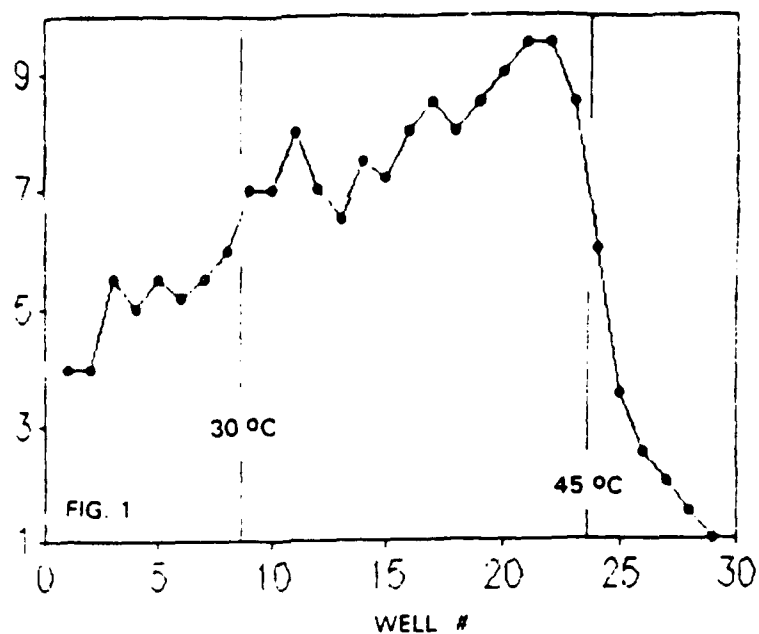
In general, the ESR curves closely resemble those obtained previously for the "high-temperature range" (about 24 - 54 °C.) Some variability has been observed in the case of the non-human samples: very high sed rates have been noted in samples from possibly sick animals as well as some cases of extremely low sed rates, — for instance for a dog (run 92TGI10B) with a sed rate of < 1 mm after 4 hours at 25 °C. However, in all cases studied a dramatic decrease in sed rate occurs for temperatures above 44 - 46 ° C. regardless of the species, suggesting as before a distinct effect of the vicinal water. Blood plasma viscosities also change near 45 °C [please see Part V: viscosity data] but not nearly enough to account for the dramatic decrease in the sed rates. On the other hand, erythrocyte morphology does change at this critical temperature and we tentatively propose that the effects of the structural changes in the vicinal water is manifested via its influence on the red cell-associated spectrin. A considerable literature now exists which strongly suggests that spectrin plays a major role in stabilizing the red cell morphology. The spectrin molecule has a MW of about 240 000 Dalton (and may form dimers and possibly larger aggregates). Thus it is hardly surprising if the structural aspects of the vicinal water of hydration of the spectrin influence the stability of the spectrin. At the thermal transition temperature, the vicinal water is believed to undergo a structural phase transition from one stabilized structure below 45 ° to another, stable but different structure above this critical temperature. Most likely the transition state between these two stabilized forms is characterized by notably increased disorder, thus likely resulting in a concommitant decrease in the stability of the spectrin conformation/association. This destabilization of the spectrin "framework" may thus lead to morphological changes of the RBC -- vividly visualized in photomicrographs of the RBC after exposure to the higher temperatures [see below.]. The tendency to rouleaux formation must be significantly reduced due to the morphological changes and this in turn is likely the primary reason for the drastic decrease in the sed rate above the critical temperature. Furthermore, changes are also expected in the nature and extent of protein adsorption on the surface of the RBC, again affecting the degree of rouleaux formation and thus affecting the sed rate.

Measurements of sed rates around the two lower vicinal transition temperatures, 15 ⁰ and 30 ⁰ C, sometime reveal changes at these critical temperatures but these effects are far smaller than for the 45 ⁰ anomaly, and in fact, sometimes not seen at all. Two relatively typical examples of sed rates at low temperatures are shown in Fig. 2 and Fig.3 - respectively for a dog and a Yucatan pig. The role of the vicinal water in these cases may be primarily via the influence on the vicinal hydration of the plasma proteins and the cell membranes. This suggestion is consistent with the frequently observed anomalies at T_k seen in the viscosity measurements on various protein solutions and blood plasmas. Likewise, the vicinal water may also influence the extent of erythrocyte surface adsorption of the proteins at low temperatures involved in the rouleaux formation.

Less pronounced suggestions of anomalies are also sometimes seen in sed rates near 21 (⁺/₋ 1) ⁰C. Such sed rate anomalies have previously been reported also by Prof. R. Glaser et al. (of Humbolt University, Berlin) and ascribed by these authors to membrane bound lipid phase transitions.

Finally, in some - but by no means all - sed rate measurements, indications of anomalies may also been seen near 37 ⁰ C. Again it is tempting to suggest that these anomalies, like the one near 21 ⁰, may be the result of a (membrane) lipid phase transition. On the other hand it is difficult to envision why anomalies should occur near this temperature as 37 ⁰ - 38 ⁰ C is close to the body temperature of most mammals. It would seem impractical during evolution to allow a homeostatic system to operate near a critical temperature where the changes in properties over a narrow temperature range might lead to notably different stabilities. In the future this point deserves close attention because of the possible clinical implications of body temperature control in the normal and febrile patient. Because of the excellent reproducibility and precision of our sed rate measurements and Mean Cell Volume data such measurements may prove uniquely well suited for a detailed study of the blood around body temperature. Thus it would be easy to program the Temperature Gradient Incubator to allow (nearly) simultaneous measurements from, say, 32 ⁰ C to about 42 ⁰ C, thus providing great resolution with data points spaced only 0.3 ⁰ apart.

DISTANCE SETTLED (mm); FOR Δt = 4.0 hr.
KILLERWHALE (MALE). 92TGI19B

FIG. 1

30 °C

45 °C

WELL #

DISTANCE SETTLED (mm); FOR Δt = 4.0 hrs
DOG 92TGI04B

FIG. 2

15 °C

[25 °C]

WELL #

LOG [DISTANCE SETTLED. mm]; FOR Δt = 1.0 hr
YUCATAN PIG. 92TGI08B

FIG. 3

15 °C

30 °C

WELL #
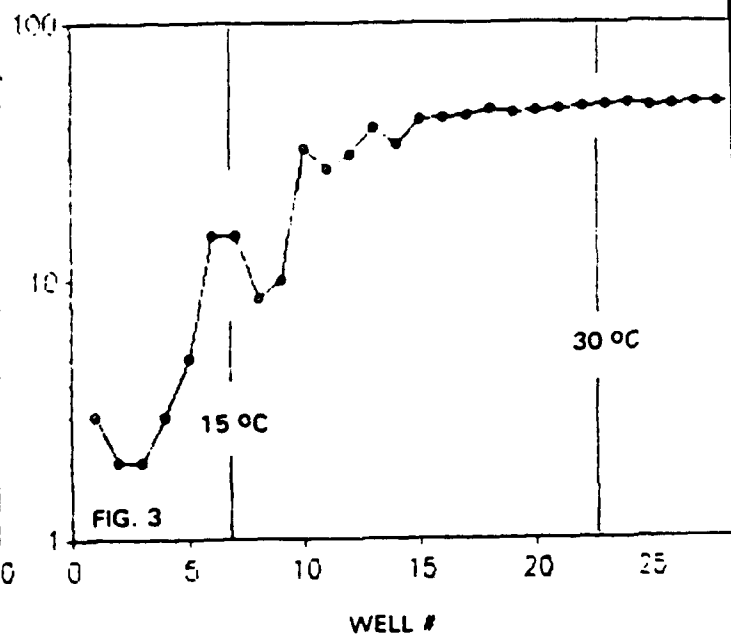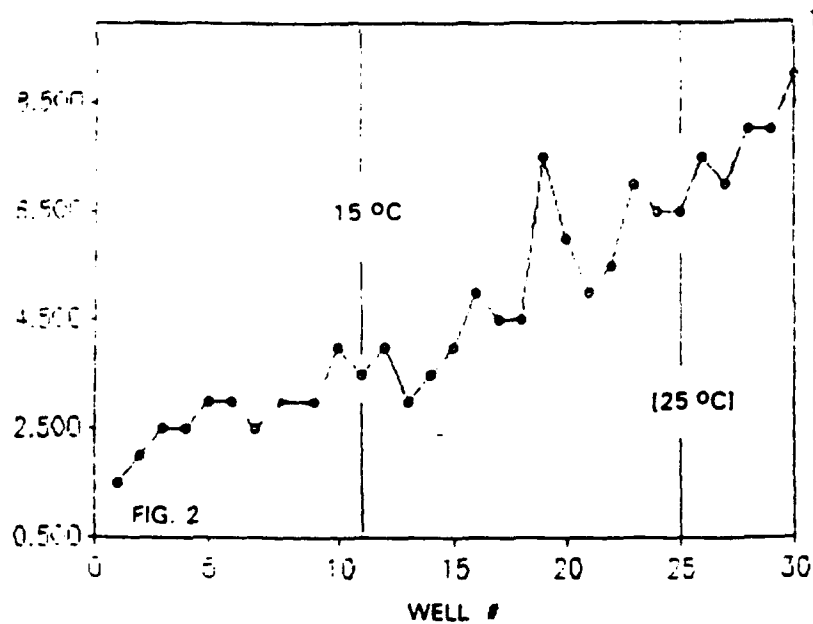
PART II.   MEAN (RED) CELL VOLUME MEASUREMENTS.

Mean Cell Volume (MCV) measurements have been continued this year both because of the potential role of the cell volumes in determining the ESR and because of the intrinsic interest of cell volumes for an understanding of the osmotic processes in living organisms. As before, the MCV data were obtained with a Baker, Model 9000, Hematology Counter. Usually, MCV measurements were made immediately after the whole (anticoagulated) blood was removed from the Temperature Gradient Incubator (the TGI) after incubation at the various temperatures. From a series of separate measurements it was shown that -- regardless of the range of incubation temperatures, -- the MCV (and MPV as well) remained unchanged for periods of at least two hours after removal of the samples from the TGI with storage at room temperature. As in earlier years, the reproducibility of the cell volume measurements was excellent, usually better [or far better] than 1 %; this is amply illustrated by an inspection of the rather smooth curves of cell volumes as a function of temperature.

As observed in our previous studies, the MCVs invariably show dramatic changes at 44 - 46 °C! Obviously something dramatic happens in this temperature range and the degree of abruptness suggests that a phase transition is most likely responsible. As there are no major lipids with a phase transition at this temperature it is almost inescapable that the transition is due to the vicinal water with its well-documented transition (T[k]) at 45 °C. However, in the past it was not at all obvious, on a molecular scale, where is the "site of action" of the vicinal water. As discussed above (under ESR) it now appears likely that the red cell structural protein spectrin is the moiety most strongly affected by the structural transition of the vicinal water. [We wish to thank Professor J.Stuart of University of Birmingham, UK, for this suggestion.] If indeed the configuration of the spectrin molecule is notably destabilized at the temperature where the vicinal hydration structures change it would be reasonable to expect that the structural integrity of the red cell membrane suffers.

Typical examples of the effects of temperature on MCV are shown in Fig.4, Fig. 5 and Fig. 6 from this years series of measurements. Fig.4 shows the data for MCV from a goat; note the rather small erythrocyte volumes. Below 46 to 47 °C, the observed volumes are nearly independent of temperature: 17.85 +/- 0.1 μ^3 while the volumes increase dramatically above 47 - 48 °C. Similarly, in Fig 5 , for the case of blood from a seal -- nearly complete temperature independence of MCV below 45 °C with an abrupt increase above this temperature (followed by a very distinct decrease) Finally, shown in Fig. 6 are the results for blood from a killerwhale, Note the large erythrocyte volumes but again no temperature variations below 44 - 45 °C, followed by the same type of pronounced MCV increase above this temperature and a subsequent

drop above 49 °C. Our data on humans generally show the same behaviour as for seals, and killerwhale..
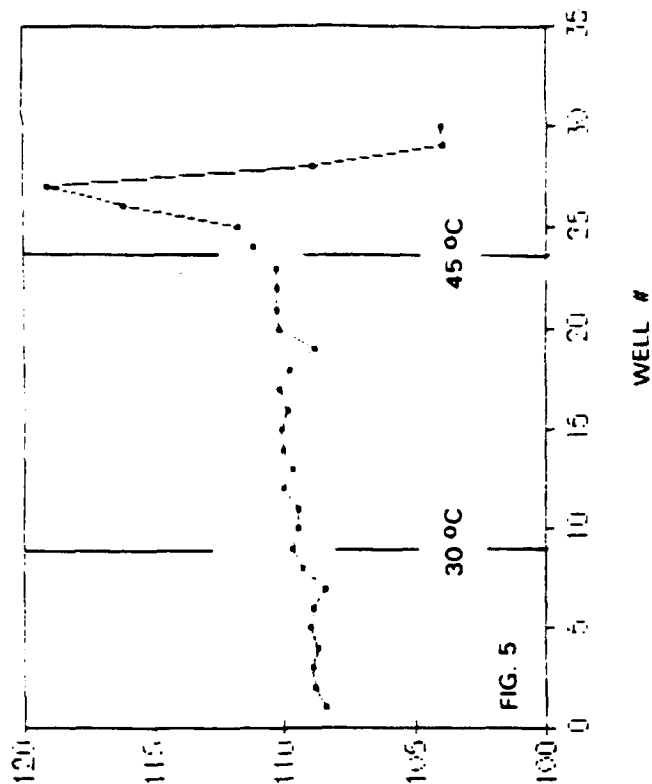
In the lower temperature range which we have now investigated it is found the MCV is generally quite unaffected by temperature. For blood from pigs the variation in MCV over the range of 8 to 35 °C is within $^+/_-$ 0.2 % (!) [with no discernable trend.] Somewhat similar, Fig.7, and Fig. 8 show MCV data for blood from, respectively, a dog and a Yucatan Pig. An inspection of these and other data obtained this summer suggests some systematic trends:: for human subjects an apparent increase in MCV above approx. 30 °C although this is not always seen. The MCV data for the Yucatan Pig decrease slightly with increasing temperature while the data for the dog show a distinct, if modest, increase up to about 25 °C followed by a slight decrease. In most of the above cases the datas suggest that some real trends may exist but overall, for the the cases discussed here, the net change with temperature is modest, less than 2 % - and in some cases much less.

As mentioned earlier in this report, reasons exist to suspect the occurrence of anomalies at or near 15 and 30 °C, related to vicinal water structure changes, while an anomaly may exist near 21 °C because of a membrane lipid phase transition at this temperature. Unfortunately, the total MCV changes seen here are generally too small, compared to the precision of the data, to allow an interpretation of the current data in terms of a structural membrane transition at (or very near) 21 °C. We hope to be able to pursue the question of all the low temperature thermal anomalies (related to vicinal water and membrane lipids) in cell volumes at a later time.

ra corui
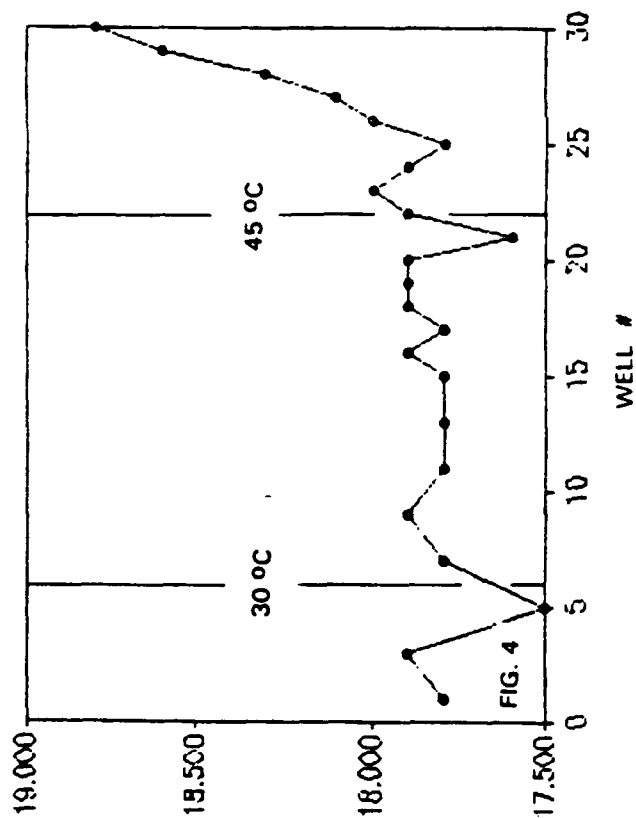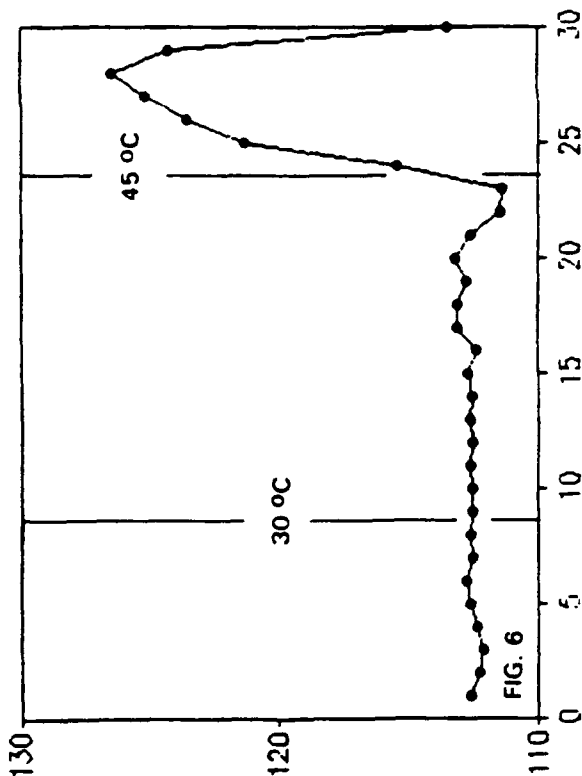
MCV (μ3) SEAL 92TGI22B (# 2. FEMALE)

45 °C

30 °C

WELL #

FIG. 5

MCV (μ3) GOAT 92TGI03B

45 °C

30 °C

WELL #

FIG. 4

MCV (μ3) DOG 92TGI04B

125 °C

15 °C

FIG. 7

MCV (μ3) KILLERWHALE (MALE) 92TGI19B

45 °C
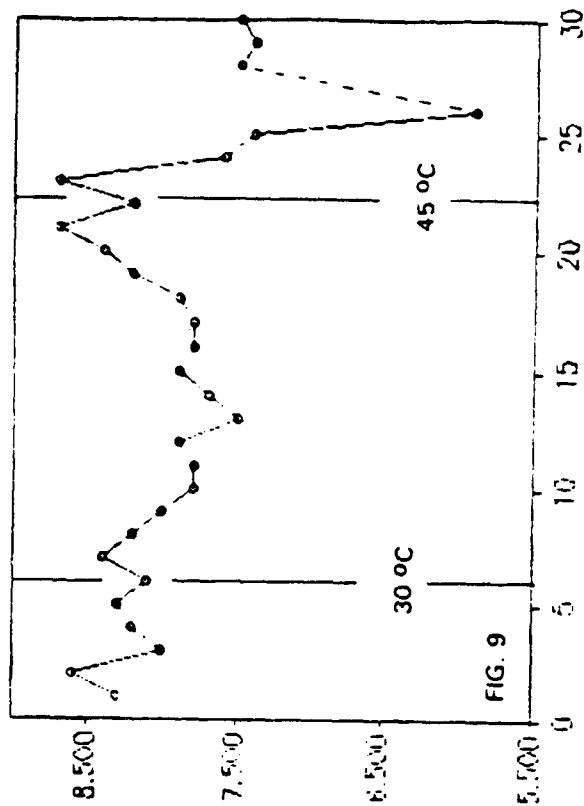
30 °C

FIG. 6

15-8
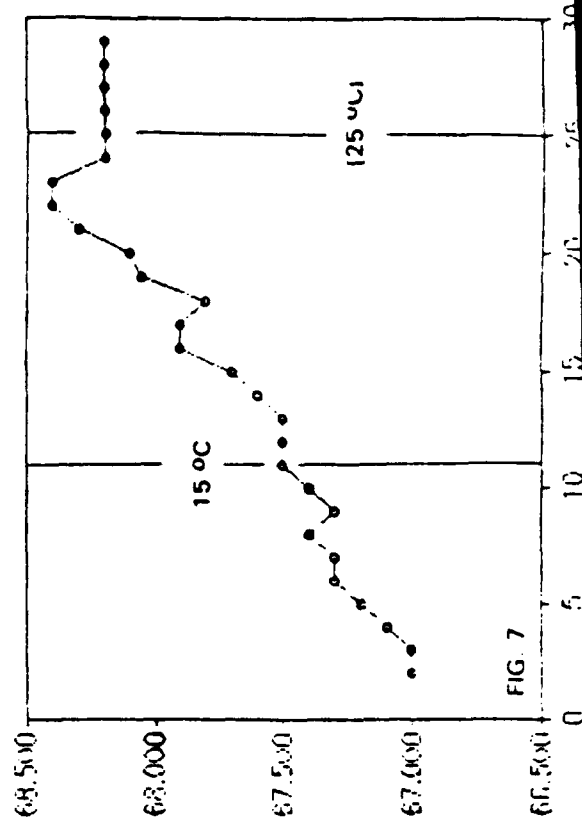
PART III   MEAN PLATELET VOLUME MEASUREMENTS

Mean Platelet Volume (MPV) measurements have been made this summer in connection with all the TGI runs (92TGI01B through 92TGI22B).   The effects of temperature on MPV previously observed at high temperatures (say, 43 to 55 °C) have been confirmed in the experiments carried out this year.   Regardless of the species studied, the most pronounced changes are usually abrupt increases in the MPV around 44 - 48 °C followed by sharp decreases in the volumes.   Part of these volume changes likely signal osmotic effects on the platelets while part of the changes may reflect the observed, strong tendency for "clumping" of the platelets above the critical temperature range of 44 - 46 °C.   [please see discussion of blood cell morphology, Part IV.] Fig.9,   Fig. 10 and Fig. 11show typical sets of data for MPV, respectively for   a human, a goat and a killerwhale.

A number of low temperature measurements of MPV have also been made over the range from about 8 to 35 °C.   Typical changes in MPV are about 10 % over this temperature range which is notably larger than the volume changes observed over the same temperature range for erythrocytes (generally less than 1 (to 2) %.)   Two typical sets of data are shown in Fig.12,   Fig. 13 and   Fig. 14,   respectively, for a dog, a Yucatan pig and a Rhesus monkey.
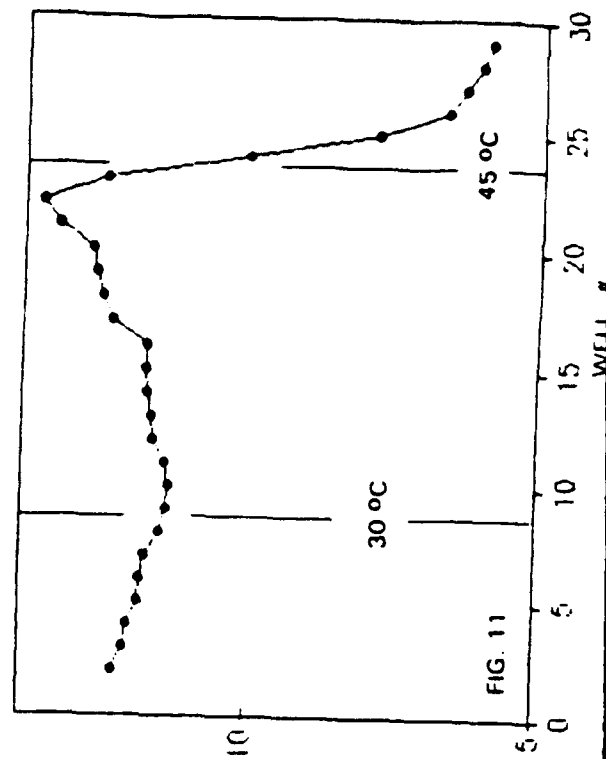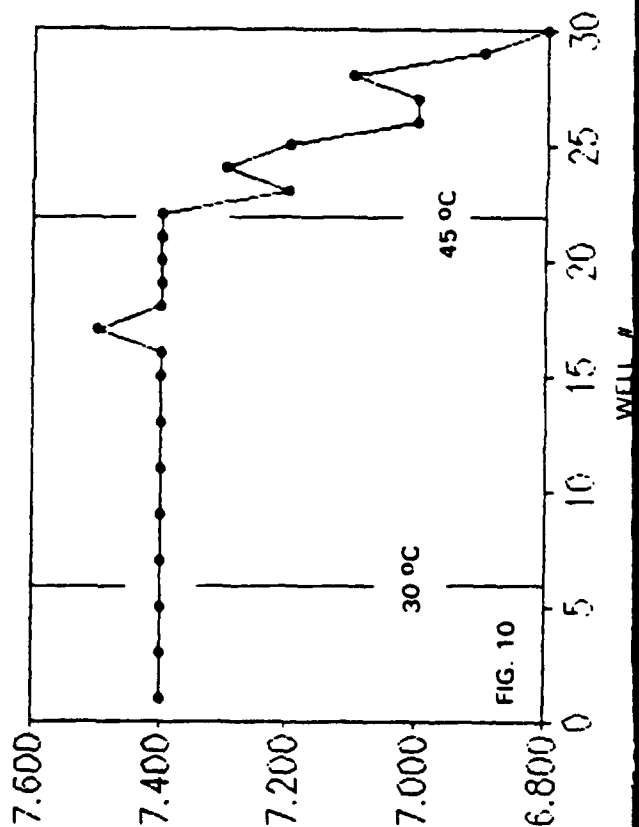
MCV (μ3) YUCATAN PIG   92TGI08B

FIG.8

MPV (μ3) SPECIMEN: HUMAN (D-H)   92TGI01B

FIG. 9

MPV (μ3) GOA   GI03B

FIG. 10

MPV (μ3) KILLERWHALE (MALE)   92TGI19B

FIG. 11

15-10

MPV (μ³) YUCATAN PIG   92TGIO8B

FIG 13

MPV (μ³) DOG   92TGIO4B

FIG. 12

MPV (μ³) RHESUS MONKEY   92TGIO5B

FIG 14

15-11
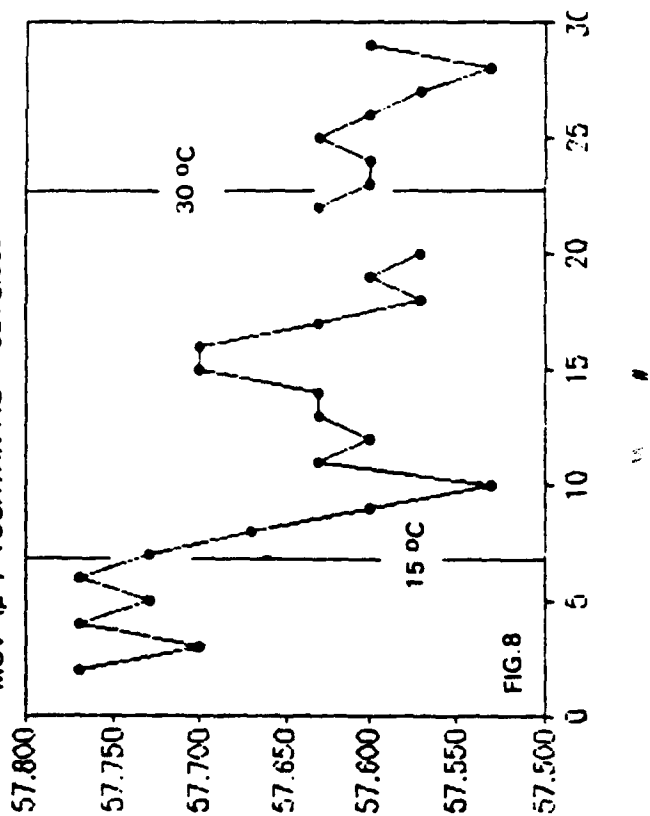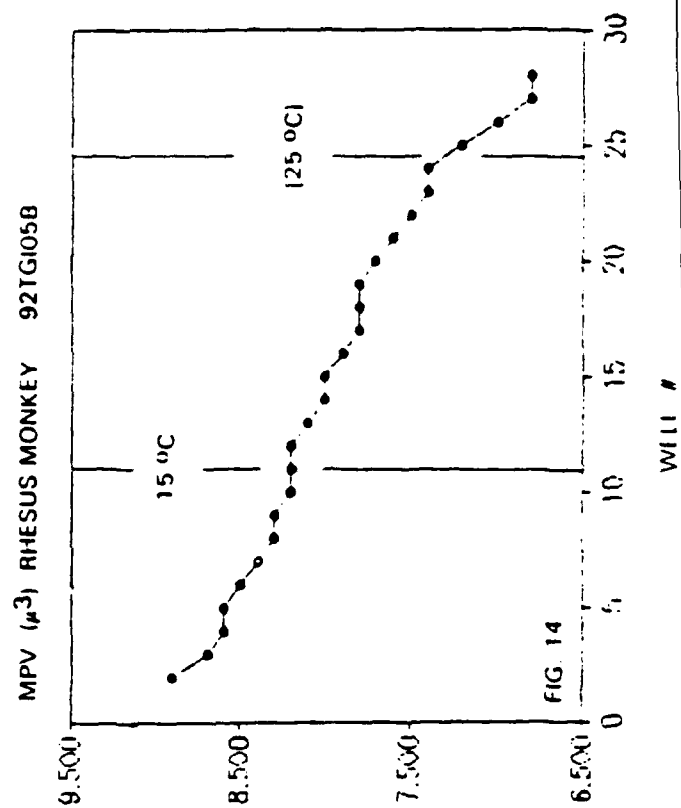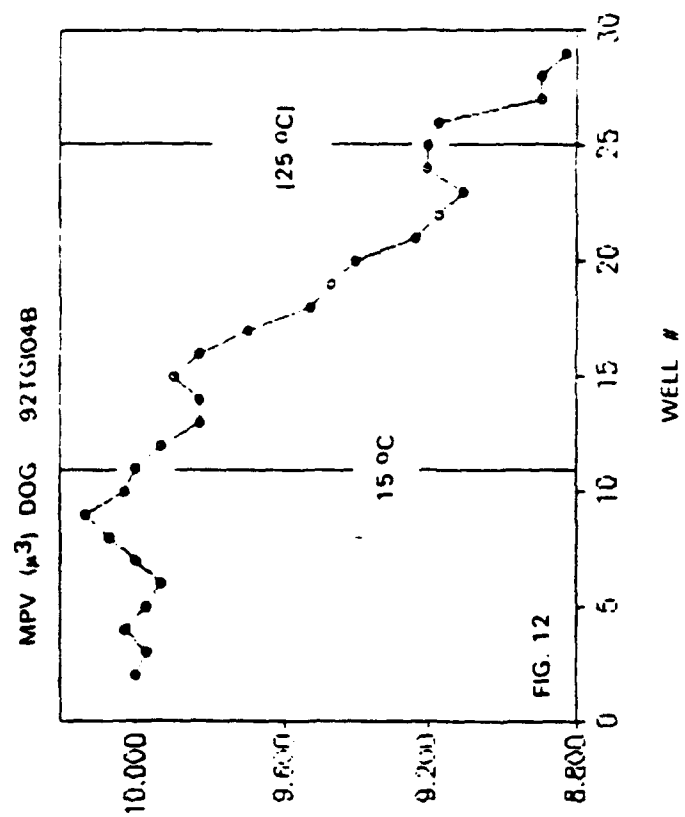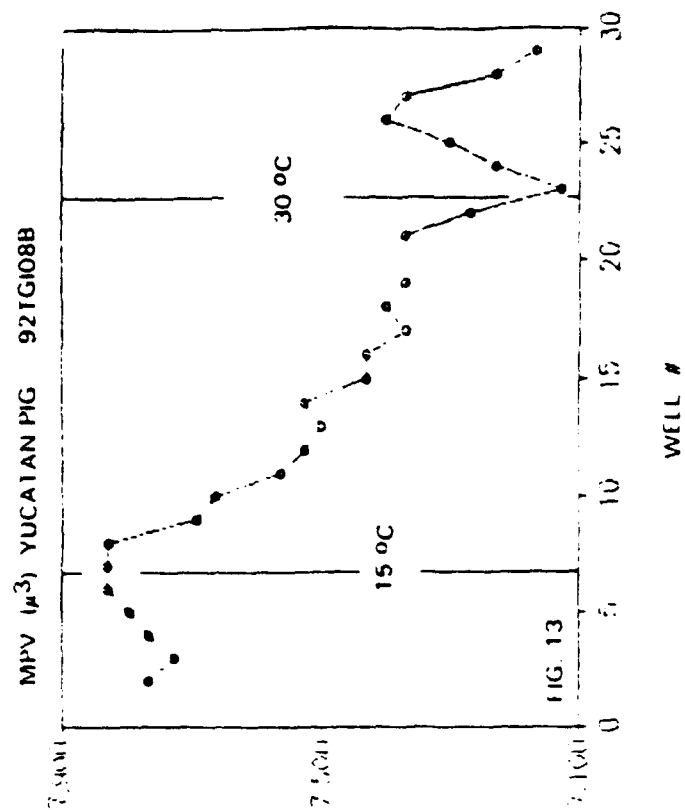
PART IV: BLOOD CELL MORPHOLOGY

In previous studies (1991) notable changes in morphology were observed in a variety of blood samples exposed to temperatures of 44 °C and above, consistent w· ·· the findings in a number of reports in the literature. This summer, 1992, we have ·...rried out a more detailed microscopic study of heated blood samples; in particular, careful observations have been made on blood cell morphology in two experiments on human samples from healthy individuals, respectively from a young male and a female; [Runs 92TGI17B and 92TGI18B]. Blood samples for microscopic examination were taken after two hours of incubation at the various temperatures. The microscopy and analysis of the findings were carried out by a Hematologist, Lt.Col. Wayne Patterson [Ph.D.]. The findings from the two set of samples were nearly identical; below are presented a synopsis of the observations made on sample 92TGI18B.

25° to 42 °C: All cells appear normal in size and shape. Platelets are singular and show granularity consistent with a non-activated state. Neutrophils display a normally appearing segmented nucleus and fine, even granularity.

43.4 °C: RBC's appear to be "stacking" somewhat and some are displaying a shape change to spherocytes and helmet shaped cells. Platelets still appear essentially normal but with some evidence that clumping is beginning to happen. Neutrophils have essentially normal segmentation but slight toxic granulation present in the cytoplasm.

44.4 °C: RBC stacking and tendency towards spherocytosis are seen. Platelets maintain granularity but beginning to aggregate. The neutrophil normally segmented but the cytoplasm is becoming more basophilic.

45.4 °C: RBC stacking evident;. platelets are clumping. The neutrophil shows more basophilic cytoplasm and moderate toxic granulation.

46.4 °C: RBC shape becoming more anomalous. Helmet cells more prevalent. Platelet aggregation is evident and at least half of the platelets are granular, indicating activation and secretion. The neutrophil nucleus is more pycnotic and the cytoplasm more basophilic (which usually indicates cell death and degeneration.)

47.4 °C: RBC shape is even more anomalous with helmet cells, spherocytes and acanthocytes present. "Blebs" on several of the RBC indicate membrane reorganization, probably due to protein conformational changes (denaturation.) Platelets are mostly agranular and aggregated. The neutrophil nucleus

is quite pycnotic and the cytoplasm is very basophilic, displaying moderate toxic granulation. Some platelets adhere to neutrophiles.

48.4 °C: Normal RBC shape is practically . non-existent. Helmet cells, spherocytes, RBC membrane fragments and other bizzare shapes are present, almost exclusively. Cytoplasmic blebbing is widespread. Platelets are aggregated and mostly agranular.. Both the nuclear and cytoplasmic membrane of the neutrophil have disintegrated: the cell itself is likewise disintegrating.

49.4 ° - 51.4 °C: All findings resemble the observations made at 48.4 °C.

The microscopic findings again suggest that dramatic events on the molecular scale occur near 45 ° to 47 °C. In all probability the major event is the 45° transition of vicinal water which most likely corresponds to some kind of transition from one stable structure below the critical transition temperature to another, stable structure above this transition range. It is surmized that a strongly disordered state of the vicinal water prevails right at the transition region, say within a temperature interval of one (to three) °C. As implied in the earlier discussion in this report, the structural membrane protein spectrin may be the major element to become destabilized at T_k. The morphological changes observed go a long way towards explaining the observed sed. rate anomalies and the observed changes in MCV and MPV.

PART V. VISCOSITY DATA

Viscosity measurements, using a Brookfield Model LVTDV-22 variable shear rate viscometer, have been made on aqueous solutions of the following polymers: Polyvinyl pyrrolidone, Polyethylene oxide (PEO), Dextran, Bovine Serum Albumin and Cytochrome-c; - as well as measurements on blood plasma from a number of mammalian species.

The viscosities of most of these systems are sensitive to one or more of the following variables: concentration, ionic strength, pH, shear rate, temperature, past thermal history, age of the solutions and possibly several other parameters not readily identified or controlled. Typical results are presented in Fig.15 through Fig. 18. The one persistent feature in all of these graphs (and indeed in ALL data sets obtained on aq. polymer solutions this summer and in 1991) is the occurrence of thermal anomalies at (or quite near) the Drost-Hansen thermal transition temperatures, T_k, of vicinal water.

Given the notable diversity of the polymers studied, it appears that the only element these macromolecules are likely to have in common is the solvent -- or, more specifically, the water of hydration. Thus it is proposed that consistent with our previous prediction (Etzler and Drost-Hansen, 1983) ALL macromolecules in aq. solution are likely vicinally hydrated and exhibit the thermal transitions of the vicinal wa'er. (Note that the same type of thermal anomalies were also observed in our 1991 AFOSR study of aq. fibrinogen solutions.)

We have previously demonstrated that most (or indeed likely ALL) solid interfaces induce vicinal water structures and as living cells provide a vast amount of intracellular interfaces they must as a result contain a great deal of vicinal water. Add to this the conclusion reached above: that all large macromolecules in aqueous solution are also vicinally hydrated, and it must be concluded that the effects of vicinal water must ramify through ALL biological cells and that many of the thermal anomalies reported above in Erythrocyte Sedimentation Rates, Mean Cell Volumes and Mean Platelet Volumes are indeed manifestations of the cell-associated, vicinal water.
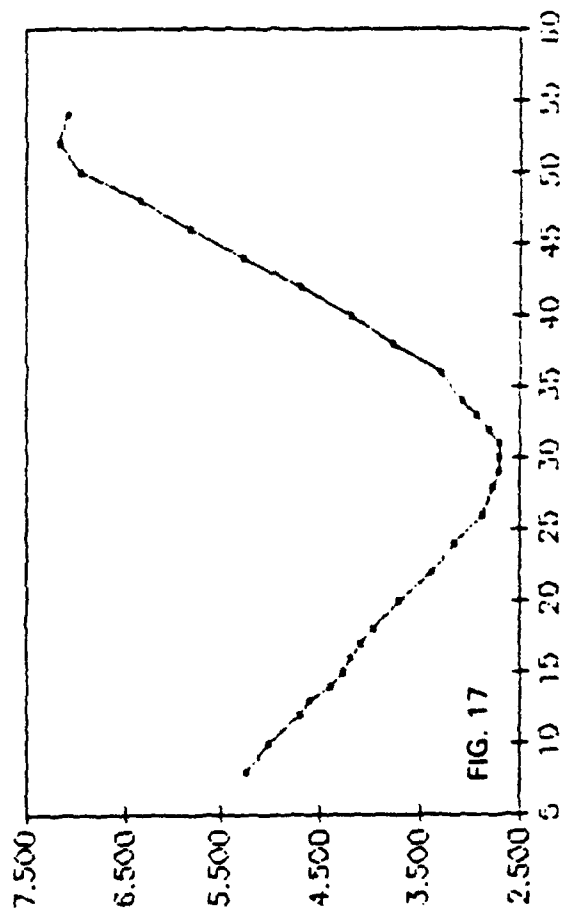
ru corem

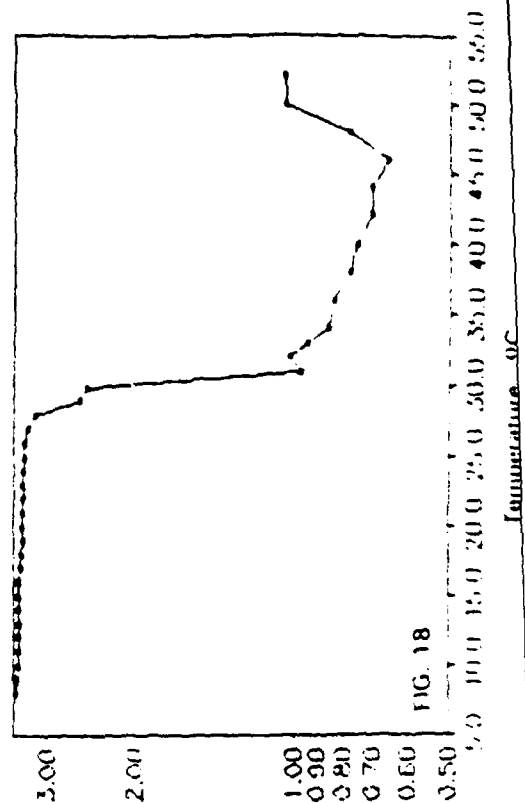log [viscosity (cP)]
DEXTRAN, 5 %, RPM = 12, 6-11-92

FIG. 15
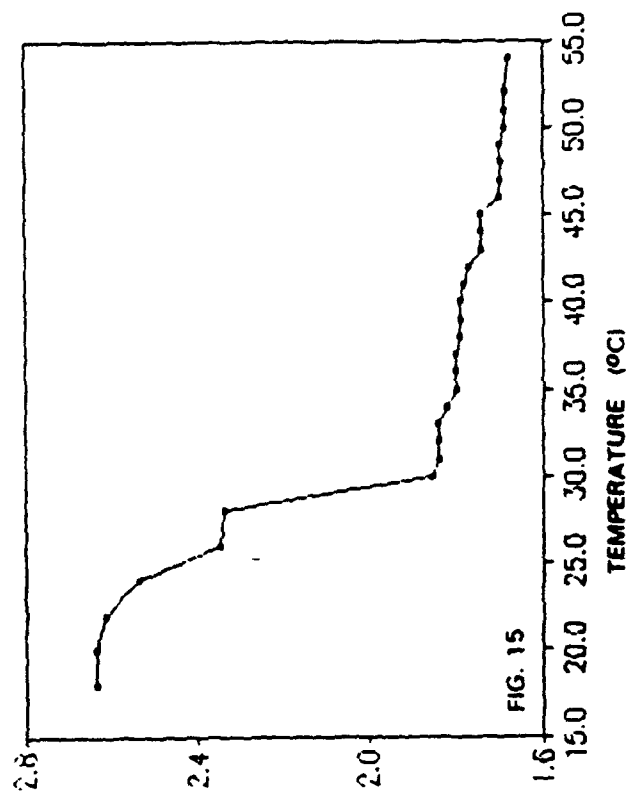
TEMPERATURE (°C)

Viscosity (cP).
BSA, 5% in dist. water   RPM = 3.0

FIG. 16
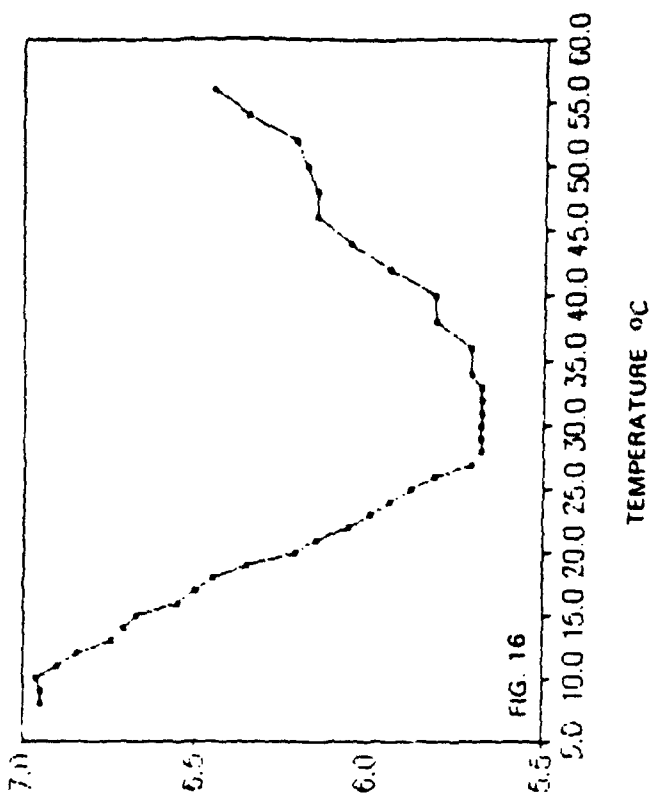
TEMPERATURE °C

Viscosity (cP).
BSA, 5% in 0.9 % NaCl.   RPM = 3.0

FIG. 17

log [viscosity(cP)] vs. temp.
PLASMA Harbor Seal 6.0 RPM. 7-10-92

FIG. 18

Temperature °C

CONCLUSIONS

The Erythrocyte Sedimentation Rate in whole blood has been found to drop abruptly for temperatures above 45 - 46 °C for blood from all species studied, consistent with our findings from 1991 and 1989. This dramatic effect is believed related to the change in vicinal water structure at that temperature (one of the "Drost-Hansen transition temperatures", T_k.) The transitions in vicinal water near 15 and 30 °C do not appear to affect sed. rates to any great extent although some evidence for anomalies in the sed. rates at these temperatures have been seen.

As in previous years, remarkable changes are found in Mean Cell (Red Cell) Volumes (MCV) near 45 - 46 °C. In some cases, notably less dramatic changes are seen also near 15 and 30 °C but in general MCV values are remarkably unaffected by temperature (typical changes less than 1 (to 2) % over a 30 degree interval, below 35 °C.)

Measurements of Mean Platelet Volumes (MPV) invariably show large variations with temperature near 45 - 46 °C. At lower temperatures (say less than 35 °C) MPV values change far more with temperature than observed with Erythrocytes (almost an order of magnitude more) but only occasionally do the thermal anomalies near 15 and 30 °C seem to affect the platelet volumes.

Blood cell morphologies are dramatically affected by temperatures around 44 - 48 °C: Erythrocytes become grossly distorted; neutrophiles disintegrate and platelets aggregate. It is almost certain that these changes must reflect the thermal transition in vicinal water at that temperature range. It is proposed that one of the major red cell structural proteins, spectrin, may be particularly sensitive to the structural aspects of the vicinal water.

As observed last year (1991) we have also this summer found anomalies in the viscosity of aqueous polymer solutions near the thermal transition temperatures of vicinal water, T_k, i.e. near 15, 30, 45 and 60 °C. In any given run, only one or two of the thermal anomalies may been seen in the viscosity data [although in some runs all the anomalies are seen] However, in NO case have we ever failed to see at least one of the vicinal water transitions (1991, 1992.)

Because of the diversity of the polymers studied (: PEO, PVP, Dextran, BSA, Fibrinogen, Cytochrome-c and blood plasma and serum) the thermal anomalies seen are unlikely to reflect some polymer-specific aspect. Instead, it is reasonable to propose that the anomalies must be caused by the one element in common for all these solutions, namely water. As bulk water definitely does not show thermal anomalies the only possible other element must be the vicinal water of hydration of the polymers. In view of this and the overwhelming evidence for vicinal water at all solid/water interfaces, it is inescapable that vicinal water must ramify through ALL of cell biology (and medicine.)

REMMONDATIONS

Let us do more ! -- especially explore the role of vicinal water in clinical medicine.

SPECIES STUDIED AT CID: 1989, 1991, 1992.
ESR,   MCV,   MPV
as well as viscosity measurements
on some model polyelectrolytes, biopolymers, blood plasma
and serum and Na/K distributions as functions of temperature.

For most of the species listed below, ESR, MCV and MPV data have been obtained (with the exception of ESR data for those rather rare cases where the sed rates were too low to yield significant information..) In nearly all cases studied, data were obtained over the range of approximately 22 to 52 $^{\circ}$C and during the 1992 period a number of measurements were also made between 4 and 35 $^{\circ}$C.

HUMANS

CHIMPANZEE
BABOON
MONKEY
PIG
YUCATAN PIG
DOG
HORSE
CAT
COW
SHEEP
GOAT
LLAMA
RAT
RABBIT
KILLER WHALE
HARBOR SEAL

As of the time of preparation of this report (Sept.   1992)   five manuscripts are in preparation for publication. These papers will deal, respectively, with: A)   ESR results;   B) MCV data;   C) MPV data;   D) viscosity data;   and E) time-of-storage effects on sed rates and cell volumes in whole blood. In addition, a major presentation, describing vicinal water and the hydration of polymers in aqueous . solution, was made at the Gordon Research Conference on Water, Aug. 1992.

ACKNOWLEDGEMENT